UNIVERSITAT POLITÈCNICA DE VALÈNCIA

IIAD

Fotónica aplicada a la monitorización de procesos y al desarrollo de sensores en la industria agroalimentaria

Juan Ángel Tomás Egea - Marzo de 2022

Dirigido por: Dra. Marta Castro Giráldez y Dr. Pedro J. Fito Suñer

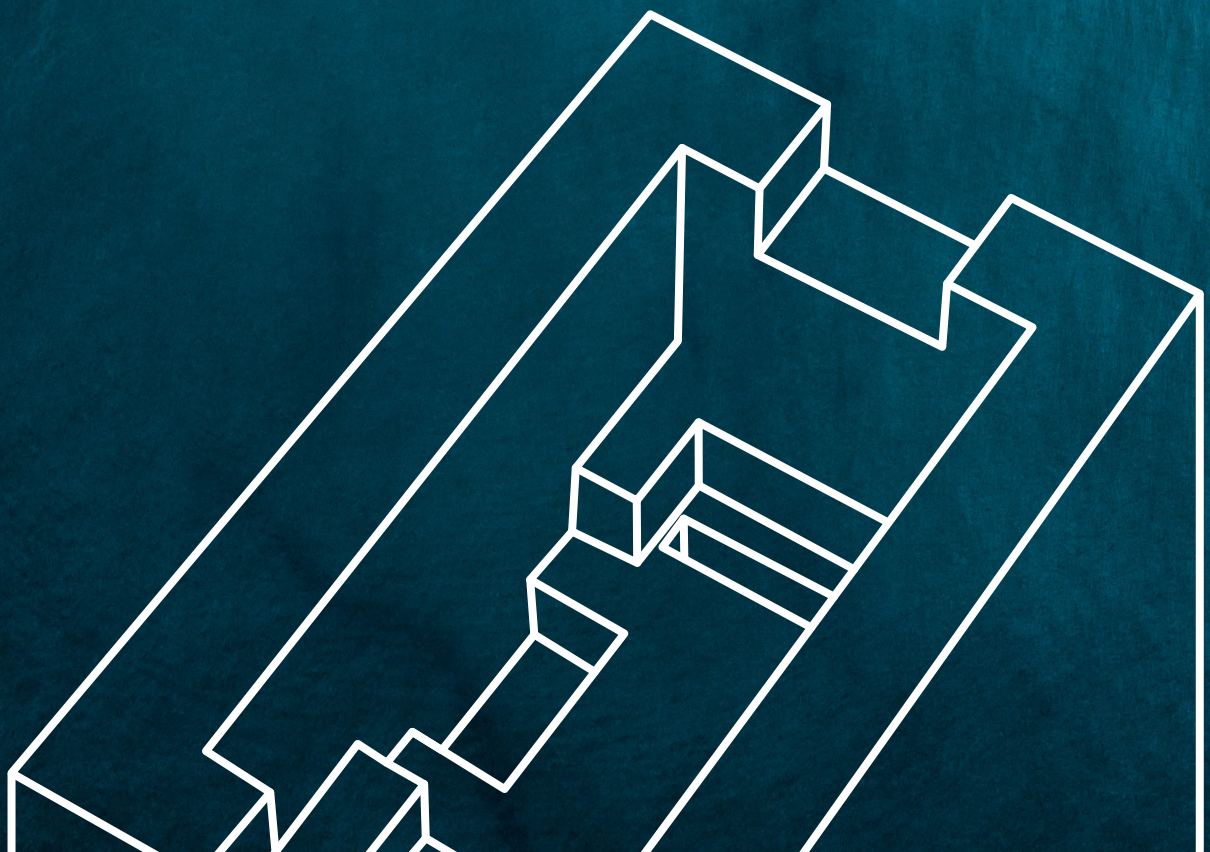

Fotónica aplicada a la monitorización de procesos y al desarrollo de sensores en la industria agroalimentaria

Autor

Juan Ángel Tomás Egea

Directores

Dr. Pedro J. Fito Suñer y Dra. Marta Castro Giráldez

Instituto Universitario de Ingeniería de los Alimentos para el Desarrollo

Universitat Politècnica de València

Marzo de 2022, Valencia, España

Dr. Pedro J. Fito Suñer, profesor titular de universidad, perteneciente al Instituto Universitario de Ingeniería de Alimentos para el Desarrollo de la Universitat Politècnica de València.

Dra. Marta Castro Giráldez, profesora titular de universidad, perteneciente al Instituto Universitario de Ingeniería de Alimentos para el Desarrollo de la Universitat Politècnica de València.

Consideran: que la memoria titulada "Fotónica aplicada a la monitorización de procesos y al desarrollo de sensores en la industria agroalimentaria" que presenta Juan Ángel Tomás Egea, para aspirar al grado Doctor por la Universitat Politècnica de València, y que ha sido realizada bajo su dirección en el Instituto Universitario de Ingeniería de Alimentos para el Desarrollo de la Universitat Politècnica de València, reúne las condiciones adecuadas para constituir su tesis doctoral, por lo que **autorizan** al interesado para su presentación.

Valencia, diciembre de 2021

Fdo: Pedro J. Fito Suñer

Fdo: Marta Castro Giráldez

Normalmente no sé qué escribir en este tipo de cosas, pero lo que sí sabía seguro es que unos agradecimientos tenían que empezar por mi madre. Es la única que puedo decir de verdad que sin ella no habría sido posible nada de esto, ojalá, si alguna vez tengo hijos, sea la mitad de buen padre de lo que tú lo has sido, muchas gracias por todo lo que me has dado y me sigues dando. A mi abuelo por ser la mejor persona que he conocido, por estar siempre de buen humor y ser así de generoso, siempre he pensado que de haber tenido acceso a la educación que tuve yo habría sido uno de los mejores ingenieros.

Obviamente tengo que agradecer estos últimos cuatro años a mis directores Marta y Pedro, Pedro y Marta, ya que, como he dicho muchas veces, no habría hecho nunca el doctorado si no es con ellos dos. El trabajo para mí es algo secundario y lo que más valoro es el trato personal; trabajar con vosotros ha sido divertidísimo y ha valido la pena, muchas gracias por todas las risas y por tratarme tan bien.

Agradecer todo este tiempo también a mi novia, Marta; tú también sabes qué es hacer un doctorado, por lo que se pasa y lo que te da, muchas gracias por estar ahí y apoyarme. Si hablo de apoyo tengo que mencionar también el resto de mi familia, mi tío y mis primos, que están ahí para lo que sea, os considero mi familia y no solamente por los lazos de sangre.

Para acabar, me gustaría mencionar a mis amigos y amigas. A mis amigos del colegio y el instituto, que parece una locura que tengamos tanta relación después de tanto tiempo; a Marta y Fran por esas sesiones de "estudio" durante la carrera, especialmente a Marta por su apoyo y ayuda; a mis amigos del máster, porque es difícil pasárselo mejor con un grupo; por último, a la gente de la universidad, gracias por el buen ambiente y las risas.

Resumen

Analizar y estudiar los procesos y operaciones que se llevan a cabo en la industria alimentaria ayuda a mejorarlos y optimizarlos, aumentando sus rendimientos y, por tanto, sus beneficios. Desarrollar modelos predictivos que mejoren las técnicas de control ya existentes o diseñar nuevos sensores basados en tecnologías menos explotadas es un buen punto de partida para aumentar la rentabilidad de estos procesos.

El secado con aire caliente (HAD), a temperaturas por debajo de la temperatura de evaporación espontánea, podría combinarse con radiación de microondas (MW) como fuente de energía térmica, con el objetivo de reducir el tiempo de secado. Un flujo de fotones en el rango de microondas interactúa con moléculas dipolares (agua) a través de la orientación y la inducción, produciendo almacenamiento de energía eléctrica y acumulación de energía térmica, generando un aumento en la energía interna de los alimentos. Los diferentes mecanismos involucrados en el transporte por agua pueden cambiar en función de si la profundidad de penetración de las microondas excede la dimensión característica de la muestra del transporte de materia. El objetivo de este trabajo es determinar el efecto de las microondas en el secado combinado HAD-MW de patata, con el fin de estudiar las fuerzas impulsoras y los mecanismos involucrados en el transporte de agua y, por tanto, optimizar la potencia utilizada. Para ello, se realizó un secado combinado en muestras de patata con diferentes potencias (0, 4 y 6 W/g). La temperatura de la superficie de la muestra se controló mediante termografía infrarroja y la masa de la muestra se midió en continuo mediante una balanza de precisión. Paralelamente se realizó otro tratamiento de secado a diferentes tiempos (20,

40, 60, 90, 120, 180, 420 min) y condiciones (0, 4 y 6 W/g) para analizar las propiedades dieléctricas, masa, humedad, volumen y actividad del agua de las muestras. Los resultados muestran que es posible monitorizar el secado combinado mediante termografía infrarroja. Además, se puede concluir que el calentamiento por convección se transforma principalmente en evaporación del agua superficial con una conducción térmica insignificante desde la superficie, y la radiación de microondas se transforma principalmente en un aumento de la energía interna de la patata.

Las operaciones de congelación de alimentos requieren un conocimiento extremo de las propiedades fisicoquímicas del alimento a congelar, con el objetivo de lograr un producto que en el momento de la descongelación conserve las mejores propiedades sensoriales y de calidad alimentaria, además de preservar la seguridad alimentaria. Dentro de estas propiedades es necesario conocer la temperatura de congelación inicial o temperatura de nucleación (T_{m0}), la temperatura de congelación de la fase líquida concentrada al máximo por la congelación (T_m') o la temperatura de transición vítrea de la fase líquida concentrada al máximo por la congelación (T_g') entre otras. Sin embargo, las técnicas para determinar estas propiedades son largas, tediosas y, en ocasiones, presentan mucha variabilidad. Entre estas técnicas se encuentra la calorimetría diferencial de barrido (DSC) o las pruebas de textura como el TPA. En este trabajo se propone el uso de la espectrofotometría en el rango de radiofrecuencia (RFP), como un método rápido y fiable para determinar las propiedades térmicas de la pechuga de pollo en el proceso de congelación, comparándola con la técnica de calorimetría diferencial de barrido. Para ello, se ha analizado la permitividad en las dispersiones alfa y beta, determinada por ambas técnicas, DSC y PFR,

donde se obtuvo una T_g' similar y comprendida dentro del rango de valores encontrados en el estudio bibliográfico.

El control de procesos en la industria requiere métodos rápidos, seguros y fáciles de aplicar. En este sentido, el uso de espectroscopía dieléctrica en el rango de microondas puede ser una gran oportunidad para monitorizar procesos en los que la movilidad y cantidad de agua son los parámetros principales a tener en cuenta para producir un producto de calidad y seguro. El confitado de frutas es una operación en la que las muestras primero se deshidratan osmóticamente y luego se exponen a una operación de secado con aire caliente. Este proceso produce cambios tanto en la estructura del tejido, como en las relaciones entre el agua, la matriz sólida y los sólidos solubles añadidos. El objetivo de este trabajo es desarrollar una herramienta dieléctrica capaz de predecir los estados de agua/sacarosa a lo largo del confitado de la manzana, considerando la complejidad del tejido, y describiendo los diferentes fenómenos de transporte y procesos de transición de la sacarosa que transcurren dentro de la muestra.

En los últimos años se ha incrementado el interés general y científico por la nutrición, la digestión y el papel que juegan ambas en nuestro organismo, y aún queda mucho trabajo por realizar en el campo del desarrollo de sensores y técnicas capaces de identificar y cuantificar las especies químicas involucradas en estos procesos. La deficiencia de hierro es el trastorno de la nutrición más común y extendido, afectando especialmente a la salud de niños y mujeres. El hierro presente en la dieta puede estar disponible como hierro hemo u orgánico, o como hierro no-hemo o inorgánico. La absorción de hierro no-hemo requiere su solubilización y reducción del estado férrico a ferroso, que comienza en el ambiente del ácido gástrico, ya que el hierro en

el estado férrico se absorbe con dificultad. También existen especies químicas con capacidad reductora (antioxidantes) capaces de reducir el hierro férrico, como el ácido ascórbico. Este trabajo tiene como objetivo desarrollar un sensor capaz de medir la liberación de compuestos activos encapsulados en diferentes medios, basado en el análisis de las propiedades dieléctricas en el rango de la radiofrecuencia. El sensor se diseñó, desarrolló y probó con cápsulas de alginato de calcio, encapsulando iones de hierro y ácido ascórbico como compuestos activos. El potencial de predicción y medición de este sensor se mejoró mediante una herramienta de predicción a partir de un modelo termodinámico, habilitando la obtención de parámetros cinéticos que permiten optimizar el diseño de las microencapsulaciones de alginato cálcico.

Resum

Analitzar i estudiar els processos i operacions que es porten a terme en la indústria alimentària ajuda a millorar-los i optimitzar-los, augmentant els seus rendiments i, per tant, els seus beneficis. Desenvolupar models predictius que milloren les tècniques de control ja existents o dissenyar nous sensors basats en tecnologies menys explotades és un bon punt de partida per a augmentar la rendibilitat d'aquests processos.

L'assecat amb aire calent (HAD), a temperatures per baix de la temperatura d'evaporació espontània, podria combinar-se amb radiació de microones (MW) com a font d'energia tèrmica, amb l'objectiu de reduir el temps d'assecat. Un flux de fotons en el rang de microones interactua amb molècules dipolars (aigua) a través de l'orientació i la inducció, produint emmagatzematge d'energia elèctrica i acumulació d'energia tèrmica generant un augment en l'energia interna dels aliments. Els diferents mecanismes involucrats en el transport per aigua poden canviar en funció de si la profunditat de penetració de les microones excedeix la dimensió característica de la mostra del transport de matèria. L'objectiu d'aquest treball es determinar l'efecte de les microones en l'assecat combinat HAD-MW de creïlla, amb la finalitat d'estudiar les forces impulsores i els mecanismes involucrats en el transportament d'aigua i, per tant, optimitzar la potència utilitzada. Per a això es va realitzar un assecat combinat en mostres de creïlla amb diferents potències (0, 4 y 6 W/g). La temperatura de la superfície de la mostra es va controlar mitjançant termografia infraroja i la massa de la mostra es va mesurar en continu mitjançant una balança de precisió. Paral·lelament es va realitzar altre tractament d'assecat a diferents temps (20, 40, 60, 90, 120, 180,

420 min) i condicions (0, 4 y 6 W/g) per a analitzar les propietats dielèctriques, massa, humitat, volum i activitat de l'aigua de les mostres. Els resultats mostren que es possible monitoritzar l'assecat combinat mitjançant termografia infraroja. A més, es pot concloure que el calfament per convecció es transforma principalment en evaporació de l'aigua superficial amb una conducció tèrmica insignificant des de la superfície, i la radiació de microones es transforma principalment en un augment de l'energia interna de la creïlla.

Les operacions de congelació d'aliments requereixen un coneixement extrem de les propietats fisicoquímiques de l'aliment a congelar, amb l'objectiu d'aconseguir un producte que en el moment de la descongelació conserve les millors propietats sensorials i de qualitat alimentària, a més de preservar la seguretat alimentària. Dins d'aquestes propietats és necessari conèixer la temperatura de congelació inicial o temperatura de nucleació (Tm0), la temperatura de congelació de la fase líquida concentrada al màxim per la congelació (Tm') o la temperatura de transició vítria de la fase líquida concentrada al màxim per la congelació (Tg') entre altres. No obstant això, les tècniques per a determinar aquestes propietats són llargues, tedioses i, a vegades, presenten molta variabilitat. Entre aquestes tècniques es troba la calorimetria diferencial d'escombratge (DSC) o les proves de textura com el TPA. En aquest treball es proposa l'ús de l'espectrofotometria en el rang de radiofreqüència (RFP) com un mètode ràpid i fiable per a determinar les propietats tèrmiques del pit de pollastre en el procés de congelació, comparant-la amb la tècnica de calorimetria diferencial d'escombratge. Per a això, s'ha analitzat la permitivitat en les dispersions alfa i beta, determinada per totes dues tècniques, DSC y PFR, on es va obtindre una Tg' similar i compresa dins del rang de valors trobats en l'estudi bibliogràfic.

El control de processos en la indústria requereix mètodes ràpids, segurs i fàcils d'aplicar. En aquest sentit, l'ús de espectroscopía dielèctrica en el rang de microones pot ser una gran oportunitat per a monitorar processos en els quals la mobilitat i quantitat d'aigua són els paràmetres principals a tindre en compte per a produir un producte de qualitat i assegurança. El confitat de fruites és una operació en la qual les mostres primer es deshidraten osmòticament i després s'exposen a una operació d'assecat amb aire calent. Aquest procés produeix canvis tant en l'estructura del teixit, com en les relacions entre l'aigua, la matriu sòlida i els sòlids solubles afegits. L'objectiu d'aquest treball és desenvolupar una eina dielèctrica capaç de predir els estats d'aigua/sacarosa al llarg del confitat de la poma, considerant la complexitat del teixit, i descrivint els diferents fenòmens de transport i processos de transició de la sacarosa que transcorren dins de la mostra.

En els últims anys s'ha incrementat l'interès general i científic per la nutrició, la digestió i el paper que juguen totes dues en el nostre organisme, i encara queda molta faena per realitzar en el camp del desenvolupament de sensors i tècniques capaces d'identificar i quantificar les espècies químiques involucrades en aquests processos. La deficiència de ferro és el trastorn de la nutrició més comuna i estesa, afectant especialment la salut de xiquets i dones. El ferro present en la dieta pot estar disponible com a ferro hemo o orgànic, o com a ferro no-hemo o inorgànic. L'absorció de ferro no-hemo requereix la seua solubilització i reducció de l'estat fèrric a ferrós, que comença en l'ambient de l'àcid gàstric, ja que el ferro en l'estat fèrric s'absorbeix amb dificultat. També existeixen espècies químiques amb capacitat reductora (antioxidants) capaces de reduir el ferro fèrric, com l'àcid ascòrbic. Aquest treball té com a objectiu desenvolupar un sensor capaç de mesurar

l'alliberament de compostos actius encapsulats en diferents mitjans, basat en l'anàlisi de les propietats dielèctriques en el rang de la radiofreqüència. El sensor es va dissenyar, va desenvolupar i va provar amb càpsules d'alginat de calci, encapsulant ions de ferro i àcid ascòrbic com a compostos actius. El potencial de predicció i mesurament d'aquest sensor es va millorar mitjançant una eina de predicció a partir d'un model termodinàmic, habilitant l'obtenció de paràmetres cinètics que permeten optimitzar el disseny de les microencapsulacions d'alginat càlcic

Abstract

Analysing and studying the processes and operations carried out in food industry helps to improve and optimize them, increasing their yields and, in other words, their profits. Developing predictive models that improve existing control techniques or designing new sensors based on less exploited technologies is a good starting point to increase the profitability of these processes.

Hot air drying (HAD) at temperatures below the spontaneous evaporation temperature could be combined with microwave (MW) radiation as a thermal energy source in order to reduce the drying time. A photon flux in the microwave range interacts with dipolar molecules (water) through orientation and induction, producing electrical energy storage and thermal energy accumulation and generating an increase in the internal energy of food. The different mechanisms involved in water transport could change when the microwave penetration depth exceeds the sample characteristic dimension of mass transport. The aim of this paper is to determine the effect of MW in the combined HAD-MW drying of raw potato in order to obtain the real driving forces and mechanisms involved in the water transport, with the purpose of optimizing the MW power used. For this purpose, combined drying was carried out on potato samples with different MW power (0, 4 and 6 W/g). The sample surface temperature was monitored by infrared thermography, and the sample mass was measured continuously through a precision balance. In parallel with continuous drying, another drying treatment was performed at different times (20, 40, 60, 90, 120, 180, 420 min) and conditions (0, 4 and 6 W/g) to analyse the dielectric properties, mass,

moisture, volume, and water activity of the sample. The results show that it is possible to monitor combined drying by infrared thermography. Furthermore, it can be concluded that the convection heating is mostly transformed into surface water evaporation, with negligible thermal conduction from the surface, and microwave radiation is mostly transformed into an increase in the potato's internal energy.

Food freezing operations require an extreme knowledge of the physicochemical properties of the food to be frozen, in order to achieve a product that at the thawing time preserves the best sensory and food quality properties, and also preserves food safety. Within these properties it is necessary to know the initial freezing temperature or nucleation temperature (T_{m0}), the freezing temperature of the maximally freeze concentrated liquid phase (T_m') or the glass-transition temperature of the maximally freeze concentrated liquid phase (T_g') among others. However, the techniques to determine these properties are long, tedious, and sometimes with high variability, among these techniques is differential scanning calorimetry (DSC) or textural tests such as TPA. In this work, the use of photospectrometry in the radiofrequency range (PFR) is proposed, as a fast and reliable method for determining the thermal properties of chicken breast in the freezing process, comparing it with the differential calorimetry technique of swept. For this purpose, the permittivity in the alpha and beta dispersions has been analysed, determined by both, DSC and PFR techniques, were a similar T_g' were obtained and comprised within the range of values found in the literature.

Process control in the industry requires fast, safe, and easily applicable methods. In this sense, the use of dielectric spectroscopy in the microwave range can be a great opportunity to monitor processes in which the mobility

and quantity of water is the main property to produce a quality and safety product. The candying of fruits is an operation in which the samples are first osmotically dehydrated and then exposed to a hot air-drying operation. This process produces changes in both the structure of the tissue and the relationships between water, the solid matrix and the added soluble solids. The aim of this paper is to develop a dielectric tool to predict the water/sucrose states throughout the candying of apple, by considering the complexity of the tissue and describing the different transport phenomena and the different transition processes of the sucrose inside the sample.

In recent years, the general and scientific interest in nutrition, digestion, and what role they play in our body has increased, and there is still much work to be carried out in the field of developing sensors and techniques that are capable of identifying and quantifying the chemical species involved in these processes. Iron deficiency is the most common and widespread nutritional disorder that mainly affects the health of children and women. Iron from the diet may be available as heme or organic iron, or as non-heme or inorganic iron. The absorption of non-heme iron requires its solubilisation and reduction in the ferric state to ferrous that begins in the gastric acid environment, because iron in the ferric state is very poorly absorbable. There are chemical species with reducing capacity (antioxidants) that also have the ability to reduce iron, such as ascorbic acid. This paper aims to develop a sensor for measuring the release of encapsulated active compounds, in different media, based on dielectric properties measurement in the radio frequency range. The sensor was designed, developed, and tested with calcium alginate beads, encapsulating iron ions and ascorbic acid as active compounds. The prediction and measurement potential of this sensor was

improved using a prediction tool based on a thermodynamic model, enabling the obtaining of kinetic parameters that allow optimizing the design of calcium alginate microencapsulations.

Índice

Introducción

1.1. Monitorización y modelización de procesos en la industria agroalimentaria

El análisis de los procesos industriales agroalimentarios es un campo de investigación que permite ajustar y optimizar los mismos, redundando en mayores beneficios, menor coste, y/o menor contaminación (Knorr y Watzke, 2019). El desarrollo de modelos predictivos que permitan estimar parámetros del proceso más precisos y óptimos (Castro-Giraldez, Tylewicz, et al., 2011; Castro-Giraldez et al., 2014; Cuibus et al., 2014; Traffano-Schiffo et al., 2014; Talens, Castro-Giraldez y Fito, 2016a; Al-Obaidi, Kara-Zaitri y Mujtaba, 2017; Talens, Castro-Giraldez y Fito, 2018; Traffano-Schiffo, Castro-Giraldez, Colom, et al., 2018b; Chen y Qin, 2019; Tomas-Egea, Fito y Castro-Giraldez, 2019; Li et al., 2020; Prithani y Dash, 2020; Soares de Melo et al., 2020; Tomas-Egea et al., 2021), y el diseño de nuevas técnicas y sensores para monitorizar y controlar los procesos (Castro-Giraldez, Fito, Toldrá, et al., 2010; Usamentiaga et al., 2014; Traffano-Schiffo, Castro-Giraldez, Colom, et al., 2017; Ciampa et al., 2018; Traffano-Schiffo, Castro-Giraldez, Herrero, et al., 2018; Song et al., 2020), son algunas de las vías para alcanzar esos objetivos.

La mayoría de las operaciones de conservación de alimentos buscan reducir la disponibilidad del agua del producto, por tanto, disminuir la actividad del agua y aumentar su estabilidad (Rockland y Beuchat, 2020). Para conseguir reducir esta disponibilidad, por ejemplo, se puede aplicar procesos de deshidratación como el secado con aire caliente (Ashtiani, Sturm y Nasirahmadi, 2018; Wei et al., 2019; Zhou et al., 2019) o la deshidratación osmótica (Phisut, 2012; Chen y Qin, 2019; Putić et al., 2021), que se encargan de eliminar el agua del producto, o procesos de congelación, que buscan

cambiar de fase el agua líquida para que no esté disponible en los procesos de degradación (Colucci, Maniaci y Fissore, 2019; Sfarra et al., 2020; Nida, Moses y Anandharamakrishnan, 2021).

Además, entre la comunidad científica, los consumidores y la industria está creciendo el interés por conocer mejor qué comemos, cómo lo digerimos y cómo lo asimila nuestro organismo. Entre otras cosas, esto nos lleva a analizar y mejorar el conocimiento que tenemos acerca de la asimilación de nutrientes, en qué cantidad llegan y si vamos a ser capaces de asimilarlos son preguntas interesantes, que obligan a estudiar el proceso de digestión. Una de las técnicas que puede ser interesante analizar es la encapsulación de compuestos, la cual permite liberarlos en el punto del sistema digestivo que deseemos (Traffano-Schiffo, Aguirre Calvo, et al., 2017; Churio, Pizarro y Valenzuela, 2018; Criado et al., 2019; Gholamian, Nourani y Bakhshi, 2021).

1.2. Sistemas alimentarios

1.2.1. Carne

El total de carne consumida en las dietas de los humanos varía enormemente entre las diferentes sociedades y entre los mismos individuos que las forman. A nivel global, tanto el consumo medio por habitante, como el consumo total de carne, están subiendo debido a un aumento del consumo y al crecimiento de la población mundial (Godfray et al., 2018). Analizando los datos más en profundidad encontramos cambios dentro de los tipos de carne que se consumen, en particular las carnes blancas como el cerdo y el pollo, percibidas como más saludables, incrementan su consumo, aunque también sigue habiendo una proporción destacable de carne procesada

(Godfray et al., 2018; Milford et al., 2019). La carne de ave es percibida como un alimento barato y con características saludables por ser una buena fuente de proteínas sin mucha grasa (Sanchez-Sabate y Sabaté, 2019), por ello, prosigue la tendencia al alza su consumo y, por tanto, su producción, alcanzando en España los 1,42 Mt en 2014, de los cuales un 86 % es carne de pollo según los datos del Ministerio de Agricultura, Pesca y alimentación (2015).

La carne es un sistema compuesto por tejido muscular y tejido conectivo, el cual, a partir de unas horas post mortem y después de sufrir ciertos procesos metabólicos de maduración, se convierten en carne (Traffano-Schiffo et al., 2021). Este se puede considerar uno de los sistemas biológicos con más complejidad que hay en la naturaleza, debido especialmente a que poseen una de las estructuras más organizadas (Huff Lonergan, Zhang y Lonergan, 2010).

1.2.1.1. Composición de la carne

La carne representa uno de los productos alimenticios más ricos en energía y nutrientes debido a la multitud de componentes que presenta, destacando los altos niveles de proteínas y con presencia de agua, vitaminas, minerales y grasas. (Ahmad, Imran y Hussain, 2018) (Tabla 1). Además, las proteínas presentes en la carne destacan por tener altos niveles de digestibilidad, determinado por la variedad de aminoácidos que componen esas proteínas. Los niveles de digestibilidad son clasificados a partir del Protein Digestibility-Corrected Amino Acid Scores (PDCAAS), que asigna los valores más altos a las proteínas del huevo o la caseína con un 1,00, un 0,92 a la carne y entre un 0,57 y un 0,71 a judías, lentejas o guisantes (Barrón-Hoyos et al., 2013; Pereira y Vicente, 2013).

Tabla 1. Composición nutricional de la carne, adaptada de (Pereira y Vicente, 2013; Ahmad, Imran y Hussain, 2018).

Corte de la carne	Prot. (g)	Gras. sat. (g)	Gras. (g)	Vit. B_{12} (mcg)	Na (mg)	Zn (mg)	P (mg)	Fe (mg)
Pollo	22.8	0.6	1.9	0.7	78	1.4	202	0.7
Pollo, pechuga	24.2	0.2	8.5	0.39	71	0.9	199	1.2
Pollo, pechuga sin piel	22.8	0.4	1.28	0.4	59	0.7	218	0.4
Pavo, sin piel	19.9	1.8	7.1	1.9	42	1.5	209	2.1
Pavo, pechuga sin piel	23.6	0.5	1.6	1	62	0.5	208	0.6
Pato, sin piel	19.4	1.8	6.6	2.8	90	1.8	201	2.5
Cerdo, chuleta	18.1	10.8	31.7	1	60	1.8	190	1.4
Cerdo, lomo	21.9	1.7	4.9	1.1	55	1.9	220	0.7
Cerdo, pierna	20.8	2.8	7.8	1.2	84	2.6	164	0.8
Ternera, lomo	20.9	1.5	3.2	2	59	3.7	142	1.6
Ternera lechal, lomo	20	3.4	7.3	1.1	22	3	193	0.1
Ternera, cortes	21	1.9	4.5	1.9	59	1.7	167	1.3
Cordero, carne o chuletas	20	2.4	4.8	2	63	3.6	221	1.9

El agua es el componente mayoritario del músculo, el cual está presente en un 75 % de su masa en el tejido vivo, y entre el 65 % y el 80 % en el tejido postmortem, transformado ya en carne (Huff-Lonergan, 2010). La mayor parte del agua se encuentra no adsorbida, principalmente en las fibras musculares y en una pequeña proporción, en los tejidos conectivos (Williams, 2007; Huff-Lonergan, 2010; Ahmad, Imran y Hussain, 2018). Dentro del músculo, es el componente principal del líquido extracelular, y dentro de las células musculares, también es el componente principal del sarcoplasma, siendo imprescindible en la regulación de la temperatura, como medio para

los procesos celulares y como transporte de nutrientes entre los diferentes sistemas (Huff-Lonergan, 2010). La carne de ave, principalmente el pollo, tiene unos valores similares al resto de las carnes en cuanto a la cantidad de agua, donde el pollo entero rondaría el 75 % de la masa según (Pereira y Vicente, 2013) y del 75,3 al 76,22 % de la masa de la pechuga sería agua según (Kim et al., 2020), valores confirmados por (Tasoniero et al., 2020) con un 75,6 % y (Pereira y Vicente, 2013) con un 75,92 %. Los alimentos perecederos, como la carne, que presentan valores tan altos de agua, son los candidatos ideales para aplicarles técnicas de conservación que permitan aumentar su vida útil (Ahmad, Imran y Hussain, 2018).

El segundo componente mayoritario en la carne es la proteína, la cual se puede encontrar presente desde el 12,3 % de la carne de pato, hasta un 34,5 % de la masa de algunas pechugas de pollo, en función de factores como la función del músculo, la especie de la que proviene o el corte que se analice (Pereira y Vicente, 2013; Ahmad, Imran y Hussain, 2018). Dentro de la carne de pollo, la media de las proteínas sería 22,9 % (Pereira y Vicente, 2013), mientras que la pechuga presenta un 22,5 % según (Tasoniero et al., 2020), de 21,8 a 22,14 % según (Kim et al., 2020), un 24,1 % según (Pereira y Vicente, 2013) y un 20,51 % según (Wang et al., 2017), que también destaca que los muslos presentan un 19,71 %.

Los dos tipos mayoritarios de grasa en el músculo esquelético son los fosfolípidos y los triglicéridos, siendo estos últimos los más asociados con el músculo (Huff-Lonergan, 2010). En la carne, la grasa actúa como depósitos de energía y como relleno para proteger la piel y los órganos, aportando aislamiento (Wood et al., 2008). El contenido de grasa en canales puede variar desde el 8 al 20 % de su masa, variando en función de la especie (Ahmad,

Imran y Hussain, 2018). La piel es la principal fuente de grasa en la carne de ave, por ejemplo una pechuga de pollo con piel y sin piel varía de 8,9 a 1,2 % según (Pereira y Vicente, 2013), por tanto, una vez retirada se encuentran valores de 1,1 % (Tasoniero et al., 2020) y 1,3 % (Kim et al., 2020) de grasa que confirman esas proporciones.

La principal fuente de carbohidratos en los animales se encuentra en el hígado, que contiene aproximadamente la mitad de los carbohidratos del cuerpo, siendo el más abundante el glucógeno, que está almacenado principalmente tanto en el hígado, como en los músculos y tiene un impacto indirecto sobre el color, la textura, la terneza y la capacidad de retención de agua que tiene la carne (Huff-Lonergan, 2010; Ahmad, Imran y Hussain, 2018). Aunque no sea uno de los componentes más abundantes, los hidratos de carbono también están presentes en cierta medida en el tejido muscular, oscilando entre el 0,5 y el 1,5 % de la masa total (Huff-Lonergan, 2010). A lo largo del proceso de maduración del músculo el glucógeno se transforma en glucosa, que a su vez se transforma en ácido láctico (Jensen et al., 2011). El ácido láctico aumenta en las primeras fases de la maduración, disminuyendo el pH, el cual influye considerablemente en los parámetros antes mencionados: textura, terneza, color y retención de agua (Ahmad, Imran y Hussain, 2018).

En la carne hay presentes otros compuestos además de los nombrados, como es el caso de los minerales, donde el potasio es el más dominante, seguido del fósforo, sodio y magnesio, y aunque no estén en cantidades tan grandes como los anteriores, la carne también representa una buena fuente de hierro (especialmente por estar en forma "hemo") y zinc (Ahmad, Imran y Hussain, 2018). La carne también está considerada la mayor fuente de vitamina B,

especialmente la B12 (Watanabe, 2007). La carne de ave, en especial la pechuga de pollo, es una buena fuente de niacina (100 g cubren el 56 % de la dos diaria recomendada) y vitamina B6 (100 g cubren el 27 % de la dos diaria recomendada) (Pereira y Vicente, 2013).

1.2.1.2. Estructura del tejido animal

El músculo esquelético está formado por una compleja distribución de fibras musculares y tejido conectivo. Una capa de tejido conectivo llamado epimisio recubre los músculos, el cual se extiende hasta el tendón en la mayoría de los músculos para unirlos con los huesos. Los músculos están formados por un conjunto de fascículos, los cuales también están recubiertos por otra capa de tejido conectivo llamada perimisio. Una vez dentro de esos fascículos, podemos encontrar las fibras musculares, las cuales a su vez están rodeadas del endomisio, otro tejido conectivo (Figura 1.1) (Guil Guerrero, 2001; Huff-Lonergan, 2010).

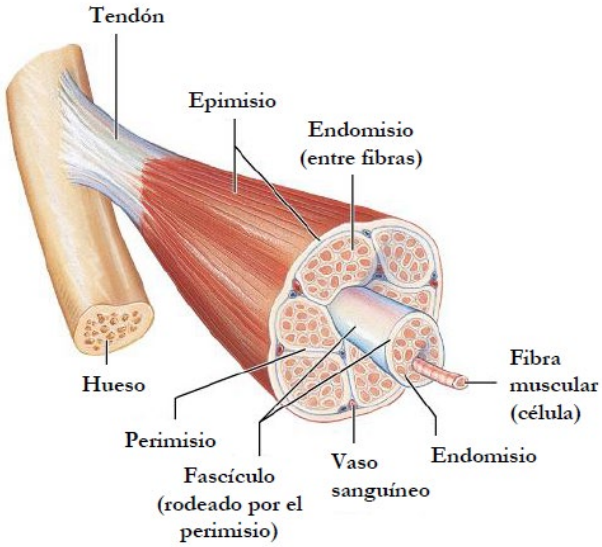

Figura 1.1. Estructura del músculo esquelético. Adaptado de (Campbell y Reece, 2008).

Cada fibra que forma el fascículo contiene todos los orgánulos que se podrían encontrar en células vivas, por lo que a nivel funcional se podría considerar equivalente a una célula. Estas fibras presentan longitudes de varios centímetros, aunque solamente tengan longitudes de 60 a 100 μm. Recubriendo cada fibra se encuentra el sarcolema, el cual está rodeado por el endomisio. Cada fibra está formada de mil a dos mil miofibrillas, representando el 80-90 % del volumen de la célula, y están constituidas por dos tipos de filamentos: filamentos delgados, compuestos principalmente por actina y de 7 nm de diámetro; filamentos gruesos, compuestos fundamentalmente por miosina y de 15 nm de diámetro. Las proteínas miofibrilares constituyen aproximadamente del 50 al 60 % del total de proteínas musculares extraíbles. Sobre la base de todo el músculo, constituyen aproximadamente el 10-12 % del peso total del músculo esquelético fresco, por tanto, son muy importantes en la química de la carne y en la determinación de la funcionalidad de las proteínas cárnicas. Son la maquinaria de contracción (Huff-Lonergan, 2010).

Las fibras musculares presentan dos bandas transversales distintas, las cuales se denominan banda A y banda I. Las bandas A están formadas por filamentos gruesos y parte de filamentos delgados superpuestos, y las bandas I están formadas por filamentos delgados. Además de las bandas, las fibras se pueden dividir en líneas M y Z, además de la zona H. Las líneas Z, que es donde se conectan los filamentos delgados, delimitan el sarcómero, la unidad básica de contracción del músculo (Figura 1.2). En músculo vivo, los sarcómeros cumplen las funciones de locomoción y como efecto secundario de esta función, también producen una parte importante del calor corporal. En el músculo postmortem, parámetros del sarcómero como la longitud

tienen efectos marcados sobre la textura de la carne cruda y cocida, la retención de agua, especialmente en la carne cruda, así como efectos indirectos sobre el color y el sabor entre otros (Ertbjerg y Puolanne, 2017).

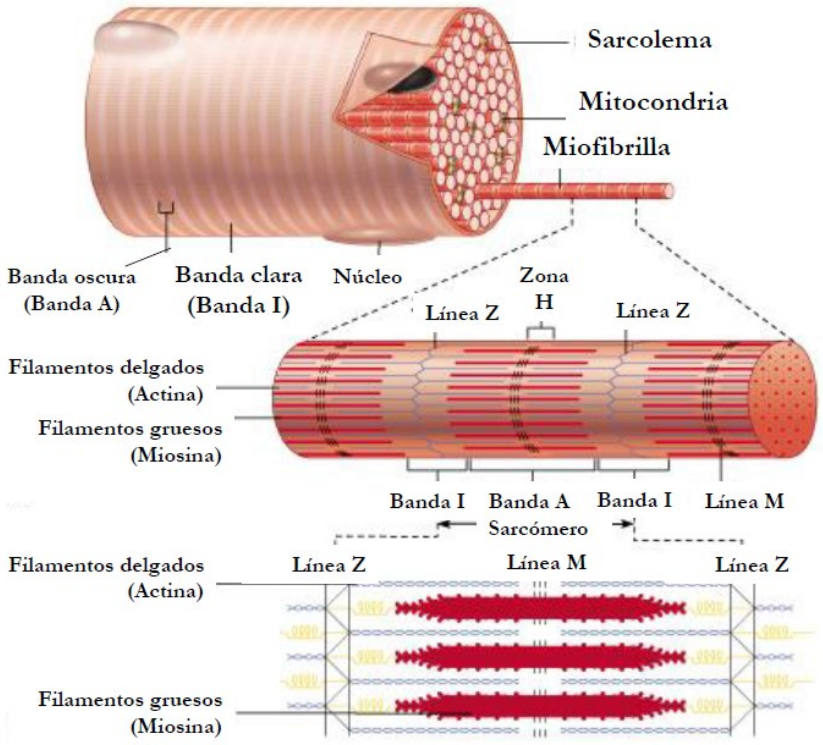

Figura 1.2. Estructura de las fibras que componen el músculo. Adaptado de (Campbell y Reece, 2008).

El mecanismo básico de retención de agua en la carne es muy complejo y solo ha llegado a comprenderse parcialmente. Las principales teorías para explicar la retención de agua incluyen el efecto de la repulsión electrostática entre los filamentos de miosina y actina (Hamm, 1972), las fuerzas osmóticas y capilares (Offer et al., 1989), el área de superficie de las proteínas que interactúan con sarcoplasma (Ertbjerg y Puolanne, 2017) y la

estructura del agua (Puolanne y Halonen, 2010). Además, cuando las proteínas solubles en agua se han desnaturalizado durante el rigor mortis, dependiendo del pH y la temperatura, se puede formar un sistema de soporte entre los filamentos (Liu et al., 2016).

Cuando el músculo entra en el estado de rigor y se contrae, la capacidad de retención de agua de la carne se reduce. Para comprender la relación entre la estructura del sarcómero y la retención de agua, se deben considerar las distancias entre los filamentos de miosina y actina durante la contracción y el rigor. A medida que el músculo entra en rigor, hay un cambio en la estructura del sarcómero como resultado de una contracción general de las miofibrillas y del acortamiento del sarcómero. Una posibilidad es que esta reducción en la retención de agua, en longitudes de sarcómero más cortas, puede deberse al tirón más fuerte creado por el mayor número de puentes cruzados. Alternativamente, también podría ser el propio sarcómero que se acorta, causando distancias más largas entre los filamentos longitudinales y, por lo tanto, una menor repulsión electrostática. Este efecto de disminución de la capacidad de retención de agua parece que es menos destacable en músculos formados por sarcómeros más largos (Ertbjerg y Puolanne, 2017).

Las variaciones en la cantidad de agua liberada, después del acortamiento muscular previo al rigor, puede explicarse en función de los cambios estructurales dentro del sarcómero. Estos cambios implican el grado de superposición de los filamentos de miosina y actina, y el número de enlaces cruzados entre ellos durante el desarrollo del rigor, el espacio entre los filamentos y la contracción de las estructuras proteicas, inducida por el pH a medida que se establece el rigor. Cuando el volumen del sarcómero se reduce, el sarcoplasma queda expulsado y se acumula en espacios entre la red

endomisial y las miofibrillas, llegando incluso a migrar hacia el área del perimisio, debido a esto, eventualmente aparecerá algo de líquido como goteo en la superficie de la carne. Observando este fenómeno de reubicación del agua dentro del músculo con el rigor mortis, se deduce que la pérdida por goteo es un proceso continuo que implica la transferencia de agua de las miofibrillas al espacio extracelular y que deben existir diferentes poblaciones de agua dentro y fuera de las miofibrillas (Hughes et al., 2014). La existencia de tres poblaciones de agua distintas en carne de cerdo se ha demostrado mediante mediciones de RMN, observando también una relación negativa entre la longitud del sarcómero y la pérdida por goteo (Bertram, Purslow y Andersen, 2002).

1.2.2. Tejido vegetal

Los tejidos vegetales están constituidos por diversos tipos de tejido, pero el más abundante es el tejido parenquimático, el cual forma un sistema con una estructura compleja de conexiones intercelulares, espacios extracelulares e intracelulares (Castro-Giraldez, Tylewicz, et al., 2011; Ahmed, Qazi y Jamal, 2016). El espacio de las células parenquimáticas está ocupado fundamentalmente por vacuolas grandes, llegando a ocupar más del 80 % del volumen, rellenas de disoluciones acuosas delimitadas por una membrana, el tonoplasto, cuya función es ser permeable de forma selectiva y mantener tanto la turgencia, como el crecimiento celular (Martinoia, Massonneau y Frangne, 2000; Martinoia et al., 2018). Estas disoluciones presentan solutos como los aminoácidos, el ácido málico dentro de los ácidos orgánicos, la fructosa dentro de los múltiples sacáridos y el potasio dentro de los iones inorgánicos (Taiz et al., 2015). Por tanto, las vacuolas son las responsables del

almacenamiento de los compuestos nombrados anteriormente, que dan el aroma y el sabor a las frutas (Shiratake y Martinoia, 2007).

Las células vegetales están delimitadas por las membranas celulares, las cuales permiten el transporte de agua mediante unas proteínas (aquaporins) que tienen una permeabilidad muy alta al agua (Agre, Bonhivers y Borgnia, 1998; Maurel y Chrispeels, 2001). Rodeando esta membrana celular se encuentra la pared celular, la cual está constituida por fibras de celulosa, formando una matriz muy hidratada, proporcionando a las células vegetales su característica flexibilidad y resistencia mecánica. Entre pared y pared celular se encuentra una lámina fina de compuestos que adhieren las células entre ellas con compuestos adhesivos, pectatos de calcio y magnesio. Además, en la pared celular se encuentran los plasmodesmos, que son unos canales que permiten la comunicación con las otras células adyacentes (Taiz et al., 2015).

Cuando un tejido parenquimático se ve sometido a una operación que le obliga a cambiar su composición, el transporte se puede dar a través de tres caminos diferentes: el transporte apoplástico, que representa el transporte de compuestos externo a las células vegetales; el transporte simplástico, que representa el transporte molecular entre células gracias a los plasmodesmos; el transporte transmembrana, que representa el intercambio de compuestos entre el interior de la célula vegetal y el espacio extracelular, fundamentalmente gracias a los aquaporins (Agre, Bonhivers y Borgnia, 1998; Maurel y Chrispeels, 2001). La principal fuerza impulsora del transporte pasivo dentro de los tejidos parenquimáticos es la diferencia de gradiente de potencial químico, mientras que el transporte activo, el cual requiere de energía (ATP), transporta agua mediante bombas de calcio (Moraga et al.,

2009), azúcares mediante bombas de sodio (Zeuthen, 2010) y electrolitos mediante bombas de potasio/sodio (Jaitovich y Bertorello, 2006).

Las manzanas se componen principalmente de agua, gases, sólidos solubles e insolubles y se distribuyen en cuatro fases (Figura 1.3) (Fito et al., 2007):

- Matriz sólida: fundamentalmente formada por los orgánulos celulares que se encuentran en el citoplasma y las distintas membranas celulares, entre las que se encuentran el tonoplasto, la plasmalema y la pared celular.
- Fase líquida intracelular.
- Fase líquida extracelular.
- Gas.

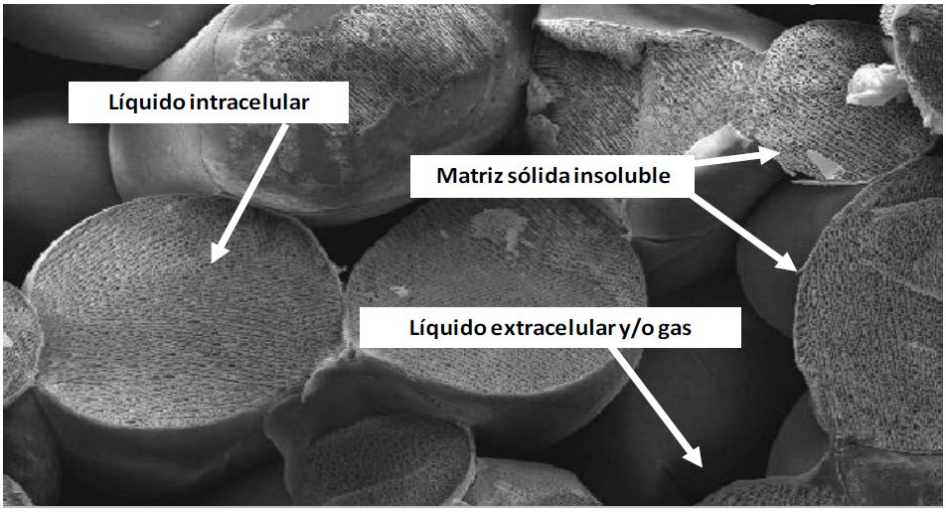

Figura 1.3. Micrografía de tejido parenquimático. Adaptada de (Fito et al., 2008).

La patata también presenta una mayoritaria presencia de tejidos parenquimáticos (Figura 1.4). En cuanto a la composición, la patata está

formada por agua y materia seca, la cual está compuesta por almidón (15 %), azúcares, compuestos nitrogenados, lípidos, ácidos orgánicos, compuestos fenólicos, minerales y polisacáridos que no son el almidón (protopectinas, pectinas solubles, hemicelulosas y celulosas) (Kita, 2002).

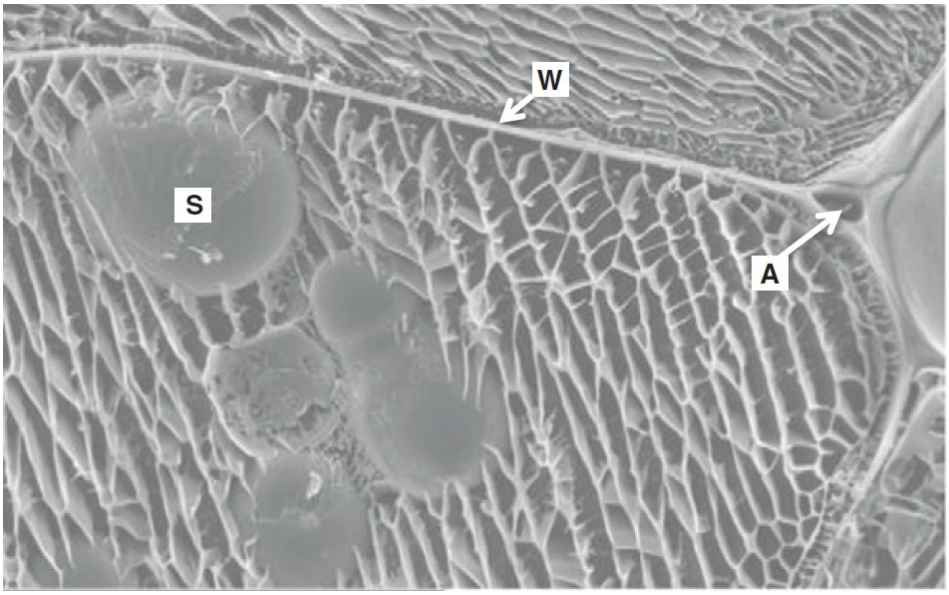

Figura 1.4. Micrografía de patata fresca a 750x. S es un gránulo de almidón, A es un espacio de aire y W es la pared celular (Cuibus et al., 2014).

1.2.3. Encapsulación de compuestos bioactivos

El trastorno nutricional más extendido y común entre la población es el déficit de hierro, el cual, según la OMS, tiene una relación estrecha con la anemia, llegando a provocar anemia hasta en el 25 % de la población mundial (De Benoist et al., 2008; Charles, 2012). Esta deficiencia afecta principalmente a países en desarrollo y a los sectores de la población de países más desarrollados con menos recursos, aunque también hay que destacar que es una deficiencia más común en periodos de crecimiento y en mujeres durante el embarazo (Charles, 2012). En los alimentos, el hierro puede estar

disponible en forma orgánica (hemo) en productos como la carne y la sangre, o en forma inorgánica (no-hemo) en productos de origen vegetal y ovolácteos (Anderson, Frazer y McLaren, 2009). El hierro hemo tan solo supone el 10-20 % del hierro presente en una dieta, pero su absorción es la más eficiente (Sharp y Srai, 2007). El hierro no-hemo, en cambio, aunque tiene una presencia mayoritaria dentro de la dieta, es mucho menos biodisponible (Sermini, Acevedo y Arredondo, 2017), por tanto, requiere de la reducción de su estado férrico (Fe^{+3}) a ferroso (Fe^{+2}), ya que en estado férrico puede ser absorbido por el organismo (Anderson, Frazer y McLaren, 2009). Para llevar a cabo esa reducción, se pueden utilizar especies químicas reductoras (antioxidantes), como sería la vitamina C. La absorción del hierro se lleva a cabo fundamentalmente en el duodeno y en el yeyuno, entrando al enterocito principalmente por el transportador Heme Carrier Protein 1 (HCP1) y por el Divalent Metal Transport 1 (DMT1) (Figura 1.5) (Anderson, Frazer y McLaren, 2009).

Por tanto, reforzar la dieta con hierro hemo, o hierro no-hemo acompañado de compuestos con capacidad antioxidante, podría reducir la incidencia de la anemia en la población. Una técnica interesante para dosificar estos complementos nutricionales puede ser la microencapsulación de los compuestos activos, ya que permitiría asegurar la liberación de los compuestos encapsulados a lo largo del intestino delgado, especialmente en el duodeno y en el yeyuno, salvando así las condiciones adversas del estómago (Churio, Pizarro y Valenzuela, 2018).

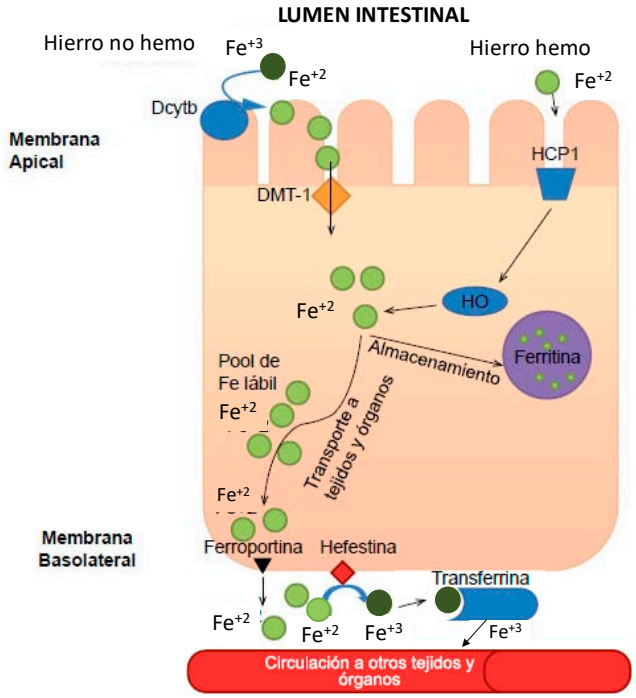

Figura 1.5. Esquema de la absorción del hierro hemo y no-hemo por parte del enterocito. Adaptada de (Sermini, Acevedo y Arredondo, 2017).

La microencapsulación mediante gelificación iónica es un técnica que se basa en incluir ciertos compuestos activos dentro de una matriz protectora para controlar su liberación y/o protegerlos de procesos de degradación como oxidación, evaporación o degradación térmica (Santagapita, Mazzobre y Buera, 2012; Traffano-Schiffo, Aguirre Calvo, et al., 2017; Traffano-Schiffo, Castro-Giraldez, Fito, et al., 2017). Entre los distintos materiales utilizados en la gelificación iónica formar esas matrices de las microencapsulaciones, la formación de hidrogeles de alginato cálcico (alginato-Ca(II)) es una de las opciones que mejores resultados ofrece (Fang et al., 2007; Santagapita, Mazzobre y Buera, 2012; Traffano-Schiffo, Aguirre Calvo, et al., 2017;

Churio, Pizarro y Valenzuela, 2018; Criado et al., 2019; Gholamian, Nourani y Bakhshi, 2021).

El alginato sódico es un polisacárido que consiste en un conjunto de polímeros lineales, constituidos por los ácidos α-L-gulurónico (G) y β-D-manurónico (M), y unidos en diferentes secuencias mediante enlaces α (1→4). Las secuencias pueden estar compuestas de las mismas unidades (GGGG o MMMM), o alternando unidades (GMGM). La cantidad y distribución de cada monómero se determina en función de la naturaleza del biopolímero (Sonego et al., 2016). La gelificación se produce fundamentalmente debido al intercambio de iones de Na^+ de los ácidos carboxílicos presentes en las moléculas de alginato de sodio, con iones de Ca^{2+} de la solución de reticulación, lo que conduce a la formación de enlaces cruzados con la estructura característica de "caja de huevos" (Figura 1.6) (Lee y Mooney, 2012; Zeeb et al., 2015; Zhang et al., 2016).

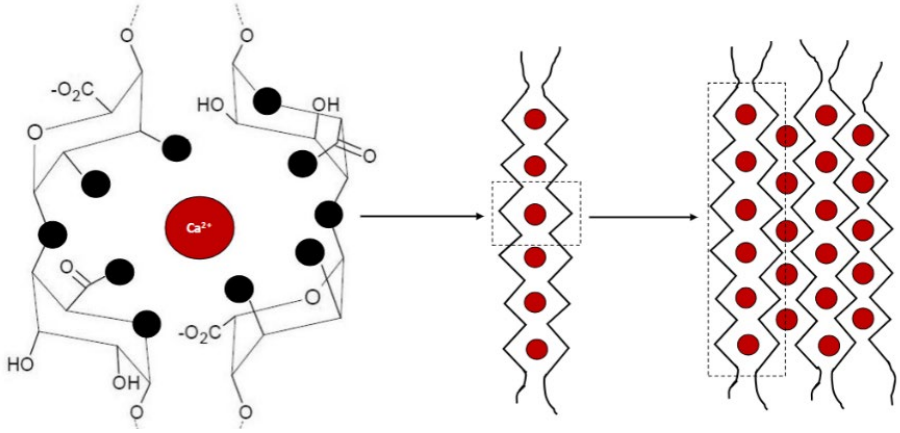

Figura 1.6. Esquema de la estructura de "caja de huevo", formada a partir del proceso de entrecruzamiento del alginato cálcico. Adaptado de (Fang et al., 2007).

Las microencapsulaciones de alginato cálcico son fáciles de producir, versátiles, biodegradables y de uso alimentario, sin embargo, presentan un tamaño de poro grande (Santagapita, Mazzobre y Buera, 2011) y niveles altos de actividad del agua, lo que las hace susceptibles al crecimiento microbiano y reacciones de degradación (Rahman y Labuza, 2020). Para cubrir los puntos débiles que tienen este tipo de cápsulas se recurre a procesos de conservación por deshidratación, como lo es el secado con aire caliente, el cual mejora la estabilidad al disminuir la actividad del agua (Traffano-Schiffo, Castro-Giraldez, Fito, et al., 2017).

1.3. Termodinámica irreversible

La termodinámica, procedente del griego terme (calor) y dinámica (fuerza), es una ciencia que estudia las transformaciones que se producen en la materia y la energía asociados a cambios de temperatura o a los cambios moleculares (Demirel y Gerbaud, 2019a), formulando las fuerzas impulsoras que los generan, a nivel promedio y basándose en las variables de estado, lo que la convierte en una ciencia macroscópica. La formulación teórica de la termodinámica clásica, nacida en el siglo XIX con Savery, Newcomen, Carnot, Clausius, Kelvin o Gibbs, es un conjunto de leyes que gobiernan el comportamiento de los sistemas macroscópicos, sin embargo, fueron precursoras de la mecánica cuántica y de la física de partícula, evolucionando a la vez durante los siglos XX y XXI con Einstein, Schrödinger, Prigogine o Onsager. Estas leyes conducen a un gran número de ecuaciones y axiomas, que han ido evolucionando con la física actual. Los principios de la termodinámica encuentran aplicaciones en todas las ramas de la ingeniería y las ciencias, con múltiples aplicaciones, por ejemplo, en el diseño de procesos, equipos y productos en la ingeniería alimentaria.

Para comenzar a hablar de las leyes de la termodinámica hay que empezar por la ley que define el equilibrio térmico o ley cero de la termodinámica, definida por Fowler en 1935 como "*Dos cuerpos en contacto con capacidad conductora entre ambos alcanzarán el equilibrio térmico intercambiando energía*". Esta ley es quizá la que más tiempo ha costado definirla, ya que no habría sido posible sin el desarrollo de la ley de enfriamiento de Newton en 1701, la definición de energía térmica y calor por parte de Thomson en 1798, la modelización de los flujos de calor mediante la ley de Fourier 1822 o el primer intento por definir el equilibrio térmico por parte de Maxwell en 1871 con la expresión "*Todo el calor es del mismo tipo*". Sin embargo, no se podría entender sin el modelo de movimiento browniano descubierto por Einstein en 1905 o sin la definición de energía interna de Schrödinger en 1926. La definición de equilibrio composicional entre especies químicas se definiría más tarde por Gibbs en 1876, definiendo los potenciales termodinámicos, térmicos y químicos, que indicaban el movimiento del calor o de las especies químicas en función de la definición del equilibrio.

Durante un proceso de transformación, la materia y la energía se puede transportar o convertir de una forma a otra, siempre que el total de la materia y/o la energía se mantenga constante, esto se conoce como el Principio de conservación de la materia y la energía, o primer principio de la termodinámica, descrito primero para la materia por Lavoisier, y posteriormente para la energía por Mayer, fusionándolos Einstein a principios del siglo XX con la teoría de la relatividad, quedando como "*La materia y la energía ni se crea ni se destruye solo se transforma*" (Fito et al., 2020). Durante este proceso de transformación los cambios se pueden producir de manera reversible, sin incremento de la entropía total del sistema, o de manera

irreversible, con incremento de la entropía. Los procesos de transformación alimentaria suelen producirse de manera irreversible, ya que implican transformaciones en la materia que no dan la posibilidad a recuperar el estado inicial, este punto de vista queda mejor explicado en el siguiente párrafo.

El segundo principio de la termodinámica, enunciado por Carnot en 1824, dice "*La cantidad de entropía del universo tiende a incrementarse con el tiempo*", lo que describe los procesos naturales como irreversibles. Este punto es importante en esta tesis, ya que algunos estudios presentados, desarrollan los potenciales químicos, que inducen los transportes y las transformaciones químicas en tejido animal y vegetal, son analizados a presión, volumen, temperatura y composición variable, es decir, considerando la irreversibilidad de las transformaciones. Por supuesto, este principio evolucionó mucho con las aportaciones, primero de Onsager en los años 30, y posteriormente por Prigogine en los años 70 del siglo XX.

Por último, la tercera ley de la termodinámica, que hace referencia al estado fundamental de la materia, ha sufrido transformaciones hasta la actualidad. Para entender esta ley hay que trasladarse a los límites de la energía interna, y con ella, los de la temperatura. En 1779 Lambert aproximó la menor temperatura posible en -270 °C, pero esta cifra bajó hasta los -273,15 °C en 1848 por Kelvin, definiendo el cero absoluto. La primera definición la propuso Planck en 1912 como "*la entropía tiende a desaparecer conforme el sistema se aproxima al cero absoluto*", esta definición la reformulo Nernst en 1916 como "*En el cero absoluto no se produce ningún cambio de entropía*", lo que generaría en la definición actual de "*En el cero absoluto una especie química alcanza la entropía de su estado fundamental*". El principio de Nernst fue demostrado experimentalmente en 2017 (Masanes y Oppenheim, 2017). El desarrollo de esta ley permitió en

1924 a Einstein y a Bose descubrir estados próximos al fundamental que han permitido desarrollar ordenadores quánticos o el propio LHC, clave de la demostración del modelo estándar de partícula.

Los sistemas físicos estudiados por la termodinámica que se comporten de forma estable y sean reversible son poco comunes. Considerando las ecuaciones que describen procesos físicos dependientes del tiempo, si no varían con respecto al signo algebraico del tiempo el proceso se denomina proceso reversible, de lo contrario, se denomina proceso irreversible (Demirel y Gerbaud, 2019b).

La modelización de procesos desde el punto de vista de la termodinámica irreversible permite estimar las propiedades termodinámicas de un alimento y su entorno, lo que mejora la comprensión de la microestructura de la interfase que hay entre el alimento y el agua y permite determinar tanto el punto hasta el cual el alimento debe ser deshidratado para que se considere estable, como la cantidad de energía necesaria para deshidratarlo (Aviara y Ajibola, 2002). El uso de los principios de la termodinámica irreversible como herramienta para modelizar y estudiar procesos ha quedado demostrado por múltiples autores desde que se formularon esos principios, habiendo evolucionado hasta la actualidad. La termodinámica irreversible se ha utilizado para estudiar el proceso de congelación, desde la nucleación y cristalización, hasta la estructura que se forma (Castro-Giraldez et al., 2014; Cuibus et al., 2014; Hudait y Molinero, 2014; Schmelzer et al., 2018; Hellmuth, Schmelzer y Feistel, 2020; Nida, Moses y Anandharamakrishnan, 2021); la refrigeración de manzanas en postcosecha (Wang y Zhang, 2021); el secado con aire caliente de alimentos (Traffano-Schiffo et al., 2014; Talens, Castro-Giraldez y Fito, 2016; Soares de

Melo et al., 2020; Tomas-Egea et al., 2021); procesos basados en la ósmosis (Al-Obaidi, Kara-Zaitri y Mujtaba, 2017; Chen y Qin, 2019; Zhao et al., 2020; Putić et al., 2021); procesos de salado (Castro-Giraldez, Fito y Fito, 2010b; Velázquez-Varela, Fito y Castro-Giraldez, 2014).

La mayoría de los alimentos son estructuras celulares o coloidales que presentan una elevada complejidad, debido fundamentalmente a que su compartimentación en fases no se encuentra en equilibrio, por tanto, los modelos termodinámicos requieren información más detallada (Mohos, 2018). Para solucionar esta falta de información, puede ser interesante combinar un enfoque fenomenológico con principios termodinámicos para investigar sistemas físicos, químicos y biológicos con procesos irreversibles (Soares de Melo et al., 2020). La ecuación de Gibbs es una relación clave, ya que combina la primera y segunda leyes de la termodinámica. La relación de Gibbs, combinada con las ecuaciones de balances basadas en el equilibrio termodinámico local, permiten estimar la entropía, lo que ayuda a analizar el nivel de disipación de energía durante un proceso y a describir los fenómenos acoplados (Herrera, 2017; Demirel y Gerbaud, 2019a).

La energía disponible para transformarse dentro de un sistema es la energía libre (G). Los alimentos son sistemas compartimentados, separados por interfases, pueden presentar múltiples componentes y, además, esos componentes pueden variar, por tanto, la energía libre depende tanto de variables de estado como la temperatura (T) o la presión (P), como de la composición del sistema. Esto se ve reflejado en la ecuación simplificada de Gibbs-Duhem (Ecuación 1.1), en la cual las variables de estado son constantes (Demirel y Gerbaud, 2019a).

$$\Delta G = -S\Delta T + V\Delta P + \sum_i \mu_i \, \Delta n_i \qquad (1.1)$$

Donde S es la entropía, V el volumen, μ el potencial químico, n la cantidad de moles y el subíndice i representa la especie química.

Además de las variables descritas en la ecuación 1.1, existen otras fuerzas impulsoras que aportan energía libre al medio añadidas por otros autores con el fin de ajustar y optimizar la ecuación de la energía libre de Gibbs, extendiéndola para hacerla más completa (Bhalekar y Andresen, 2017; Wahid, 2018; Calvo-Schwarzwälder, 2019). En la ecuación 1.2 se pueden ver los términos de elongación (FΔl) y el término que describe el efecto del campo eléctrico en el sistema inducido por los iones disueltos (ΨΔe) (Castro-Giraldez, Fito y Fito, 2010b).

$$\Delta G = -S\Delta T + V\Delta P + F\Delta l + \Psi\Delta e + \sum_i \mu_i \, \Delta n_i \qquad (1.2)$$

El potencial químico representa la energía libre que hay en un sistema por mol de componente. En sistemas con una presión y una temperatura constante en el que el componente no interacciona con el resto de especies químicas presentes, el potencial químico se puede expresar como en la ecuación 1.3 (Xiong et al., 2020).

$$\mu_i = \left(\frac{G}{n_i}\right)_{T,P,n_{j\neq i}} = RT \, Ln(a_i) \qquad (1.3)$$

Siendo R la constante de gases ideales (0,08205746 atm L/mol K) y a_i la actividad, definida como la relación entre la fugacidad de la especie química estudiada (i) y la fugacidad máxima.

Cuando se combinan la ecuación 1.2 (Gibbs-Duhem extendida) y la ecuación 1.3, se obtiene la ecuación 1.4. Mediante la ecuación 1.4 es posible cuantificar y estudiar las distintas fuerzas impulsoras del movimiento molecular. En el caso de los alimentos se podría aplicar al agua, que es el principal indicador de estabilidad, para modelizar distintos procesos de deshidratación.

$$\Delta\mu_i = \frac{\Delta G}{\Delta n_i} = -\bar{s}_i\Delta T + \bar{v}_i\Delta P + \bar{F}_i\Delta l + \bar{\Psi}_i\Delta e + \mu_i|_{T,P,n_{j\neq i}} + \sum \mu_j\Big|_{T,P,n_{j\neq i}} \quad (1.4)$$

Donde s es la entropía parcial molar y v es el volumen parcial molar.

Las leyes fenomenológicas pueden describir muchos procesos irreversibles comunes con simetría temporal rota. En los casos en los que se aplican principios termodinámicos de no-equilibrio, pero en sistemas cercanos al equilibrio global, las ecuaciones de transporte y velocidad se expresan en formas lineales y las relaciones recíprocas de Onsager son válidas (Onsager, 1931a, 1931b). La formulación de la termodinámica lineal de no equilibrio ha demostrado ser válida y útil para una amplia gama de procesos de transporte y velocidad de sistemas físicos, químicos y biológicos (Santos et al., 2018). Las relaciones de Onsager establecen que, haciendo una elección correcta para los flujos y fuerzas, la matriz de coeficientes fenomenológicos es simétrica. Los coeficientes fenomenológicos cruzados se definen como (Ecuaciones 1.5 y 1.6) (Demirel y Gerbaud, 2019b):

$$L_{ik} = \left(\frac{\partial J_i}{\partial X_k}\right)_{X_j} = \left(\frac{J_i}{X_k}\right)_{X_j=0} (i \neq k) \quad (1.5)$$

$$K_{ik} = \left(\frac{\partial X_i}{\partial J_k}\right)_{J_i} = \left(\frac{X_i}{J_k}\right)_{J_i=0} \quad (i \neq k) \tag{1.6}$$

La primera relación de Onsager (Ecuación 1.7) determina que el flujo de una especie química determinada (J_i) se puede estimar a partir de la relación entre el coeficiente fenomenológico (L_i), que se utiliza para describir la relación entre esa especie química y el medio a través del cual circula, y la fuerza impulsora que mueve la especie química como el potencial químico (μ_i).

$$J_i = L_i \Delta\mu_i \tag{1.7}$$

La aplicación de la primera relación de Onsager se ha utilizado con éxito para relacionar los flujos de agua y sal en salado de carne de cerdo (Castro-Giraldez, Fito y Fito, 2010b), en el proceso de salado de queso (Velázquez-Varela, Fito y Castro-Giraldez, 2014), para modelizar el secado con aire caliente combinado con microondas de piel de naranja, permitiendo estudiar el término mecánico (Talens, Castro-Giraldez y Fito, 2016), en deshidratación osmótica de kiwi para describir los términos mecánicos asociados (Traffano-Schiffo et al., 2016) y para estudiar los fenómenos de contracción/expansión en secado con aire caliente de carne (Traffano-Schiffo et al., 2014).

1.4. Procesos

1.4.1. Secado con aire caliente (HAD)

El secado es el proceso de conservación de alimentos más común y se basa generalmente en la eliminación de parte del agua de un tejido, sistema coloidal o disolución. Miles de años de experiencia y métodos de prueba y

error, así como la investigación realizada durante los últimos cien años, dieron como resultado el desarrollo de una variedad enorme de métodos y equipos de secado (Lewicki, 2006; Mujumdar, 2014; Onwude et al., 2019; X. Wang et al., 2019; Zhou et al., 2019). El secado con aire caliente, en concreto, se basa en generar un gradiente de potencial químico de agua entre un fluido con un potencial químico menor (aire caliente y seco), y un producto con un potencial químico mayor (alimento), para inducir una migración del agua de dentro del producto a la superficie, donde se evapora y se incorpora al fluido. El proceso es complejo, ya que implica el transporte simultáneo de masa y energía en un sistema higroscópico que sufre cambios en su estructura (Ratti, 2001). El objetivo del secado con aire caliente (HAD) es el de reducir la actividad del agua de los productos mediante la eliminación del agua presente en el producto, hasta niveles en los que sea estable, ya que la mayoría de los alimentos presentan niveles muy altos, lo que favorece el crecimiento microbiano y aumenta la velocidad de las reacciones de degradación (Liu et al., 2019). El proceso de conservación de secado es uno de los que más energía consumen, además, suelen utilizarse combustibles fósiles, por lo que es necesaria la investigación para optimizar el proceso y el desarrollo de nuevas fuentes de energía (Ratti, 2001).

Uno de los parámetros más utilizados en el secado con aire caliente es la velocidad de secado (v_s), es decir, la velocidad a la que se elimina la humedad (X_w)del producto (Ecuación 1.8), marcando dicha velocidad las distintas etapas de secado.

$$-(dX_w/dt) = (fX_w) = v_s \tag{1.8}$$

La operación de secado con aire caliente se divide en tres etapas (Figura 1.7), dependiendo del mecanismo que determine la velocidad de secado. El transporte del agua durante el secado contempla tres fenómenos: transporte de agua por el interior hasta la superficie, evaporación del agua en la superficie con el correspondiente transporte de calor procedente del aire y el transporte del agua a través del aire. Inicialmente dichos fenómenos se producen de manera desacoplada, marcando la primera etapa denominada inducción que, con el tiempo acaban acoplándose para formar un único flujo de agua de salida, gobernado por el mecanismo más lento. La segunda etapa, o periodo de velocidad constante, se caracteriza por alcanzar y mantener la máxima velocidad de secado. Durante la etapa anterior, la temperatura de la superficie ha evolucionado hasta alcanzar la temperatura húmeda del aire (o de saturación adiabática), manteniéndose constante en este periodo, y utilizando el flujo de calor para evaporar agua exclusivamente; durante este periodo el factor limitante es la velocidad de evaporación de agua de la superficie ya que tanto el transporte interno de agua como el transporte a través del aire son más rápidos. La movilidad del agua en el interior del alimento va disminuyendo conforme se reduce la disponibilidad de la misma, y cuando dicha velocidad se iguala a la velocidad de evaporación superficial (humedad crítica), se pasa a una nueva etapa en la que la velocidad interna sigue disminuyendo, pasando a ser el factor limitante, y por tanto la velocidad de secado decrece, dicha etapa se denomina periodo de velocidad decreciente. Durante esta etapa, el calor procedente del aire es invertido en evaporar y calentar el alimento. En este periodo el alimento sufre distintas transformaciones que definen las propiedades de calidad y seguridad del

producto final, algunas físicas como la transición vítrea, otras químicas como las reacciones de Maillard, de Strecker o de caramelización.

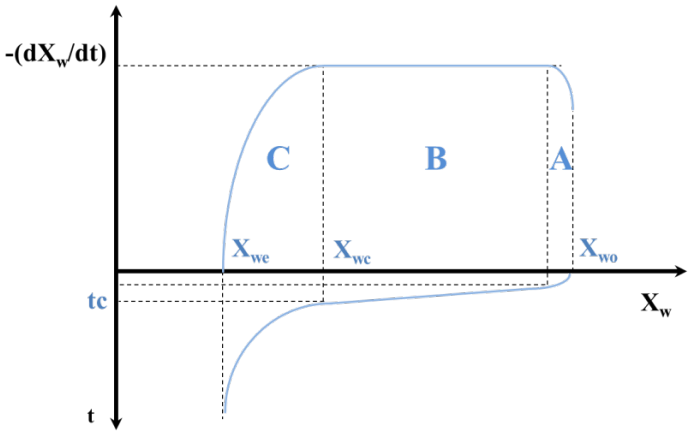

Figura 1.7. Curva de secado de productos húmedos, donde A representa el periodo de inducción, B el periodo de velocidad constante y C el periodo de velocidad decreciente.

Mediante la aplicación de la termodinámica irreversible para modelizar procesos biológicos utilizando ecuaciones como la de Gibbs-Duhem (apartado 1.3 de la introducción) es posible estimar el gradiente de potencial químico del agua para temperaturas de secado inferiores a la del cambio de estado (ecuación 1.9) (Traffano-Schiffo et al., 2014).

$$\Delta\mu_w = \frac{\Delta G}{\Delta n_w} = -\overline{s_w}\Delta T + \overline{v_w}\Delta P + RT\,Ln\frac{\varphi}{a_w} \qquad (1.9)$$

Donde φ es la humedad relativa del aire de secado.

En el secado con aire caliente, la energía necesaria para hacer el cambio de estado de líquido a gas en la superficie del producto, procede mayoritariamente del aire en función del régimen de circulación del mismo (Talens, Castro-Giraldez y Fito, 2016a). Para que estas condiciones se

cumplan, la velocidad del aire debe ser superior a 5,13 m/s, donde la temperatura superficial baja hasta la temperatura de saturación adiabática y el incremento del trabajo de flujo compensa las pérdidas de energía interna (Green y Southard, 2019).

1.4.2. HAD combinado con microondas

Como ya se ha comentado en el apartado anterior, la diferencia de potencial químico del agua que hay entre un producto con una actividad del agua alta y un fluido con una humedad relativa muy baja impulsa el transporte del agua del producto, al fluido. Este transporte exige un cambio de estado de primer orden, de líquido a gas, por tanto, necesita energía para llevarlo a cabo. En el secado con aire caliente, la energía necesaria para este cambio de estado se aporta desde la energía interna del aire, disminuyendo su temperatura y, por ende, subiendo su humedad relativa, pero si aparecen en el sistema fuentes de energía alternativas, este fenómeno se vería reducido (Dehghannya, Bozorghi y Heshmati, 2018).

Una de las técnicas más extendidas que consiguen aportar esa energía extra es el secado combinado con microondas (Dehghannya et al., 2019), debido a las interacciones que tienen los fotones con las moléculas dipolares en este rango de frecuencias. La molécula dipolar más extendida en los tejidos biológicos es el agua, la cual, al entrar en contacto con un flujo de fotones en el espectro de las microondas comienza a inducirse y orientarse, generando fricción y colisiones con otras moléculas, lo que aumenta su energía interna (Tanaka y Sato, 2007).

Los fotones emitidos en microondas (2,45 GHz en Europa; 915 MHz en EE. UU.) penetran en el producto en función de la humedad que tenga y

la frecuencia de los fotones, donde a mayor frecuencia, mayor calentamiento, pero menor penetración. Gracias a la penetración no sólo se aporta energía en la superficie, por lo que no solamente se favorece el cambio de estado en la superficie, si no que favorece también la transición en el interior, lo que puede provocar fenómenos de expansión (Talens, Castro-Giraldez y Fito, 2016; Dehghannya, Hosseinlar y Heshmati, 2018; Tomas-Egea et al., 2021). Por tanto, combinar ambas técnicas no sólo acelera el proceso de deshidratación, si no que reduce también los fenómenos de encostramiento y compactación gracias a la expansión de los tejidos internos (İlter et al., 2018), aumentando la porosidad del producto deshidratado. Por tanto, es útil e interesante la investigación en torno a modelizar y analizar el proceso combinado de secado de aire caliente con microondas para poder optimizarlo (İlter et al., 2018; Xu et al., 2018).

1.4.3. Deshidratación osmótica

La deshidratación osmótica (DO) es esencialmente un proceso de transferencia de masa que implica la inmersión de alimentos en soluciones hipertónicas, lo que provoca tres flujos de materia simultáneos y en direcciones contrarias, deshidratando e impregnando el producto (Ramya y Jain, 2017). El primer flujo es de agua que se mueve desde el producto hasta la solución, cuyo objetivo es disminuir su actividad del agua para aumentar la estabilidad, con una velocidad de deshidratación que va decayendo conforme se equilibran las concentraciones; el segundo flujo es una transferencia de solutos desde la disolución hacia el producto, lo que se puede utilizar para introducir principios activos, agentes conservantes o simplemente mejorar las propiedades organolépticas; el tercer flujo representa el transporte de solutos nativos del producto hacia la solución osmótica, que, aunque el flujo sea

despreciable cuantitativamente, es importante tener en cuenta este fenómeno para estimar la composición final (Ramya y Jain, 2017; Prithani y Dash, 2020), ya que puede representar una pérdida de electrolitos, antioxidantes o vitaminas hidrosolubles. La fuerza impulsora responsable de este transporte son los gradientes de potencial químico de agua y solutos (Muñiz-Becerá, Méndez-Lagunas y Rodríguez-Ramírez, 2017; Shete et al., 2018). Esta operación de conservación es muy extendida en productos de origen vegetal, como la fruta, debido a su estructura interna y las características que le confiere al producto final (Ahmed, Qazi y Jamal, 2016; Bozkir et al., 2019). Si se aplica la DO a un producto como pretratamiento y posteriormente se le somete a un secado con aire caliente para secarlo, se consigue el caramelizado (Tomas-Egea, Fito y Castro-Giraldez, 2019).

El transporte de materia que ocurre durante el proceso de deshidratación osmótica de tejidos vegetales transcurre por vías apoplásticas (extracelulares), vías simplásticas (intracelulares) y transmembrana (Figura 1.8). En células vegetales, la pared celular no presenta selectividad al transporte de solutos, mientras que la membrana celular es selectiva, es decir, semipermeable, y controla el transporte de solutos de la solución osmótica (Phisut, 2012). La difusión o impregnación de solutos a través de la membrana celular depende de las condiciones del proceso, la capacidad de la membrana para contraerse o estirarse y las propiedades fisicoquímicas de las estructuras celulares (Muñiz-Becerá, Méndez-Lagunas y Rodríguez-Ramírez, 2017). Cuando un alimento de origen vegetal se sumerge en una solución hipertónica, las células de la primera capa entran en contacto con la solución osmótica, comienzan a perder agua debido al gradiente de concentración y comienzan a encogerse. Posteriormente, se establece una diferencia de

potencial químico del agua entre la primera y la segunda capa de células del alimento y la segunda capa comienza a bombear agua hacia la primera (Muñiz-Becerá, Méndez-Lagunas y Rodríguez-Ramírez, 2017).

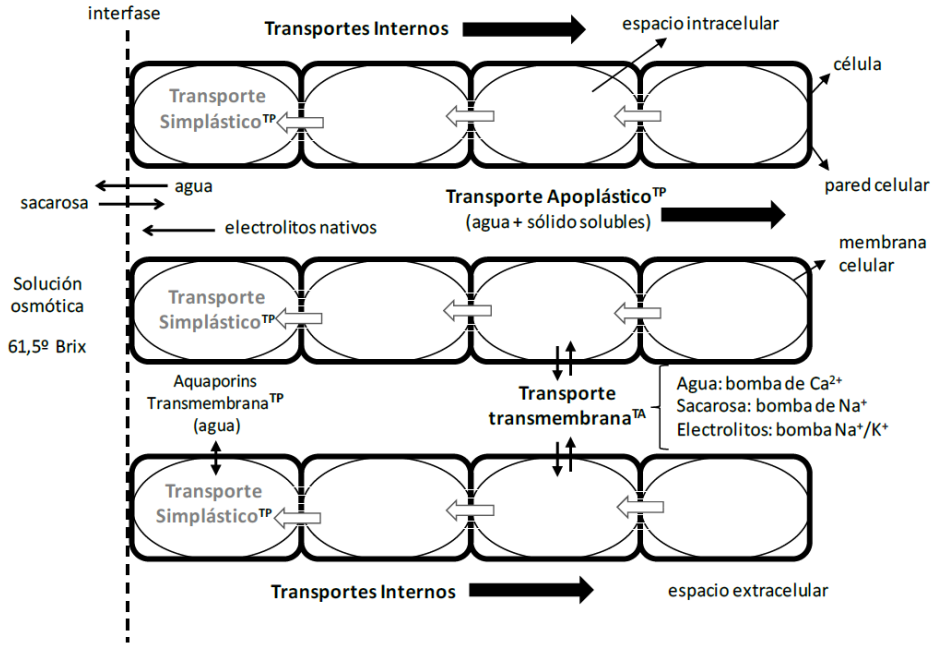

Figura 1.8. Esquema de los distintos transportes de materia que se llevan a cabo dentro de un tejido vegetal durante la DO (Traffano-Schiffo et al., 2016). Representando TA el transporte activo y TP el transporte pasivo.

El proceso de deshidratación osmótica aplicado a tejidos vegetales se puede analizar mediante la termodinámica irreversible, estudiando el potencial químico del agua, y las fuerzas impulsoras que lo forman, en la interfase que hay entre la disolución hipertónica y el alimento (Ecuación 1.10) (Traffano-Schiffo et al., 2016).

$$\Delta\mu_w = \overline{v_w}\Delta P + \overline{F_w}\Delta l + RT\left(\frac{a_w^e}{a_w^i} + \frac{a_s^e}{a_s^i}\cdot\frac{dn_s}{dn_w}\right) \qquad (1.10)$$

Siendo a y n la actividad de la especie química y los moles de la especie química, respectivamente. Además, el subíndice e representa el exterior, i el interior, w el agua y s el soluto.

1.4.4. Congelación

La congelación como operación de conservación es muy utilizada, siendo muy interesante su aplicación a productos cárnicos frescos (Palacz et al., 2021). El objetivo del proceso de congelación es cambiar de fase el agua no adsorbida, evitando que se encuentre disponible para el crecimiento de microorganismos y las reacciones de degradación, es decir, disminuir la actividad del agua para aumentar su estabilidad (James, Purnell y James, 2015; Zhang, Zhu y Sun, 2018). Además de la disminución de la actividad del agua, la reducción de la temperatura también contribuye a la conservación, ralentizando los procesos de degradación.

Cuando el proceso de congelación se da a presión atmosférica se forma hielo de la región Ih, lo cual es lo más común para la conservación de productos cárnicos, y se puede dividir en tres fases. Durante la primera fase, el producto baja de temperatura y se enfría hasta la temperatura inicial de congelación (T_m^0), donde empieza el proceso de nucleación y el agua líquida no adsorbida empieza a solidificar (Castro-Giraldez et al., 2014). Una vez alcanzada la T_m^0, comienza la segunda fase, donde empiezan a aparecer los primeros puntos de agua del producto que se encuentran en la temperatura de congelación (T_m), en los cuales se desarrolla el fenómeno de la nucleación. La nucleación (Figura 1.9) consiste en que cuando empiezan a aparecer los primeros núcleos de hielo en el producto, el agua empieza a moverse hacia ellos por la tensión superficial, aglomerándose, congelándose y aumentando el volumen de esos núcleos (Castro-Giraldez et al., 2014; Schmelzer et al.,

2018; You, Kang y Jun, 2021). Debido a la nucleación aparece otro fenómeno, la crioconcentración de los solutos del sistema; cuando el agua empieza a concentrarse en torno a los núcleos, los solutos comienzan a concentrarse en la fase líquida restante, lo que baja la temperatura de congelación de esa fase líquida, hasta que llega al punto en el que los solutos están tan concentrados que la fase líquida no puede cristalizar (T_m') y, por ende, el producto alcanza su actividad del agua más baja (a_{wc}) (Roudaut et al., 2004; Roos, 2021). Cuando el producto llega a T_m' continúa bajando su temperatura hasta la temperatura de transición vítrea (T_g), donde la estructura es vítrea y se alcanza la estabilidad.

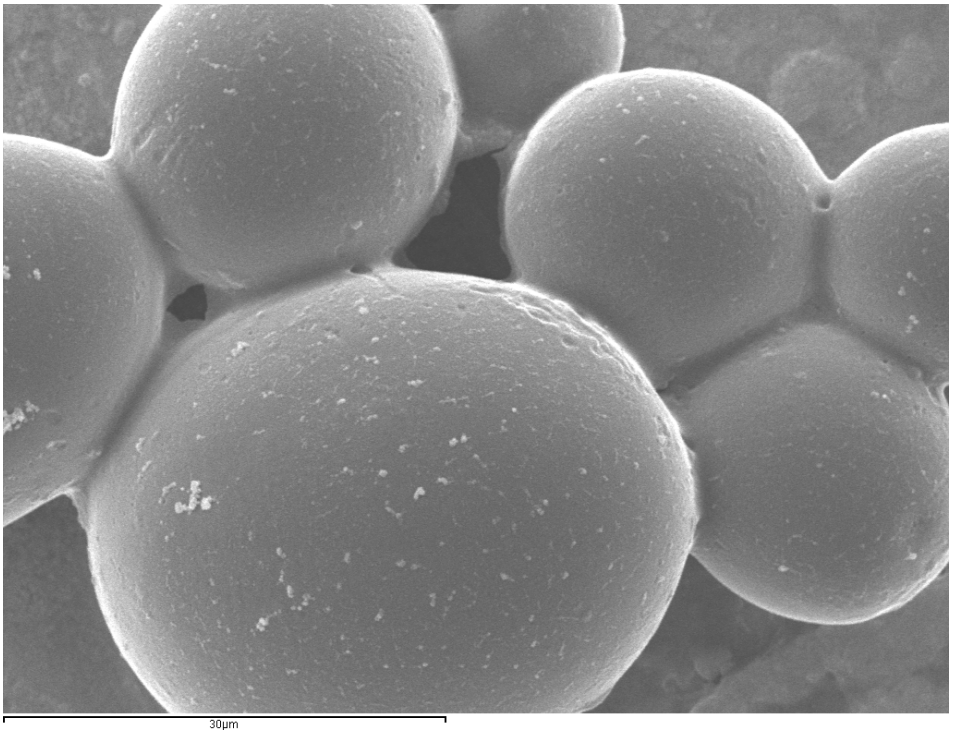

Figura 1.9. Micrografía de núcleos de hielo formándose durante la congelación de carne de cerdo (2000x).

El tamaño, la distribución y la ubicación de los cristales de hielo se ven muy influidos por la velocidad de la congelación. La congelación rápida forma núcleos de hielo intracelulares más pequeños y uniformes, lo que conlleva una disminución de los daños por frío a las células y estructuras musculares, mejorando la capacidad de retención de agua de la carne y minimizando la oxidación de lípidos y proteínas (Kim et al., 2017, 2018; Li, Zhu y Sun, 2018). La congelación lenta tiene más desventajas, como la una mayor pérdida de agua durante la descongelación por culpa de la rotura de tejidos, pero también puede alcanzar temperaturas finales más bajas (Zhang y Ertbjerg, 2019).

1.4.5. Liberación de compuestos bioactivos

En los últimos años ha aumentado considerablemente el estudio de la encapsulación de compuestos activos, desde bacterias probióticas, hasta nutrientes básicos, pasando por enzimas beneficiosas para el organismo (Gandomi et al., 2016; Traffano-Schiffo, Aguirre Calvo, et al., 2017; Churio, Pizarro y Valenzuela, 2018). Estos compuestos pueden perder eficacia a su paso por el sistema digestivo, para lo cual se formulan matrices para encapsular que sean compatibles con cada compuesto y, a su vez, sean capaces de resistir las distintas fases de la digestión que sea necesario, como por ejemplo el pH ácido del estómago (Cook et al., 2012).

A pesar de que el estudio de la liberación de compuestos encapsulados está bastante extendido, hay pocos modelos que permitan describir y estimar las cinéticas de liberación. Además, las técnicas utilizadas para medir la liberación de los compuestos microencapsulados o nanoencapsulados en medio líquido son técnicas estáticas e invasivas, como por ejemplo tomar una muestra del medio y medirla en un espectrofotómetro (Tu et al., 2005; Colinet

et al., 2009; Liakos et al., 2013; Criado et al., 2019; Miere et al., 2019), mediante análisis composicional (Folin-Ciocalteu principalmente) (Najafi-Soulari, Shekarchizadeh y Kadivar, 2016; Orozco-Villafuerte et al., 2019; Apoorva et al., 2020; Gholamian, Nourani y Bakhshi, 2021; Hoseyni et al., 2021), o mediante HPLC (Moschona y Liakopoulou-Kyriakides, 2018).

1.5. Fotónica

1.5.1. Espectrofotometría de baja frecuencia

La espectrofotometría es una técnica que se basa en el efecto que tiene un flujo de fotones sobre un medio. Los fotones son partículas elementales del grupo de los bosones, los cuales son capaces de transmitir campos o fuerzas universales que, en el caso concreto de los fotones, es la fuerza electromagnética. Al carecer de masa, los fotones no interaccionan con la malla de Higgs, por tanto, mantienen siempre la velocidad de la luz (299792458 m/s). Además, al tener un spin de 1, solamente puede acumular energía en la vibración, ya que no genera una acumulación del movimiento por rotación (Molina-Terriza, Torres y Torner, 2007). Al presentar estas características, la interacción de un fotón con la materia se define indistintamente a partir de la frecuencia a la que vibra (Hz), la amplitud de la onda (m) o la energía (eV) (Figura 1.10). Aunque para describir las interacciones entre partículas se puede utilizar el modelo estándar de partícula, en el campo de la fotónica se siguen utilizando las relaciones de Maxwell (Hawton, 2019; Li et al., 2020). Los fotones que vibran a frecuencias bajas, es decir, que tienen bajo un nivel de energía, presentan una elevada penetración en la materia, que junto a que interaccionan con las distintas especies químicas presentes en la materia en función de la frecuencia, generan una herramienta útil para analizar y estudiar los tejidos biológicos, pudiendo

determinar y cuantificar las especies químicas presentes (Gabriel y Peyman, 2018; Self et al., 2018). Considerando que el medio que atraviesa el flujo de fotones es un medio dieléctrico, las propiedades simplificadas del flujo son las propiedades dieléctricas.

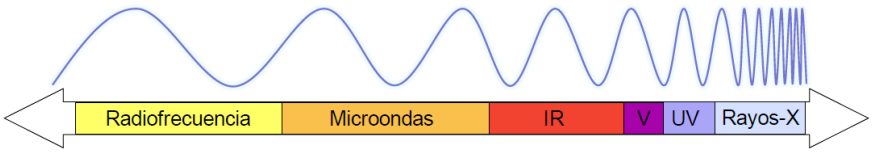

Figura 1.10. Esquema del espectro electromagnético.

La primera propiedad que se puede utilizar para analizar las interacciones del flujo de fotones con un medio es la impedancia, que combina las interacciones eléctricas y magnéticas (Ecuación 1.11).

$$Z = R + Xj \tag{1.11}$$

Representando Z la impedancia, X la resistividad y R la resistencia.

El campo electromagnético transmitido por un fotón en movimiento se puede dividir entre la vibración transversal (campo eléctrico) y la vibración longitudinal (campo magnético) (Figura 1.11). Dependiendo de la trayectoria que siga el flujo de fotones, se decantará más hacia la fuerza eléctrica, o la hacia la fuerza magnética. Al entrar en contacto el flujo de fotones con un medio dieléctrico, este genera una resistencia a su paso, lo que provoca un desplazamiento tanto del campo eléctrico, como del magnético, lo que se expresa mediante las ecuaciones 1.12 y 1.13.

$$\bar{D} = \vec{\varepsilon} \cdot \varepsilon_0 \cdot E = (\varepsilon' - \varepsilon'' j) \cdot \varepsilon_0 \cdot E \tag{1.12}$$

$$\bar{B} = \vec{\mu} \cdot \mu_0 \cdot H = (\mu' - \mu'' j) \cdot \mu_0 \cdot H \quad (1.13)$$

Representando D el desplazamiento del campo eléctrico, B el desplazamiento del campo electromagnético, E el campo eléctrico, H el campo magnético, ε la permitividad y μ la permeabilidad.

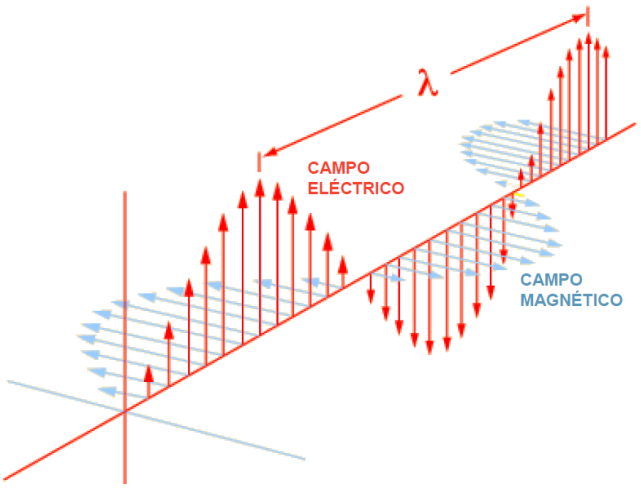

Figura 1.11. Representación del campo electromagnético, formado por el campo eléctrico (rojo) y el campo magnético (azul).

Los sistemas biológicos interaccionan con mayor intensidad con el campo eléctrico, por lo que, a menos que se disponga una trayectoria del flujo de fotones que anule el campo eléctrico (como en el caso de la resonancia magnética nuclear), se puede asumir que la permeabilidad de estos tejidos es próxima a la del vacío ($\mu=\mu_0 \rightarrow \mu=4\cdot\pi\cdot10^{-7}$ H/m) y se podría despreciar la interacción del campo magnético (Regier, Knoerzer y Schubert, 2016). Por tanto, se puede utilizar la permitividad para analizar las interacciones de un flujo de fotones en un medio dieléctrico (Nelson y Datta, 2001; Mello, Barin

y Guarnieri, 2014). La permitividad (ε) se puede definir mediante la ecuación 1.14.

$$\varepsilon = \varepsilon' + \varepsilon'' j \tag{1.14}$$

Si expresamos la permitividad como un número complejo, la parte real se denomina "constante dieléctrica" (ε'), la cual refleja la capacidad para almacenar energía que tiene el material cuando interacciona con un campo eléctrico (Amin et al., 2019). Este almacenamiento se debe al desplazamiento de las cargas positivas y negativas de la posición de equilibrio mediante la aplicación de un campo eléctrico, en contra de la atracción molecular y atómica (Maraj et al., 2019). Cuando la onda se propaga por un medio dieléctrico que no es perfecto, parte de la energía se pierde, lo que da valor a la parte imaginaria de la expresión compleja de la permitividad. La parte imaginaria se denomina "factor de pérdidas" (ε") y refleja la disipación de la energía del campo eléctrico, que se transforma en otras formas de energía. Por tanto, en tejidos biológicos como los alimentos, los fenómenos de polarización van relacionados con fenómenos de disipación y absorción de parte de la energía del campo eléctrico en el material, decayendo la constante dieléctrica (Teseme y Weldeselassie, 2020).

Por otra parte, como la permitividad es una propiedad vectorial (Figura 1.12), no solo es posible describirla como un número complejo, sino que también es posible describirla como un número polar. La permitividad polar tendrá como módulo la hipotenusa o resultante del factor de pérdidas y la constante dieléctrica y como desfase el ángulo que forma con la constante dieléctrica. La tangente del desfase se obtiene al dividir la parte real y la imaginaria, a esta tangente se le denomina tangente de pérdidas (Ecuación

1.15). Esta tangente es una herramienta útil para expresar la capacidad que tiene un tejido biológico de disipar energía (Içier y Baysal, 2004).

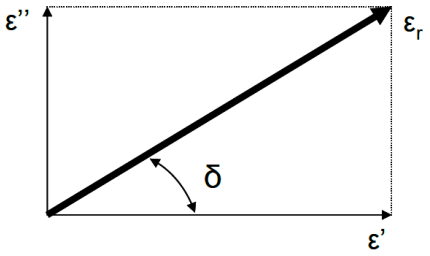

Figura 1.12. Representación del vector de permitividad.

$$tg\delta = \frac{\varepsilon'}{\varepsilon''} = \frac{|\varepsilon| \cdot sen\delta}{|\varepsilon| \cdot cos\delta} \tag{1.15}$$

Donde δ es el ángulo del vector de permitividad con respecto al eje real.

Cuando el campo eléctrico (entre Hz y MHz) interacciona con especies químicas con mucha fuerza iónica se generan pérdidas de energía, este les produce una vibración, que acaba disipándose en forma de calor, a este fenómeno se le denomina "conductividad iónica" (σ). La conductividad se puede cuantificar para el tramo de Hz a 1 GHz mediante la ecuación 1.16 (Nelson y Datta, 2001).

$$\sigma = \omega \cdot \varepsilon_0 \cdot \varepsilon'' \tag{1.16}$$

Donde ω es la frecuencia angular y ε_0 representa la permitividad en el vacío ($8{,}8542 \cdot 10^{-12}$ Fm^{-1}).

En función de la frecuencia a la que vibre el fotón, se presentan diferentes interacciones con un sistema dieléctrico como tejido biológico,

sistema coloidal o disolución (Figura 1.13). Dentro del espectro electromagnético, los fotones que vibran en las frecuencias de radiofrecuencia y microondas no tienen la suficiente energía como para desplazar electrones o romper enlaces químicos (Shukla y Anantheswaran, 2001). En cada rango de frecuencias se pueden diferenciar distintas dispersiones.

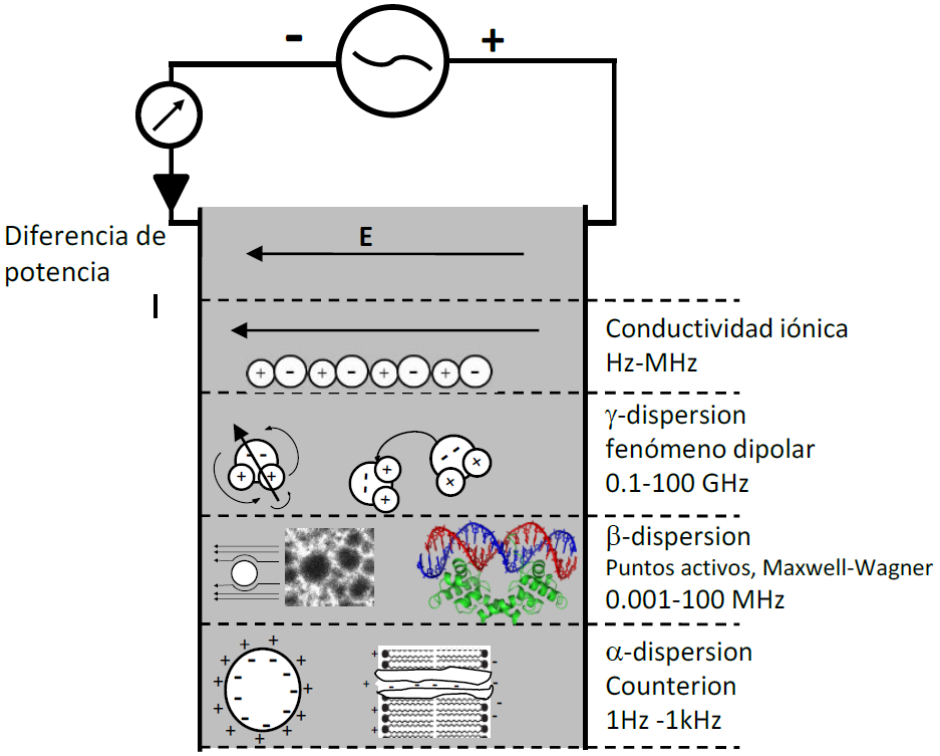

Figura 1.13. Esquema de los diferentes fenómenos que ocurren cuando un tejido biológico está bajo la influencia de un campo eléctrico. Adaptado de (Castro-Giraldez, Fito, Toldrá, et al., 2010).

En el rango de la radiofrecuencia podemos encontrar dos dispersiones distintas: α y β. La dispersión α se puede encontrar entre el rango de los Hz a los kHz y describe la orientación de las cargas móviles (electrolitos, por ejemplo) presentes en el tejido biológico, este fenómeno

también se denomina "efecto counterion" (Gabriel y Peyman, 2018). La dispersión β, en cambio, se encuentra en el rango de kHz a MHz y describe las interacciones del flujo de fotones con las cargas fijas o con poca movilidad del tejido biológico (Li et al., 2020), donde se puede encontrar interacciones con las proteínas e hidratos de carbono en el rango de los kHz, o interacciones asociadas a la tensión superficial (efecto Maxwell-Wagner) en el rango de los MHz (Dean et al., 2008).

En el rango de las microondas, sin embargo, solamente podemos encontrar la dispersión γ, la cual comprende desde 100 MHz hasta 100 GHz (Kent, 2001). Esta dispersión describe la orientación e inducción de moléculas dipolares como el agua, las cuales orientan su spin en la misma dirección que el campo eléctrico cuando éste circula a través del sistema, generando una rotación o inducción de la molécula dipolar alrededor del spin (Dean et al., 2008; Li et al., 2020).

Los espectros obtenidos a partir de la evolución de la permitividad a lo largo de las distintas frecuencias de las dispersiones α, β y γ se pueden modelizar mediante la ecuación de Traffano-Schiffo (Traffano-Schiffo, Castro-Giraldez, Colom, et al., 2017) (Ecuación 1.17), a partir de la ecuación de Gompertz, ideal para sigmoides. Aplicando esta modelización, es posible obtener distintos parámetros del espectro, como las relajaciones del sistema.

$$log\varepsilon'(\omega) = log\varepsilon'_{\infty} + \sum_{n=1}^{3} \frac{\Delta log\varepsilon'_n}{1 + e^{(log\omega^2 - log\tau_n^2)\cdot\alpha_n}} \qquad (1.17)$$

La absorción de energía por parte del sistema determinará la penetración del flujo dentro del mismo. La profundidad de la penetración (Dp) se puede estimar a partir de la ecuación 1.18.

$$Dp = \frac{c\sqrt{\varepsilon'}}{2\pi f \varepsilon''} \quad (1.18)$$

Donde la c es la velocidad de la luz (299792458 m/s).

La espectrofotometría de baja frecuencia se ha utilizado con éxito en el desarrollo de sensores para el control de calidad, como es el caso del sensor de contacto para detectar la miopatía del pectoral profundo en canales de ave (Traffano-Schiffo, Castro-Giraldez, Herrero, et al., 2018), en la detección de estrías blancas en pechugas de pollo mediante las relajaciones (Traffano-Schiffo, Castro-Giraldez, Colom, et al., 2017), en la estimación de la composición de pasta cárnica (Lyng, Zhang y Brunton, 2005; Zhang, Lyng y Brunton, 2007), en el establecimiento de marcadores de calidad de la carne en función de los espectros dieléctricos obtenidos (Castro-Giraldez, Botella, et al., 2010; Castro-Giraldez, Dols, et al., 2011; Trabelsi, Roelvink y Russell, 2014; Traffano-Schiffo, Castro-Giraldez, Colom, et al., 2018a), en analizar la desnaturalización de las proteínas en carne de ternera (Brunton et al., 2006), en la evaluación del grado de maduración en húmedo de la ternera (Ihara et al., 2019), en el desarrollo de un sensor capacitivo para estimar la humedad en arroz (Song et al., 2020), en la clasificación de las variedades de manzana (Shang, Guo y Nelson, 2015) y grado de madurez (Castro-Giraldez, Fito, Chenoll, et al., 2010), en la segregación de los tejidos de una mandarina (Traffano-Schiffo, Castro-Giraldez, Colom, et al., 2018b), el grado de madurez de la granada (Castro-Giraldez et al., 2013); y en la monitorización de procesos como el secado con aire caliente de carne de cerdo (Traffano-Schiffo et al., 2015), el proceso de salado de cerdo (Castro-Giraldez, Fito y Fito, 2010a), el proceso de maduración de la carne de pollo (Traffano-Schiffo et al., 2021), el caramelizado de manzanas (Tomas-Egea, Fito y Castro-

Giraldez, 2019), la deshidratación osmótica de kiwi (Castro-Giraldez, Fito, et al., 2011), el secado con aire caliente combinado con microondas de piel de naranja (Talens, Castro-Giraldez y Fito, 2016b), el inflado de semillas de amaranto (Castro-Giraldez et al., 2012) y pellets de snacks (Gutiérrez et al., 2017), el tratamiento térmico para la estabilización del germen de trigo (Ling, Lyng y Wang, 2018), la leche (Muñoz et al., 2018), el arroz (Auksornsri et al., 2018) y distintas salsas (Hernandez-Gomez et al., 2021), la obtención de harina de bananas verdes (Ahmed, Thomas y Khashawi, 2020), la congelación de patatas (Cuibus et al., 2014).

1.5.2. Termografía infrarroja

La termografía infrarroja consiste en medir la temperatura de la superficie de un material mediante la captación de los fotones emitidos por la misma en el espectro de infrarrojo lejano o FIR. Es por tanto, una tecnología que permite monitorizar en el tiempo y estudiar la distribución de temperaturas que presenta una superficie (Meola, Boccardi y Carlomagno, 2017a). Entre las ventajas que ofrece esta técnica, podemos encontrar que es un método no invasivo, ni destructivo, ya que no entra en contacto con la superficie en ningún momento, y que puede monitorizar un proceso en dinámico, a tiempo real (Usamentiaga et al., 2014).

La energía interna de un átomo se acumula fundamentalmente en el electrón del orbital de valencia, ya que es la partícula elemental de mayor movilidad. En el modelo atómico de Schrödinger se demostraba mediante un modelo de energías cinéticas como el aporte de este electrón es mayoritario en el cómputo de la energía interna de cualquier átomo, por tanto, es posible predecir la temperatura de un material, analizando el comportamiento de este electrón. Al mismo tiempo, es la partícula más expuesta en el átomo, por lo

que recibe constantemente fotones externos que le generan una excitación y un desequilibrio orbital, que termina con la liberación de un fotón y una relajación energética y orbital que permite al electrón volver al equilibrio nativo. Este fotón emitido mantiene la movilidad del (nivel energético) del electrón emisor (Figura 1.14), observación que le permitió a Plank desarrollar una ley de predicción de la temperatura superficial de cualquier cuerpo analizando su radiación (emisión de fotones), esta ley fue modificada tiempo después por Stefan-Boltzman conformando el sistema que se utiliza en la actualidad para determinar temperaturas superficiales mediante infrarrojos. Según esta ley, un cuerpo emite fotones con un nivel de energía (frecuencia) en función de su temperatura superficial, cuerpos a temperaturas próximas al cero absoluto emiten en microondas (MW), los seres vivos emiten en infrarrojo lejano (FIR), el sol (3000 K) emite en visible (VIS) y una enana blanca (12000 K) emite en ultravioleta (UV) (Usamentiaga et al., 2014). Una técnica empleada para determinar fotones en el espectro de FIR es la utilización de material piroeléctrico, que varíe su carga eléctrica en función de la radiación recibida en este espectro, con ellos se diseñan sensores como las cámaras termográficas (Gaussorgues y Chomet, 1993).

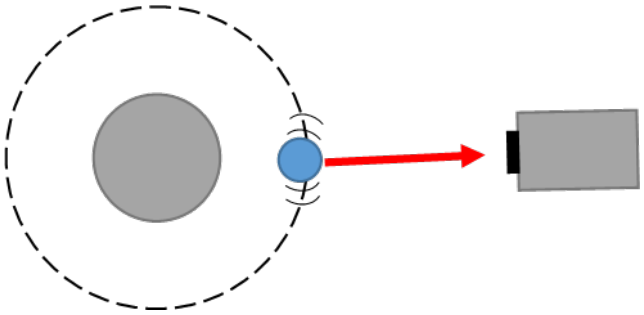

Figura 1.14. Representación del fotón emitido por el electrón del orbital, siendo recogido por la cámara termográfica.

Existen tres formas de disipar la radiación que alcanza un objeto: absorción, reflexión y transmisión (Möllmann et al., 2005). A su vez, existen tres parámetros para describir estos fenómenos: absorbancia, (α_λ), reflectancia (ϱ_λ) y transmitancia (τ_λ) (Howell et al., 2020). La suma de estos tres parámetros debe ser uno en cualquier longitud de onda (Ecuación 1.19).

$$\alpha_\lambda + \rho_\lambda + \tau_\lambda = 1 \tag{1.19}$$

Los materiales que son incapaces de reflejar o transmitir la radiación se denominan cuerpos negros, por tanto, absorben toda la energía radiante ($\alpha_\lambda = 1$). La radiación electromagnética emitida por un cuerpo negro ($E_{\lambda b}$) se puede calcular utilizando la ley de Planck.

Para obtener la energía radiante total de un cuerpo negro se puede aplicar la ley de Planck a todas las longitudes de onda, obteniendo así la ecuación de Stefan-Boltzmann para cuerpos negros (Ecuación 1.20).

$$E_b = 1 \cdot T^4 \tag{1.20}$$

Un cuerpo real emite solo una fracción de la energía térmica emitida por un cuerpo negro a la misma temperatura (Meola, Boccardi y Carlomagno, 2017a). La emisividad de un cuerpo se define como la relación entre la energía radiante emitida por un cuerpo (E) y la radiación que emitiría un cuerpo negro a la misma temperatura (E_b). Si la emisividad es constante e independiente de la longitud de onda, el cuerpo es gris. Por tanto, se puede expresar como la ecuación 1.21:

$$\varepsilon = \frac{E}{E_\mathrm{b}} \tag{1.21}$$

Aun así, la emisividad de los objetos reales no es constante, por lo que tampoco pueden considerarse cuerpos grises. Sin embargo, generalmente se asume que, en intervalos cortos, la emisividad es constante, por lo que, bajo esa condición, se puede tratar los objetos reales como cuerpos grises. Este promedio es posible para objetos sólidos porque la emisividad varía muy poco, sin embargo, esto no se aplica a gases o líquidos (Usamentiaga et al., 2014; Meola, Boccardi y Carlomagno, 2017a). Utilizando las ecuaciones 1.20 y 1.21, se obtiene la ecuación 1.22. Esta ecuación es la fórmula de Stefan-Boltzmann cuerpos grises.

$$E = \varepsilon \cdot \sigma \cdot T^4 \tag{1.22}$$

Representando σ la constante de Stefan-Boltzmann (5,670373·10^{-8} W/m^{2}K^4).

La energía medida con una cámara termográfica no es la energía real que está emitiendo por radiación la superficie de un cuerpo (Usamentiaga et al., 2014). Normalmente, parte de la radiación se ve absorbida por el medio que hay entre la cámara y el cuerpo, si la transmitancia de ese cuerpo no es 1, y además, la cámara puede estar captando energía de reflexión del medio, por lo que la temperatura obtenida por la cámara se debe corregir (Traffano-Schiffo et al., 2014; Tomas-Egea et al., 2021) (Figura 1.15).

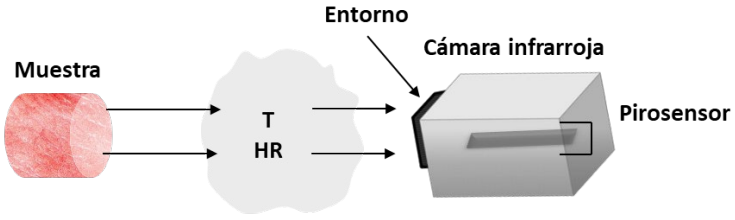

Figura 1.15. Esquema del balance de energías que recoge la cámara infrarroja.

Se ha demostrado que la termografía infrarroja es una técnica muy interesante para analizar materiales, alcanzando un uso muy extendido desde los laboratorios, hasta la industria. Se ha utilizado con éxito para analizar componentes aeroespaciales (Meola, Boccardi y Carlomagno, 2017b; Ciampa et al., 2018; Sfarra et al., 2020), en la construcción (Lucchi, 2018; Glowacz, 2021; Yang et al., 2021) y en la monitorización de procesos industriales (Osornio-Rios, Antonino-Daviu y Romero-Troncoso, 2019), pero también se ha utilizado con éxito en la industria agroalimentaria (Ferreira, 2020), tanto en postcosecha (Gan-Mor et al., 2011; Baranowski et al., 2012; Gonçalves et al., 2016), como en procesado de alimentos (Costa et al., 2007; Gowen et al., 2010; Cuibus et al., 2014; Traffano-Schiffo et al., 2014; Colucci, Maniaci y Fissore, 2019; Q. Wang et al., 2019; Stegner, Schäfernolte y Neuner, 2019; Tomas-Egea et al., 2021).

Objetivos y plan de trabajo

2.1. Objetivos

El objetivo de la presente tesis es el de desarrollar y utilizar técnicas basadas en la fotónica de baja frecuencia, como la radiofrecuencia, las microondas y los infrarrojos, para monitorizar de forma no destructiva procesos utilizados en la industria agroalimentaria, desde el punto de vista de la termodinámica irreversible.

2.1.1. Objetivos particulares

Para cumplir el objetivo general, se plantearon cuatro objetivos específicos:

1. Estudiar los distintos fenómenos que ocurren durante la operación de deshidratación de patata mediante el secado con aire caliente combinado con microondas, utilizando la termografía infrarroja para monitorizar los perfiles de temperatura superficial que presenta la muestra, la espectrofotometría en el rango de las microondas y la termodinámica irreversible para modelizar el proceso.
2. Desarrollar un sistema de monitorización de la congelación de la carne de pollo, que permita obtener datos del proceso a tiempo real y de forma no invasiva mediante la espectrofotometría en el rango de la radiofrecuencia y la termografía infrarroja. A su vez, con esos datos se modelizará el comportamiento del producto a lo largo del proceso de congelación, utilizando los principios de la termodinámica irreversible para estimar los distintos fenómenos que ocurren.

3. Desarrollar una herramienta de predicción de los distintos estados del agua y la sacarosa durante el proceso de caramelizado de manzanas, basada en las propiedades dieléctricas obtenidas mediante la espectrofotometría en el rango de las microondas.
4. Diseñar y desarrollar un sensor basado en las propiedades dieléctricas en el rango de la radiofrecuencia, capaz de monitorizar en tiempo real y de forma no invasiva con el medio las cinéticas de liberación de compuestos encapsulados en matrices de alginato en un medio líquido. Utilizando este nuevo sensor se pueden modelizar y estudiar las cinéticas de liberación y utilizarse para diseñar la encapsulación de compuestos.

2.2. Plan de trabajo

Para cumplir los objetivos de la tesis, cada objetivo específico se ha dividido en distintas tareas a cumplir.

1. Estudio del secado de patata con aire caliente combinado con microondas utilizando termografía infrarroja y midiendo la permitividad en rango de microondas.
   1.1. Caracterización de las propiedades físicas de las esferas de patata frescas. Actividad del agua y humedad inicial.
   1.2. Monitorización en continuo del proceso de secado combinado a distintas potencias (0, 4 y 6 $W/g_{inicial}$), midiendo la masa, la temperatura con termopares y cámara de infrarrojos, y las propiedades dieléctricas (solo a 0 W/g).
   1.3. Caracterización de las muestras a distintas potencias (0, 4 y 6 $W/g_{inicial}$) y tiempos (20, 40, 60, 90, 120, 180 y 420 min). Se

miden las propiedades dieléctricas, la masa inicial y final, la actividad del agua y el volumen de la muestra.

1.4. Corrección de las temperaturas obtenidas con la cámara termográfica.

1.5. Estudio de los mecanismos de transporte del agua y sus fuerzas impulsoras durante el secado de aire caliente combinado con microondas.

1.6. Estudio del efecto que tienen distintas potencias de microondas aplicadas al secado con aire caliente.

2. Monitorización de la congelación de carne de pollo con espectrofotometría en radiofrecuencia y cámara termográfica.

2.1. Diseño e impresión con impresora 3D de un soporte adaptado a temperaturas de congelación para instalar las muestras, una balanza, los termopares, la pegatina de emisividad de referencia y los electrodos usados para la espectrofotometría.

2.2. Caracterización de la humedad y la actividad del agua de las muestras de pollo en fresco.

2.3. Monitorización del proceso de congelación utilizando una cámara termográfica y termopares para medir las distintas temperaturas, el analizador de impedancias para medir las propiedades dieléctricas y una balanza para la masa.

2.4. Corrección de las temperaturas obtenidas mediante la cámara termográfica.

2.5. Modelización y estudio del proceso utilizando la termodinámica irreversible para estudiar los distintos fenómenos que ocurren durante la congelación.

3. Desarrollo de una herramienta de predicción de la actividad del agua y la sacarosa durante la caramelización de manzanas, utilizando la espectrofotometría en el rango de las microondas.
   3.1. Caracterización de las muestras frescas y deshidratadas en equilibrio. Permitividad en microondas, masa, volumen, actividad del agua, humedad y contenido de sólidos solubles.
   3.2. Desarrollo de siete isotermas de sorción, una para cada tiempo de deshidratación osmótica (0, 360, 720, 1722, 3375, 4320 y 10270 min).
   3.3. Estudio de los mecanismos que gobiernan la relación entre el agua y la sacarosa en la manzana, los fenómenos del transporte y las diferentes transiciones.
   3.4. Desarrollo de una herramienta predictiva del estado del agua y la sacarosa a partir de las propiedades dieléctricas obtenidas mediante la espectrofotometría en el rango de las microondas.

4. Diseño de un sensor capaz de monitorizar la liberación de compuestos encapsulados en un medio líquido mediante la espectrofotometría en el rango de la radiofrecuencia.
   4.1. Estudio de distintos materiales resistentes al pH del medio, tanto para el electrodo del sensor como para el contenedor.

4.2. Diseño y desarrollo del sensor basado en la espectrofotometría en el rango de la radiofrecuencia utilizando impresión 3D.

4.3. Estudio y caracterización de las capsulas de alginato cálcico con hierro y vitamina C.

4.4. Estudio de la expansión de las cápsulas en medios líquidos con distintos pH mediante microscopía óptica y análisis de imagen.

4.5. Desarrollo de rectas patrón que permitan relacionar las propiedades dieléctricas de un medio líquido con la concentración que tengan del compuesto.

4.6. Monitorización del proceso de liberación de los compuestos encapsulados mediante el sensor diseñado.

4.7. Estudio de las cinéticas de liberación obtenidas y desarrollo de una herramienta de predicción del compuesto liberado.

Materiales y métodos

3.1. Materias primas

3.1.1. Patata cv. Melody

Para el estudio de los fenómenos que afectan a la patata durante el secado con aire caliente combinado con distintas potencias de microondas se utilizaron patatas (*Solanum Tuberosum* (L.) cv. Melody) de calibres similares y suministradas por Mercadona S.A. (Valencia, España). Las patatas se lavaron y pelaron para extraer esferas de 10 mm mediante un sacabocados esférico de acero inoxidable.

3.1.2. Pechuga de pollo (pectoralis major)

Para la modelización y estudio de la congelación de carne de ave se utilizaron pechugas de pollo de calibres similares y sin miopatías. Las pechugas fueron proporcionadas por el matadero "Productos Florida" (Almazora, Castellón, España) con un tiempo postmortem de 36 h. Las muestras se extrajeron en perpendicular a las fibras, mediante un sacabocados y con unas dimensiones de 20 mm de alto y 20 mm de diámetro.

3.1.3. Manzana var. Granny Smith

Para desarrollar la herramienta de predicción de los estados del agua y la sacarosa durante el caramelizado de manzanas se utilizaron manzanas de la variedad Granny Smith, de calibres similares y suministradas por Mercadona S.A. (Valencia, España). Las muestras de manzana se extrajeron del tejido parenquimático en cilindros de 10 mm de alto y 20 mm de diámetro mediante un sacabocados.

3.1.4. Microencapsulaciones de alginato cálcico

3.1.4.1. Reactivos

Los reactivos utilizados en la preparación de las microencapsulaciones fueron el ácido acético, el acetato de sodio y el cloruro de calcio proporcionados por Scharlab S.L. (Barcelona, España); alginato de sodio proporcionado por Panreac Química S.L.U. (Castellar del Valles, Barcelona, España) con una pureza del 90 %; proteinsuccinilato férrico de 40 mg / 15 ml (Ferplex, Italfarmaco S.A., Madrid, España); ácido ascórbico (Scharlab S.L., Barcelona, España); y ácido clorhídrico a 1 N (Panreac Química S.L.U., Castellar del Valles, Barcelona, España).

3.1.4.2. Tampón

El tampón utilizado para la preparación de las cápsulas de alginato se preparó con ácido acético y acetato de sodio (Scharlab S.L., Barcelona, España), con un pH de 3,8 y una concentración de 0,05 M. El propósito de este buffer es establecer un pKa óptimo para la formación de la matriz (Santagapita, Mazzobre y Buera, 2011).

3.1.5. Acrilonitrilo butadieno estireno (ABS)

Para la impresión mediante impresora 3D se utilizó el acrilonitrilo butadieno estireno (ABS) proporcionado por FrontierFila (China), con un diámetro de 1,75. Los parámetros de impresión fueron: 235 °C de temperatura de extrusión, 90 °C de temperatura en la superficie de impresión, un relleno del 100 %, una velocidad de impresión de 40 mm/s y una altura de capa de 0,1 mm.

3.2. Técnicas

3.2.1. Determinación de la Humedad

3.2.1.1. Patata

La determinación de la humedad de las muestras de patata se realizó gravimétricamente, secando las muestras en una estufa de vacío a 60 °C, hasta alcanzar la masa constante , según el método de la AOAC de 1990 (Horowitz, 2000).

3.2.1.2. Carne de pollo

La humedad de las muestras frescas de pollo se determinó siguiendo la normativa ISO 1442 (1997) de determinación de humedad para productos cárnicos, basada en deshidratar las muestras en una estufa a 105 °C, a presión atmosférica, durante 48 h.

3.2.1.3. Manzana

La humedad de las muestras de manzana se determinó de forma gravimétrica, secándolas en una estufa de vacío a 60 °C hasta alcanzar una masa constante, según el método de la AOAC de 1990 (Horowitz, 2000).

3.2.2. Determinación del volumen

3.2.2.1. Patata y manzana

Las medidas de volumen se analizaron mediante análisis de imágenes, utilizando el software Adobe Photoshop® CS5 y CS6 (Adobe Systems Inc., San José, CA, EE. UU.) para obtener las dimensiones en píxeles de las muestras y transformarlas a metros mediante una superficie milimetrada de referencia. Las imágenes de las muestras se obtuvieron con una cámara digital (Canon EOS 550D, con un tamaño de 2592 x 1728 píxeles y una resolución de 16 píxeles/mm).

3.2.2.2. Microencapsulaciones de alginato cálcico

El volumen de las cápsulas se determinó utilizando el microscopio Juision USB Microscope, conectado a un ordenador MacBook Air (Apple, EE. UU.), obteniendo las imágenes con el software Photo Booth. Como distancia de referencia se colocó en la base un cristal micrometrado (Figura 3.1). Las imágenes obtenidas se analizaron mediante el Adobe Photoshop® CS5 (ver. 12, Adobe Systems Inc., San José, CA, EE. UU.), utilizando la herramienta de medir y transformando las distancias en píxeles a milímetros.

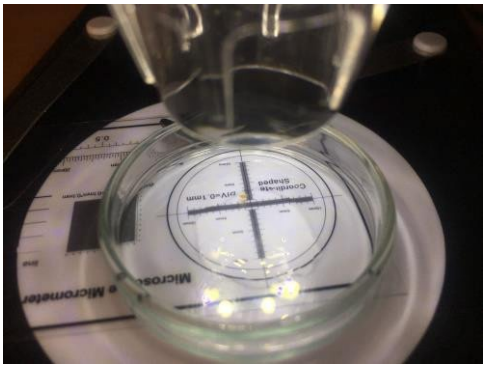

Figura 3.1. Crisol con el cristal micrometrado, enfocado por el microscopio, con una cápsula en el centro.

3.2.3. Determinación de la actividad del agua

La actividad del agua de las muestras se determinó mediante un higrómetro de punto de rocío Aqualab®, serie 3 TE (± 0,003) (Decagon Devices Inc., Pullman, WA, EE. UU.).

3.2.4. Espectrofotometría en el rango de la radiofrecuencia

La medida de las propiedades dieléctricas se hizo utilizando un analizador de impedancias Agilent 4294A (Agilent Technologies, Santa Clara, CA, EE. UU.) (Figura 3.2). Para medir se realiza una calibración previa

midiendo abierto/corto. El rango de frecuencias utilizado es desde 40 Hz hasta 1 MHz.

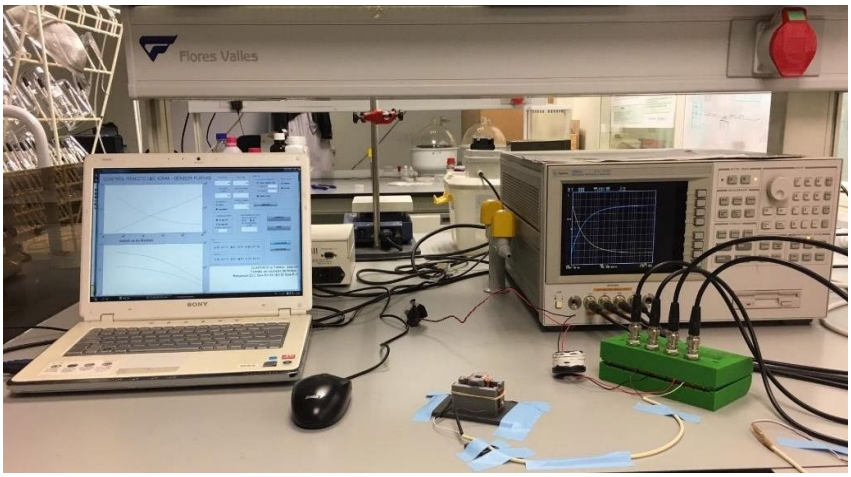

Figura 3.2. Analizador de impedancias Agilent 4294A conectado a un ordenador para obtener los espectros.

Para monitorizar el proceso de congelación de la carne de pollo se desarrolló un sensor de puntas, basándose en utilizar dos agujas como electrodos y la carne como medio dieléctrico (Figura 3.3). Las dimensiones de las agujas del sensor eran de 10 mm de longitud, 0,8 mm de diámetro y 1,3 mm de distancia entre las puntas. Las dos puntas se clavaron en el centro de la muestra, por el lateral del cilindro, para medir las propiedades dieléctricas en perpendicular a la dirección de las fibras.

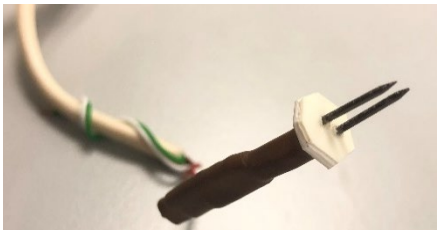

Figura 3.3. Sensor de puntas utilizado para medir propiedades dieléctricas.

Para estudiar las cinéticas de liberación de los compuestos encapsulados se diseñó y desarrolló un sensor específico que consiste en dos partes: una carcasa exterior y un contenedor de medida, ambos impresos en ABS y utilizando electrodos de tantalio de 7,5 x 15 mm y 99 % de pureza. Los electrodos de tantalio se colocaron dentro del tanque de medida, pegados a la pared interior, de forma que el medio líquido donde se liberan los compuestos actúe de dieléctrico (Figura 3.4).

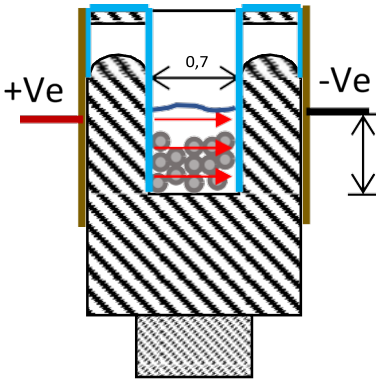

Figura 3.4. Esquema del sensor utilizado para la monitorización de los compuestos liberados. Siendo el color azul el tantalio y el marrón cobre. Las medidas están en centímetros.

3.2.5. Espectrofotometría en el rango de las microondas

Las propiedades dieléctricas de las muestras en el rango de microondas se midieron usando un analizador de redes Agilent E8362, con una sonda coaxial Agilent 85070E conectada (Agilent Technologies, Santa Clara, CA, EE. UU.) (Figura 3.5). El sistema de medida se calibró previamente haciendo un abierto, un corto y midiendo agua Milli®-Q a 25 °C. El rango de frecuencias utilizado por en analizador es de 500 MHz a 20 GHz. La sonda se coloca en la superficie de la muestra.

Figura 3.5. Analizador de redes E8362B de Agilent y sonda coaxial 85070E de Agilent.

3.2.6. Termografía infrarroja

La termografía infrarroja se llevó a cabo utilizando la cámara termográfica, modelo Optris PI 160 (Optris GmbH, Berlín, Alemania). Este modelo es capaz de medir temperaturas superficiales de -20 a 900 °C, con una precisión de ± 2 % y una resolución de 0,05 °C. El campo de visión es de 23°x17°, 2 cm de distancia mínima, una resolución de 160x120 píxeles y un rango espectral de 7,5 hasta 13 µm. La cámara termográfica se conecta a un ordenador con el software Optris PI Connect (Optris GmbH, Berlín, Alemania) con el que hacer el tratamiento de datos.

3.2.7. Protocolo de impresión 3D

El protocolo de impresión 3D que se utilizó para el desarrollo de los sensores se puede dividir en tres pasos: primero se diseñó la pieza utilizando el software de diseño 3D Tinkercad (Autodesk, Inc., Mill Valley, CA, EE. UU.), donde se establecen las dimensiones de la pieza; el segundo paso es elaborar un archivo donde se establecen los parámetros de impresión (en función del diseño y el material de impresión) y se procesa el diseño 3D, todo esto se realizó con el software Repetier-Host y la herramienta Slic3r que

incorpora (Hot-World GmbH & Co., Knickelsdorf, Alemania); el último paso consistió en introducir el filamento seleccionado y abrir el archivo con los datos del segundo paso en la impresora Anet A8 (Anet Technology Co., Ltd., Shenzen, China) (Figura 3.6).

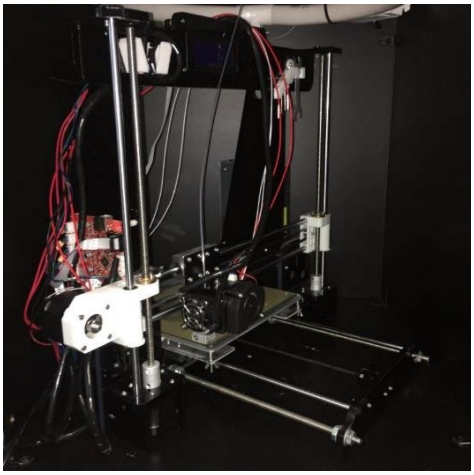

Figura 3.6. Impresora 3D modelo Anet A8.

3.3. Metodologías experimentales

3.3.1. Monitorización del proceso de secado de patata con aire caliente combinado con microondas

Las esferas de patata se secaron utilizando el secado con aire caliente (HAD) y HAD combinado con microondas a distintas potencias en un equipo especialmente diseñado para ello, conectado a un magnetrón de hasta 2000 W de potencia a 2450 MHz (Navarrete et al., 2003). El equipo estaba conectado a un ordenador para monitorizar la energía que hay dentro de la cámara de secado durante el proceso. Las condiciones del aire secado fueron una temperatura de 40 °C y 1,5 m/s de velocidad. Las potencias de

microondas seleccionadas para el experimental fueron 0, 4 y 6 W/g (en función de la masa inicial de muestra). Todos los procesos de secado fueron de 420 min de duración.

Cada proceso consistía en colocar dos muestras de patata en el mismo plano, para poder comparar resultados, y en el interior del equipo de secado: la primera iba sobre una cesta de malla que, unida a una balanza Mettler Toledo AB304-S (precisión de ± 0,01 g), permitía medir la masa de la muestra a lo largo del proceso; la segunda muestra iba sobre un soporte de malla y se utilizó para monitorizar los perfiles de temperatura de la muestra mediante termografía infrarroja. Además, durante el proceso de secado de 0 W/g se monitorizó la temperatura superficial de la segunda muestra y de una superficie de emisividad conocida ($\varepsilon = 0{,}95$) mediante termopares conectados al multiplexor Agilent 34901A del equipo de adquisición de datos Agilent 34972A (Agilent Technologies, Malasia), para así poder corregir las temperaturas obtenidas con la cámara termográfica. Por último, también se registraron las temperaturas y humedades relativas ambientales que había durante el proceso.

3.3.2. Caracterización de muestras de patata deshidratadas mediante HAD combinado con microondas a distintos tiempos y potencias

Para complementar los datos obtenidos durante la monitorización del proceso, se obtuvieron datos de muestras en tiempos específicos (0, 20, 40, 60, 90, 120, 180, 420 min) para cada potencia (0, 4 y 6 W/g) y por triplicado. Las muestras se caracterizaron en fresco, nada más salir del equipo de secado y equilibradas, después de estar refrigeradas durante 24 h a 4 °C. Cada muestra

se caracterizó determinando su permitividad, masa, volumen, actividad del agua y humedad, teniendo en cuenta que la determinación de la humedad es un análisis destructivo, por lo que sólo se realizaba a la muestra equilibrada.

3.3.3. Monitorización del proceso de congelación de carne de pollo

El proceso de congelación se llevó a cabo en un arcón congelador de convección forzada ACR-45/87 (Dycometal, S.L, Barcelona, España), durante 35 minutos a -40 °C. Las muestras se encontraban en condiciones de turbulencia, en el centro del congelador y sobre un soporte impreso con impresora 3D. La tapa del congelador se sustituyó por una lámina aislante de poliestireno extruido (Chovafoam tipo 4I, Leroy Merlín S.L., Valencia, España) con un agujero en el centro, donde se colocó la cámara termográfica.

Para monitorizar la congelación de las muestras de pechuga de pollo se colocaron dos cilindros: el primer cilindro se puso sobre una célula de carga FS2030-000X-0500-G para registrar la masa y la temperatura de la superficie plana con la cámara termográfica Optris PI 160; el segundo cilindro se colocó a un lateral del primero y se utilizó para monitorizar la temperatura superficial y del centro con termopares, y la permitividad con un sensor de puntas introducido en el centro de la muestra. Además, se monitorizó la temperatura de una superficie de emisividad conocida ($\varepsilon = 0{,}95$), utilizando simultáneamente la cámara termográfica y un termopar. También se registró la temperatura del interior del congelador mediante un termopar. Los termopares y la célula de carga estaban conectados al multiplexor Agilent 34901A introducido en el equipo de adquisición de datos Agilent 34972A (Agilent Technologies, Malasia), y el sensor de puntas estaba conectado al analizador de impedancias Agilent 4294A.

3.3.4. Caracterización de las muestras de manzana durante el caramelizado

La solución hipertónica de sacarosa que se utilizó en este experimental estaba concentrada al 65 % m/m y se mantuvo isoterma a 30 °C. La proporción de fruta y disolución osmótica era de 1:20 (m/m), la cual se mantuvo constante cubriendo el recipiente con una lámina de plástico impermeable. Una vez deshidratadas osmóticamente, las muestras se equilibraron durante 24 horas a 30 °C y posteriormente se les aplicó un secado con aire caliente (40 °C y 1,5 m/s), después del cual se volvieron a equilibrar las muestras bajo las mismas condiciones.

Para desarrollar la herramienta predictiva se desarrollaron siete isotermas de sorción distintas (I_0 a I_7), que se dividieron en función del tiempo de exposición de las muestras a la solución hipertónica de sacarosa: 0, 360, 720, 1722, 3375, 4320, 10270 min. Cada isoterma estaba formada por seis puntos (t_0 a t_6), correspondientes a los tiempos de secado: 0, 30, 60, 120, 955, 1368 min. A cada muestra se le caracterizó la permitividad, la masa, el volumen, la actividad del agua, la humedad y la cantidad de sólidos solubles.

3.3.5. Calibración del sensor de monitorización de la liberación de compuestos

Con el objetivo de monitorizar la liberación de hierro y vitamina C encapsulado se desarrollaron distintas rectas de calibración para relacionar la concentración en el medio de esos compuestos con las propiedades dieléctricas del medio. Para ello se prepararon distintas disoluciones de concentración conocida a dos pH distintos: 3 y 4,7. Las concentraciones de hierro iban desde 100 hasta 500 ppm y las de ácido ascórbico desde 50 hasta

las 3000 ppm. Una vez preparadas las disoluciones, se midieron sus propiedades dieléctricas con el sensor diseñado.

3.3.6. Protocolo de obtención de microencapsulaciones de alginato cálcico

Las encapsulaciones de hierro y ácido ascórbico se obtuvieron mediante la técnica de la gelificación iónica, formando matrices de alginato cálcico. Para ello se prepararon dos disoluciones: una de alginato sódico con tampón de acetato sódico a concentración de 1:100 (junto al hierro o la vitamina C), y otra de cloruro cálcico y tampón de acetato sódico con una concentración de 1:100. Una vez preparadas las disoluciones, la bomba peristáltica CPM-045B (Damova S.L., Barcelona, España,), regulada por un variador de frecuencia Inverter DV-700 (Panasonic, Osaka, Japón) para controlar el caudal, bombea la disolución de alginato para que gotee en la disolución de cloruro cálcico con una proporción de 1:10 respectivamente. Durante el goteo, la disolución de cloruro cálcico se mantiene en constante agitación con un agitador (IKA® MS3 basic, Staufen im Breisgau, Alemania). La altura de caída de la gota de alginato antes de sumergirse en la disolución de cloruro cálcico es de 10 cm.

Una vez formadas las cápsulas se mantienen en agitación en la disolución de cloruro cálcico constante durante 15 minutos para asegurar una formación de la matriz óptima, se extraen de la disolución y se lavan cinco veces con agua bidestilada. Como las cápsulas frescas presentan una actividad del agua muy alta se deshidratan para aumentar su estabilidad, para ello se introducen en una estufa a vacío Vaciotem-T JPSELECTA a 40 °C durante 24 horas, donde alcanzan una actividad del agua de 0,35.

3.3.7. Monitorización de los fenómenos de expansión de microencapsulaciones en medio líquido

Una vez deshidratadas las cápsulas se determinó la capacidad de expandirse de nuevo al entrar en contacto con diferentes medios líquidos (con un pH de 3 y 4,7). Cada cápsula se introdujo en el medio líquido y se realizaron fotografías de su evolución a distintos tiempos: 5, 15, 30, 60, 120, 150, 200, 240, 300, 360, 420, 480, 540, 600 s y a partir de aquí, cada 5 min hasta 30 min. Esta determinación se realizó mediante el análisis de imagen descrito en el apartado 3.2.2.2.

3.3.8. Monitorización de la liberación de compuestos encapsulados en medio líquido

Para monitorizar la liberación de los compuestos encapsulados se utilizaron tres tipos de cápsulas: alginato cálcico, alginato cálcico con hierro y alginato cálcico con vitamina C. Cada experimental se llevó a cabo con 0,05 g de cápsulas y 200 µL de medio, tomando un espectro en el rango de la radiofrecuencia en los tiempos: 5, 15, 30, 60, 120, 150, 200, 240, 300, 360, 420, 480, 540, 600, 1200, 1500, 1800, 2500, 3600, 4500 s.

3.4. Diagramas de los experimentales

3.4.1. Experimental de secado de patata mediante HAD combinado con microondas

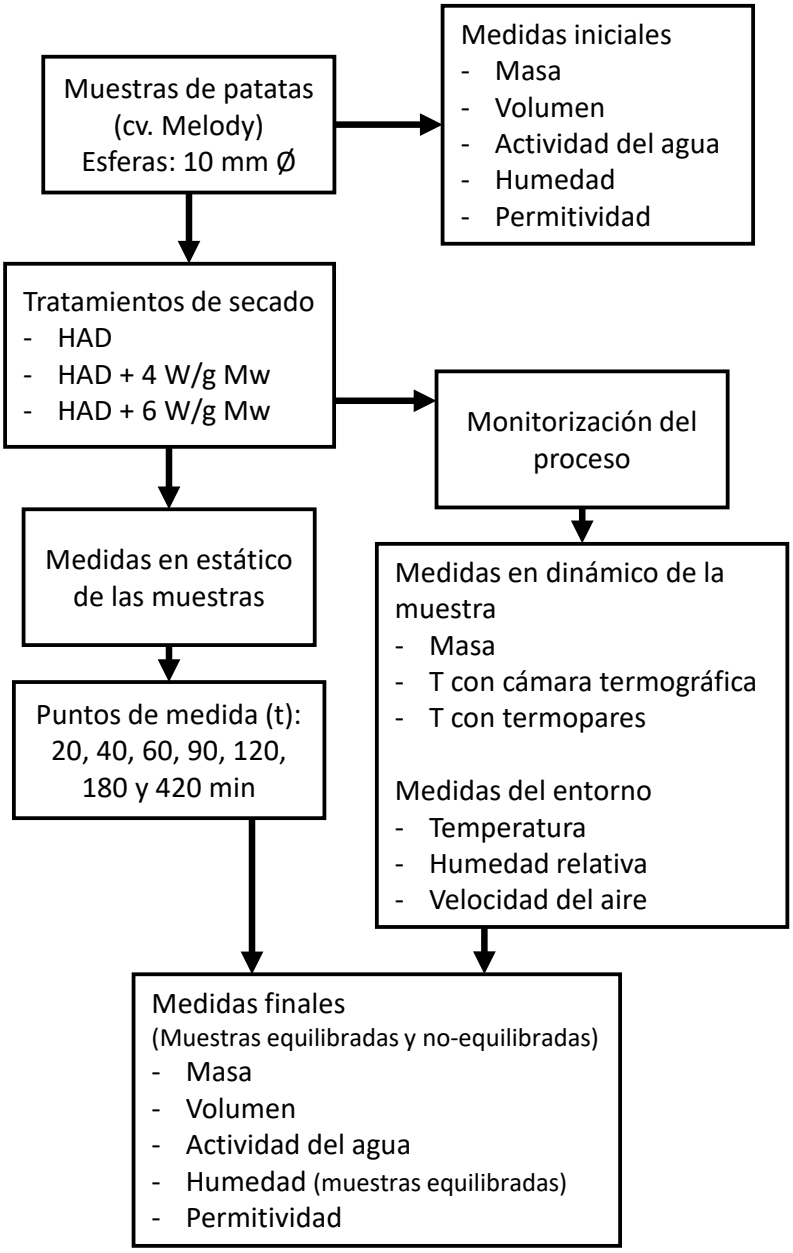

3.4.2. Experimental de congelación de carne de pollo

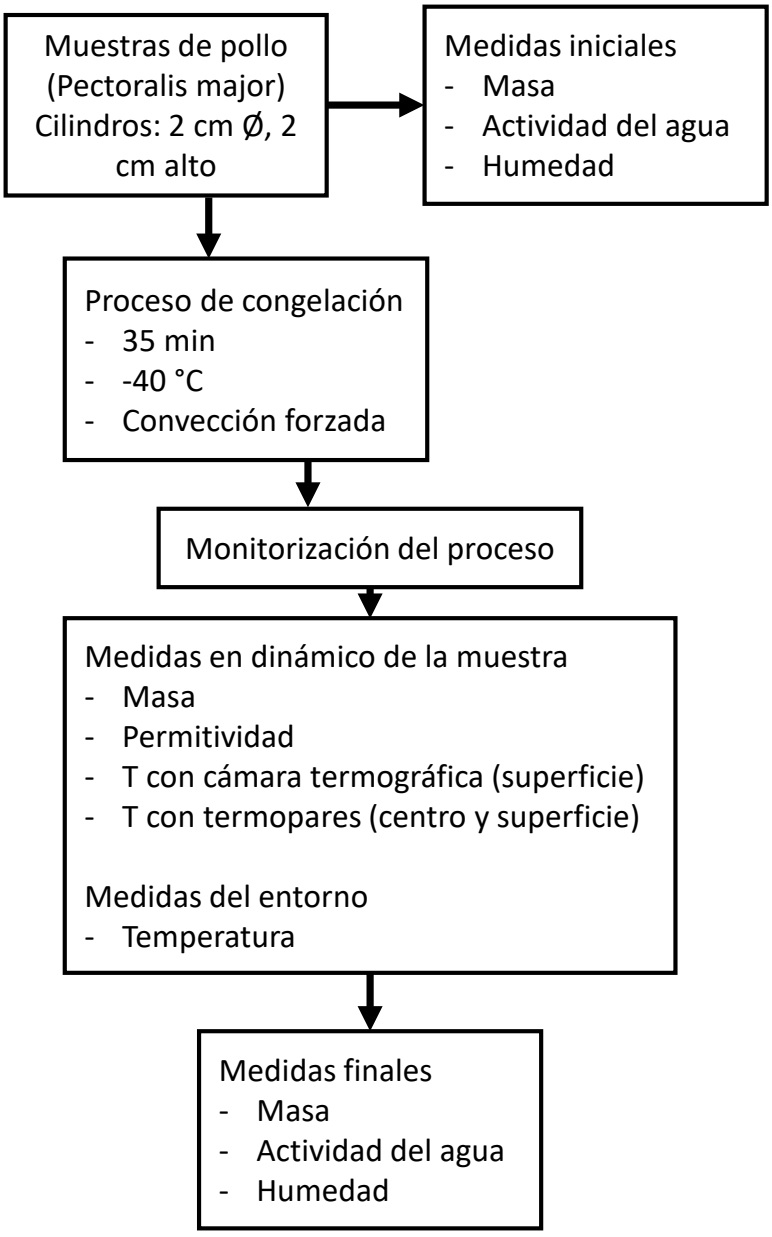

3.4.3. Experimental de caramelizado de manzana

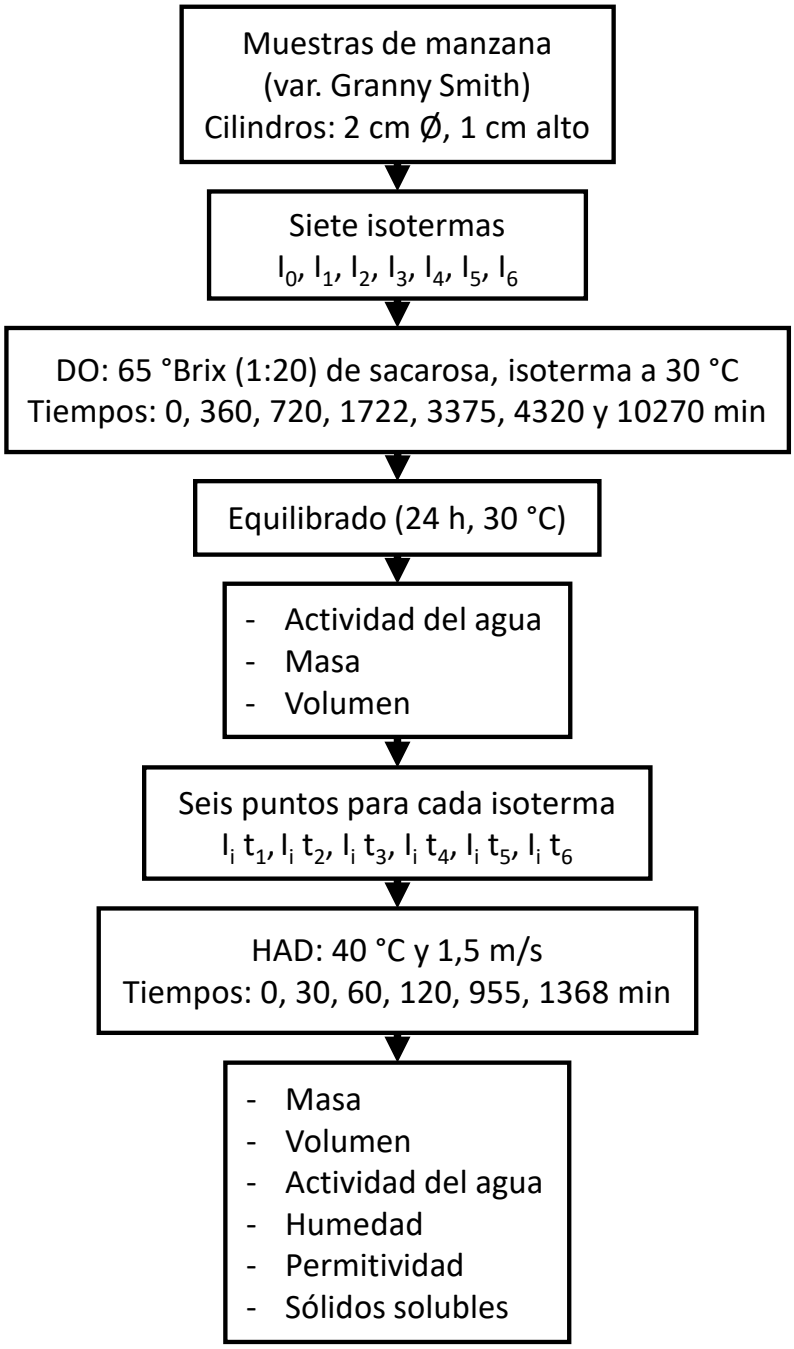

3.4.4. Experimental de cinéticas de liberación de compuestos encapsulados

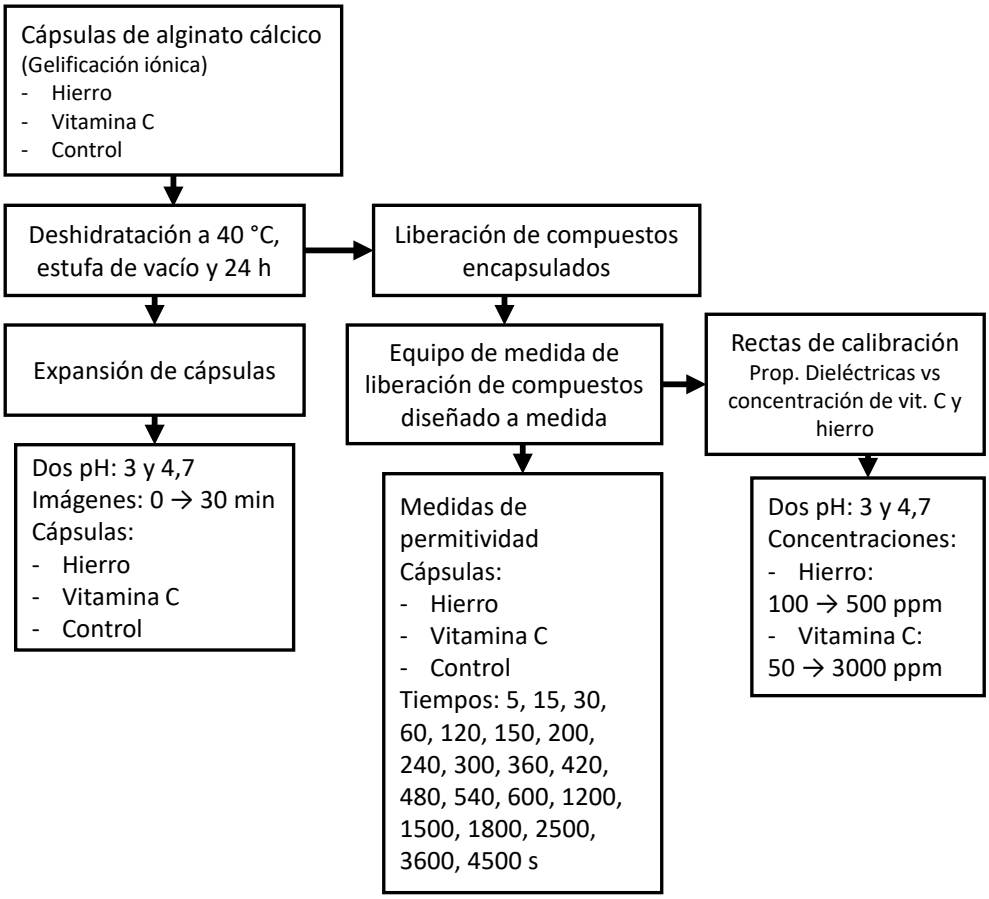

Resultados

applied sciences

MDPI

Hot air and microwave combined drying of potato monitored by infrared thermography

J.A. Tomas-Egea [1], M.V. Traffano-Schiffo [2], P.J. Fito [1] and M. Castro-Giraldez [1]

[1] Instituto Universitario de Ingeniería de Alimentos para el Desarrollo, Universitat Politècnica de València, Camino de Vera s/n, 46022 Valencia, Spain
[2] Instituto de Química Básica y Aplicada del Nordeste Argentino, IQUIBA-NEA, UNNE-CONICET, Avenida Libertad 5460, 3400 Corrientes, Argentina

Applied Science

https://doi.org/10.3390/app11041730

Published: February 15, 2021

Hot air drying (HAD) at temperatures below the spontaneous evaporation temperature could be combined with microwave (MW) radiation as a thermal energy source in order to reduce the drying time. A photon flux in the microwave range interacts with dipolar molecules (water) through orientation and induction, producing electrical energy storage and thermal energy accumulation and generating an increase in the internal energy of food. The different mechanisms involved in water transport could change when the microwave penetration depth exceeds the sample characteristic dimension of mass transport. The aim of this paper is to determine the effect of MW in the combined HAD-MW drying of raw potato in order to obtain the real driving forces and mechanisms involved in the water transport, with the purpose of optimizing the MW power used. For this purpose, combined drying was carried out on potato samples (0, 4 and 6 W/g). The sample surface temperature was monitored by infrared thermography, and the sample mass was measured continuously through a precision balance. In parallel with continuous drying, another drying treatment was performed at different times (20, 40, 60, 90, 120, 180, 420 min) and conditions (0, 4 and 6 W/g) to analyse the dielectric properties, mass, moisture, volume and water activity. The results show that it is possible to monitor combined drying by infrared thermography, and it can be concluded that the convection heating is mostly transformed into surface water evaporation, with negligible thermal conduction from the surface, and microwave radiation is mostly transformed into an increase in the potato's internal energy.

Keywords: drying; hot air drying; microwave drying; infrared thermography; water transport; combined drying.

Hot air and microwave combined drying of potato monitored by infrared thermography

J.A. Tomas-Egea [1], M.V. Traffano-Schiffo [2], P.J. Fito [1] and M. Castro-Giraldez [1]

[1] Instituto Universitario de Ingeniería de Alimentos para el Desarrollo, Universitat Politècnica de València, Camino de Vera s/n, 46022 Valencia, Spain

[2] Instituto de Química Básica y Aplicada del Nordeste Argentino, IQUIBA-NEA, UNNE-CONICET, Avenida Libertad 5460, 3400 Corrientes, Argentina

Abstract: Hot air drying (HAD) at temperatures below the spontaneous evaporation temperature could be combined with microwave (MW) radiation as a thermal energy source in order to reduce the drying time. A photon flux in the microwave range interacts with dipolar molecules (water) through orientation and induction, producing electrical energy storage and thermal energy accumulation and generating an increase in the internal energy of food. The different mechanisms involved in water transport could change when the microwave penetration depth exceeds the sample characteristic dimension of mass transport. The aim of this paper is to determine the effect of MW in the combined HAD-MW drying of raw potato in order to obtain the real driving forces and mechanisms involved in the water transport, with the purpose of optimizing the MW power used. For this purpose, combined drying was carried out on potato samples (0, 4 and 6 W/g). The sample surface temperature was monitored by infrared thermography, and the sample mass was measured continuously through a precision balance. In

parallel with continuous drying, another drying treatment was performed at different times (20, 40, 60, 90, 120, 180, 420 min) and conditions (0, 4 and 6 W/g) to analyse the dielectric properties, mass, moisture, volume and water activity. The results show that it is possible to monitor combined drying by infrared thermography, and it can be concluded that the convection heating is mostly transformed into surface water evaporation, with negligible thermal conduction from the surface, and microwave radiation is mostly transformed into an increase in the potato's internal energy.

Keywords: drying; hot air drying; microwave drying; infrared thermography; water transport; combined drying.

1. Introduction

During hot air drying (HAD) at temperatures below the spontaneous evaporation temperature, the main force that drives water removal from the product is the gradient of water chemical potential generated between the air, with a very low relative humidity, and the product, with high water activity, causing a water flux from the product to the air (Traffano-Schiffo et al., 2014). Liquid water is transported from inside the sample to the surface, where it evaporates (Dehghannya et al., 2019; Turkan, Canbolat and Etemoglu, 2019). This state change requires the input of energy, which is generally obtained from the internal energy of the air in the sample surroundings, decreasing its temperature. However, it can also be obtained from the internal energy of the surface of the product, thus cooling it. The diversity of water molecule interactions that occur inside the potato tissue (Cuibus et al., 2014), as well as the different ways that water molecules have to reach the surface, make the internal water transport fast at the beginning of drying, as the water molecules with high mobility are mobilized through the fastest route (apoplastic pathways). In this drying period, surface evaporation is the limiting factor of the overall transport. After this period, more retained molecules (critical moisture) are mobilized through slower routes, causing slower internal transport. In this period, the internal transport becomes the limiting factor (Castro-Giraldez, Fito and Fito, 2011).

Another possibility is to combine the thermodynamic inertia of HAD with another source of heat, such as microwave radiation (Talens, Castro-Giraldez and Fito, 2016). The interaction of photons with biological systems at low frequencies of the electromagnetic spectrum (Hz to GHz) causes

orientation and induction phenomena. Gamma (γ) dispersion occurs at microwave frequencies (between MHz and GHz), and it is produced by the orientation and induction of dipolar molecules (Markx and Davey, 1999), water being the most important dipolar molecule in biological systems. Gamma dispersion produces the transformation of photonic energy into electrical energy by molecular spin orientation and into thermal energy by molecular collisions and frictions. Many food products have an important aqueous phase; therefore, the application of microwaves in heating processes is a possible source of energy. Microwave radiation has a high penetration depth, producing an internal heating front (Ashtiani, Sturm and Nasirahmadi, 2018; Dehghannya, Bozorghi and Heshmati, 2018). Therefore, combined HAD-MW drying could reduce the drying time (Swain et al., 2012; Dehghannya, Bozorghi and Heshmati, 2018). This technique has been applied in different foods: in orange peel (Talens, Castro-Giraldez and Fito, 2018), in nectarine slices (Ashtiani, Sturm and Nasirahmadi, 2018) and in shiitake mushrooms (Wang et al., 2019).

In order to evaluate the effect of HAD and MW, it is necessary to analyze thermal conditions on the surface of the product. Infrared thermography (FTIR) is a technique that measures the surface temperature of materials in a non-destructive way (Gowen et al., 2010; Gonçalves et al., 2016; Glowacz, 2021). This technique has been used in the food industry to evaluate pork quality (Costa et al., 2007), to detect differences between raw and cooked chicken meat (Ibarra et al., 2000; Ibarra, Tao and Xin, 2000), to evaluate the freezing process of potato (Cuibus et al., 2014), to control disinfection with the steam of carrots (Gan-Mor et al., 2011), to detect the position and depth of bruises in apples (Baranowski et al., 2012) and to

evaluate injuries of cold-stored guava (Gonçalves et al., 2016). Thermal imaging has also been demonstrated to be a useful tool in monitoring the surface temperature in drying processes in the food industry in combined dryings of kiwifruits (Zhou et al., 2019), HAD combined with microwaves to dry mushrooms (Su et al., 2020), HAD of corn kernels (Wei et al., 2019) and vacuum drying of banana slices (Pu et al., 2018).

The aim of this paper is to determine the effect of MW in the combined HAD-MW drying of raw potato at a drying air temperature below the spontaneous evaporation temperature, with the potato having a smaller characteristic dimension than the MW penetration depth, in order to obtain the real driving forces and the mechanisms involved in the water transport, with the purpose of optimizing the MW power used.

2. Materials and Methods

2.1. Materials

Potatoes (*Solanum Tuberosum* (L.) cv. Melody) were acquired from the Mercadona supermarket (Valencia, Spain). They were washed and peeled, and spheres of 10 mm diameter were obtained using a stainless-steel core borer.

2.2. Kinetics experimental procedure

Potato sample spheres were dried by hot air drying (HAD) and hot air drying assisted by microwaves (HAD + MW) using a specially designed HAD-MW oven (Navarrete et al., 2003), connected to a magnetron to provide energy, with a maximum output of 2000 W at 2450 MHz. The oven was connected to a computer to measure the incident and reflected energy using a directional coupler with a power meter in the waveguide of the

magnetron. The drying chamber had a mode stirrer to ensure a homogeneous distribution of microwaves. The selected drying conditions were an air velocity of 1.5 m/s, hot air temperature of 40 °C and MW energy of 0, 4 or 6 W/g (referring to the initial mass of the sample). All treatments were carried out for 420 min. The oven door is a ventilation grill with a mesh size of 2 mm, where the air and the infrared radiation can cross without limitation, but the microwave radiation, with a longer wavelength, cannot.

During the HAD treatment (0 W/g), a sample was placed inside the oven to continuously monitor and record the mass using a Mettler Toledo AB304-S balance (precision of ± 0.01 g). A second sample (or reference sample) was placed next to the previous one and in front of an infrared camera (Optris PI® 160 thermal imager; Optris GmbH, Berlin, Germany) to record the infrared emission of the surface of the potato. The surface temperature of this sample was measured using a K-thermocouple connected to an Agilent 34901A multiplexer (Agilent Technologies, Malaysia) and recorded by an Agilent 34972A data logger (Agilent Technologies, Malaysia). Finally, a certified emissivity label (ε = 0.95), provided by Optris GmbH, was placed in the same plane as the reference sample, and its temperature was also registered by a K-thermocouple. For HAD-MW treatments (4 and 6 W/g), the experimental procedure was similar, but the surface temperature of the reference samples and the certified emissivity label were monitored only by the infrared camera (Figure 4.1.1).

The environmental conditions (relative humidity and temperature) were also registered.

2.3. Static experimental procedure

In parallel with continuous drying, drying treatments at different times (20, 40, 60, 90, 120, 180, 420 min) and conditions (0, 4 and 6 W/g) were performed in triplicate. After drying, samples were kept in Aqualab® cups, sealed with Parafilm® and maintained at 4 °C for 24 h in order to reach an internal equilibrium (mechanical and chemical) (Traffano-Schiffo et al., 2014). The following determinations were performed for raw samples, dried (non-equilibrated) samples and samples after they were left for 24 h at 4 °C (equilibrated samples): permittivity, mass, volume and surface water activity (Figure 4.1.1). Considering that moisture is determined using a destructive method, this analysis was carried out only for equilibrated samples.

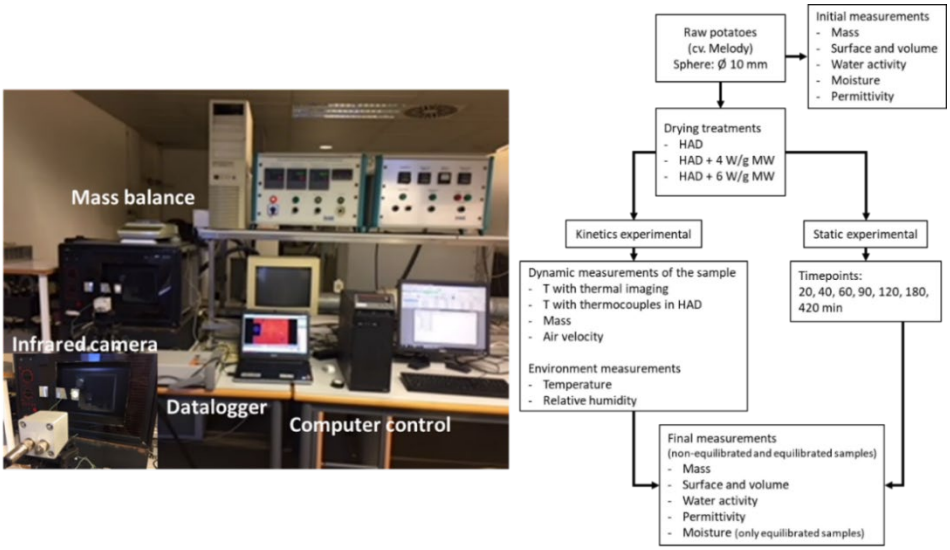

Figure 4.1.1. Experimental setup and diagram of the experimental procedure.

2.4. Potato sample determinations

Every physicochemical property was measured at each drying time explained in Section 2.3. The moisture of the spheres was obtained

gravimetrically by drying the samples in a vacuum oven at 60 °C until a constant weight (AOAC, 1990). Water activity was measured with an Aqualab® dew-point hygrometer, series 3 TE (± 0.003) (Decagon Devices Inc., Pullman, WA, USA). The volume and surface of the spheres were obtained by image analysis using Adobe® Photoshop® CS6 software (Adobe Systems Inc., San Jose, CA, USA).

2.5. Dielectric properties

Dielectric properties were measured at each drying time as explained in Section 2.3 by using an Agilent 85070E open-ended coaxial probe (Agilent, Santa Clara, CA, USA) connected to an Agilent E8362B vector network analyzer (Agilent, Santa Clara, CA, USA). The system was calibrated by using three different types of loads: air, short-circuit and 25 °C Milli®-Q water. Once the calibration was completed, 25 °C Milli®-Q water was measured again to check calibration suitability. The dielectric properties were measured by attaching the probe to the surface of the samples. All determinations were made at 500 MHz to 20 GHz. The measurements were made in triplicate.

3. Results

The drying process at temperatures below the spontaneous evaporation temperature implies that evaporation occurs through thermodynamic inertia in the air/sample interface, that is, the gradient of water chemical potential between the air surrounding the sample and its surface. Then, water evaporation occurs from the sample surface, and thus, the water transport inside the sample occurs in the liquid state. The terms of the water chemical potential that drive the water transport are those

associated with the difference between the surface water activity of the sample and the relative humidity of the drying air and also the difference between the drying air temperature and the sample surface temperature. These differences are produced in a thin air layer, called a boundary layer, with a thickness dependent on the phenomena of water transfer and heat transmission. Figure 4.1.2 shows a scheme of heat and mass exchange throughout the boundary layer. In this figure, it is possible to observe two planes in which some mechanisms converge; the first is the interface between the air and the surface of the sample, where heat convection is used to evaporate water (induced by the water chemical potential) and to heat the surface, and the second is the microwave heating plane, which is defined by the microwave penetration depth.

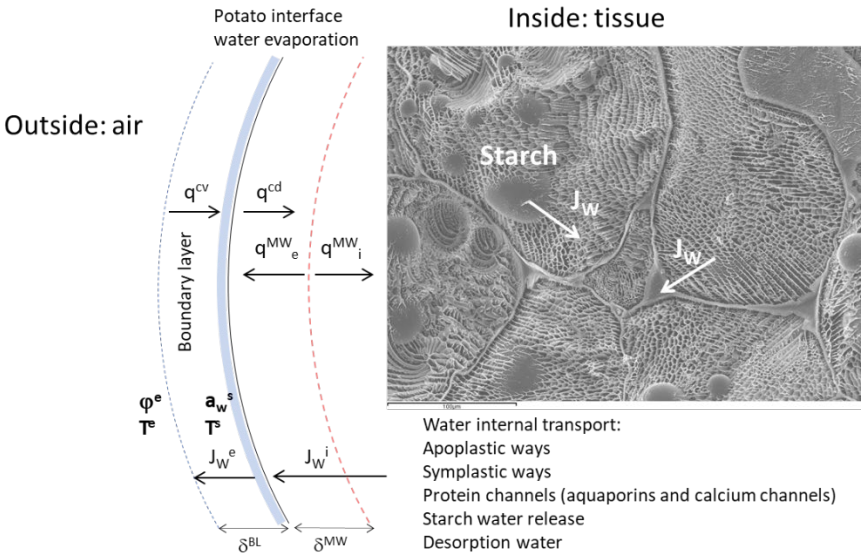

Figure 4.1.21. Scheme of heat and water mass transport mechanisms in a combined hot air drying (HAD) and MW drying process, where q represents heat, J_W represents water flux, φ^e is the drying relative humidity, T^e is the drying temperature, T^s is the surface of the sample temperature, $a_w{}^s$ is the water activity of the sample in the surface, the superscript MW means microwave, CV means convective and cd is conduction.

It is necessary to define the variables that characterize each of these planes in order to quantify the phenomena that occur in the combined process of HAD and MW. As explained in the Materials and Methods section, the surface temperature was obtained by FTIR, with a reference material with known emissivity to remove the effect of the reflected energy from the sample surroundings using the equation of (Traffano-Schiffo et al., 2014). With this expression, it is possible to obtain the emissivity of the sample and, therefore, its surface temperature. Figure 4.1.3a shows the emissivity with respect to the sample moisture (expressed on a dry basis), since in the far IR spectrum, the water molecule proportion is one of the main factors that affect the emissivity (Talens, Castro-Giraldez and Fito, 2016). It is possible to observe how the emissivity decreases as the moisture decreases. In Figure 4.1.3b, it is possible to observe the relationship between the emissivity and the energy emitted by the sample without the effect of the reflected energy from the surroundings. This energy was estimated with two reference materials, one situated close to the sample and the other situated toward the door of the dryer (the door is a ventilation grill with a mesh size of 2 mm, where the air can cross without limitation, as can photons in the infrared range, but photons in the microwave range cannot pass). This energy is needed to obtain, with the emissivity, the real surface temperature.

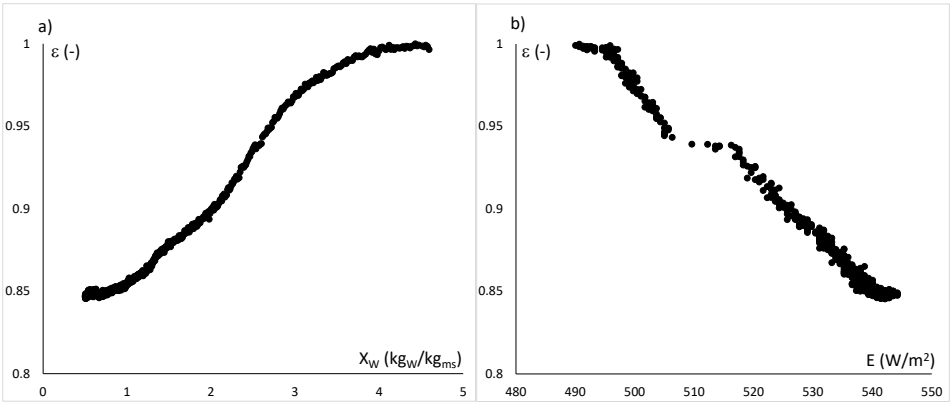

Figure 4.1.3. Emissivity in the HAD treatment with regard to (a) moisture on a dry basis and (b) IR energy emitted by the sample.

Considering that the K-thermocouples could only be used in the HAD experiment, the emissivity obtained in this experiment was used to correct the surface temperature measured by FTIR in combined HAD-MW experiments, using the moisture of the sample to obtain the value. Figure 4.1.4 shows the evolution of surface temperature in each treatment. This figure shows how the surface temperature increases, in all treatments, throughout the drying time. In the case of the HAD treatment, the surface temperature increases and reaches equilibrium with the drying temperature; however, the combined HAD-MW treatments increase the surface temperature throughout the drying time to above that in the HAD treatment; that is, the temperature increases beyond the drying temperature. However, at the end of drying, the surface temperature decreases when the product already has low moisture.

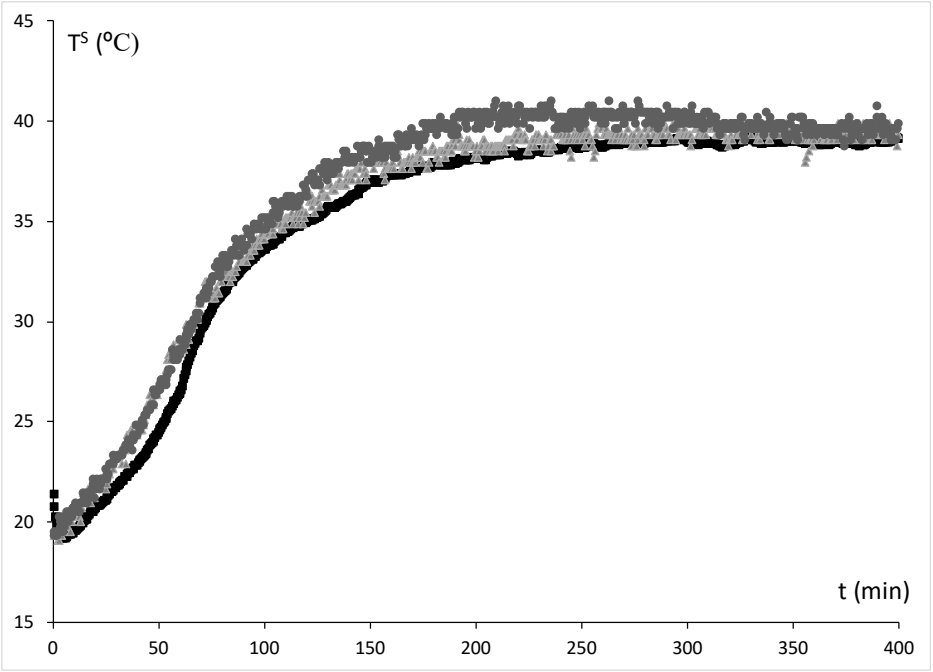

Figure 4.1.4. Evolution of surface temperature in the HAD treatment (■), HAD + 4 W/g treatment (▲) and HAD + 6 W/g treatment (●).

In order to understand the phenomena that occur at the sample/air interface, it is necessary to calculate the thermal energy consumed on the potato surface. The convective heat that the surface receives is used to evaporate the water that has reached the sample surface and to heat this interface. Therefore, the thermal energy expended in evaporation (Q^V) is estimated as (see Equation 4.1.1):

$$Q^v = \frac{\Delta M_w \cdot \Delta G^v}{S \cdot \Delta t} \qquad (4.1.1)$$

where ΔM_w is the water loss (g) in Δt time (s), ΔG^v is the latent heat of water (J/g) and S is the sample surface (m^2).

The thermal energy consumed by surface heating (Q^U) will depend on the increase in surface temperature, the heat flowing to the inside of the sample by conduction (q^{cd}), the specific heat of the sample and the sample mass. The relation between the thermal energy consumed in the interface and the heat flowing to the inside of the sample by conduction can be expressed as follows (see Equation 4.1.2):

$$Q^U - q^{cd} = \frac{\Delta T \cdot M \cdot C_P}{S \cdot \Delta t} \tag{4.1.2}$$

where ΔT is the surface temperature variation in Δt time, M is the mass of the sample (g) and C_P is the specific heat of the potato, estimated with the water and starch mass fraction (kJ/kgK).

If this calculation is carried out, the thermal energy relation oscillates between 3 % and 0.1 % of the heat consumed by evaporating water, making it practically negligible.

On the other hand, the heat that reaches the surface can be estimated by the following equation:

$$q^{cv} = h \cdot S \cdot (T^e - T^s) \tag{4.1.3}$$

where q^{cv} is the heat by the convective mechanism (W), h is the individual coefficient of heat convection (W/m^2K), T^e is the external or air-drying temperature (°C) and T^S is the surface or interface temperature (°C).

In the case of the HAD treatment, the energy consumption in the interface is equal to the heat received by convection; therefore, it is possible to calculate the individual coefficient of heat convection using the following equation:

$$h = \frac{Q^v + Q^U - q^{cd}}{S \cdot (T^e - T^s)} \tag{4.1.4}$$

where T^e is the air-drying temperature (°C), T^S is the surface temperature (°C), $Q^U - q^{cd}$ is estimated using Equation 4.1.2 and Q^V is estimated using Equation 4.1.1.

Figure 4.1.5 shows the individual coefficient of heat convection estimated by Equation 4.1.4 for the HAD treatment. In Figure 4.1.5a, it is possible to observe how h increases exponentially when the interface reaches the air-drying temperature. The same occurs in Figure 4.1.5b, where the h evolution increases with the treatment time, and the external resistance of heat transmission can be neglected after approximately 230 min. The individual coefficient of heat convection will depend on the turbulence and the interface temperature; thus, it is possible to apply the relation between h and the surface temperature to obtain the h evolution in HAD-MW combined treatments.

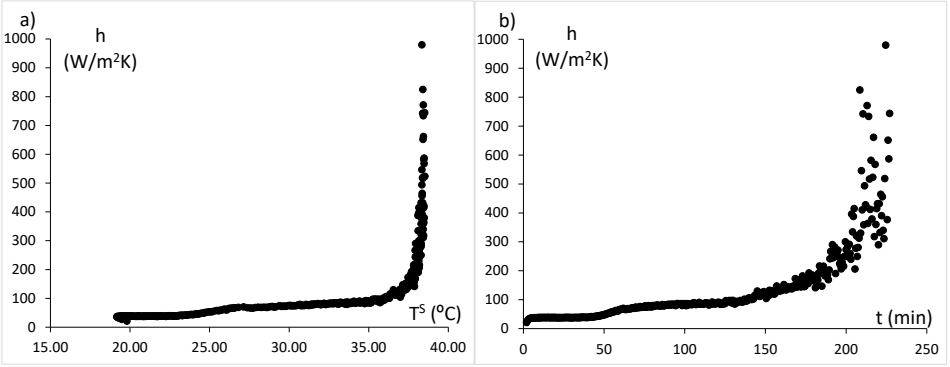

Figure 4.1.5. The individual coefficient of heat convection with regard to (a) surface temperature in the HAD treatment and (b) drying time.

Furthermore, h can be defined by the relation between the thermal conductivity of air and the boundary layer depth. The air thermal conductivity can be estimated with the water mass fraction in air, calculated with the thermodynamic properties of air (Talens, Castro-Giraldez and Fito, 2018). Thus, the boundary layer depth can be estimated as follows:

$$\delta^{BL} = \frac{k_{air}}{h} = \frac{k_{dry\ air} \cdot (1 - x_v) + k_w \cdot x_v}{h} \tag{4.1.5}$$

Figure 4.1.6a shows the variation of water and dry air thermal conductivity with the temperature needed in Equation 4.1.5. Figure 4.1.6b represents the boundary layer depth for all treatments, where it is possible to observe how the thickness decreases faster depending on the power of the MW treatment.

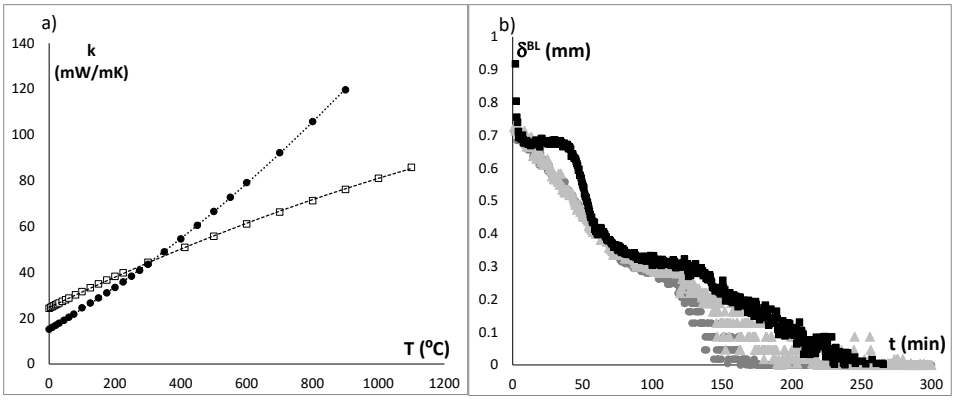

Figure 4.1.6. (a) Plot of the thermal conductivity of dry air (●) and vapor (□) with regards to the temperature and (b) plot of the boundary layer depth with regards to the drying time: HAD treatment (■), HAD + 4 W/g treatment (▲) and HAD + 6 W/g treatment (●).

In the case of combined drying methods, the microwaves absorbed by the samples represent the quantity of photonic energy at 2.45 GHz that dissipates in electric and thermal energy throughout the microwave

penetration depth (δ^{MW}). In this frequency range, the main effect of photon radiation is the gamma dispersion, which consists in the orientation and induction of dipolar molecules, water being the main dipolar molecule in potato tissue. The microwave penetration depth can be estimated as follows (Talens, Castro-Giraldez and Fito, 2016):

$$\delta^{MW} = \frac{|\varepsilon|}{2\pi f}\frac{\sqrt{\varepsilon'}}{\varepsilon''} \quad (4.1.6)$$

where $|\varepsilon|$ represents the modulus of permittivity at 2.45 GHz, ε' is the dielectric constant, ε'' is the loss factor and *f* is the frequency expressed in Hz (2.45 GHz).

An important characteristic of microwave heating is that when the characteristic dimension of the sample (radius) is less than microwave penetration depth, heating occurs from the centre of the sample to the surface (Talens, Castro-Giraldez and Fito, 2016). In this experiment, δ^{MW} was estimated using Equation 4.1.6, obtaining, for raw potato, a value of 1.62 ± 0.06 and decreasing throughout the drying process to 0.83 ± 0.08 at 440 min, always being greater than the radius measured at each time.

The proportion of microwave energy that has been absorbed and transformed into thermal energy can be estimated by the dielectric properties at 2.45 GHz. In order to estimate the amount of microwave energy absorbed as thermal energy, the microwave energy distribution ratio (r_{MW}) from (Talens, Castro-Giraldez and Fito, 2016) was used by means of dielectric properties (Equation 4.1.7).

$$r_{MW} = \frac{\varepsilon''}{\varepsilon' + \varepsilon''} \quad (4.1.7)$$

Figure 4.1.7a shows the relationship between r_{MW} and sample moisture expressed on a dry basis, where it is possible to observe that the microwave energy distribution ratio remains constant while the moisture is high, and when it reaches a moisture of around 0.7 on a dry basis, it decreases exponentially. This phenomenon may be because the critical moisture of the potato is approximately 0.7, and with that value, the water that remains in the tissue has less mobility, and the ease of inducing water molecules is less than the ease of orienting them. Consequently, the absorption of energy as electrical energy storage increases compared with the dissipation as thermal energy.

The HAD + MW combined drying equipment measures the total power emitted by the magnetron and the power returned to the emission tube (reflected power). The difference between the two is the microwave power absorbed (P_{abs}) by the sample. Therefore, with the absorbed power and r_{MW}, the heating by microwaves (q^{MW}) can be calculated with the following equation.

$$q^{MW} = P_{abs} \cdot r_{MW} \quad (4.1.8)$$

Figure 4.1.7b shows the evolution of microwave heating throughout the treatment. It is possible to observe that the heat remains constant until a process time of 180 min, whereupon the microwave heat decreases. This drying time represents the moment when the sample reaches critical moisture, whereupon the water molecules reduce their mobility and hinder the

induction phenomena, while their capacity to store electric energy remains, as seen in Figure 4.1.7a.

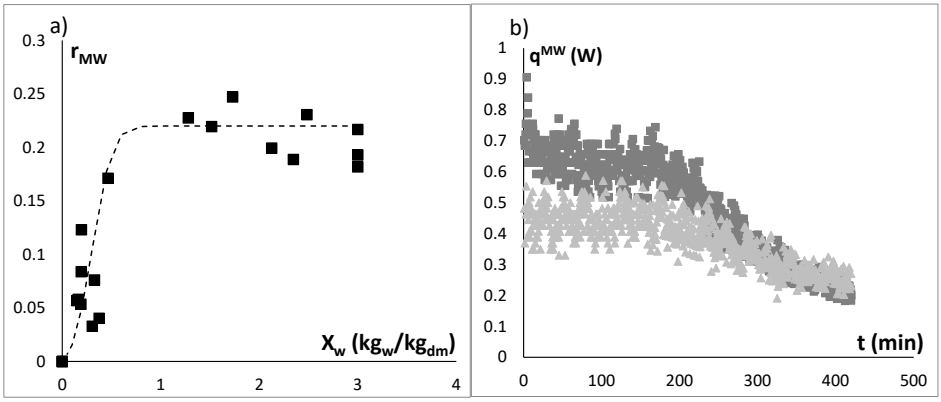

Figure 4.1.7. Microwave sample effect: (a) The relationship between the microwave energy distribution ratio and the sample moisture expressed on a dry basis and (b) microwave heating throughout the drying time for HAD + 4 W/g (▲) and HAD + 6 W/g (■) treatments.

If an energy balance is applied to the total sample (Equation 4.1.9), the heat contribution by convection (q^{cv}) and by microwaves (q^{MW}) will be distributed in heating by conduction from the surface ($Q^U - q^{cd}$), the internal energy variation associated with microwave heating and surface water evaporation. This balance is shown in the following equation:

$$q^{cv} + q^{MW} = Q^U - q^{cd} + \left.\frac{\partial U}{\partial t}\right|_{MW} + Q^V \qquad (4.1.9)$$

where U is the internal energy of the sample and E^v is the evaporation energy.

With Equation 4.1.9, it is possible to estimate the internal energy variation associated with microwave heating. Figure 4.1.8a shows the internal energy variation associated with microwave heating, obtained from Equation 4.1.9, with regard to the sample moisture on a dry basis.

In order to better understand the heating process of microwave radiation, Figure 4.1.8c shows a diagram of the photon input at 2.45 GHz in the potato sphere, with a radius smaller than the microwave penetration depth, producing an accumulation of heat dissipation at the centre of the sample. This phenomenon generates heat, which flows by conduction from the centre to the surface. However, a small part of the dissipation of the electromagnetic energy of the photons is lost along the way, which is more evident in water molecules in the gas state because of their high mobility, flowing through the boundary layer, increasing the air surface temperature or producing more evaporation.

Considering that the evolution of the individual coefficient of heat convection is similar in all treatments, it is possible to calculate the surface heating by microwaves (E_{MW}) by comparing, at each time, the surface temperature of each combined treatment with the HAD treatment, according to the following equation:

$$E_{MW} = S \cdot \delta^{BL} \cdot \rho_{AIR} \cdot X \cdot C_P^v \cdot (T_{HAD+MW}^S - T_{HAD}^S) \quad (4.1.10)$$

where ϱ_{AIR} is the air density (kg/m^3) obtained by the thermodynamic properties or air (Talens, Castro-Giraldez and Fito, 2016), X is the absolute moisture of air (kg_w/kg_{dryair}) and $C_P{}^v$ is the specific heat of vapor at the surface temperature.

Figure 4.1.8b shows the surface heating by microwave evolution for combined drying treatments, where it is possible to observe that internal heating (Figure 4.1.8a) is 10,000 times higher than the surface heating by microwaves (Figure 4.1.8b). Consequently, in a combined drying process of hot air and microwaves at temperatures lower than the spontaneous

evaporation temperature and in samples with a characteristic dimension less than the microwave penetration depth, it is possible to conclude that the convection heating is mostly transformed into surface water evaporation, and microwave heating is mostly transformed into an increase in the internal energy of the food, that is, an increase in the internal temperature.

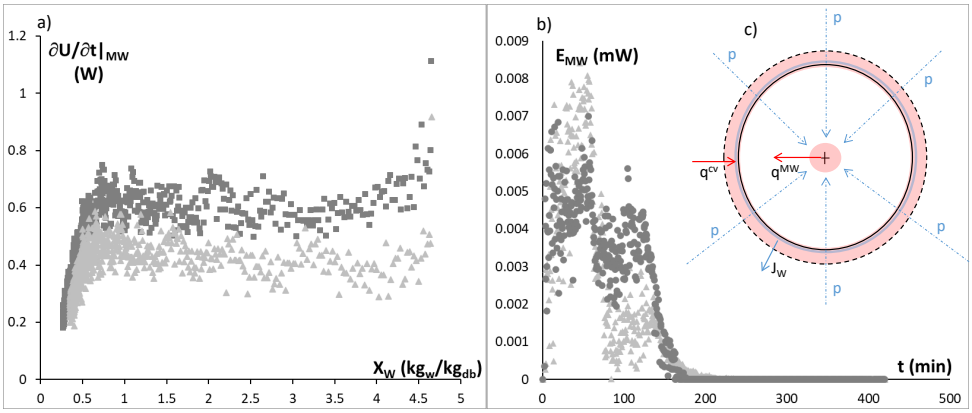

Figure 4.1.8. (a) Internal energy accumulation throughout the drying time for HAD + 4 W/g (▲) and HAD + 6 W/g (■) treatments, (b) microwave heating of the boundary layer throughout the drying time for HAD + 4 W/g (▲) and HAD + 6 W/g (■) treatments. (c) Scheme of the effect of microwaves in sample heating, where p represents the photon fluxes, q_{MW} represents the heat conduction produced by the microwave heating source in the sample center, Jw is the water flux and q^{cv} is the heat convection.

Therefore, the measurement of the surface temperature by FTIR in the HAD process combined with microwave heating allows the HAD process and surface water evaporation to be monitored, but not the microwave heating process, because MW heats with high penetration. Thus, the FTIR technology allows the segregation of the effect of HAD and microwave heating in combined drying processes, making it possible to determine water removal. In the future, IR cameras with a higher frequency spectrum will be able to make direct measurements of the surface water content.

4. Conclusions

It is possible to apply FTIR to a HAD-MW combined drying process using an oven grill door with a mesh size that allows the hot air and photon radiation in the infrared spectrum to cross it, but not the photons in the microwave spectrum. As a result, the evolution of the drying process can be determined through the surface temperature of the sample.

It is shown that the higher effect of microwaves in the drying process occurs at moistures above the drying critical moisture, where the water molecules reduce their mobility and hinder the induction phenomena.

In a combined drying process of hot air and microwaves at temperatures lower than spontaneous evaporation and in samples with a characteristic dimension less than the microwave penetration depth, it is possible to conclude that the convection heating is mostly transformed into surface water evaporation, with negligible thermal conduction from the surface. Furthermore, microwave radiation is mostly transformed into an increase in the internal energy of the food, that is, an increase in the internal temperature, from the centre to the surface.

5. Acknowledgments

The authors acknowledge the financial support from THE SPANISH MINISTERIO DE ECONOMÍA, INDUSTRIA Y COMPETITIVIDAD, Programa Estatal de I+D+i orientada a los Retos de la Sociedad AGL2016-80643-R, Agencia Estatal de Investigación (AEI) and Fondo Europeo de Desarrollo Regional (FEDER). Juan Ángel Tomás-Egea wants to thank the

FPI Predoctoral Program of the Universitat Politècnica de València for its support.

6. References

Ashtiani, S.-H.M., Sturm, B. and Nasirahmadi, A. (2018) 'Effects of hot-air and hybrid hot air-microwave drying on drying kinetics and textural quality of nectarine slices', *Heat and Mass Transfer*, 54(4), pp. 915–927. doi:https://doi.org/10.1007/s00231-017-2187-0.

Baranowski, P. *et al.* (2012) 'Detection of early bruises in apples using hyperspectral data and thermal imaging', *Journal of Food Engineering*, 110(3), pp. 345–355. doi:https://doi.org/10.1016/j.jfoodeng.2011.12.038.

Castro-Giraldez, M., Fito, P.J. and Fito, P. (2011) 'Nonlinear thermodynamic approach to analyze long time osmotic dehydration of parenchymatic apple tissue', *Journal of food engineering*, 102(1), pp. 34–42. doi:https://doi.org/10.1016/j.jfoodeng.2010.07.032.

Costa, N. *et al.* (2007) 'The use of thermography on the slaughter-line for the assessment of pork and raw ham quality', *Italian journal of animal science*, 6(sup1), pp. 704–706. doi:https://doi.org/10.4081/ijas.2007.1s.704.

Cuibus, L. *et al.* (2014) 'Application of infrared thermography and dielectric spectroscopy for controlling freezing process of raw potato', *Innovative Food Science & Emerging Technologies*, 24, pp. 80–87. doi:https://doi.org/10.1016/j.ifset.2013.11.007.

Dehghannya, J. *et al.* (2019) 'Ultrasound-assisted intensification of a hybrid intermittent microwave - hot air drying process of potato: Quality aspects and energy consumption', *Ultrasonics*, 96, pp. 104–122. doi:10.1016/j.ultras.2019.02.005.

Dehghannya, J., Bozorghi, S. and Heshmati, M.K. (2018) 'Low temperature hot air drying of potato cubes subjected to osmotic dehydration and intermittent microwave: drying kinetics, energy consumption and product quality indexes', *Heat and Mass Transfer*, 54(4), pp. 929–954. doi:https://doi.org/10.1007/s00231-017-2202-5.

Gan-Mor, S. *et al.* (2011) 'Adapted thermal imaging for the development of postharvest precision steam-disinfection technology for carrots', *Postharvest Biology*

and Technology, 59(3), pp. 265–271. doi:https://doi.org/10.1016/j.postharvbio.2010.10.003.

Glowacz, A. (2021) 'Fault diagnosis of electric impact drills using thermal imaging', *Measurement*, 171, p. 108815. doi:10.1016/j.measurement.2020.108815.

Gonçalves, B.J. *et al.* (2016) 'Using infrared thermography to evaluate the injuries of cold-stored guava', *Journal of food science and technology*, 53(2), pp. 1063–1070. doi:DOI 10.1007/s13197-015-2141-4.

Gowen, A.A. *et al.* (2010) 'Applications of thermal imaging in food quality and safety assessment', *Trends in food science & technology*, 21(4), pp. 190–200. doi:https://doi.org/10.1016/j.tifs.2009.12.002.

Ibarra, J.G. *et al.* (2000) 'Cooked and raw chicken meat: Emissivity in the mid-infrared region', *Applied Engineering in Agriculture*, 16(2), p. 143. doi:10.13031/2013.5060.

Ibarra, J.G., Tao, Y. and Xin, H. (2000) 'Combined IR imaging-neural network method for the estimation of internal temperature in cooked chicken meat', *Optical Engineering*, 39(11), p. 3032. doi:10.1117/1.1314595.

Markx, G.H. and Davey, C.L. (1999) 'The dielectric properties of biological cells at radiofrequencies: applications in biotechnology', *Enzyme and Microbial Technology*, 25(3–5), pp. 161–171. doi:https://doi.org/10.1016/S0141-0229(99)00008-3.

Navarrete, N.M. *et al.* (2003) 'Diseño y construcción de una instalación experimental para el estudio de la cinética de secado combinado por aire caliente y microondas', *Alimentación, equipos y tecnología*, 22(181), pp. 101–106.

Pu, Y.-Y. *et al.* (2018) 'Nondestructive quality evaluation of banana slices during microwave vacuum drying using spectral and imaging techniques', *Drying technology*, 36(13), pp. 1542–1553.

Su, D. *et al.* (2020) 'Drying characteristics and water dynamics during microwave hot-air flow rolling drying of Pleurotus eryngii', *Drying Technology*, 38(11), pp. 1493–1504. doi:10.1080/07373937.2019.1648291.

Swain, S. *et al.* (2012) 'Modeling of microwave assisted drying of osmotically pretreated red sweet pepper (Capsicum annum L.)', *Food Science and Biotechnology*, 21(4), pp. 969–978. doi:DOI 10.1007/s10068-012-0127-9.

Talens, C., Castro-Giraldez, M. and Fito, P.J. (2016) 'A thermodynamic model for hot air microwave drying of orange peel', *Journal of Food Engineering*, 175, pp. 33–42. doi:http://dx.doi.org/10.1016/j.jfoodeng.2015.12.001.

Talens, C., Castro-Giraldez, M. and Fito, P.J. (2018) 'Effect of microwave power coupled with hot air drying on sorption isotherms and microstructure of orange peel', *Food and bioprocess technology*, 11(4), pp. 723–734. doi:https://doi.org/10.1007/s11947-017-2041-x.

Traffano-Schiffo, M.V. *et al.* (2014) 'Thermodynamic model of meat drying by infrarred thermography', *Journal of Food engineering*, 128, pp. 103–110. doi:https://doi.org/10.1016/j.jfoodeng.2013.12.024.

Turkan, B., Canbolat, A.S. and Etemoglu, A.B. (2019) 'Numerical Investigation of Multiphase Transport Model for Hot-Air Drying of Food', *Journal of Agricultural Sciences*, 25(4), pp. 518–529. doi:10.15832/ankutbd.441925.

Wang, Q. *et al.* (2019) 'Quality evaluation and drying kinetics of shitake mushrooms dried by hot air, infrared and intermittent microwave–assisted drying methods', *LWT*, 107, pp. 236–242. doi:https://doi.org/10.1016/j.lwt.2019.03.020.

Wei, S. *et al.* (2019) 'Simulation and experimental studies of heat and mass transfer in corn kernel during hot air drying', *Food and Bioproducts Processing*, 117, pp. 360–372. doi:10.1016/j.fbp.2019.08.006.

Zhou, X. *et al.* (2019) 'Combined radio frequency-vacuum and hot air drying of kiwifruits: Effect on drying uniformity, energy efficiency and product quality', *Innovative Food Science & Emerging Technologies*, 56, p. 102182. doi:10.1016/j.ifset.2019.102182.

Journal of Food Engineering

ELSEVIER

New technique for determining the critical freezing temperatures of chicken breast based on radiofrequency photospectrometry

J.A. Tomas-Egea [1], M. Castro-Giraldez [1] and P.J. Fito [1]

[1] Instituto Universitario de Ingeniería de Alimentos para el Desarrollo, Universitat Politècnica de València, Camino de Vera s/n, 46022 Valencia, Spain

Journal of Food Engineering

Submitted: December 10, 2021

Food freezing operations require an extreme knowledge of the thermal properties of the food to be frozen, in order to achieve a product that at the thawing time preserves the best sensory and food quality properties, and also preserves food safety. Within these properties it is necessary to know the initial freezing temperature (T_{m0}), the freezing temperature of the maximally freeze concentrated liquid phase (T_m'), the glass-transition temperature of the maximally freeze concentrated liquid phase (T_g') and others. However, the techniques to determine these properties are long, tedious, and sometimes with high variability, one of the most important techniques is Differential Scanning Calorimetry (DSC). In this work, the use of photospectrometry in the radiofrequency range (PFR) is proposed, as a fast and reliable method for determining the thermal properties of chicken breast in the freezing process, comparing it with the DSC technique. The results showed a Tg' of -17.50 ± 1.05 °C, obtained by the PFR technique, using the beta dispersion, similar as the result obtained by DSC technique (-16.73 ± 0.13 °C). Therefore, the PFR is a fast, reliable, and easy technique to determine the critical temperatures of the food freezing process.

Keywords: permittivity; glass transition; chicken freezing; dielectric properties.

New technique for determining the critical freezing temperatures of chicken breast based on radiofrequency photospectrometry

J.A. Tomas-Egea [1], M. Castro-Giraldez [1] and P.J. Fito [1]

[1] Instituto Universitario de Ingeniería de Alimentos para el Desarrollo, Universitat Politècnica de València, Camino de Vera s/n, 46022 Valencia, Spain

Abstract: Food freezing operations require an extreme knowledge of the thermal properties of the food to be frozen, in order to achieve a product that at the thawing time preserves the best sensory and food quality properties, and also preserves food safety. Within these properties it is necessary to know the initial freezing temperature (T_{m0}), the freezing temperature of the maximally freeze concentrated liquid phase (T_m'), the glass-transition temperature of the maximally freeze concentrated liquid phase (T_g') and others. However, the techniques to determine these properties are long, tedious, and sometimes with high variability, one of the most important techniques is Differential Scanning Calorimetry (DSC). In this work, the use of photospectrometry in the radiofrequency range (PFR) is proposed, as a fast and reliable method for determining the thermal properties of chicken breast in the freezing process, comparing it with the DSC technique. The results showed a T_g' of -17.50 ± 1.05 °C, obtained by the PFR technique, using the beta dispersion, similar as the result obtained by DSC technique (-16.73 ± 0.13 °C). Therefore, the PFR is a fast, reliable,

and easy technique to determine the critical temperatures of the food freezing process.

Keywords: permittivity; glass transition; chicken freezing; dielectric properties.

1. Introduction

The food freezing operation, as well as the freezing of any biological system, has been studied for a long time due to its high preservation capacity, remaining good quality and safety parameters (Kumar et al., 2020; van der Sman, 2020). The mathematical models developed to predict the stability of frozen food are based on the knowledge of physical and chemical properties that determine the different behaviours induced, in raw matter tissue, during the freezing process. Some of these properties are: the medium capacity to store or transmit heat, the state variables variation to produce the water freezing (and other compounds with change state capacity), the medium glass transition and the nature of solutes with cryoprotective capacity to minimize the internal breakage (Elliott, Wang and Fuller, 2017).

Freezing theory explains that the ice nucleation (formation of the incipient crystalline phase), in biological systems, is produced in supercooling and heterogeneous liquid phase, with thermal fluctuations produced by the exothermic transition (You, Kang and Jun, 2021), followed by ice clusters formation or ice crystals growth induced by ice surface tension and water phase transition (Castro-Giraldez et al., 2014). When freezing operation is produced slowly, at the melting temperature ('T_m'), the amount of ice formed is maximum and the remaining liquid phase is called the maximally freeze concentrated solution. If temperature continues decreasing, the system reaches the glass transition temperature ('T_g') and the maximally freeze concentrated solution increases dramatically its viscosity and becomes a supercooling liquid glass. Foods below glass transition temperature show maximum stability. This is why it is important to know the critical

temperatures of the food freezing process, initial freezing temperature (T_{m0}), the freezing temperature of sample with the maximally freeze-concentrated solute matrix (T_m') or the glass transition temperature of the maximally freeze-concentrated solute matrix (T_g') (Roos, 2021), which means the product has reached its lowest water activity (a_w^c) (Roudaut et al., 2004).

The changes in the state of the unfrozen phase during the freezing operation are shown in the food diagram State (van der Sman, 2020), where freezing line and glass transition curve are limited by the critical temperatures exposed before. Freezing line was modelled by Robinson and Stokes (2002), Chirife and Fontan (1980) or Chen (1986). The prediction of the water activity and the initial freezing point from composition of meat products was model by van der Sman and Boer (2005). A model based on thermodynamics to study the driving forces and to explain the nucleation of water was reported by Hellmuth et al. (2020). Glass transition line was modelled by Gordon and Taylor (1952), being the most widely used model to describe this transformation.

Photospectrometry in different ranges of the electromagnetic spectrum has been used to determine different properties of water in food. At low energy range, radiofrequency and microwave ranges, the interaction with matter can be modelled by Schrodinger's equation (Roychoudhuri, Kracklauer and Creath, 2008) attending to the quantum theory. However, at the macroscopic level, it is possible to apply the Maxwell's equations (Horie, Ushiki and Winnik, 2008) where the physical property that describes the electric effect is the complex permittivity and for the magnetic effect is the complex permeability (Baker-Jarvis and Kim, 2012).

In the radiofrequency range, the main effect is electrical, having three molecular interactions of photons; the alpha dispersion or counterion effect (in the Hz-kHz range), where photons induce an orientation to electrolytes with high ionic strength, the beta dispersion or Maxwell-Wagner effect (in the MHz range), where fixed charges from macromolecules or charges generated by surface tension are oriented (Traffano-Schiffo et al., 2018), and finally, the ionic conductivity (in the Hz-1 GHz range), a phenomenon that only generates electrical losses due to the vibration of low molecular weight electrolytes with high ionic strength. Some authors relate the variation of permittivity in alpha and beta dispersions with the glass transition (Ahmed, Rahman and Roos, 2017; Roos, 2021).

The aim of this work is to develop a new technique to determine the critical freezing and glass temperatures of chicken breast using the photospectrometry in the radiofrequency range technique (PRF).

2. Materials and Methods

2.1. Experimental procedure

Each experiment was carried out using two cylinders of 2 cm in diameter and 2 cm in height, obtained from boneless chicken breasts at "Productos Florida" slaughterhouse, located in Almazora, Castellón, Spain, with 36 hours postmortem. The cylinders were obtained perpendicular to the fibres using a 2 cm diameter coreborer. One of the cylinders was used to record the mass variation using a load cell (FS2030-000X-0500-G, TE Connectivity, Schaffhausen, Switzterland) and to obtain the variations of temperature on its slab surface using the thermographic camera Optris PI®

160 (Optris GmbH, Berlin, Germany). The other cylinder was used to monitor the temperatures of the surface and the centre using K-type thermocouples, and to measure dielectric properties with a two-needle sensor inserted into the centre of the sample and connected to the Agilent 4294A Impedance Analyzer. In addition, the temperature of a certified emissivity surface (Optris GmbH, Berlin, Germany) was recorded both using a K-type thermocouple and the thermographic camera. The ambient temperature was also recorded using another K-type thermocouple. All thermocouples and the load cell were connected to an Agilent 34901A multiplexer in a data acquisition equipment Agilent 34972A (Agilent Technologies, Malaysia) (Figure 1).

The experiment, explained above, was repeated eight times, to obtain significant critical freezing temperatures.

The freezing of the samples was carried out at -40 °C for 35 minutes in an air forced freezing chamber (Model ACR-45/87, Dycometal S.L, Barcelona, Spain). The samples were placed in the centre of the freezer, under turbulent conditions, on a support printed in PLA with a 3D printer. An extruded polystyrene insulation sheet (68 × 52 × 4) was used as the freezer cover (Chovafoam type 4I, Leroy Merlin S.L., Valencia, Spain) with a hole in the middle to put the thermographic camera.

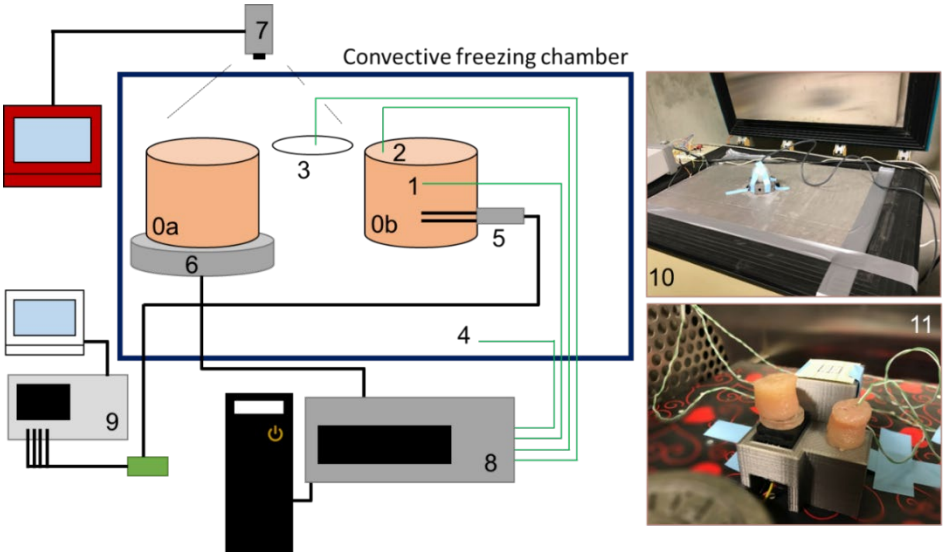

Figure 4.2.11. Experimental setup diagram. 0a, Sample to measure weight and surface temperature by FTIR; 0b, Sample to measure dielectric properties and temperatures using the thermographic camera and K-type thermocouples; 1, K-type thermocouple to measure the temperature of the sample centre; 2, K-type thermocouple to measure the temperature of the sample surface; 3, Certified emissivity surface and K-type thermocouple to measure its temperature; 4 K-type thermocouple to measure the air temperature; 5, Two-needle dielectric sensor; 6, Load cell; 7, Infrared Camera; 8, Data acquisition equipment Agilent 34972A; 9, Agilent 4294A Impedance Analyzer; 10, photo of the extruded polystyrene insulation sheet, with a hole for the thermographic camera, used as the freezer cover; 11, photo of the internal assembly.

2.2. Physicochemical parameters

Before and after freezing, mass was measured using a Mettler Toledo AB304-S precision balance (± 0.001) and water activity was measured with a Decagon Aqualab, series 3 TE dew point hygrometer (± 0.003) (Decagon Devices Inc., USA). The moisture of the fresh product was obtained following the ISO 1442 (1997) standard for meat products, drying the samples at 105 °C and atmospheric pressure for 48 hours.

2.3. Infrared thermography

Thermal images were acquired using the Optris PI 160 Thermal Imager (Optris GmbH, Berlin, Germany). It uses a two-dimensional focal plane array with 160x120 pixels, a spectral range of 7.5 to 13 μm, a resolution of 0.05 °C, and an accuracy of ± 2%. The camera measures a temperature range between -20 and 900 °C. It has a field of view of 23°x17° with a minimum distance of 2 cm. The camera uses Optris PI Connect software (Optris GmbH, Berlin, Germany). The camera was directly connected to a computer to record the entire process. A certified emissivity surface of 25 mm diameter (ε = 0.95) (Optris GmbH, Berlin, Germany) was used as reference to calculate the reflected energy received by the infrared camera.

2.4. Dielectric properties

The sensor consists of two steel-needles with 10 mm long, 0.8 mm of diameter and 1.3 mm of distance between needles. The sensor was inserted into the centre of the sample, penetrating from the lateral surface of the cylinder (through the cylindrical surface), so that the dielectric properties were measured perpendicular to the direction of the fibres (Figure 6). The sensor was developed in the Instituto universitario de Ingeniería de Alimentos para el Desarrollo (IIAD), at the Universitat Politècnica de València (Traffano-Schiffo et al., 2021). The sensor was connected to a 4294A impedance analyser (Agilent Technologies, Santa Clara, CA, USA). Permittivity was estimated using equations (1-3) (see Results Sections). Dielectric spectrum was measured in the frequency range from 40 Hz to 1 MHz. The equipment calibration was performed in open (air) and short-circuit.

2.5. Differential scanning calorimetry

T_g' and the mass fraction of freezable water values was determined using a Differential Scanning Calorimeter (DSC, 1 StareE System, Mettler-Toledo, Switzerland). Poultry meat samples (10 to 20 mg) were accurately weighted using Mettler Toledo XS-205 balance into 40 μL DSC aluminium pans (Mettler Toledo, ME-00026763). Filled pans were hermetically sealed. An empty aluminium pan was used as a reference in all measurements. Liquid nitrogen was used as coolant, poured into the cooling can of the DSC equipment; gas nitrogen was flowed in the purge line, to control the environment of the sample, with a flow rate of 60 mL/min. Calibration was performed by FlexCal, an automatic calibration function supplied by the manufacturers. To perform the experiments, the samples were cooled at 5 °C/min until -80 °C, held for 15 min, warmed to the annealing temperature (-20ºC, based on the work of Delgado and Sun (2002)), held for 60 min, cooled at 5 °C/min until -80 °C, held for 15 min and scanned at 5 °C/min until 20 °C. The protocol followed in this research work was the one established by Delgado and Sun (2002). These authors improved the protocol of Brake and Fennema, (1999) which was based on the method used by Carrington et al., (1994) involving annealing. The glass transition analysis reports the starting, midpoint and end temperatures of a step, once the limits of the transition was provided, and the midpoint temperature was taken as T_g'. Mass fraction of freezeable and unfreezeable water was estimated by the proposed method of Ross (1978), described in Delgado and Sun (2002).

DSC measurements were made by triplicate. The obtained data was analysed with the DSC software provided (STARe software, Mettler Toledo, Barcelona, Spain).

3. Results

The freezing of the chicken samples was carried out in an air forced freezing chamber at -40 °C. An example of temperature evolution of the centre of the sample throughout the process can be observed in Figure 4.2.2. In the figure it can be observed that the temperature falls below zero degrees, and the onset of freezing occurs at temperatures close to -1.6 °C, reaching freezing temperatures of -4 °C due to the cryoscopic decrease. The duration of the freezing process is approximately 7 minutes due to the small size of the sample. After this time there is a drop in temperature until the sample equilibrates at -40 °C, which is the freezing air temperature.

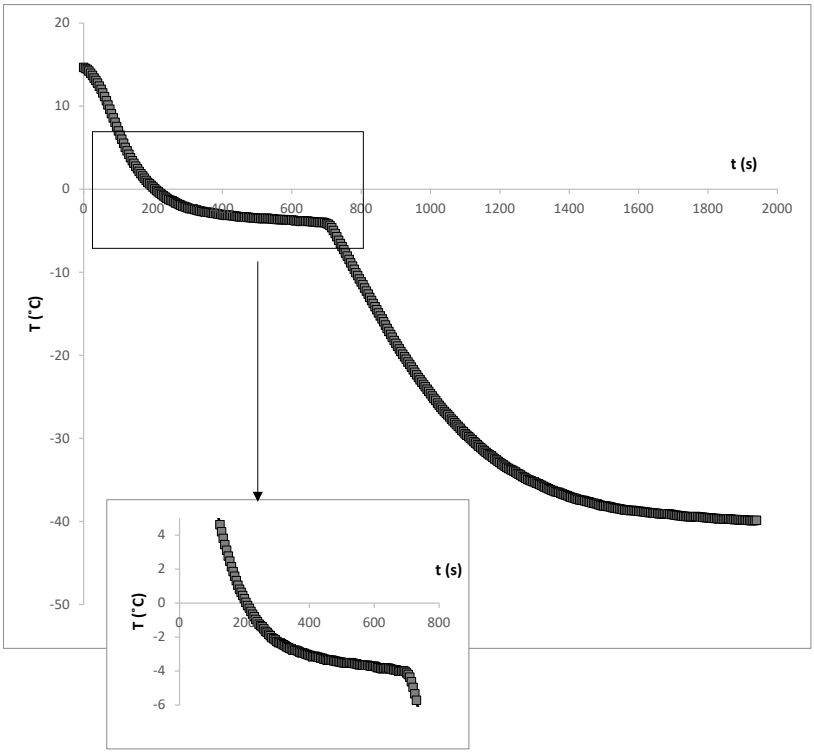

Figure 4.2.22. Freezing curve of one meat breast sample in an air forced freezing chamber at -40 °C.

Glass transition temperature is important for food stability (Delgado and Sun, 2002). The glass transition temperature of the maximum cryo-concentrated solution (T_g') was measured in annealed samples by using Differential Scanning Calorimetry. Figure 4.2.3 shows an example of the thermogram obtained. In the figure, the glass transition is clearly appreciated. An average of T_g' value of -16.73 °C was obtained. This value is close to that obtained by other authors for chicken meat: -17.08 °C (Akköse, 2018); -16.83 °C (Delgado and Sun, 2002); -16.63 °C (Sunooj et al., 2009). The unfreezeable water content has been also estimated by DSC, 0.23 ± 0.02 similar than the value obtained by Delgado and Sun (2002).

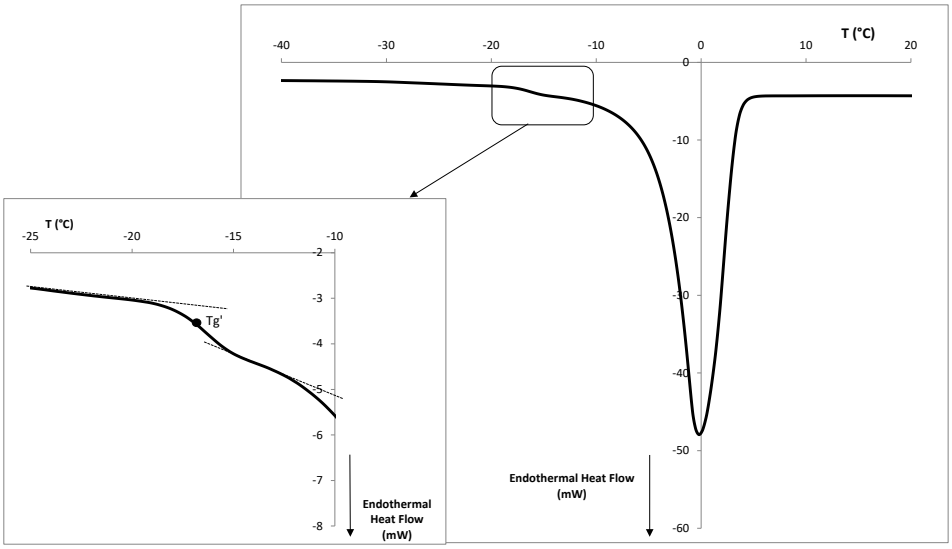

Figure 4.2.3. DSC thermogram for meat breast samples. A detailed of glass transition and the location of T_g' are also shown.

Different analysis techniques based on photonics in the radio frequency range to analyze the freezing process were used by research groups from different fields; it is possible to classify these analyses into two groups:

first the impedance analysis, focusing on the reactance, and the second the analysis of the dielectric properties, focusing on the permittivity.

In a study published by Chin et al., (2007) it is explained that the appearance of an ice phase in a dielectric medium produces a phenomenon in the radiofrequency impedance spectrum, which allows detecting the onset of freezing. Smith and Polygalov (2019), determine a procedure for the detection of the initiation of nucleation by analyzing the imaginary part of the impedance, the reactance. Figure 4.2.4 shows the reactance spectra in the radio frequency range of a of chicken breast sample during freezing. Figure 4.2.4a shows the reactance spectra of the first process times (meat refrigeration from 0 to 370 s), following with the typical gaussian bell shape in the early stages of freezing (660 s) and finishing with the reactance spectra in the glass transition (840 s). The same spectra at long freezing times are shown in Figure 4.2.4b. It is possible to observe how the frequencies at which the maximum reactance appear are of the order of MHz and at the end of the freeze the order is of kHz.

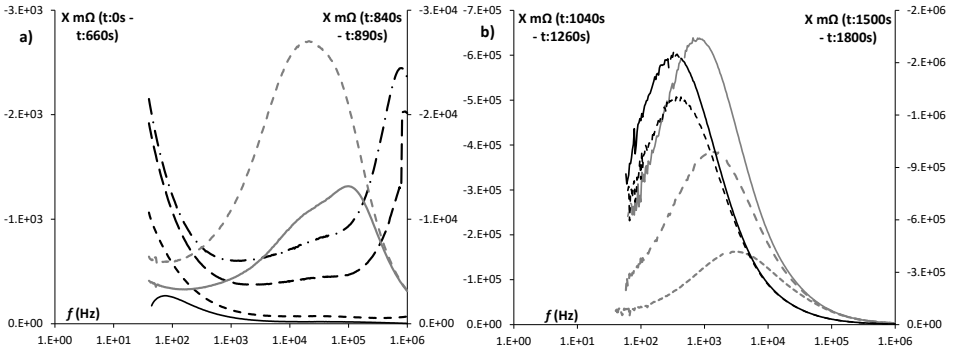

Figure 4.2.4. Reactance spectrum during the breast freezing process of one sample, where a) represents the freezing time from 0 to 890 s (on the left, — 0 s; --- 370 s; – – 660 s and – • – 710 s; and on the right, — 840 s and -- 890 s) and b) from 1040 to 1800s (on the left -- 1040 s; – – 1140 s and — 1260 s; and on the right **--** 1500 s and **—** 1800 s).

Figure 4.2.5 shows the exponential relationship of the maximum effect on reactance and the corresponding relaxation frequency of this phenomenon, compared to the temperature of the sample. As can be seen in this figure, it has not been possible to determine the onset of the phenomenon, since the initial relaxation frequencies are greater than the measurement range of the equipment used (1 MHz). Therefore, this technique requires a measurement equipment capable of analyzing freezing at frequencies close to the microwave spectrum. Furthermore, the representation of the maximum reactance values and their respective frequencies do not allow to determine any change in the physical properties of the meat during the freezing process. For this reason, this technique is not useful to determine quality properties during the meat freezing process, in which the properties of the tissue are as important at the beginning of freezing as at any other key point of freezing process, such as point of maximum cryoconcentrated liquid phase or the glass transition.

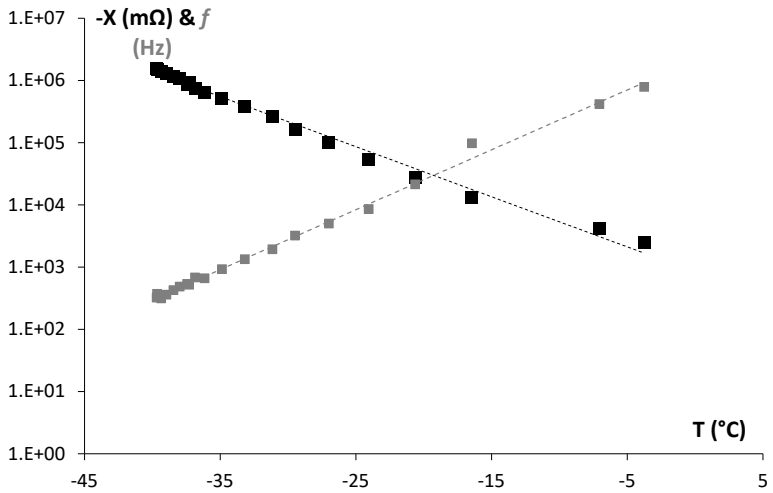

Figure 4.2.5. Relaxation reactance (■) and frequency (■) versus temperature in one sample freezing process.

As the emitter and the receiver are arranged in parallel, the impedance measurements have been transformed into dielectric properties according to the equations 1, 2 and 3 in Figure 4.2.6. Considering that its capacitance in vacuum is a function of the geometry of the sensor and its value is equal to 0.175 pF (Equation 1 in Figure 6).

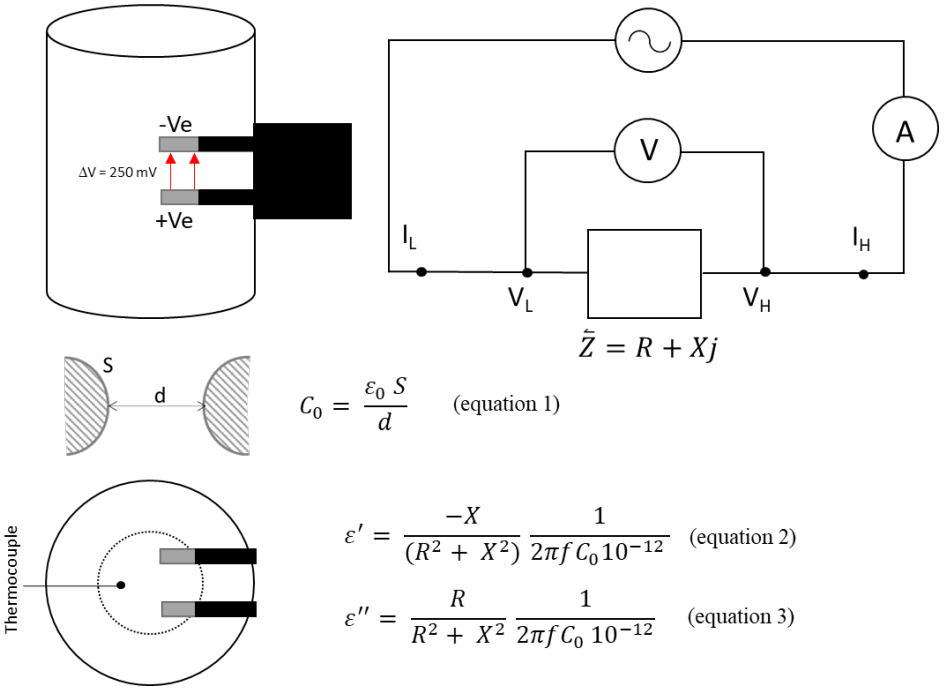

Figure 4.2.6. Diagram of sensor based on impedance measurements, the electric circuit, the detail of capacitance in vacuum determination and the equations used to determine the complex permittivity.

Figure 4.2.7 shows an example of the evolution of the spectra of complex permittivity, dielectric constant (ε') and loss factor (ε") at different freezing times, where it is possible to observe how the spectra decrease in value as the freezing process progresses.

In order to describe the effect of tissue on photons, it is necessary to obtain the alpha and beta relaxations properties in the radiofrequency range. For this purpose, the Traffano-Schiffo model (Equation 4) was applied:

$$log\varepsilon'(\omega) = log\varepsilon'_{\infty} + \sum_{n=1}^{3} \frac{\Delta log\varepsilon'_n}{1 + e^{(log\omega^2 - log\tau_n^2)\cdot\alpha_n}} \quad (4)$$

Where, logε' represents the decimal logarithm of the dielectric constant, logε'$_\infty$ the logarithm of the dielectric constant at high frequencies, logω represents the decimal logarithm of the angular frequency, Δlogε'$_n$ (Δlε'$_n$ = logε'$_n$ - logε'$_{n-1}$) the amplitude of the dispersion, logτ$_n$ the logarithm of the angular frequency at relaxation time for each dispersion n, and α$_n$ are the dispersion slopes. Following Traffano-Schiffo et al., (2017), it is possible to estimate the dielectric constant at relaxation frequencies, (ε'$_\alpha$ and ε'$_\beta$) and the relaxation frequencies (f_α and f_β).

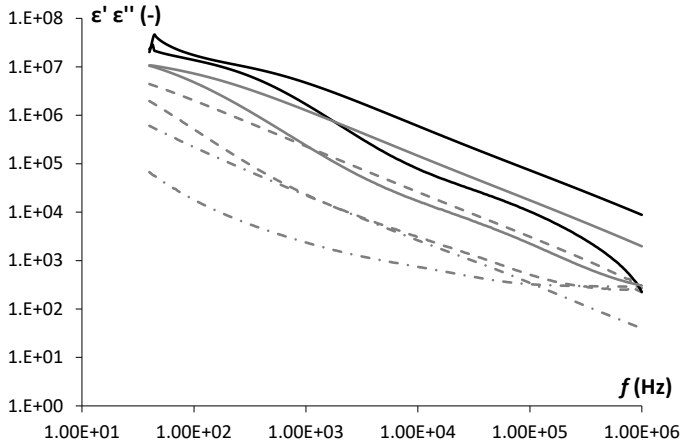

Figure 4.2.7. Permittivity spectra of one freezing process sample, were **—** is 0s; — is 370 s; – – is 660 s; – · – is 840 s; and ···· is 1410 s.

Some authors describe the possibility of determining first or second order transitions in protein structures from the permittivity in the radiofrequency spectrum. In this sense, Roos (2010) explains that it is possible to determine the glass transition of proteins or even freezing processes in the variation of the loss factor in the beta relaxation. In this sense, the beta dispersion represents the orientation and induction of the fixed charges of the macromolecules, or the surface charges associated with surface tension phenomena, also called the Maxwell-Wagner phenomenon. For this reason, the appearance of ice Ih, with a hexagonal crystal conformation, with a high surface tension, which allows it to quickly attract the closest molecules of liquid water, can generate an interaction in the beta dispersion, which should change according to the variation of surface tension throughout the freezing process.

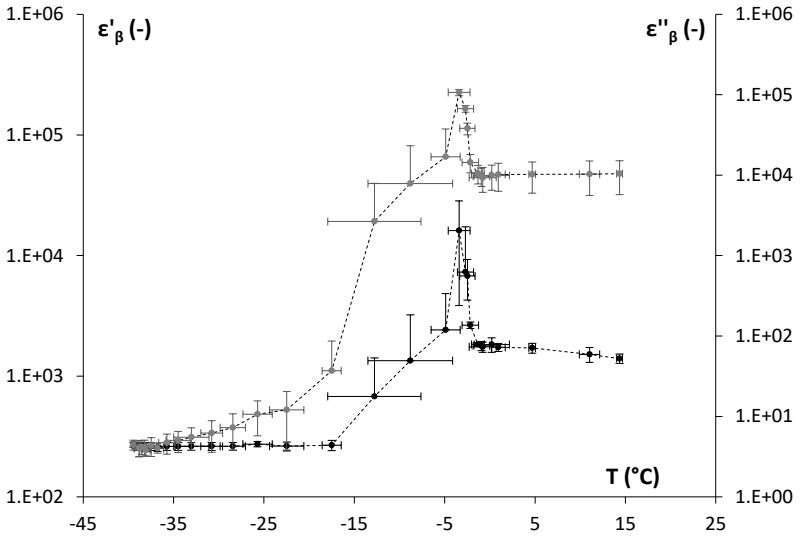

Figure 4.2.8. On the left dielectric constant (●) and on the right loss factor (●) in beta relaxation versus temperature.

Figure 4.2.8 shows, in black, the evolution of the dielectric constant and, in gray, the evolution of the loss factor, in the beta dispersion during the freezing process. In both, a minimal change is observed until the beginning of freezing is reached, at -1.32 °C ± 0.7 °C, which can be considered as the ice nucleation. This agrees with the measurements observed in the freezing curve (Figure 2), around -1.6 °C. Both curves reach a maximum value at a temperature of -3.4 °C ± 1.2 °C, which could represent the end point of freezing, which in the case of the freezing curve was estimated to be around -4 °C.

According to Roos (2010), the glass transition can be determined in the decrease of the loss factor, at the point of the change of slope. In figure 4.2.8 it is possible to determine this point at -17.50 ± 1.05 °C. However, it is difficult to correctly determine this point because in beta dispersion, the loss factor is influenced by the Maxwell-Wagner phenomenon and by ionic conductivity, being the meat a strongly ionic system. An alternative is the use of the dielectric constant, which is only influenced by the Maxwell-Wagner phenomenon. In figure 4.2.8 it is possible to see how the dielectric constant becomes constant with respect to the temperature upon reaching the glass transition. Therefore, the dielectric constant in the beta dispersion is more reliable for the determination of the glass transition than the loss factor.

The alpha dispersion represents the interactions of low weight ionic molecules, such as electrolytes, with a flux of photons in the radio frequency spectrum. The electrolytes in the meat liquid phase will have interactions with the ice, so it is possible to think that the value of the permittivity in this dispersion will change as ice is formed.

Figure 4.2.9 shows the variation of the dielectric constant in the alpha dispersion throughout freezing. It is possible to observe, as the beta dispersion analysis showed, that the value of the dielectric constant remains almost constant until reaching a value, which, in this case, corresponds to a temperature of -2.17 ± 0.91 °C and rises to a maximum which corresponds to a temperature of -4.9 ± 1.6 °C. The critical temperatures observed in the alpha dispersion are lower than in the beta dispersion, this difference may be due to the fact that the beta dispersion is a direct measure of the interaction of ice with the photons field, while the alpha measure is an indirect measure of the state of the ice, since it analyzes the state of the electrolytes. It means, that the spin orientation of electrolytes is changing with the variation of ice surface tension. Alpha dispersion detects this electrolytic phenomenon and, indirectly, the ice surface variation with delay. For this reason, the measurements in alpha dispersion suffer a delay of the phenomenon, in terms of freezing temperature.

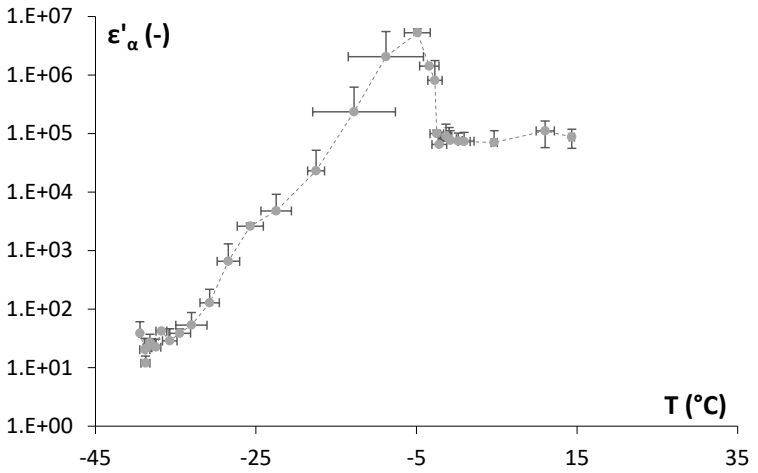

Figure 4.2.9. Dielectric constant in alpha relaxation versus temperature.

Then, it is possible to conclude that the measurement of the dielectric constant in the beta dispersion makes it possible to determine the critical temperatures of the food freezing process, initial freezing temperature (T_{m0}), the freezing temperature of sample with the maximally freeze-concentrated solute matrix (T_m') or the glass transition temperature of the maximally freeze-concentrated solute matrix (T_g').

4. Conclusions

The critical temperatures of the food freezing process, initial freezing temperature, the freezing temperature of sample with the maximally freeze-concentrated solute matrix or the glass transition temperature of the maximally freeze-concentrated solute matrix of chicken breast have been determined by means of calorimetry techniques, being similar than those of other authors. Moreover, these temperatures were determined using photospectrometry in radiofrequency range, showing that this technique is fast, reliable, and easy to implement in a dynamic freezing system.

5. Acknowledgments

This paper is part of the I+D+i PID2020-116816RB-I00 project, funded by MCIN/ AEI/10.13039/501100011033.

6. References

Ahmed, J., Rahman, M.S. and Roos, Y.H. (2017) *Glass Transition and Phase Transitions in Food and Biological Materials*. John Wiley & Sons.

Akköse, A. (2018) 'Effect of Various Biopolymers on Glass Transition Temperature of Chicken Breast Meat', *Akademik Gıda*, 16(2), pp. 120–126. doi:10.24323/akademik-gida.449572.

Baker-Jarvis, J. and Kim, S. (2012) 'The Interaction of Radio-Frequency Fields with Dielectric Materials at Macroscopic to Mesoscopic Scales', *Journal of Research of the National Institute of Standards and Technology*, 117, p. 1. doi:10.6028/jres.117.001.

Brake, N.C. and Fennema, O.R. (1999) 'Glass Transition Values of Muscle Tissue', *Journal of Food Science*, 64(1), pp. 10–15. doi:10.1111/j.1365-2621.1999.tb09851.x.

Carrington, A.K. *et al.* (1994) 'Ice crystallization temperatures of sugar/polysaccharide solutions and their relationship to thermal events during warming', *Cryo-letters* [Preprint].

Castro-Giráldez, M. *et al.* (2014) 'Thermodynamic approach of meat freezing process', *Innovative Food Science & Emerging Technologies*, 23, pp. 138–145. doi:10.1016/j.ifset.2014.03.007.

Chen, C.S. (1986) 'Effective molecular weight of aqueous solutions and liquid foods calculated from the freezing point depression', *Journal of food science*, 51(6), pp. 1537–1539.

Chin, K.B. *et al.* (2007) 'Investigation of water and ice by ac impedance using electrochemical properties cup', *Review of Scientific Instruments*, 78(1), p. 016104. doi:10.1063/1.2424443.

Chirife, J. and Fontan, C.F. (1980) 'Prediction of water activity of aqueous solutions in connection with intermediate moisture foods: experimental investigation of the aw lowering behavior of sodium lactate and some related compounds', *Journal of Food Science*, 45(4), pp. 802–804. doi:10.1111/j.1365-2621.1980.tb07453.x.

Delgado, A.E. and Sun, D.-W. (2002) 'Desorption isotherms and glass transition temperature for chicken meat', *Journal of food engineering*, 55(1), pp. 1–8.

Elliott, G.D., Wang, S. and Fuller, B.J. (2017) 'Cryoprotectants: A review of the actions and applications of cryoprotective solutes that modulate cell recovery from ultra-low temperatures', *Cryobiology*, 76, pp. 74–91.

Gordon, M. and Taylor, J.S. (1952) 'Ideal copolymers and the second-order transitions of synthetic rubbers. i. non-crystalline copolymers', *Journal of Applied Chemistry*, 2(9), pp. 493–500. doi:10.1002/jctb.5010020901.

Hellmuth, O., Schmelzer, J.W.P. and Feistel, R. (2020) 'Ice-Crystal Nucleation in Water: Thermodynamic Driving Force and Surface Tension. Part I: Theoretical Foundation', *Entropy*, 22(1), p. 50. doi:10.3390/e22010050.

Horie, K., Ushiki, H. and Winnik, F.M. (2008) *Molecular photonics: fundamentals and practical aspects*. John Wiley & Sons.

Kumar, P.K. *et al.* (2020) 'State/Phase Transitions, Ice Recrystallization, and Quality Changes in Frozen Foods Subjected to Temperature Fluctuations', *Food Engineering Reviews*, 12(4), pp. 421–451. doi:10.1007/s12393-020-09255-8.

Robinson, R.A. and Stokes, R.H. (2002) *Electrolyte solutions*. Courier Corporation.

Roos, Y.H. (2010) 'Glass transition temperature and its relevance in food processing', *Annual review of food science and technology*, 1, pp. 469–496. doi:https://doi.org/10.1146/annurev.food.102308.124139.

Roos, Y.H. (2021) 'Glass Transition and Re-Crystallization Phenomena of Frozen Materials and Their Effect on Frozen Food Quality', *Foods*, 10(2), p. 447. doi:10.3390/foods10020447.

Ross, K.D. (1978) 'Differential scanning calorimetry of nonfreezable water in solute—macromolecule—water systems', *Journal of Food Science*, 43(6), pp. 1812–1815.

Roudaut, G. *et al.* (2004) 'Molecular mobility around the glass transition temperature: a mini review', *Innovative Food Science & Emerging Technologies*, 5(2), pp. 127–134. doi:10.1016/j.ifset.2003.12.003.

Roychoudhuri, C., Kracklauer, A.F. and Creath, K. (2008) *The Nature of Light*. 1st edition. Boca Ratón, USA: CRC Press. Available at: https://doi.org/10.1201/9781420044256 (Accessed: 27 April 2021).

van der Sman, R.G.M. (2020) 'Impact of Processing Factors on Quality of Frozen Vegetables and Fruits', *Food Engineering Reviews*, 12(4), pp. 399–420. doi:10.1007/s12393-020-09216-1.

van der Sman, R.G.M. and Boer, E. (2005) 'Predicting the initial freezing point and water activity of meat products from composition data', *Journal of Food Engineering*, 66(4), pp. 469–475. doi:10.1016/j.jfoodeng.2004.04.018.

Smith, G. and Polygalov, E. (2019) 'Through Vial Impedance Spectroscopy (TVIS): A Novel Approach to Process Understanding for Freeze-Drying Cycle

Development', in Ward, K.R. and Matejtschuk, P. (eds) *Lyophilization of Pharmaceuticals and Biologicals: New Technologies and Approaches*. New York, NY: Springer (Methods in Pharmacology and Toxicology), pp. 241–290. doi:10.1007/978-1-4939-8928-7_11.

Sunooj, K.V. *et al.* (2009) 'Factors influencing the calorimetric determination of glass transition temperature in foods: A case study using chicken and mutton', *Journal of Food Engineering*, 91(2), pp. 347–352. doi:10.1016/j.jfoodeng.2008.09.014.

Traffano-Schiffo, M.V. *et al.* (2017) 'Development of a Spectrophotometric System to Detect White Striping Physiopathy in Whole Chicken Carcasses', *Sensors*, 17(5), p. 1024. doi:10.3390/s17051024.

Traffano-Schiffo, M.V. *et al.* (2018) 'Development of a non-destructive detection system of Deep Pectoral Myopathy in poultry by dielectric spectroscopy', *Journal of Food Engineering*, 237, pp. 137–145. doi:10.1016/j.jfoodeng.2018.05.023.

Traffano-Schiffo, M.V. *et al.* (2021) 'New methodology to analyze the dielectric properties in radiofrequency and microwave ranges in chicken meat during postmortem time', *Journal of Food Engineering*, 292, p. 110350. doi:10.1016/j.jfoodeng.2020.110350.

You, Y., Kang, T. and Jun, S. (2021) 'Control of Ice Nucleation for Subzero Food Preservation', *Food Engineering Reviews*, 13(1), pp. 15–35. doi:10.1007/s12393-020-09211-6.

foods

MDPI

Analysis of apple candying by microwave spectroscopy

J.A. Tomas-Egea [1], P.J. Fito [1] and M. Castro-Giraldez [1]

[1] Instituto Universitario de Ingeniería de Alimentos para el Desarrollo, Universitat Politècnica de València, Camino de Vera s/n, 46022 Valencia, Spain

Foods

https://doi.org/10.3390/foods8080316

Published: August 04, 2019

Process control in the industry requires fast, safe and easily applicable methods. In this sense, the use of dielectric spectroscopy in the microwave range can be a great opportunity to monitor processes in which the mobility and quantity of water is the main property to produce a quality and safety product. The candying of fruits is an operation in which the samples are first osmotically dehydrated and then exposed to a hot air-drying operation. This process produces changes in both the structure of the tissue and the relationships between water, the solid matrix and the added soluble solids. The aim of this paper is to develop a dielectric tool to predict the water/sucrose states throughout the candying of apple, by considering the complexity of the tissue and describing the different transport phenomena and the different transition processes of the sucrose inside the sample.

Keywords: dielectric spectroscopy; permittivity; dehydration; candying; hot air drying; isotherms; sucrose.

Analysis of apple candying by microwave spectroscopy

J.A. Tomas-Egea [1], P.J. Fito [1] and M. Castro-Giraldez [1]

[1] Instituto Universitario de Ingeniería de Alimentos para el Desarrollo, Universitat Politècnica de València, Camino de Vera s/n, 46022 Valencia, Spain

Abstract: Process control in the industry requires fast, safe and easily applicable methods. In this sense, the use of dielectric spectroscopy in the microwave range can be a great opportunity to monitor processes in which the mobility and quantity of water is the main property to produce a quality and safety product. The candying of fruits is an operation in which the samples are first osmotically dehydrated and then exposed to a hot air-drying operation. This process produces changes in both the structure of the tissue and the relationships between water, the solid matrix and the added soluble solids. The aim of this paper is to develop a dielectric tool to predict the water/sucrose states throughout the candying of apple, by considering the complexity of the tissue and describing the different transport phenomena and the different transition processes of the sucrose inside the sample.

Keywords: dielectric spectroscopy; permittivity; dehydration; candying; hot air drying; isotherms; sucrose.

1. Introduction

Dehydration is probably one of the most important methods of foods preservation. The main objective in dehydrating agricultural products is the removal of water in the foods up to a certain level of water activity, at which microbial spoilage and deterioration chemical reactions are minimized (Krokida and Marinos-Kouris, 2003). Apples are consumed either fresh or in the form of various processed products such as juice, jam, marmalade, and dried products (Sacilik and Elicin, 2006), being the dried apples in extensive demand. Candying is an industrial operation, which consists on osmotic dehydration (OD) followed by a hot-air drying (HAD) treatment. OD consists of the immersion of foods in hypertonic solutions with the objective of producing a water flow out of the food and a simultaneous flow of solutes inside the tissue. In fruits, these mass transfer phenomena affect to apple structure. Fruits are formed by vegetal cells, conforming the parenchyma tissue, which is a complex structure with intercell connections (plasmodesmata), intracellular and extracellular spaces (Fito et al., 2007; Castro-Giraldez, Tylewicz, et al., 2011; Ahmed, Qazi and Jamal, 2016). Intracellular volume is mainly occupied by vacuoles, which are fundamentally a water solution with multiple solutes. The membrane of the cell is named protoplast, it is selectively permeable (active and passive protein channels) and controls turgor and the cell growth (Salisbury and Ross, 1992). The cell membrane has protein channels named aquaporin and calcium protein channel that are responsible of the water transport and the cell homeostasis (Agre, Bonhivers and Borgnia, 1998). The cell wall provides mechanical resistance to the cell. In the union between cell walls and protoplast are bonds of Na^+, protein microtubules and conduits named plasmodesmata that allow

the transport between the adjacent cells (symplastic pathways). Extracellular volume comprehends the cell wall and the spaces between cells (Ahmed, Qazi and Jamal, 2016). OD produces different phenomena in the cellular tissue, first a dehydration with shrinkage and solute intake in extracellular space. Continuous shrinkage produces a breakdown between wall and protoplast called plasmolysis causing mechanical driving forces (swelling/shrinkage) (Alzamora et al., 2000; Mavroudis, Dejmek and Sjöholm, 2004; Vicente et al., 2012; Nieto et al., 2013). The changes in cellular tissue affect the water mobility and its distribution (Mauro et al., 2016).

HAD influences on fruit quality because it produces chemical, physical and biological changes in food (Lewicki, 2006). Moreover, the internal structure undergoes deformation and could be locally damaged. Removal of water adds rigidity to the external layers and simultaneously builds up moisture gradients, which create shrinkage stresses (Lewicki and Jakubczyk, 2004). The understanding of these effects is still limited, and more studies are necessary in this field in order to improve food quality and nutritional characteristics of dehydrated foods.

During the candying process, crystallization of sucrose occurs. Sucrose crystallizes in supersaturated aqueous solutions. The sucrose molecule has eight hydroxyl groups, which can be involved in hydrogen bond formation. In sufficiently diluted aqueous solutions, all the hydroxyl groups form hydrogen bonds with water molecules. If the concentration increases, the molecules start to interact forming an intramolecular bond and then two intermolecular bonds (Mathlouthi, 1981). If sucrose concentration in the solution increases, aggregation phenomena occur between sucrose molecules, leading to stable three-dimensional nucleus (Mathlouthi and Genotelle,

1998). After nucleus formation, the crystal growth consists in the incorporation of sucrose molecules to the crystal lattice, which requires the migration of hydration water from the crystal surface to the solution (Mathlouthi, 1995).

The analysis of the electromagnetic field (EMF) properties in range of microwaves could be a good tool to monitor and improve apple candying. The development of sensors to determine the dielectric properties of biological tissues, in range of radiofrequency and microwaves, has been demonstrated to be a useful tool for monitoring the quality of many products: poultry (Samuel et al., 2012; Trabelsi, Roelvink and Russell, 2014; Traffano-Schiffo et al., 2017; Traffano-Schiffo, Castro-Giraldez, Colom, et al., 2018a; Traffano-Schiffo, Castro-Giraldez, Herrero, et al., 2018), pork (Kent et al., 2002; Castro-Giraldez, Aristoy, et al., 2010; Castro-Giraldez, Botella, et al., 2010; Castro-Giraldez, Dols, et al., 2011; Castro-Giraldez, Toldrá and Fito, 2011), beef (Brunton et al., 2006), goat (Mohiri, Burhanudin and Ismail, 2011), meat products (Lyng, Zhang and Brunton, 2005), cheese (Everard et al., 2006), mandarin (Traffano-Schiffo, Castro-Giraldez, Colom, et al., 2018b), potato (Cuibus et al., 2014), wheat (Nelson and Trabelsi, 2006), agricultural products (Venkatesh and Raghavan, 2004; Nelson, 2005, 2008), pomegranate (Castro-Giraldez et al., 2013) and apple (Castro-Giraldez, Fito, et al., 2010b, 2010a; Shang, Guo and Nelson, 2015), and for monitoring processes of pork meat HAD (Traffano-Schiffo et al., 2015) and salting (Castro-Giraldez, Fito and Fito, 2010), orange peel drying (Talens, Castro-Giraldez and Fito, 2016), cheese salting (Velázquez-Varela et al., 2018), brewing (Velázquez-Varela, Castro-Giraldez and Fito, 2013), puffing of

amaranth seeds (Castro-Giraldez et al., 2012), OD of kiwi (Castro-Giraldez, Fito, et al., 2011) and apple (Castro-Giraldez, Fito and Fito, 2011a).

The EMF is a flux of photons (Baker-Jarvis and Kim, 2012) and the interaction with matter can be modelled by Schrodinger's equation (Roychoudhuri, Kracklauer and Creath, 2008) attending to the quantum theory. However, at macroscopic level, it is possible to apply the Maxwell's equations (Horie, Ushiki and Winnik, 2008), where the physical property that describes the electric effect is the complex permittivity and for the magnetic effect is the complex permeability (Baker-Jarvis and Kim, 2012). In microwave range ($1.24 \cdot 10^{-6}$ to $1.24 \cdot 10^{-3}$ eV or 300 MHz to 300 GHz), these interactions are described by γ-dispersion and ionic conductivity. γ-dispersion is caused by the induction and orientation of dipolar molecules, being water the most important in biological systems (Crane, Pantoya and Weeks, 2013). These phenomena generate electric energy accumulation caused mainly by water spin reorientation and it is represented by the real part of the permittivity (ε'). On the other hand, a part of the electrical energy of photons is transformed in other energies (mechanical or calorific) due to the collisions or frictions associated to the increase of molecular mobility; this part of the electric energy is called loss factor (ε"). In microwave range, the vibration of chemical species with very high ionic strength causes a part of the losses of electrical energy; this is called ionic conductivity (σ) (Castro-Giraldez, Fito and Fito, 2011b).

The aim of this paper is to develop a dielectric tool to predict the water/sucrose states throughout the candying of apple, by considering the complexity of the tissue and describing the different transport phenomena and the different transition processes of the sucrose inside the sample.

2. Materials and methods

Apples (var. Granny Smith) were bought from a local supermarket and kept refrigerated until use. The apples were cut with a calliper and a cork borer in cylinders (1 cm thickness, 2 cm diameter) from the parenchymatic tissue. There were prepared 126 samples in order to obtain 7 isotherms (Figure 4.2.1). 18 samples were used to obtain the isotherm of raw apple (I_0): 3 samples to characterize the raw material, it is without hot air dehydration, and 15 exposed to hot air dehydration. The remaining 108 samples were dehydrated osmotically to obtain 6 isotherms (I_1 to I_6); 18 samples were used for each selected time of OD: 3 samples to characterize osmotic dehydrated samples, it is without hot air dehydration, and 15 exposed to hot air dehydration. In conclusion, 7 isotherms were obtained, considering that the samples of an isotherm have the same solid matrix/sucrose weight relation.

Sucrose solution (65% w/w, 30 °C), prepared with commercial sugar and distilled water, was used as an osmotic agent. The relation between the fruit and the osmotic solution was of 1:20 (w/w) to avoid changes in the solution during the process. The system was maintained at 30 °C in a constant-temperature chamber. To prevent evaporation the vessel was covered with a sheet of plastic wrap. Preliminary kinetic studies were done at the same working conditions in order to select the OD treatment times. The OD treatment times in the preliminary studies were: 180, 360, 720, 1463, 1577, 1722, 3375, 4320, 7200, 8640, 10270, 14590 and 23230 min. Based on the results (Castro-Giraldez, Fito and Fito, 2011b), OD treatment times were selected for this research: 0, 360, 720, 1722, 3375, 4320, 10270 min. After the treatment, the samples were removed from the solution and blotted with a

paper to remove the superficial osmotic solution. Then, the samples were kept at 30 °C for 24 h, on AquaLab disposable sample containers, closed with parafilm®. The mass, volume and water activity of the 126 samples were measured after the repose. Moreover, permittivity, moisture and soluble solids content (°Brix) of three samples of each OD treatment time were measured to characterize each solid matrix/sucrose weight relation. The remaining samples in each isotherm were hot air dried (times of HAD treatment: 30, 60, 120, 955, 1368 min). Three samples were used in each HAD treatment time. The drying experiments were carried out at 40 °C drying air temperature. The convective dryer was designed and built in the Food Technology Department of Universitat Politècnica de València, has a control unit for setting the velocity and temperature of air, which is heated through electrical resistances. Air velocity was kept at a constant value of 1.5 ± 0.2 m s^{-1} in all experiments.

After the drying treatment, samples were maintained at 30 °C for 24 h, on AquaLab disposable sample containers, closed with parafilm®. After this repose time, the permittivity, mass, volume, water activity, moisture and soluble solids content were measured.

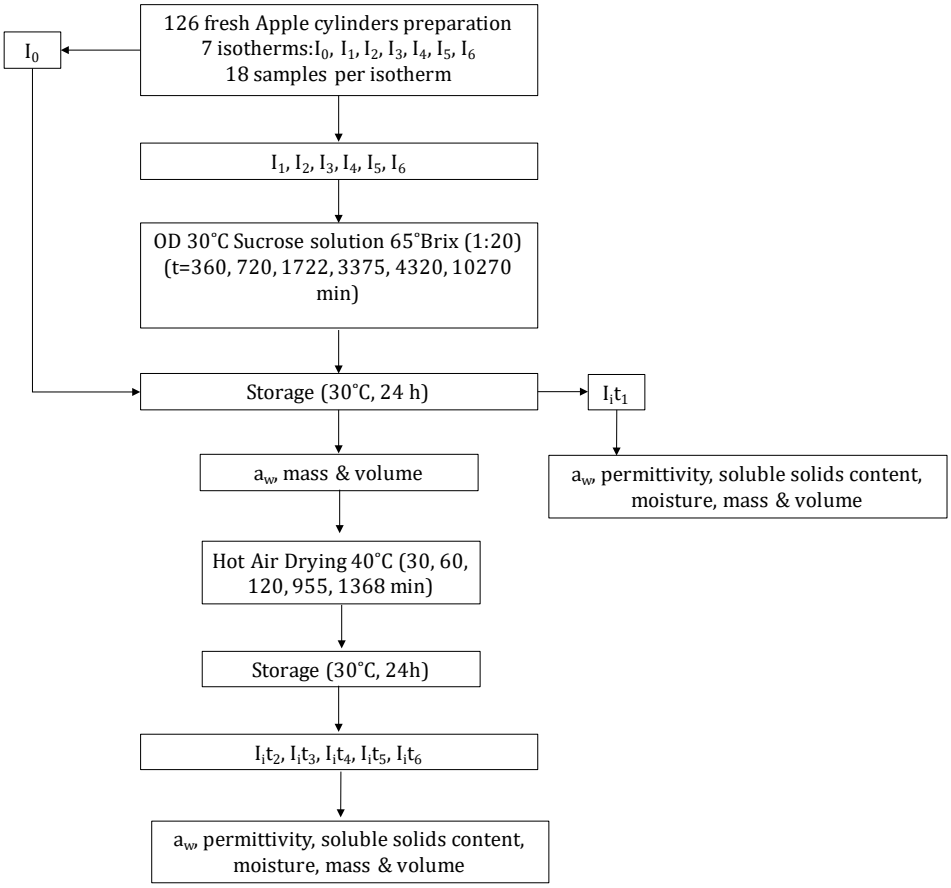

Figure 4.2.1. Flow diagram of the experimental procedure, where I represents each isotherm, subscript i from 0 to 6 of each isotherm represent a concrete sucrose/solid matrix weight relation, t_1 to t_6 represent the different times of hot-air drying (HAD).

Volume measurements were analysed by image analysis and the software Adobe Photoshop® CS5 (Adobe Systems Inc., San Jose, CA, U.S.A.) to get the diameter and the thickness of the samples. The images of the samples were obtained with a digital camera (Canon EOS 550D, with a size of 2592 x 1728 pixels and a resolution of 16 pixel/mm).

Mass was determined by using a Mettler Toledo Balance (± 0.0001 g; Mettler-Toledo, Inc., Columbus, OH, USA). Measurements were done in

structured samples (not minced), thus the obtained a_w is considered to be the surface a_w (Castro-Giraldez, Fito and Fito, 2011b).

Water activity was measured in the structured samples with a dew point hygrometer Decagon (Aqualab® series 3TE) with precision ± 0.003.

Moisture content in the apple cylinders was determined gravimetrically at 60 °C in a vacuum oven until constant weight was reached (Horowitz, 2000). Sugar content was determined in a refractometer (ABBE, ATAGO Model 3-T, Japan).

The system used to measure permittivity consists of an Agilent 85070E open-ended coaxial probe (Agilent, Santa Clara, CA, USA) connected to an Agilent E8362B Vector Network Analyzer (Agilent, Santa Clara, CA, USA). The system was calibrated using three different types of loads: open (air), short-circuit and 30 °C Milli-Q water. Once the calibration was carried out, 30 °C Milli-Q water was measured again to check calibration suitability. Permittivity was measured from 500 MHz to 20 GHz. The measurements were performed in triplicate. Dielectric constant (ε') was modelled adjusting the experimental data using Traffano-Schiffo model (Traffano-Schiffo et al., 2017) (Equation 4.2.1) in order to obtain information of γ-dispersion:

$$log\varepsilon'(\omega) = log\varepsilon'_{\infty} + \sum_{n=1}^{3} \frac{\Delta log\varepsilon'_n}{1 + e^{(log\omega^2 - log\tau_n^2)\cdot\alpha_n}} \qquad (4.2.1)$$

where n represents α, β or γ dispersion, logε' represents the decimal logarithm of the dielectric constant, logε'∞ the logarithm of the dielectric constant at high frequencies, logω represents the decimal logarithm of the angular

velocity (obtained from the frequency), $\Delta \log \varepsilon'_n$ ($\Delta \varepsilon'_n = \log \varepsilon'_n - \log \varepsilon'_{n-1}$) the amplitude of the n dispersion, $\log \tau_n$ the logarithm of the angular velocity at relaxation time for each n dispersion, and α_n are the dispersion slopes. In this work, this model has been applied for γ-dispersion only.

3. Results

In order to understand the mechanisms that govern the relationship between water and sucrose in plant tissue matrix during OD and HAD treatments, and thus develop dielectric predictive tools that not only explain the water state but also explain the state of the whole internal liquid phase of the vegetal tissue, a kinetic analysis of the variation of overall mass, water and sucrose is proposed as a first step. Overall mass, water and sucrose mass variations throughout the OD treatment are shown in Figure 4.2.2. These parameters were estimated by Equations 4.2.2 to 4.2.4, respectively.

$$\Delta M = \frac{M_t - M_0}{M_0} \tag{4.2.2}$$

$$\Delta M_w = \frac{M_t x_{wt} - M_0 x_{w0}}{M_0} \tag{4.2.3}$$

$$\Delta M_s = \frac{M_t x_{st} - M_0 x_{s0}}{M_0} \tag{4.2.4}$$

where M represents the mass (kg), x_i is the mass fraction of the compound i (kg_i/kg_T), being the different compounds represented by subscripts: w the water, and s the soluble solids; moreover, the subscripts t represents the treatment time, being 0 the initial value.

In Figure 4.2.2, it can be observed that the greatest loss of mass occurs during the first 1722 min of OD treatment. From that moment, there is no variation in the total mass of the sample nor in the mass of water. In contrast, the increase in soluble solids occurs during the first 720 min, being this content stabilized from this point.

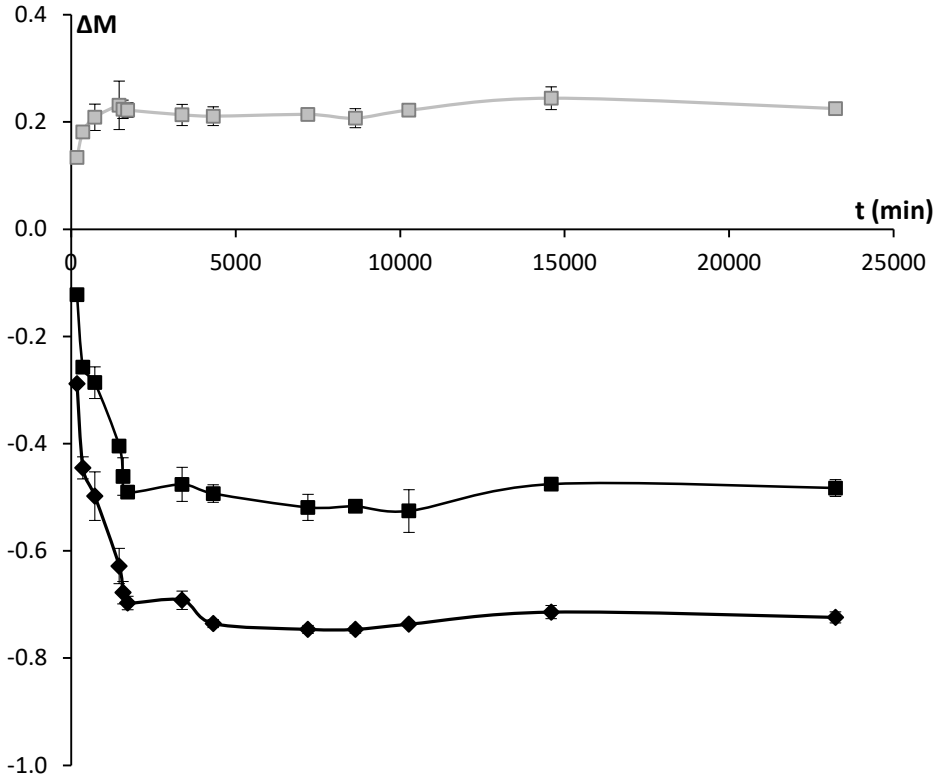

Figure 4.2.2. Evolution of overall mass (■), water mass (♦) and sucrose mass (■) through the osmotic treatment.

The mass variation evolution does not allow to observe correctly the chemical equilibrium that happens when the plasmolysis occurs (Castro-Giraldez, Fito and Fito, 2011b). The plasmolysis or breakdown the bonds between the protoplast and the wall precedes tissue shrinkage and swelling

(Tylewicz et al., 2011), and these phenomena change the amount of liquid phase but not its composition. For this reason, the relationship between the sucrose content and the solid matrix with respect to the treatment time is shown in Figure 4.2.3.

In Figure 4.2.3, it is possible to observe how the sucrose/solid matrix weight relation reaches a maximum (cellular plasmolysis) at 1722 min. Seven different osmodehydration treatment times were selected which correspond to seven different sucrose/solid matrix weight relations: 0 min of OD (1.33 $kg_{sucrose}/kg_{solid\ matrix}$), 360 min of OD (3.58 $kg_{sucrose}/kg_{solid\ matrix}$), 720 min of OD (4.27 $kg_{sucrose}/kg_{solid\ matrix}$), 1722 min of OD (7.28 $kg_{sucrose}/kg_{solid\ matrix}$), 3375 min of OD (4.31 $kg_{sucrose}/kg_{solid\ matrix}$), 4320 min of OD (3.20 $kg_{sucrose}/kg_{solid\ matrix}$), 10270 min of OD (6.82 $kg_{sucrose}/kg_{solid\ matrix}$). Two OD treatment times were selected before the plasmolysis in order to study the samples before the chemical equilibrium. After the plasmolysis, the samples suffer mechanical phenomena (swelling and shrinkage), which are responsible for the osmotic solution intake or outflow; from this time there are no longer diffusional driving forces. After 1722 min of OD, the samples suffered a shrinkage causing the outflow of liquid phase, and therefore the decrease in the sucrose content (decrease in the weight relation sucrose/solid matrix). Two OD treatment times were selected in this period (3375 and 4320 min of OD). After the shrinkage, swelling phenomenon occurs, which could be observed by the increase of sucrose/solid matrix weight relation. One OD treatment time was selected in this period: 10270 min.

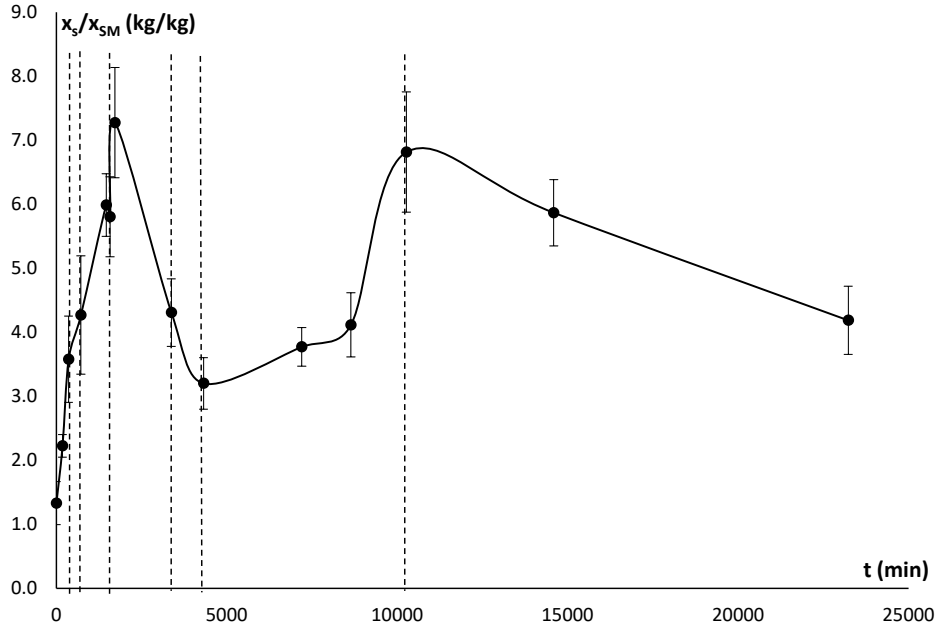

Figure 4.2.3. Sucrose/solid matrix relation with regard to osmotic dehydration (OD) time. Dotted lines represent the OD samples times chosen for the samples that will be dehydrated later by HAD.

Figure 4.2.4 shows the relationship between the water activity of samples in equilibrium (24 h after HAD treatment) and moisture in dry matter ($x_w/1-x_w$), or isotherm at 30 °C. Moreover, Figure 4.2.4 shows the isotherm of pure water/sucrose solution at 30 °C from (Starzak and Mathlouthi, 2006), where it is possible to observe that the apple isotherm data are around the isotherm of pure solution. The range of water activity measured covers some state transitions associated with water and sucrose. Thus, it is necessary to analyse the possible transitions that occur during the HAD treatment.

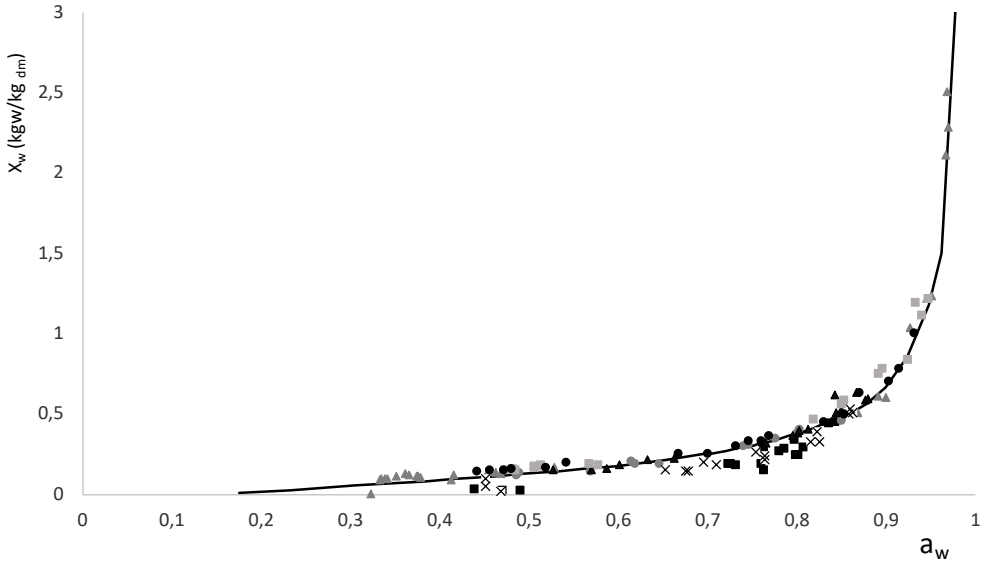

Figure 4.2.4. Moisture (kg water/kg dry matter) with regard to the water activity, where: (—) represents a water-sucrose solution (Starzak and Mathlouthi, 2006), (▲) 1.33 $kg_{sucrose}/kg_{solid\ matrix}$, (■) 3.58 $kg_{sucrose}/kg_{solid\ matrix}$, (●) 4.27 $kg_{sucrose}/kg_{solid\ matrix}$, (▲) 7.28 $kg_{sucrose}/kg_{solid\ matrix}$, (x) 4.31 $kg_{sucrose}/kg_{solid\ matrix}$, (●) 3.20 $kg_{sucrose}/kg_{solid\ matrix}$ and (■) 6.82 $kg_{sucrose}/kg_{solid\ matrix}$.

Figure 4.2.5 shows the diagram state of the sucrose-water solution represented as water activity versus temperature. In this figure, it is possible to observe how at 30 °C the samples cross the saturation and supersaturation curve as the viscosity of the liquid phase increases. This represents that the liquid phase analysed could be in the stable, metastable or supersaturated region. Therefore, when developing a predictive tool for water state during an OD or HAD treatment, is important to predict, not only the composition but also to predict the water mobility or the state of the liquid phase of the tissue being treated.

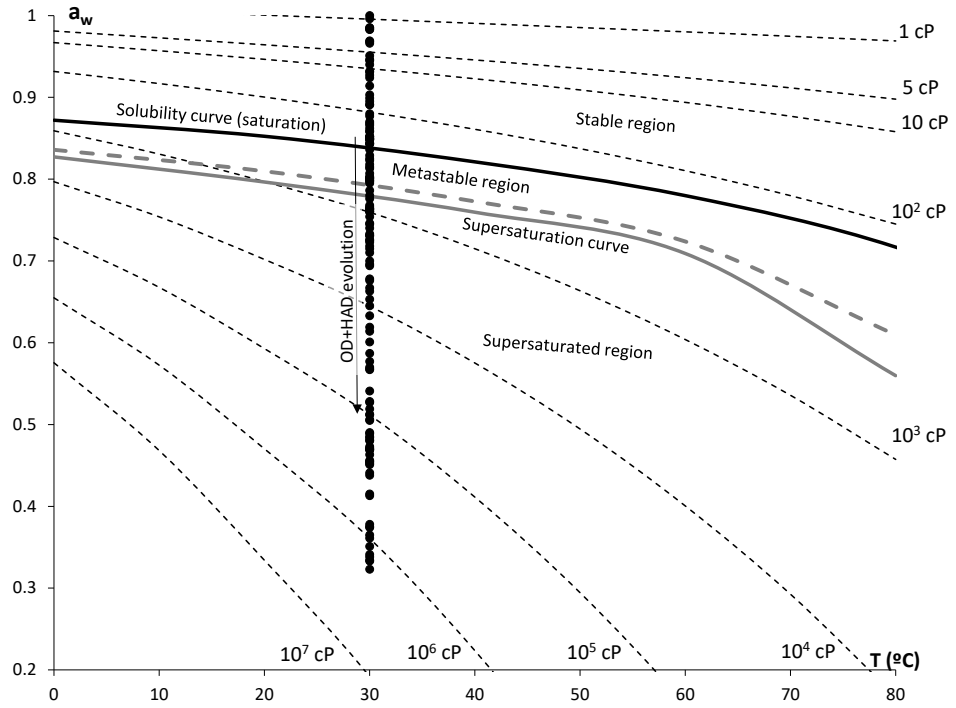

Figure 4.2.5. Diagram state of sucrose solution represented as water activity vs. temperature, where (▬) and (▬) lines represent the saturation and supersaturation curves obtained from (Mathlouthi and Genotelle, 1998), (**---**) lines represent different values of viscosity obtained from Lewis (1990) (Jackson, 1990), and (●) represent the different experimental values of samples with OD and HAD treatments.

In order to develop a tool to predict the state of the liquid phase throughout the treatment of OD or HAD, the dielectric properties have been analysed in the range of microwaves, where the γ (dipolar effect) affects mainly the water molecules, generating an orientation and induction effect that is greater when the mobility of the molecules is greater.

Figure 4.2.6 shows the dielectric constant and loss factor spectra of samples treated 360 min with OD and different HAD treated times, as an example of spectra variation throughout the HAD treatment. The dielectric phenomena by orientation and induction occur in the range of

radiofrequency and microwaves. The phenomena are three, α, β and γ and occur in a large frequency range. It is considered that each phenomenon has a maximum effect when the losses are maximum and the frequency at which the maximum effect occurs are called relaxation frequency. In order to understand the relationship of each phenomenon with the molecules affected, it is necessary to adjust the spectrum to a model that obtains the relaxation values of each phenomenon. The Traffano-Schiffo model (Traffano-Schiffo et al., 2017) has been applied to obtain the relaxation values in the γ-dispersion. In Figure 4.2.6, it is possible to observe some relaxation frequencies decreasing with the HAD treatment time.

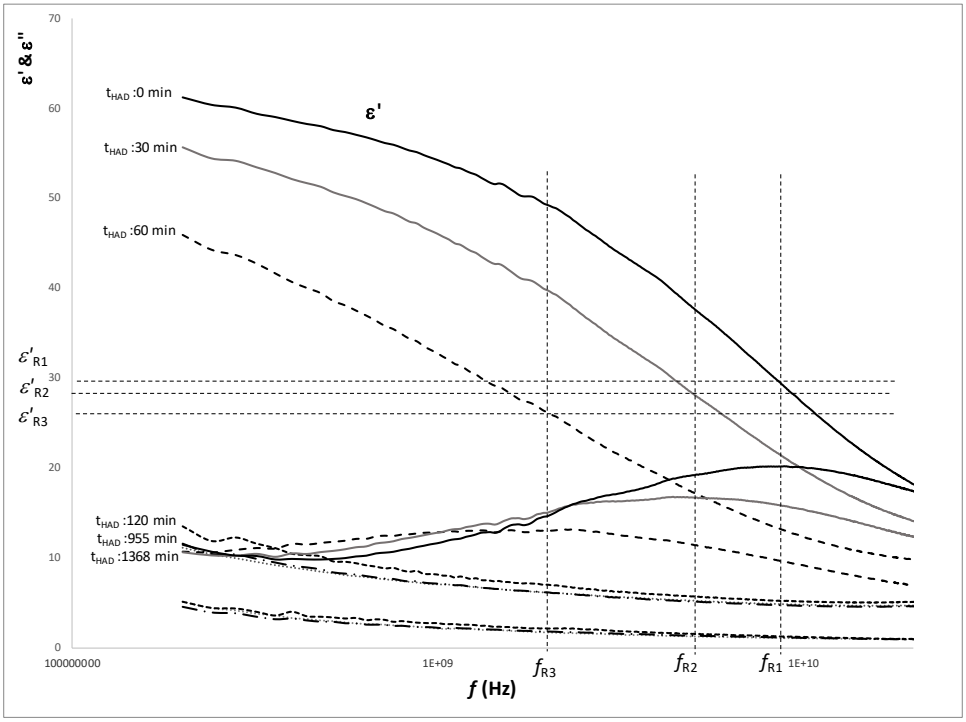

Figure 4.2.6. Dielectric constant and loss factor spectra of samples treated 360 min with OD and different HAD treatment times (t_{HAD}), where: f_R is the relaxation frequency, and sub-indexes R1, R2 and R3 refer to the relaxation of γ-dispersion of samples dehydrated 0, 30 and 60 min, respectively.

The dielectric constant is the part of the permittivity that describes the orientation (electrical storage) of the water molecule. Dielectric constant is higher when the movement capacity of the water molecules is greater, as well as higher is the number of water molecules is.

Figure 4.2.7 shows the relation between the dielectric constant at relaxation frequency and the water activity, where it is possible to observe a linear relation between the dielectric constant at relaxation frequency and the water activity, regardless of the sucrose/solid matrix weight relation, the structure changes or the rheologic transitions. Therefore, only the water mobility affects to the water orientation, and thus, dielectric constant in relaxation frequency represents an excellent tool to predict the water activity but not the transitions of water/sucrose.

The linear regression obtained was ($R^2 = 0.944$):

$$a_w = 0.0346 \cdot \varepsilon'_{relaxation} + 0.2363 \quad (4.2.5)$$

The constant of the equation (0.2363), which represents the activity of water for a null dielectric constant or null water capacity for orientation, coincides with the water activity at which sucrose crystallize (0.23) (Roos and Karel, 1991).

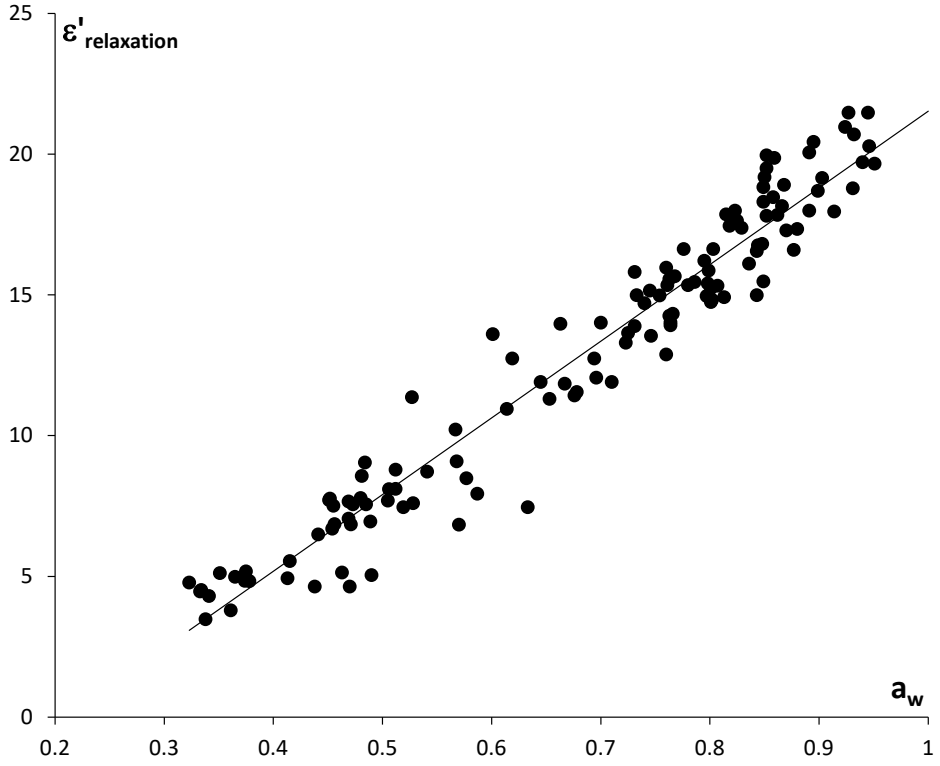

Figure 4.2.7. Relation between the dielectric constant at relaxation frequency and the water activity.

Figure 4.2.8 shows the relationship between the moisture in dry basis and the relaxation frequency in the different regions described in Figure 4.2.5. As it is possible to observe in this figure, only the samples that are in the stable region showed a linear relation, in this region, the liquid phase has great mobility, and the viscosity was low. Samples located in a metastable or supersaturated region move away from linearity. This means that it is possible to discriminate the regions of the state diagram of sucrose/water by analysing the frequency of relaxation.

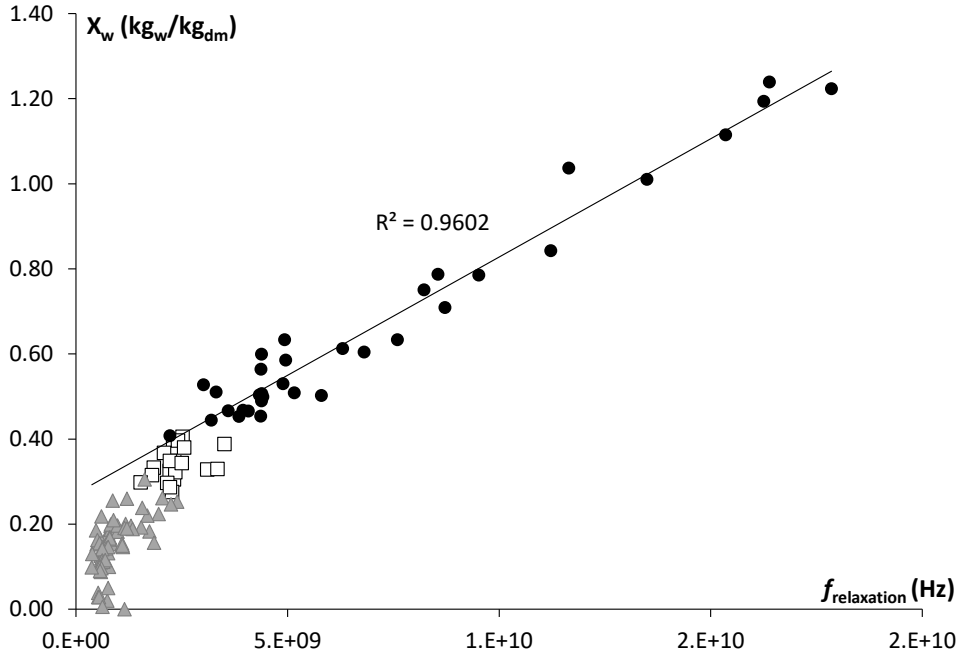

Figure 4.2.8. Relation between the moisture in dry basis ($kg_{water}/kg_{dry\ matter}$) with the relaxation frequency, where (●) represents the samples in stable region, (□) represents the samples in metastable region and (▲) the samples in the supersaturated region.

With the purpose of being able to use dielectric measurements in the microwave range to predict the sorption isotherm of apples in the process of OD and HAD, besides being able to correctly describe the water/sucrose state, the frequency of relaxation was compared with the loss factor.

Figure 4.2.9 shows the semilogarithmic relationship of the relaxation frequency and the loss factor at relaxation frequency, segregated according to the stability region. As it is possible to observe the relation between both was linear in all the regions and did not allow the separation. Nevertheless, at very low mobility zone in the supersaturated region, new behaviour appears because the relaxation frequency remains constant while the loss factor is reduced, this might be due to the vitrification process (glass transition).

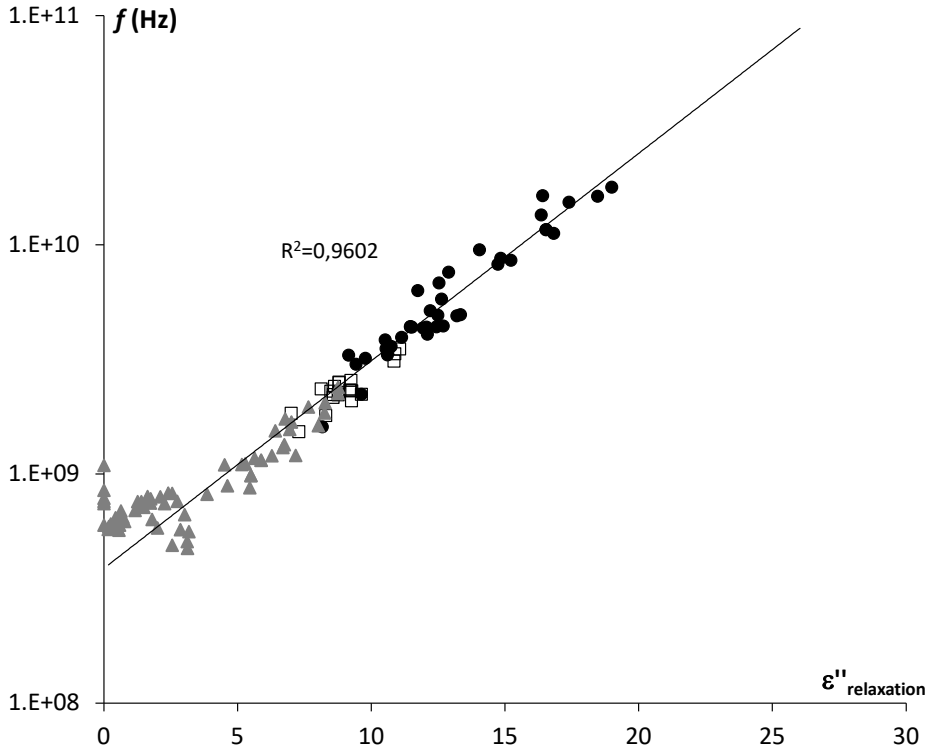

Figure 4.2.9. Semi-logarithmic relation between the relaxation frequency and the loss factor at relaxation frequency, where (●) represents the samples in stable region, (□) represents the samples in metastable region, (▲) the samples in the supersaturated region and (—) represents the linear regression of all data together.

4. Discussion

The treatment of OD produces compositional and structural transformations within the tissue and the HAD treatments produce water losses, structural transformations and transitions in the liquid phase. In order to analyse the two treatments, it is necessary to include several critical points of both processes such as plasmolysis, compression/relaxation phenomena or saturation and supersaturation of the liquid phase. In Figure 4.2.3, it is

possible to observe how the sucrose/solid matrix weight relation reaches a maximum (plasmolysis) at 1722 min.

Samples treated with OD and HAD, plasmolyzed or not, cross the saturation and supersaturation curve as the viscosity of the liquid phase increases. This represents that the liquid phase of samples analysed could be in the stable, metastable or supersaturated region. Therefore, when developing a predictive tool for describing the water state during an OD or HAD treatment, is important to predict, not only the composition but also to predict the water mobility or the state of the liquid phase of the tissue being treated.

The Traffano-Schiffo model allows obtaining the relaxation values in the microwave range, it allows us to represent the dielectric constant at relaxation frequency versus the water activity, where it is possible to observe a linear relation between both variables. Therefore, only the water mobility affects to the water orientation, and thus, dielectric constant in relaxation frequency represents an excellent tool to predict the water activity but not the transitions of water/sucrose. Moreover, the good fit of the data is shown in the good values of the correlation coefficient and also in the coincidence between the constant of the equation and the water activity at which sucrose crystallizes (0.23).

The relationship between the moisture in dry basis and the relaxation frequency in the different regions described shows that only the samples that are in the stable region have a linear relation. In this region, the liquid phase has great mobility and the viscosity is low. Samples located in a metastable or supersaturated region move away from linearity. This means that it is possible

to discriminate the regions of the state diagram of sucrose/water by analysing the frequency of relaxation.

The relaxation frequency and the loss factor at relaxation frequency has a semilogarithmic, relationship in all the regions, and does not allow the separation. Nevertheless, at very low mobility zone in the supersaturated region, new behaviour appears because the relaxation frequency remains constant while the loss factor was reduced, this may be due to the vitrification process (glass transition).

In the dielectric analysis in γ-dispersion, samples before and after the OD plasmolysis show no differences, therefore, in this case of parenchymatic tissue, the effect of membrane plasmolysis had no effect in the water orientation or induction. Therefore, in similar fruit tissue, with high quantity of parenchymatic tissue and low vascular tissue, the behaviour could be expected to be similar.

5. Conclusions

The use of specific frequencies of the dielectric properties in γ-dispersion did not allow us to correctly analyse the mobility of water and it makes it necessary to determine the dielectric properties at the relaxation frequency. It was demonstrated that the dielectric constant (at relaxation frequency) was linearly related to the water activity and not to the moisture, it means that it was affected by water mobility and therefore by the structure. In addition, it was possible to determine sucrose supersaturation processes by analysing the relaxation frequency, which depends on the deformation of the water molecule. Therefore, it was demonstrated that the use of dielectric

properties in γ-dispersion at relaxation frequency allowed us not only to monitor the OD and HAD processes of the apple candying, but also to predict the supersaturation state of the liquid phase until vitrification.

6. Acknowledgments

This research was funded by THE SPANISH MINISTERIO DE ECONOMÍA, INDUSTRIA Y COMPETITIVIDAD, Programa Estatal de I+D+i orientada a los Retos de la Sociedad AGL2016-80643-R, Agencia Estatal de Investigación (AEI) and Fondo Europeo de Desarrollo Regional (FEDER). The author Juan Ángel Tomás-Egea wants to thank the FPI Predoctoral Program of the Universidad Politécnica de Valencia for its support.

7. References

Agre, P., Bonhivers, M. and Borgnia, M.J. (1998) 'The Aquaporins, Blueprints for Cellular Plumbing Systems', *Journal of Biological Chemistry*, 273(24), pp. 14659–14662. doi:10.1074/jbc.273.24.14659.

Ahmed, I., Qazi, I.M. and Jamal, S. (2016) 'Developments in osmotic dehydration technique for the preservation of fruits and vegetables', *Innovative Food Science & Emerging Technologies*, 34, pp. 29–43. doi:10.1016/j.ifset.2016.01.003.

Alzamora, S.M. *et al.* (2000) 'The role of tissue microstructure in the textural characteristics of minimally processed fruits', *Minimally processed fruits and vegetables*, pp. 153–169.

Baker-Jarvis, J. and Kim, S. (2012) 'The Interaction of Radio-Frequency Fields with Dielectric Materials at Macroscopic to Mesoscopic Scales', *Journal of Research of the National Institute of Standards and Technology*, 117, p. 1. doi:10.6028/jres.117.001.

Brunton, N.P. *et al.* (2006) 'The use of dielectric properties and other physical analyses for assessing protein denaturation in beef biceps femoris muscle during cooking from 5 to 85°C', *Meat Science*, 72(2), pp. 236–244. doi:10.1016/j.meatsci.2005.07.007.

Castro-Giraldez, M., Fito, P.J., *et al.* (2010a) 'Development of a Dielectric Spectroscopy Technique for Determining Key Chemical Components of Apple Maturity', *Journal of Agricultural and Food Chemistry*, 58(6), pp. 3761–3766. doi:10.1021/jf903338b.

Castro-Giraldez, M., Fito, P.J., *et al.* (2010b) 'Development of a dielectric spectroscopy technique for the determination of apple (Granny Smith) maturity', *Innovative Food Science & Emerging Technologies*, 11(4), pp. 749–754. doi:10.1016/j.ifset.2010.08.002.

Castro-Giraldez, M., Botella, P., *et al.* (2010) 'Low-frequency dielectric spectrum to determine pork meat quality', *Innovative Food Science & Emerging Technologies*, 11(2), pp. 376–386. doi:10.1016/j.ifset.2010.01.011.

Castro-Giraldez, M., Aristoy, M.C., *et al.* (2010) 'Microwave dielectric spectroscopy for the determination of pork meat quality', *Food Research International*, 43(10), pp. 2369–2377. doi:10.1016/j.foodres.2010.09.003.

Castro-Giraldez, M., Tylewicz, U., *et al.* (2011) 'Analysis of chemical and structural changes in kiwifruit (Actinidia deliciosa cv Hayward) through the osmotic dehydration', *Journal of Food Engineering*, 105(4), pp. 599–608. doi:10.1016/j.jfoodeng.2011.03.029.

Castro-Giraldez, M., Fito, P.J., *et al.* (2011) 'Application of microwaves dielectric spectroscopy for controlling osmotic dehydration of kiwifruit (Actinidia deliciosa cv Hayward)', *Innovative Food Science & Emerging Technologies*, 12(4), pp. 623–627. doi:10.1016/j.ifset.2011.06.013.

Castro-Giraldez, M., Dols, L., *et al.* (2011) 'Development of a dielectric spectroscopy technique for the determination of key biochemical markers of meat quality', *Food Chemistry*, 127(1), pp. 228–233. doi:10.1016/j.foodchem.2010.12.089.

Castro-Giraldez, M. *et al.* (2012) 'Study of the puffing process of amaranth seeds by dielectric spectroscopy', *Journal of Food Engineering*, 110(2), pp. 298–304. doi:10.1016/j.jfoodeng.2011.04.012.

Castro-Giraldez, M. *et al.* (2013) 'Study of pomegranate ripening by dielectric spectroscopy', *Postharvest Biology and Technology*, 86, pp. 346–353. doi:10.1016/j.postharvbio.2013.07.024.

Castro-Giraldez, M., Fito, P.J. and Fito, P. (2010) 'Application of microwaves dielectric spectroscopy for controlling pork meat (Longissimus dorsi) salting process', *Journal of Food Engineering*, 97(4), pp. 484–490. doi:10.1016/j.jfoodeng.2009.11.005.

Castro-Giraldez, M., Fito, P.J. and Fito, P. (2011a) 'Application of microwaves dielectric spectroscopy for controlling long time osmotic dehydration of parenchymatic apple tissue', *Journal of Food Engineering*, 104(2), pp. 227–233. doi:10.1016/j.jfoodeng.2010.10.034.

Castro-Giraldez, M., Fito, P.J. and Fito, P. (2011b) 'Nonlinear thermodynamic approach to analyze long time osmotic dehydration of parenchymatic apple tissue', *Journal of Food Engineering*, 102(1), pp. 34–42. doi:10.1016/j.jfoodeng.2010.07.032.

Castro-Giraldez, M., Toldrá, F. and Fito, P. (2011) 'Low frequency dielectric measurements to assess post-mortem ageing of pork meat', *LWT - Food Science and Technology*, 44(6), pp. 1465–1472. doi:10.1016/j.lwt.2011.01.002.

Crane, C.A., Pantoya, M.L. and Weeks, B.L. (2013) 'Spatial observation and quantification of microwave heating in materials', *Review of Scientific Instruments*, 84(8), p. 084705. doi:10.1063/1.4818139.

Cuibus, L. *et al.* (2014) 'Application of infrared thermography and dielectric spectroscopy for controlling freezing process of raw potato', *Innovative Food Science & Emerging Technologies*, 24, pp. 80–87. doi:10.1016/j.ifset.2013.11.007.

Everard, C.D. *et al.* (2006) 'Dielectric properties of process cheese from 0.3 to 3GHz', *Journal of Food Engineering*, 75(3), pp. 415–422. doi:10.1016/j.jfoodeng.2005.04.027.

Fito, P. *et al.* (2007) 'Advanced food process engineering to model real foods and processes: The "SAFES" methodology', *Journal of Food Engineering*, 83(2), pp. 173–185. doi:10.1016/j.jfoodeng.2007.02.017.

Horie, K., Ushiki, H. and Winnik, F.M. (2008) *Molecular photonics: fundamentals and practical aspects*. John Wiley & Sons.

Horowitz, W. (2000) *Moisture in dried fruits. Method 934.06*, *Official Methods of Analysis of AOAC International*,. Association of Official Analytical Chemists International.

Jackson, E.B. (1990) *Sugar confectionery manufacture*. Glasgow, UK: Blackie.

Kent, M. *et al.* (2002) 'Determination of added water in pork products using microwave dielectric spectroscopy', *Food Control*, 13(3), pp. 143–149. doi:10.1016/S0956-7135(01)00066-4.

Krokida, M.K. and Marinos-Kouris, D. (2003) 'Rehydration kinetics of dehydrated products', *Journal of Food Engineering*, 57(1), pp. 1–7. doi:10.1016/S0260-8774(02)00214-5.

Lewicki, P.P. (2006) 'Design of hot air drying for better foods', *Trends in Food Science & Technology*, 17(4), pp. 153–163. doi:10.1016/j.tifs.2005.10.012.

Lewicki, P.P. and Jakubczyk, E. (2004) 'Effect of hot air temperature on mechanical properties of dried apples', *Journal of Food Engineering*, 64(3), pp. 307–314. doi:10.1016/j.jfoodeng.2003.10.014.

Lyng, J.G., Zhang, L. and Brunton, N.P. (2005) 'A survey of the dielectric properties of meats and ingredients used in meat product manufacture', *Meat Science*, 69(4), pp. 589–602. doi:10.1016/j.meatsci.2004.09.011.

Mathlouthi, M. (1981) 'X-ray diffraction study of the molecular association in aqueous solutions of d-fructose, d-glucose, and sucrose', *Carbohydrate Research*, 91(2), pp. 113–123. doi:10.1016/S0008-6215(00)86024-3.

Mathlouthi, M. (1995) 'Amorphous sugar', in *Sucrose*. Springer, pp. 75–100.

Mathlouthi, M. and Genotelle, J. (1998) 'Role of water in sucrose crystallization1Presented at the Second International Meeting of the Portuguese Carbohydrate Chemistry Group.1', *Carbohydrate Polymers*, 37(3), pp. 335–342. doi:10.1016/S0144-8617(98)00079-4.

Mauro, M.A. *et al.* (2016) 'Calcium and ascorbic acid affect cellular structure and water mobility in apple tissue during osmotic dehydration in sucrose solutions', *Food Chemistry*, 195, pp. 19–28. doi:10.1016/j.foodchem.2015.04.096.

Mavroudis, N.E., Dejmek, P. and Sjöholm, I. (2004) 'Osmotic-treatment-induced cell death and osmotic processing kinetics of apples with characterised raw material properties', *Journal of Food Engineering*, 63(1), pp. 47–56. doi:10.1016/S0260-8774(03)00281-4.

Mohiri, A., Burhanudin, Z.A. and Ismail, I. (2011) 'Dielectric properties of slaughtered and non-slaughtered goat meat', in *2011 IEEE International RF & Microwave Conference*. IEEE, pp. 393–397.

Nelson, S.O. (2005) 'Dielectric spectroscopy in agriculture', *Journal of Non-Crystalline Solids*, 351(33), pp. 2940–2944. doi:10.1016/j.jnoncrysol.2005.04.081.

Nelson, S.O. (2008) 'Dielectric properties of agricultural products and some applications', *Research in Agricultural Engineering*, 54, pp. 104–112. doi:https://doi.org/10.17221/1000-RAE.

Nelson, S.O. and Trabelsi, S. (2006) 'Dielectric spectroscopy of wheat from 10 MHz to 1.8 GHz', *Measurement Science and Technology*, 17(8), pp. 2294–2298. doi:10.1088/0957-0233/17/8/034.

Nieto, A.B. *et al.* (2013) 'Osmotic dehydration of apple: Influence of sugar and water activity on tissue structure, rheological properties and water mobility', *Journal of Food Engineering*, 119(1), pp. 104–114. doi:10.1016/j.jfoodeng.2013.04.032.

Roos, Y.H. and Karel, M. (1991) 'Water and Molecular Weight Effects on Glass Transitions in Amorphous Carbohydrates and Carbohydrate Solutions', *Journal of Food Science*, 56(6), pp. 1676–1681. doi:https://doi.org/10.1111/j.1365-2621.1991.tb08669.x.

Roychoudhuri, C., Kracklauer, A.F. and Creath, K. (2008) *The Nature of Light | Taylor & Francis Group*. 1st edition. Boca Ratón, USA: CRC Press. Available at: https://doi.org/10.1201/9781420044256 (Accessed: 27 April 2021).

Sacilik, K. and Elicin, A.K. (2006) 'The thin layer drying characteristics of organic apple slices', *Journal of Food Engineering*, 73(3), pp. 281–289. doi:10.1016/j.jfoodeng.2005.03.024.

Salisbury, F.B. and Ross, C.W. (1992) 'Plant physiology and plant cells', *Plant physiology*, pp. 3–26.

Samuel, D. *et al.* (2012) 'The Use of Dielectric Spectroscopy as a Tool for Predicting Meat Quality in Poultry', *International Journal of Poultry Science*, 11, pp. 551–555. doi:10.3923/ijps.2012.551.555.

Shang, L., Guo, W. and Nelson, S.O. (2015) 'Apple Variety Identification Based on Dielectric Spectra and Chemometric Methods', *Food Analytical Methods*, 8(4), pp. 1042–1052. doi:10.1007/s12161-014-9985-5.

Starzak, M. and Mathlouthi, M. (2006) 'Temperature dependence of water activity in aqueous solutions of sucrose', *Food Chemistry*, 96(3), pp. 346–370. doi:10.1016/j.foodchem.2005.02.052.

Talens, C., Castro-Giraldez, M. and Fito, P.J. (2016) 'Study of the effect of microwave power coupled with hot air drying on orange peel by dielectric spectroscopy', *LWT - Food Science and Technology*, 66, pp. 622–628. doi:10.1016/j.lwt.2015.11.015.

Trabelsi, S., Roelvink, J. and Russell, R.B. (2014) 'Investigating the Influence of Aging on Radiofrequency Dielectric Properties of Chicken Meat', *Journal of Microwave Power and Electromagnetic Energy*, 48(4), pp. 215–220. doi:10.1080/08327823.2014.11689885.

Traffano-Schiffo, M.V. *et al.* (2015) 'Study of the application of dielectric spectroscopy to predict the water activity of meat during drying process', *Journal of Food Engineering*, 166, pp. 285–290. doi:10.1016/j.jfoodeng.2015.06.030.

Traffano-Schiffo, M.V. *et al.* (2017) 'Development of a Spectrophotometric System to Detect White Striping Physiopathy in Whole Chicken Carcasses', *Sensors*, 17(5), p. 1024. doi:10.3390/s17051024.

Traffano-Schiffo, M.V., Castro-Giraldez, M., Herrero, V., *et al.* (2018) 'Development of a non-destructive detection system of Deep Pectoral Myopathy in poultry by dielectric spectroscopy', *Journal of Food Engineering*, 237, pp. 137–145. doi:10.1016/j.jfoodeng.2018.05.023.

Traffano-Schiffo, M.V., Castro-Giraldez, M., Colom, R.J., *et al.* (2018a) 'Innovative photonic system in radiofrequency and microwave range to determine chicken meat quality', *Journal of Food Engineering*, 239, pp. 1–7. doi:10.1016/j.jfoodeng.2018.06.029.

Traffano-Schiffo, M.V., Castro-Giraldez, M., Colom, R.J., *et al.* (2018b) 'New Spectrophotometric System to Segregate Tissues in Mandarin Fruit', *Food and Bioprocess Technology*, 11(2), pp. 399–406. doi:10.1007/s11947-017-2019-8.

Tylewicz, U. *et al.* (2011) 'Analysis of kiwifruit osmodehydration process by systematic approach systems', *Journal of Food Engineering*, 104(3), pp. 438–444. doi:10.1016/j.jfoodeng.2011.01.007.

Velázquez-Varela, J. *et al.* (2018) 'Study of the cheese salting process by dielectric properties at microwave frequencies', *Journal of Food Engineering*, 224, pp. 121–128. doi:10.1016/j.jfoodeng.2017.12.024.

Velázquez-Varela, J., Castro-Giraldez, M. and Fito, P.J. (2013) 'Control of the brewing process by using microwaves dielectric spectroscopy', *Journal of Food Engineering*, 119(3), pp. 633–639. doi:10.1016/j.jfoodeng.2013.06.032.

Venkatesh, M.S. and Raghavan, G.S.V. (2004) 'An Overview of Microwave Processing and Dielectric Properties of Agri-food Materials', *Biosystems Engineering*, 88(1), pp. 1–18. doi:10.1016/j.biosystemseng.2004.01.007.

Vicente, S. *et al.* (2012) 'Changes in Structure, Rheology, and Water Mobility of Apple Tissue Induced by Osmotic Dehydration with Glucose or Trehalose', *Food and Bioprocess Technology*, 5(8), pp. 3075–3089. doi:10.1007/s11947-011-0643-2.

sensors

MDPI

New sensor to measure the microencapsulated active compounds released in an aqueous liquid media based in dielectric properties in radiofrequency range

J.A. Tomas-Egea [1], P.J. Fito [1], R.J. Colom [2] and M. Castro-Giraldez [1]

[1] Instituto Universitario de Ingeniería de Alimentos para el Desarrollo, Universitat Politècnica de València, Camino de Vera s/n, 46022 Valencia, Spain
[2] Instituto de Instrumentación para Imagen Molecular, Universitat Politècnica de València, Camino de Vera s/n, 46022 Valencia, Spain

Sensors

https://doi.org/10.3390/s21175781

Published: August 27, 2021

In recent years, the general and scientific interest in nutrition, digestion, and what role they play in our body has increased, and there is still much work to be carried out in the field of developing sensors and techniques that are capable of identifying and quantifying the chemical species involved in these processes. Iron deficiency is the most common and widespread nutritional disorder that mainly affects the health of children and women. Iron from the diet may be available as heme or organic iron, or as non-heme or inorganic iron. The absorption of non-heme iron requires its solubilization and reduction in the ferric state to ferrous that begins in the gastric acid environment, because iron in the ferric state is very poorly absorbable. There are chemical species with reducing capacity (antioxidants) that also have the ability to reduce iron, such as ascorbic acid. This paper aims to develop a sensor for measuring the release of encapsulated active compounds, in different media, based on dielectric properties measurement in the radio frequency range. An impedance sensor able to measure the release of microencapsulated active compounds was developed. The sensor was tested with calcium alginate beads encapsulating iron ions and ascorbic acid as active compounds. The prediction and measurement potential of this sensor was improved by developing a thermodynamic model that allows obtaining kinetic parameters that will allow suitable encapsulation design for subsequent release.

Keywords: sensor; impedance; microencapsulation; radiofrequency.

New sensor to measure the microencapsulated active compounds released in an aqueous liquid media based in dielectric properties in radiofrequency range

J.A. Tomas-Egea [1], P.J. Fito [1], R.J. Colom [2] and M. Castro-Giraldez [1]

[1] Instituto Universitario de Ingeniería de Alimentos para el Desarrollo, Universitat Politècnica de València, Camino de Vera s/n, 46022 Valencia, Spain

[2] Instituto de Instrumentación para Imagen Molecular, Universitat Politècnica de València, Camino de Vera s/n, 46022 Valencia, Spain

Abstract: In recent years, the general and scientific interest in nutrition, digestion, and what role they play in our body has increased, and there is still much work to be carried out in the field of developing sensors and techniques that are capable of identifying and quantifying the chemical species involved in these processes. Iron deficiency is the most common and widespread nutritional disorder that mainly affects the health of children and women. Iron from the diet may be available as heme or organic iron, or as non-heme or inorganic iron. The absorption of non-heme iron requires its solubilisation and reduction in the ferric state to ferrous that begins in the gastric acid environment, because iron in the ferric state is very poorly absorbable. There are chemical species with reducing capacity (antioxidants) that also have the ability to reduce iron, such as ascorbic acid. This paper aims to develop a sensor for measuring the release of encapsulated active compounds, in

different media, based on dielectric properties measurement in the radio frequency range. An impedance sensor able to measure the release of microencapsulated active compounds was developed. The sensor was tested with calcium alginate beads encapsulating iron ions and ascorbic acid as active compounds. The prediction and measurement potential of this sensor was improved by developing a thermodynamic model that allows obtaining kinetic parameters that will allow suitable encapsulation design for subsequent release.

Keywords: sensor; impedance; microencapsulation; radio frequency.

1. Introduction

Even though in recent years the general and scientific interest in nutrition, digestion, and what role they play in our body has increased, there is still much work to be carried out in the field of developing sensors and techniques that are capable of identifying and quantifying the chemical species involved in these processes. Until now, researchers have been monitoring the release of microencapsulated or nanoencapsulated compounds in liquid media in a static process, taking a sample of the medium and measuring it by a spectrophotometer (Tu et al., 2005; Colinet et al., 2009; Liakos et al., 2013; Criado et al., 2019; Miere et al., 2019), proximate analysis (Folin–Ciocalteu method) (Najafi-Soulari, Shekarchizadeh and Kadivar, 2016; Orozco-Villafuerte et al., 2019; Apoorva et al., 2020; Gholamian, Nourani and Bakhshi, 2021; Hoseyni et al., 2021), or HPLC (Moschona and Liakopoulou-Kyriakides, 2018), which are static and invasive measurements.

According to WHO (Geneva, Switzerland), at present, more than 25 % of the world's population suffers from anaemia, mainly due to iron deficiency (De Benoist et al., 2008; Charles, 2012). Therefore, it can be considered that iron deficiency is the most common and widespread nutritional disorder; it is a deficiency disease that mainly affects the health of children and women, mainly in developing countries, but also in industrialized countries (Charles, 2012). Iron from the diet may be available as heme (organic iron), or as non-heme (inorganic iron). Heme iron is found mainly in meats (myoglobin) and blood (haemoglobin) and, on the other hand, the main sources of non-heme iron are of plant origin, milk and eggs, and it is found mostly in its oxidized form (Fe^{+3}) and bound to various

macromolecules (Anderson, Frazer and McLaren, 2009). Although non-heme iron is the most predominant form in the usual diet (80–90 % of total iron), it is the one with the lowest bioavailability since its absorption may be interfered with by other factors in the diet, such as phytates, calcium, or mucin (Sermini, Acevedo and Arredondo, 2017). On the other hand, heme iron only represents 10–20 % of the iron present in the diet, but its absorption is more efficient (Sharp and Srai, 2007). The absorption of non-heme iron requires its reduction from the ferric state (Fe^{+3}) to ferrous (Fe^{+2}) that begins in the gastric acid environment, because iron in the ferric state is not absorbable (Anderson, Frazer and McLaren, 2009). There are chemical species with reducing capacity (antioxidants) that also can reduce iron, such as ascorbic acid (vitamin C), cysteine and histidine.

For all the above, reinforcing the diet with foods that include ferrous salts, or ferric salts accompanied by species with antioxidant activity, which can be dosed throughout the digestive system, could increase the assimilation of iron and thus reduce the problems associated with diets with little or no heme iron. In this context, it is important to study the encapsulation of ferrous salts, or ferric salts accompanied by species with antioxidant activity, and their release under gastrointestinal conditions. This encapsulation has several utilities; firstly, it ensures the release throughout the entire small intestine, mainly in the duodenum and jejunum. In addition, it prevents the reaction of ferric and ferrous salts with other chemical species of gastric juices, masking the metallic taste of these salts and eliminating the staining effect that some vitamin complexes have on food and teeth (Durán et al., 2017).

Encapsulation is a process in which certain active compounds are included within a protective matrix in order to control their release and/or protect them from degradation processes such as oxidation, evaporation or thermal degradation (Santagapita, Mazzobre and Buera, 2012; Traffano-Schiffo, Aguirre Calvo, et al., 2017; Traffano-Schiffo, Castro-Giraldez, Fito, et al., 2017). In the search for suitable matrices, both calcium alginate hydrogels (alginate-Ca (II)) and powders obtained by spray drying have been widely studied (Estevinho et al., 2013; Aguirre-Calvo, Busch and Santagapita, 2017; Aguirre-Calvo et al., 2020). Alginate is an anionic polyelectrolyte, made up of β-D-manuronic (M) and α-L-guluronic (G) residues linked by α bonds (1 → 4), and generate a hydrogel matrix, due to the ionic crosslinking of the G blocks with di- or trivalent cations such as Ca^{2+} or Ce^{3+} (among others), forming the structure known as "egg box" (Traffano-Schiffo, Castro-Giraldez, Fito, et al., 2018). Ca (II)-alginate is non-toxic, biodegradable and biocompatible, the process for the production of beads being cheap, easy and versatile, in addition to offering extremely manageable operating conditions. However, it has certain disadvantages such as the loss of encapsulated compounds, low mechanical resistance, large pore size (Santagapita, Mazzobre and Buera, 2011) and high-water activity, which makes it susceptible to microbial deterioration (Rahman and Labuza, 2020). This is why the coupled application of a conservation treatment such as hot air drying will improve the stability of the system for the subsequent release of bioactive compounds.

To describe and estimate a mass transport process, such as the release of encapsulated compounds from the bead to the medium, irreversible thermodynamics can be used. They have been applied successfully in a salting

cheese (Velázquez-Varela et al., 2018), orange peel and potato dried with hot air drying combined with microwaves (Talens, Castro-Giraldez and Fito, 2016; Tomas-Egea et al., 2021), potato and pork freezing (Castro-Giraldez et al., 2014; Cuibus et al., 2014), glass transition and driving forces in the water nucleation process (Schmelzer et al., 2018; Hellmuth, Schmelzer and Feistel, 2020), estimation of crystal internal energy in meat (Berezovskiy, Korolev and Sarantsev, 2020) and a state diagram to determine the quality of foodstuff (Roos, 2021).

There are different spectrophotometric techniques widely used for the control, characterization and monitor processes in the food industry (Traffano-Schiffo, Aguirre Calvo, et al., 2017; Tomas-Egea, Fito and Castro-Giraldez, 2019; Traffano-Schiffo et al., 2021). Among the most promising techniques is radiofrequency (RF) spectroscopy. It is important to highlight that any physical, chemical, and compositional changes that occur in the hydrogel matrices will generate changes in the dielectric properties in this section of the spectrum, which is why this technique represents a great advance for monitoring the release of active substances during the digestive process. The application of this technique to the development of sensors has been shown to be useful and reliable with sensors capable of performing quality controls such as detecting the deep pectoral myopathy (Traffano-Schiffo, Castro-Giraldez, Herrero, et al., 2018) and white striping (Traffano-Schiffo, Castro-Giraldez, Colom, et al., 2017) in poultry, estimating the meat batter composition (Zhang, Lyng and Brunton, 2007), determining the pork (Castro-Giraldez et al., 2010) and chicken (Trabelsi, Roelvink and Russell, 2014; Traffano-Schiffo, Castro-Giraldez, Colom, et al., 2018a) meat quality, assessing the protein denaturation in beef (Brunton et al., 2006), identifying

the variety of an apple (Shang, Guo and Nelson, 2015), segregating the different tissues of a mandarin (Traffano-Schiffo, Castro-Giraldez, Colom, et al., 2018b) and monitoring the freezing process of potatoes (Cuibus et al., 2014).

The aim of this paper is to develop a sensor for measuring the release of encapsulated active compounds, in different media, based on dielectric properties measurement in the radiofrequency range.

The aim of this paper is to determine the effect of MW in the combined HAD-MW drying of raw potato at a drying air temperature below the spontaneous evaporation temperature, with the potato having a smaller characteristic dimension than the MW penetration depth, in order to obtain the real driving forces and the mechanisms involved in the water transport, with the purpose of optimizing the MW power used.

2. Materials and Methods

2.1. Buffer

The buffer solution, characterized by a pH of 3.8 and a 0.05 M concentration, was prepared from acetic acid and sodium acetate (Scharlab S.L., Barcelona, Spain). The purpose of the reactants was to lower the alginate pKa, getting it to be negatively charged, ensuring an optimal interaction between alginate and calcium (Santagapita, Mazzobre and Buera, 2011).

2.2. Reagents

The reagents used in the preparation of the samples, together with the buffer, were calcium chloride ($CaCl_2$) (Scharlab SL, Barcelona, Spain),

sodium alginate (Panreac Química SLU, Castellar del Valles, Barcelona, Spain) with a purity of 90 %, iron-protein- succinylate (Ferplex, Italfarmaco SA, Madrid, Spain), with a purity of 40 mg/15 mL, L(+)-Ascorbic acid (Scharlab SL, Barcelona, Spain) and hydrochloric acid (1N) (Panreac Química SLU, Castellar del Valles, Barcelona, Spain).

2.3. Solutions of different pH

For the preparation of the solutions at different pH 3 and 4.7, hydrochloric acid was added to double-distilled water until the final pH was reached. pH was monitored by pH meter (S20 SevenEasy TM, Mettler Toledo, Greifensee, Switzerland).

2.4. 3D Printing material: Acrylonitrile Butadiene Styrene (ABS)

This material (FrontierFila, Shenzen, China) was printed with the following parameters: 235 °C extrusion temperature, 90 °C bed temperature, 100 % filling, 40 mm/s print speed and a layer height of 0.1 mm. The filament has a diameter of 1.75 mm according to the specifications of the printer extruder.

2.5. Experimental procedure

A specific measurement system for dielectric properties was designed to allow continuous measurements during the release of active compounds. This measuring system consists of an outer shell and a measuring tank, both printed by 3D printing. Subsequently, the parts and metals chosen to obtain the dielectric properties sensor were assembled and connected to an impedance analyzer in order to perform measurements.

Standard solutions were prepared with known amounts of iron-protein-succinylate and L(+)-Ascorbic acid. In both cases, they were

prepared at both pHs (3 and 4.7). Standard solutions were prepared with mass fractions from 100 to 500 ppm of iron ion, and of ascorbic acid in mass fractions from 50 to 3000 ppm. Once the standard solutions were prepared, they were measured to analyze the possibility of determining specific amounts of these compounds in different media using the developed sensor.

Standard solutions of active compounds were made from mass fractions of 100–500 ppm of iron ion, and of ascorbic acid in mass fractions from 50–3000 ppm at two pH levels: 3 and 4.7.

After this process of tuning and testing the sensor, three types of beads were made: calcium alginate (alginate beads), calcium alginate with iron-protein-succinylate (iron ion beads), and finally, with L(+)-Ascorbic acid (ascorbic acids beads), all submitted to a drying process at 40 °C and 0.2 bar for 24 h in a vacuum drying oven (Vaciotem-T, Grupo Selecta, Abrera, Barcelona, Spain). Amounts of 0.05 g of beads and 200 μL of medium (solutions at different pH 3 and 4.7) were put into the measuring tank and measurements of dielectric properties were made for two hours. These measurements were taken at 5, 15, 30, 60, 120, 150, 200, 240, 300, 360, 420, 480, 540, 600, 1200, 1500, 1800, 2500, 3600, 4500 s.

Finally, a measure of expansion was made within different media (solutions at both pH 3 and 4.7) of the alginate beads, iron ion beads and ascorbic acid beads.

2.6. 3D printing protocol

The protocol followed for the design and obtaining of the external shell and the measuring tank is divided into three steps. First, the piece was designed using a 3D design program (Tinkercad, Autodesk, Inc., Mill Valley,

CA, USA), in which all the dimensions of the desired pieces were specified (Figure 4.4.1). Once the design prototype is obtained, it is sent to the 3D printer (Anet A8), setting all the previously established parameters. For this purpose, the Repetier–Host software was used to control and calibrate the printer, as well as to transmit data in GCode file to be replicated by the 3D printer, previously heated to the optimum temperature established for each material. To convert the 3D digital design into the instructions and steps necessary to achieve the physical design, the Slic3c tool was used to cut the model into layers, generate the paths to fill it and calculate the amount of material that will need to be extruded.

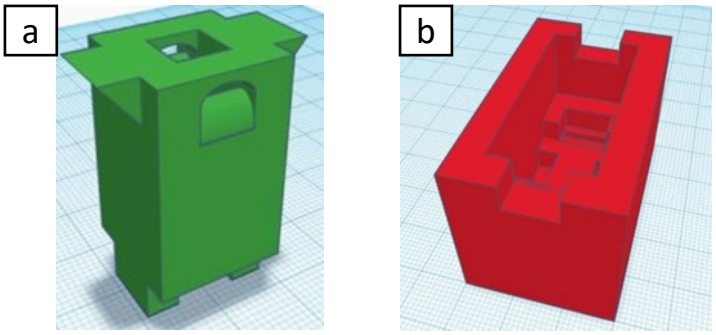

Figure 4.4.1. Design of the sensor: (a) measuring tank (b) outer shell. The ground shows millimeter graph paper.

2.7. Calcium alginate beads encapsulating iron-protein-succinylate and ascorbic acid preparation Protocol

Alginate and iron ion or ascorbic acids beads were prepared by ionic gelation. For this, it was necessary to prepare a 1:100 solution of sodium alginate (together with the reagent to be encapsulated: iron-protein-succinylate or L(+)-ascorbic acid) and another 1:100 solution of calcium chloride, both prepared with the sodium acetate buffer. A frequency inverter

(Inverter DV-700 Panasonic, Osaka, Japan) was installed to control the revolutions per minute of the peristaltic pump (Damova S.L, Barcelona, Spain, model CPM-045B). The peristaltic pump drips the solution formed by sodium alginate and the reagent that was to be encapsulated on the $CaCl_2$ solution with a ratio of 1:10, the $CaCl_2$ solution was in continuous agitation (IKA® MS3 basic, Staufen im Breisgau, Germany). The speed used to make a correct drip must be based on the percentage of power that the frequency inverter gives to the pump, in this case, it was 30 % and the distance between the tip of the needle (Thermo Fisher Scientific Oy, Vantaa, Finland) and the solution of $CaCl_2$ is 10 cm.

Once the beads were obtained, they were left under stirring in the $CaCl_2$ solution for 15 min to ensure optimum gelation (Deladino et al., 2008). After 15 min, the beads were extracted from the solution and washed 5 times with distilled water to remove the excess of $CaCl_2$.

Once the wet beads of calcium alginate and iron-protein-succinylate or calcium alginate and L(+)-ascorbic acid were formed, they were put into previously weighed crucibles and the total mass was registered. The crucibles were then placed in a vacuum drying oven (Vaciotem-T, JPSELECTA, Barcelona, Spain) at 40 °C and 0.8 bar for 24 h. After 24 h, the dried samples with a water activity (a_w) less than 0.35 were weighed and subsequently stored in Aqualab® (Pullman, WA, USA) capsules sealed with Parafilm® (Sigma-Aldrich, San Louis, USA) to avoid possible rehydration.

2.8. Protocol for the determination of the expansion capacity of the beads in different media

Once the dry beads were obtained, the protocol for determining the capacity of expansion was performed in triplicate: expansion capacity of the control beads in the different media (pH 3 and 4.7), expansion capacity of ascorbic acid beads in the different media (pH 3 and 4,7) and, the expansion of iron ion beads in the different media (pH 3 and 4,7). The beads were subjected to a rehydration process to quantify and replicate the increase in size that they experience inside the sensor when they come into contact with a solution of a specific pH. The assembly consists of a microscope (Juision USB Microscope) connected to a computer (MacBook Air, Apple, Cupertino, CA, USA), using the "Photo Booth" software for taking photos. As a reference distance, a micrometered glass located at the base of the bead was used (Figure 4.4.2).

A single bead was placed inside a glass crucible, then 100 μL of the corresponding pH (3 and 4.7) solution was added. The first photo was taken once the liquid phase comes into contact with the bead. After this the first, more photographs were taken at 5, 15, 30, 60, 120, 150, 200, 240, 300, 360, 420, 480, 540, 600 s from that time a measurement was taken every 5 min until 30 min.

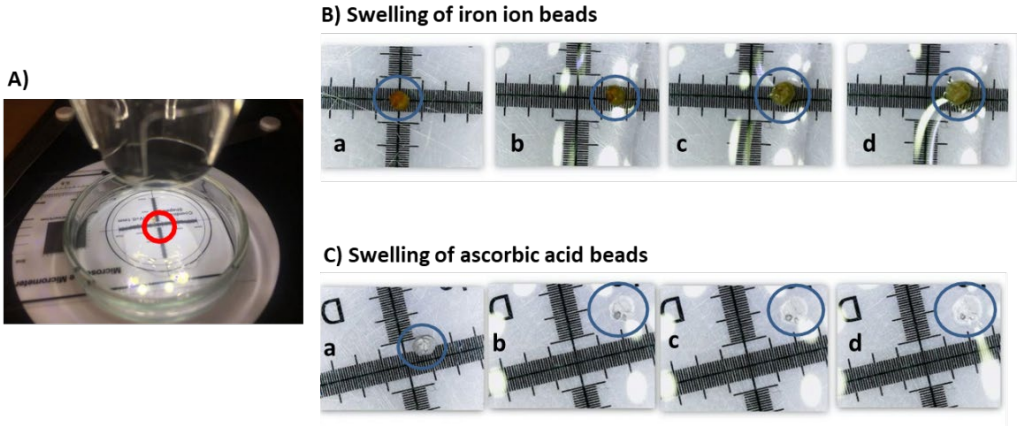

Figure 4.4.2. (A) Crucible containing the bead and the liquid phase to analyze the swelling by a microscope; (B) Swelling of an iron ion bead at pH 4.7 at the following times: (a) 0 min; (b) 0.367 min; (c) 6 min; (d) 30 min; (C) Swelling of an ascorbic acid bead at pH 4.7 at the following times: (a) 0 min; (b) 0.6 min; (c) 4 min; (d) 30 min.

The images were analyzed in Photoshop® (CS5, ver. 12, Adobe Systems InCorp. San Jose, CA, USA) by analyzing with the measuring tools the circumference of the 2D image of the bead with a sphere shape and a square millimeter provided by the micrometered glass, in order to transform the measurement from square pixels to square millimeters, thus obtaining the radius of the remainder of the bead sphere, and finally, the volume of each time point.

2.9. Determination of liberation kinetics

In order to obtain the release kinetics of bioactive compounds in different media, a system for measuring dielectric properties was designed and constructed (See results section). The measurement system was connected to an Agilent 4294A Impedance Analyzer, (Agilent Technologies, Santa Clara, CA, USA) (Figure 4.4.3). An open and short calibration was performed. The measurement range was from 40 Hz to 1 MHz. A triplicate

of each release process was performed: release of alginate beads in different media (pH 3 and 4.7), release of iron ion beads in different media (pH 3 and 4.7), and finally, release of ascorbic acid beads in different media (pH 3 and 4.7).

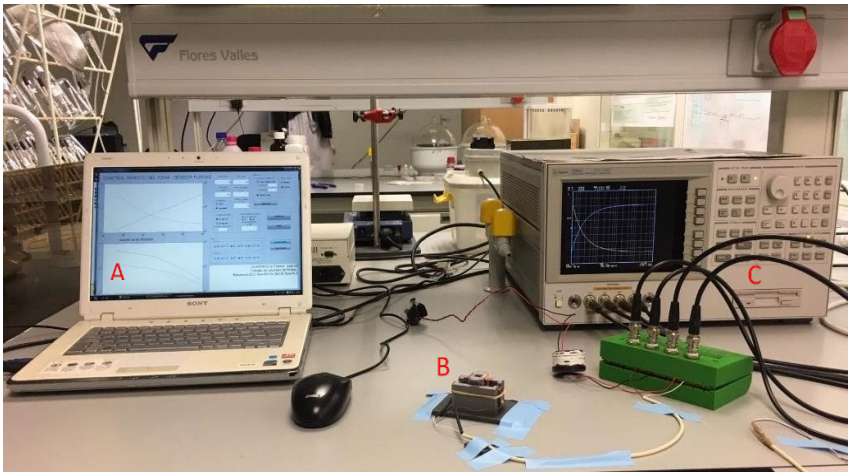

Figure 4.4.3. Set-up used to determine release kinetics. (A) Computer that collects the data from the impedance analyzer; (B) measuring tank and outer shell; (C) Impedance analyzer.

3. Results

Throughout the last decade, the scientific community has tried to simulate human digestive processes, which allow the design of more efficient foods and drugs, where the design of sensors gains relevance, representing a technological and scientific challenge for the research community. In this context, the design of encapsulates that allow the release of active compounds to fix digestive problems, nutritional deficiencies or diseases, requires the design of digestive simulation sensors to quantify said release. In this context, a sensor was developed for measuring the release of encapsulated active

compounds in different media, based on dielectric properties measurement in the radio frequency range.

The sensor consisted of two parts (see Figure 4.4.4), an outer shell, and a measuring tank. Figure 4.4.4 a, b and c show the measuring tank in plan, elevation and cross-section view, and Figure 4.4.4 d and e, the outer shell where the measuring tank is fixed to the circuit (shown in plan and cross-section view). The material selected for the final design was ABS, due to its ability to resist acidic and basic pH medium.

The measuring tank was designed with the aim of introducing the two parallel tantalum plates (0.75 cm × 1.5 cm) inside the tank, glued to the inner walls, between which the liquid phase and the beads were located (see Figure 4.4.5). In addition, two clamping rectangles were added to the base, which were put into the outer shell to improve its fixation. The measuring tank is connected to the impedance analyser, as Figure 4.4.5 shows, obtaining the complex impedance, being able to transform to complex permittivity, dielectric constant (ε') and loss factor (ε''), by means of the equations shown in this figure, thanks to the parallel arrangement of the tantalum plates.

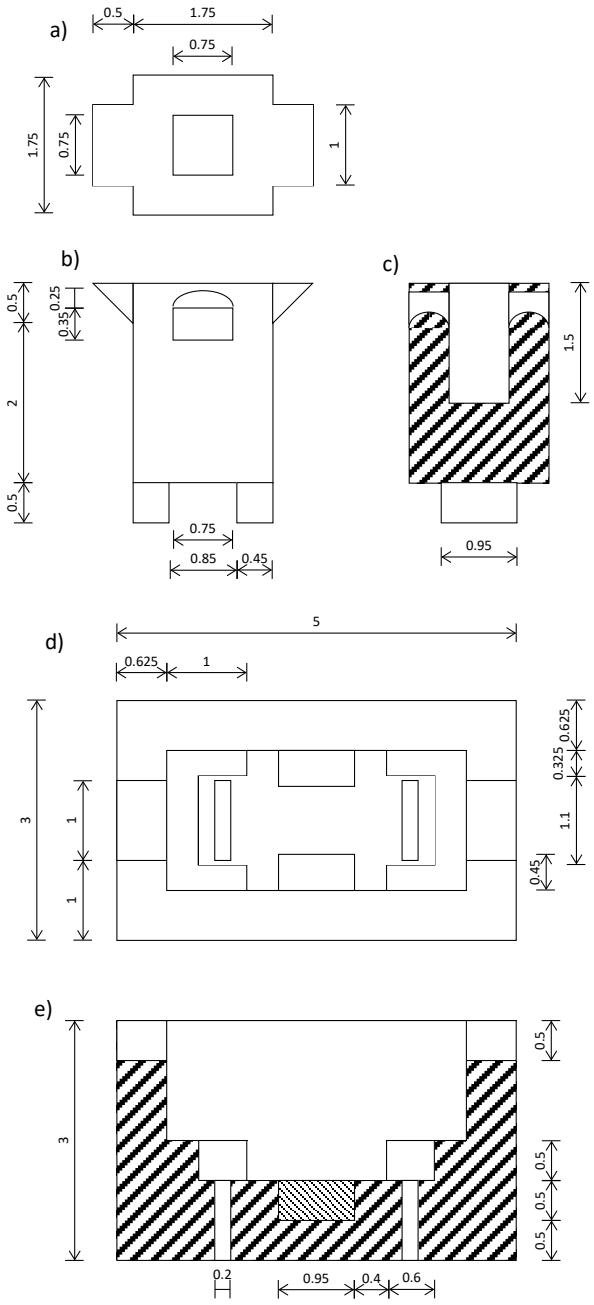

Figure 4.4.4. (a) Plan view of the measuring tank; (b) Elevation view of the measuring tank; (c) Cross-section section of the measuring tank; (d) Plan view of the outer shell; (e) Cross-section of the measuring tank. The dimensions of the whole figure are in centimetres.

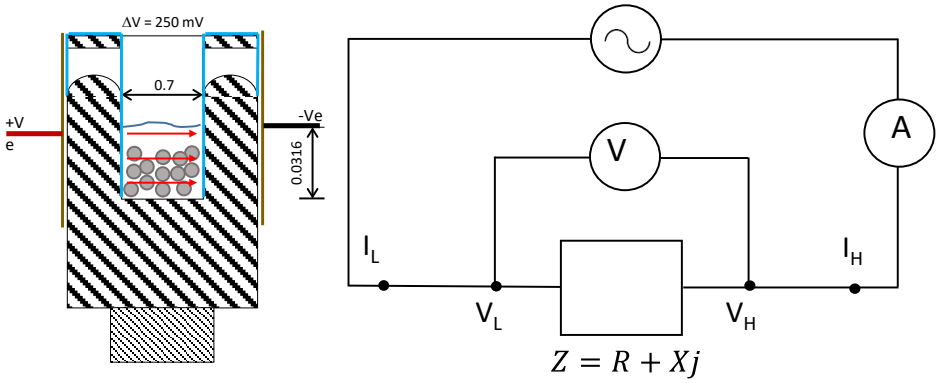

Equations

$$C_0 = \frac{\varepsilon_0 S}{d}$$

$$\varepsilon' = \frac{-X}{(R^2 + X^2)} \frac{1}{2\pi C_0 10^{-12}}$$

$$\varepsilon'' = \frac{R}{R^2 + X^2} \frac{1}{2\pi f C_0 10^{-12}}$$

Figure 4.4.5. Detail of sensor of Impedance measurement in radiofrequency range, to determine the release of encapsulated active compound, the electric circuit of sensor and the equations to determine the permittivity.

Figures 4.4.6a and 4.4.7a show the swelling of alginate beads with iron ion and ascorbic acid, respectively, when they are put into both pH media. The swelling of both types of beads in the different media causes a subatmospheric pressure variation inside the beads that causes the entry of media from the outside. The liquid phase (LP) flux entering the beads is calculated from the volume variation, using the following equation:

$$J_{LP} = \frac{\Delta V \cdot \rho_{LP}}{S \cdot t \cdot} \qquad (4.4.1)$$

where ΔV is the volume change, ϱ_{LP} is the density of LP (being considered equal to the density of water since the content of solutes is very low), S is the

bead surface and t is the time in seconds. The evolution of the LP flux entering the alginate beads with iron ion and ascorbic acid is shown in Figures 4.4.6b and 4.4.7b.

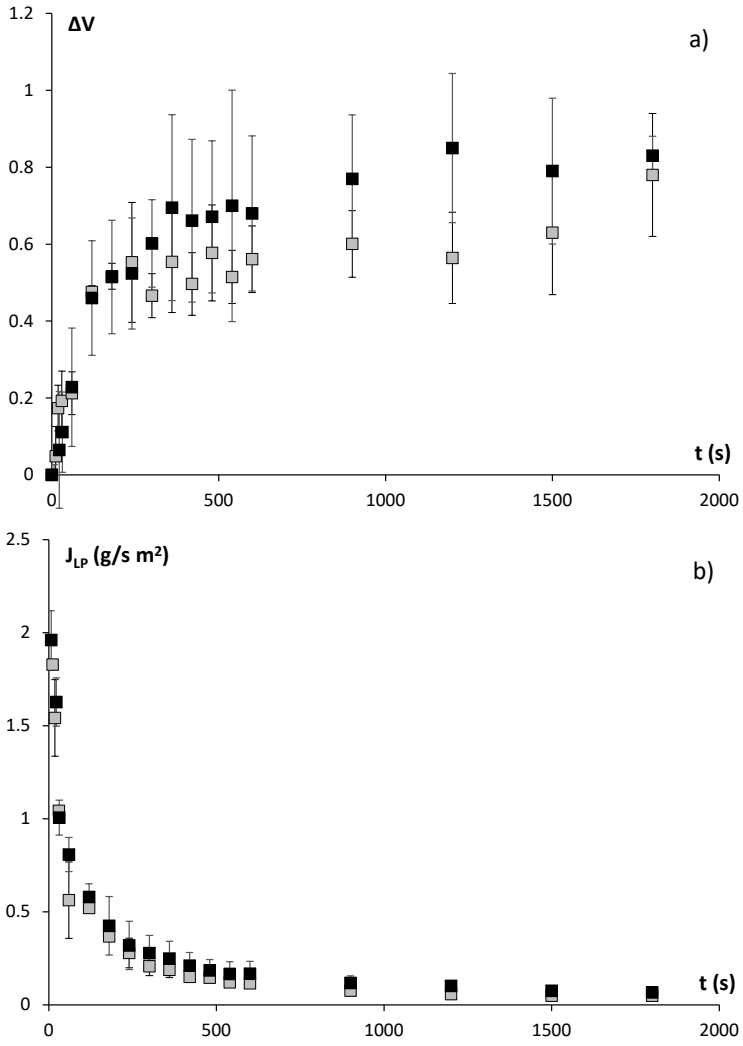

Figure 4.4.6. (a) Evolution of the volume variation of alginate beads with iron ion; (b) Evolution of the LP flux entering the calcium alginate beads with iron ion. Symbol ■ refers to pH = 3 and ■ refers to pH = 4.7.

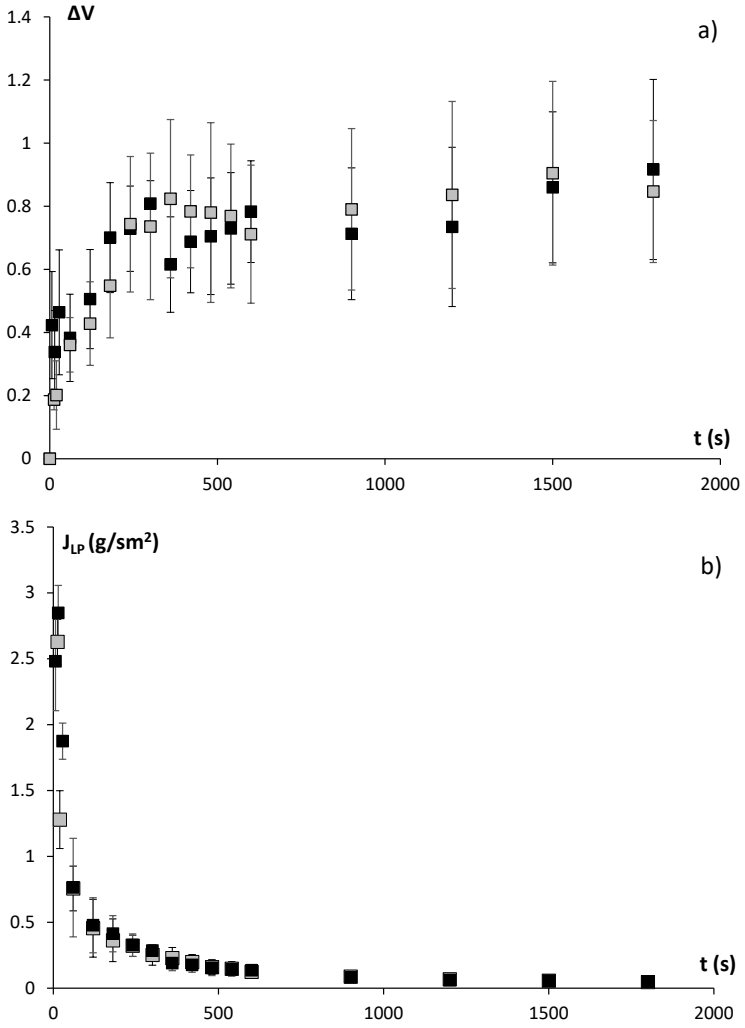

Figure 4.4.7. (a) Evolution of the volume variation of alginate beads with ascorbic acid; (b) Evolution of the liquid phase flux entering the calcium alginate beads with vitamin C. Symbol ■ refers to pH = 3 and ■ refers to pH = 4.7.

The beads immersed in an aqueous medium will release the active compound, with high ionic strength (iron ion) or moderate (ascorbic acid), varying the dielectric properties of the medium depending on the concentration of these chemical species. It will be necessary to determine the

relationship of this compound with the dielectric properties and the swelling of the beads, and thus quantify the release of the active compound from the encapsulation. In Figures 4.4.6a and 4.4.7a, it is possible to observe how the swelling of the beads relaxes after 360 s, the volume variation remains constant approximately over 60 % in the case of iron ion at pH 3, 70 % at pH 4.7, and in the case of ascorbic acid, 80 % in both cases.

In order to obtain the calibration of the release measurement system, standard solutions of active compounds were made from mass fractions of 100–500 ppm of iron ion, and of ascorbic acid in mass fractions from 50–3000 ppm at two pH levels: 3 and 4.7. Considering the nature of the chemical species released, with a high or moderate ionic strength, a relation between the content of these species and the dielectric properties should be observed, in the section of the electromagnetic spectrum comprised in the alpha dispersion, the counterion effect. For this reason, the spectra in the region of 40 Hz to 1 kHz were analysed, observing a greater relationship at 200 Hz, mainly in the reactance. Moreover, it was observed that the pH had no significant effect on the measurements of dielectric properties at frequencies of kHz. For this reason, all the measurements were grouped in the same graph that related, on the one hand, the mass fraction of iron ion with regard to the reactance, and on the other hand, the amount of ascorbic acid with the reactance (Figure 4.4.8). This figure shows that there is a linear relationship between the mass fraction of iron and the reactance at 200 Hz. Ascorbic acid also had a linear relationship with the reactance at 200 Hz.

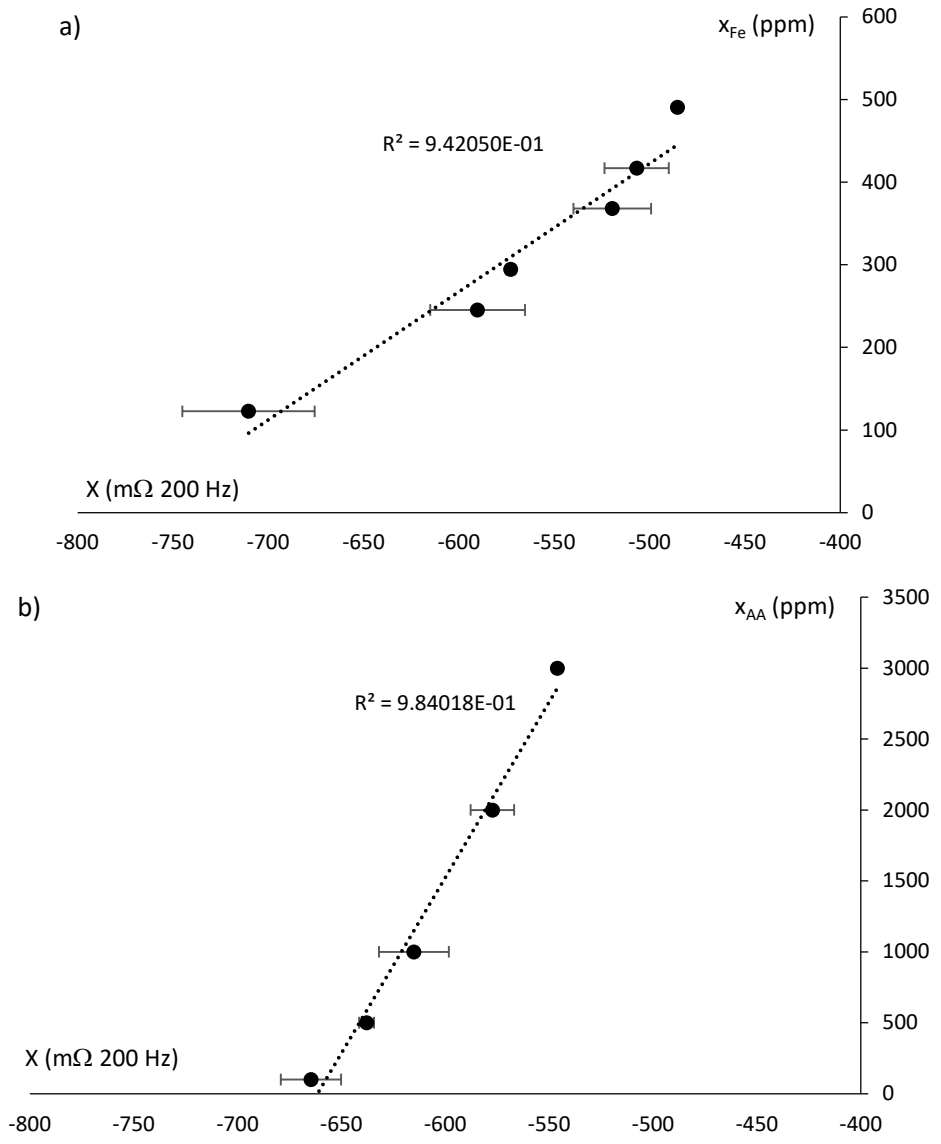

Figure 4.4.8. (a) Mass fraction of iron ion (ppm) vs. reactance at 200 Hz (mΩ); (b) Mass fraction of ascorbic acid (ppm) vs. reactance at 200 Hz (mΩ). Notation is according to IuPAC.

During the releasing process of each active compound in the measuring tank, the evolution of the reactance was obtained at 200 Hz, for

each condition of the external liquid phase, as was specified in the materials and methods section. These measurements are shown in Figure 4.4.9a.

With the values of reactance measured at 200 Hz, and from the calibration of standard solutions shown in Figure 4.4.8, the dielectric measurement was transformed into the concentration of each chemical species in the liquid phase. As can be seen in Figure 4.4.9b, the main quantity of iron ion and ascorbic acid is released in the first 450 s, reaching the asymptote of release at approximately 900 s for the two active compounds.

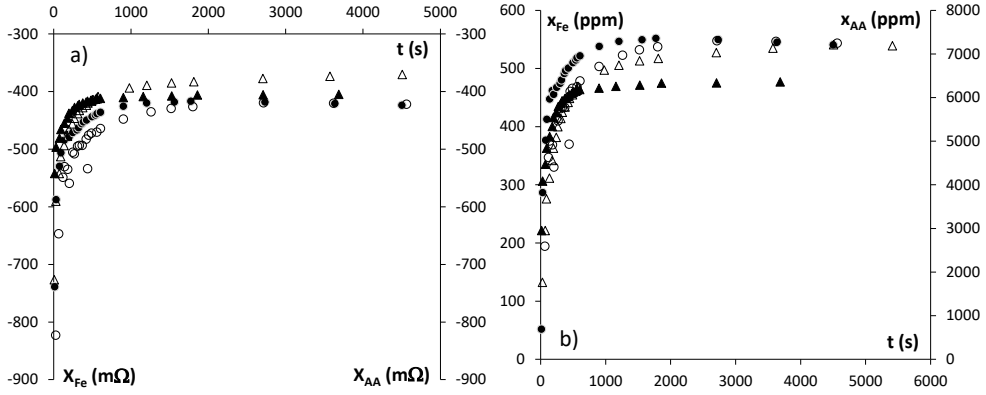

Figure 4.4.9. (a) Evolution of reactance at 200 Hz (mΩ) throughout the release process; (b) Evolution of mass fraction of each active compound (ppm) throughout the release process. Where (●) is iron ion released at pH of 3; (○) is iron ion released at pH of 4.7; (▲) is ascorbic acid released at pH of 3 and (Δ) is ascorbic acid released at pH of 4.7.

In order to obtain the release flux of each active compound, it is necessary to establish mass balances to the system bead/liquid phase. Figure 4.4.10 shows an outline of the bead/liquid phase system and the mass balances applied to this system. From these balances, it is possible to obtain the variation in mass fraction of each active compound, inside beads, during the active compound release process.

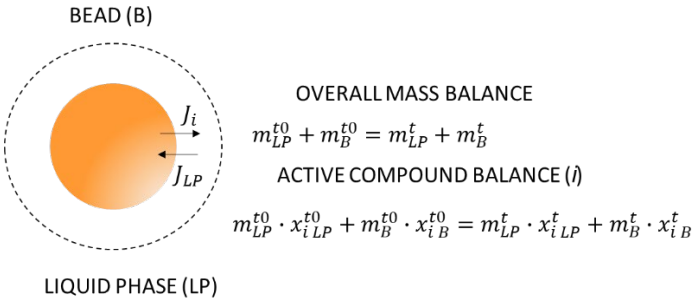

Figure 4.4.10. Outline of the bead in the liquid phase during the release of the active compound, with details of the fluxes and mass balances applied to the bead–liquid phase system. Where the subscripts: liquid phase (LP), bead phase (B) and active compound (i), and superscripts: t_0 (initial time) and t (process time).

Once the mass fractions of each active compound are obtained, during the release process, it is possible to calculate its flux with the following equation:

$$J_i = \frac{\Delta m_i^B}{\Delta t \cdot S^B \cdot M^i} \tag{4.4.2}$$

where J_i es de molar flux ($mol_i/s\ m^2$), Δm_i^B is the active compound mass variation in bead (g), during Δt time (s), S^B (m^2) is the bead surface at this process time, and M^i is the molecular weight of the active compound (g/mol).

Figure 4.4.11 shows the active compound fluxes release from the beads in a liquid media.

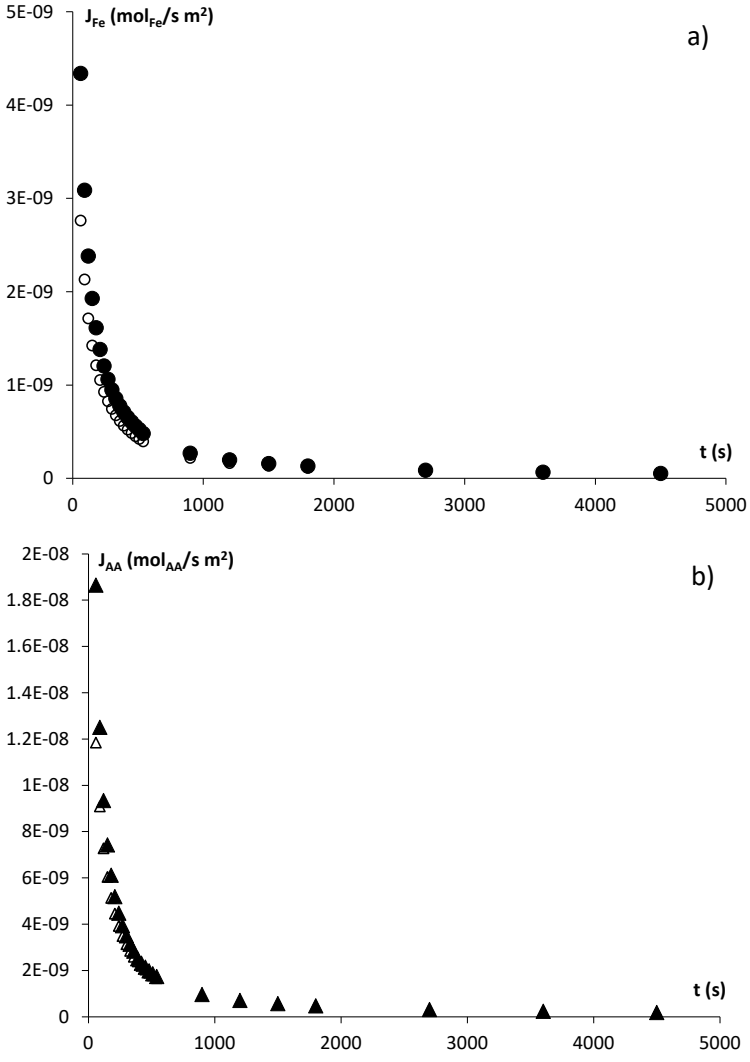

Figure 4.4.11. (a) Evolution of iron release flux (J_{Fe})and (b) Evolution of ascorbic acid release flux (J_{AA}). Where (●) is iron ion released at pH of 3; (○) is iron ion released at pH of 4.7; (▲) is ascorbic acid released at pH of 3 and (Δ) is ascorbic acid released at pH of 4.7. Notation is according to IuPAC.

The engine that produces the release of active compounds is the chemical potential gradient at the bead–liquid phase interface. Within the chemical potential, there are chemical or mechanical gradients that will affect

mass transport. The main engines for the active compound transport are the gradient concentration of the chemical species and the pressure variation induced by the bead swelling, therefore, the gradient of the chemical potential of each active compound may be defined by the Gibbs–Duhem expression as (Castro-Giraldez, Fito and Fito, 2010):

$$\Delta\mu_i = RT\ ln\frac{c_i^{LP}}{c_i^{B}} + v_i \cdot \Delta P \tag{4.4.3}$$

where $\Delta\mu_i$ is the chemical potential of each active compound, R is the ideal gas constant (8.314 J/mol K), T is the temperature (K), c_i is the molar concentration (mol_i/m^3), v_i is the specific volume of i and ΔP is the pressure gradient between bead and LP.

The relationship between the molar flux and the chemical potential is defined by the first Onsager reciprocity relation, according to the following equation (Gambár and Márkus, 1993):

$$J_i = L_i \cdot \Delta\mu_i \tag{4.4.4}$$

where L_i is the phenomenological coefficient expressed in $mol^2/J\ s\ m^2$. This phenomenological coefficient describes the ability of a chemical species to transport itself through a medium. From the mass flux and the chemical potential, it is possible to calculate the phenomenological coefficient. However, with the experimental data obtained, it is only possible to calculate the term of concentrations of the chemical potential, as shown in Equation 4.4.5.

$$\Delta\mu_i^* = RT\ ln\frac{c_i^{LP}}{c_i^B} \tag{4.4.5}$$

where $\Delta\mu_i^*$ is the chemical potential of each active compound, considering only the concentration term.

In Figure 4.4.12, the chemical potential is shown without the mechanical term; however, it is possible to assume that when the swelling of the capsule is negligible, the mechanical term will be as well.

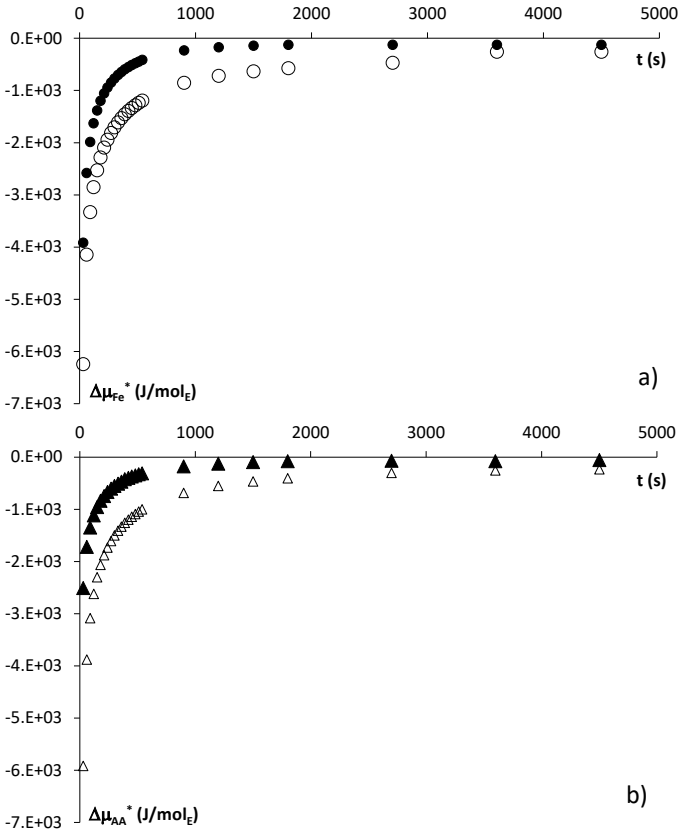

Figure 4.4.12. (a) Gradient of partial iron chemical potential and (b) gradient of partial ascorbic acid chemical potential in the bead–liquid phase interface. Where (●) is iron ion released at pH of 3; (○) is iron ion released at pH of 4.7; (▲) is ascorbic acid released at pH of 3 and (Δ) is ascorbic acid released at pH of 4.7. Notation is according to IuPAC.

Considering the mechanical term negligible when the bead swelling is negligible, it is possible to calculate the phenomenological coefficient for each type of bead. The result from this is $5.6 \pm 0.7 \cdot 10^{-10}$ mol^2/J s m^2 for iron ion at pH 3, $2.0 \pm 0.3 \cdot 10^{-10}$ mol^2/J s m^2 for iron ion at pH 4.7, $3.7 \pm 0.3 \cdot 10^{-10}$ mol^2/J s m^2 for ascorbic acid at pH 3 and $9.8 \pm 0.8 \cdot 10^{-10}$ mol^2/J s m^2 for ascorbic acid at pH 4.7.

Using these phenomenological coefficients, it is possible to obtain the gradients of the chemical potential during the entire release process, and with it and using Equation 4.4.3, the mechanical term can be obtained.

Figure 4.4.13 a and b shows the evolution of the mechanical term throughout the active compound release process. This mechanical term is induced by the swelling of the beads. This phenomenon occurs since, in their preparation, the beads undergo a dehydration process, which generates a drastic shrinkage and vitrification that causes storage of mechanical energy, which can only be released when hydrated again, changing to a rubbery state, and recovering its native elasticity.

The mechanical term causes a flux of external liquid phase to enter, and slows the transport of active compound to the outside of beads.

This phenomenon is observed in Figure 4.4.13 c and d, where the mechanical term is compared with bead swelling. It is possible to observe that both evolve together and stop at the same time, the moment where they reach the maximum swelling. Moreover, these figures show that the mechanical terms are higher in the iron beads, although the ascorbic acid beads have more swelling, this may be due to the fact that the iron ions have a greater

ionic strength, which will affect the formation of the beads and which are based on ionic gelation.

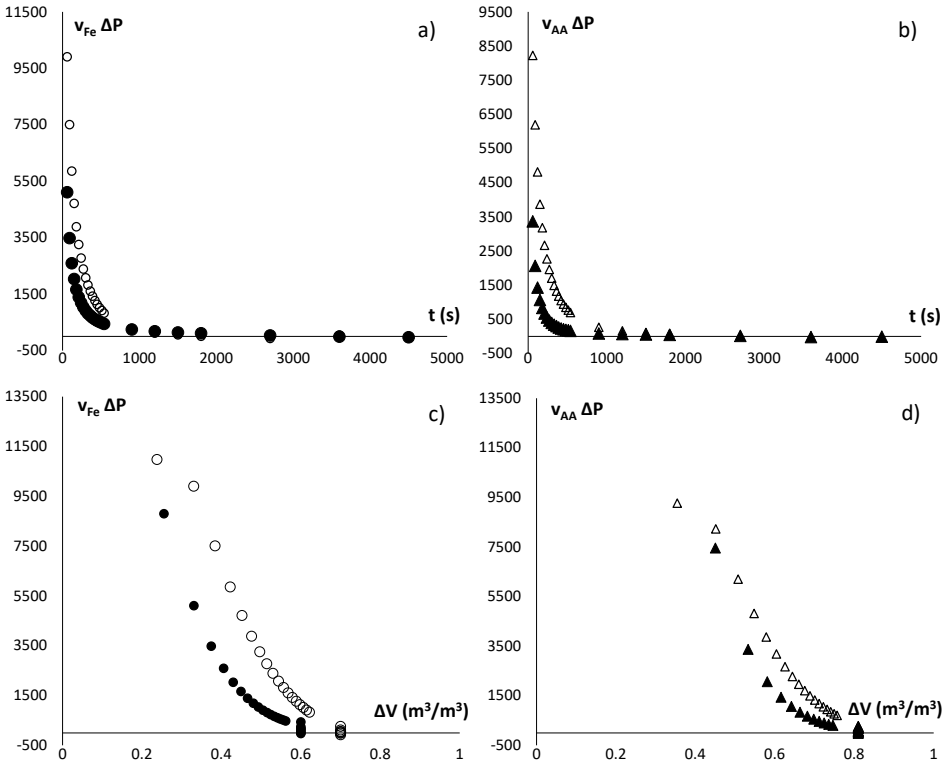

Figure 4.4.13. (**a**) and (b) represents the evolution of the mechanical gradient of (a) the iron ion beads and (b) the ascorbic acid beads at 3 and 4.7 pH; (b) and (c) is the relationship between the mechanical gradient and volume variation of (c) the iron ion beads and (d) the ascorbic acid beads at 3 and 4.7 pH. Where (●) is iron ion released at pH of 3; (○) is iron ion released at pH of 4.7; (▲) is ascorbic acid released at pH of 3 and (Δ) is ascorbic acid released at pH of 4.7.

4. Conclusions

A system for measuring the release of microencapsulated active compounds was developed from impedance measurements in the radio

frequency range. This system was tested with calcium alginate beads encapsulating iron ions and ascorbic acid as active compounds.

The prediction and measurement potential of this sensor was improved by developing a thermodynamic model that allows quantifying kinetic design parameters such as the phenomenological coefficient.

The sensor was tested in an aqueous liquid medium in the pH range in which digestive media are found in the stomach phase, in order to determine interferences in impedance measurements in the radio frequency range, showing great precision in the measurements and no interference with the medium. However, an effect of pH was observed on the swelling processes of the beads, possibly induced by ion–ion relationships in the gel matrix of calcium alginate.

The phenomenological coefficients obtained are in the same range of values, for iron ($2–5.6 \cdot 10^{-10}$ $mol^2/J\ s\ m^2$) and ascorbic acid ($3.7–9.8 \cdot 10^{-10}$ $mol^2/J\ s\ m^2$), showing adequate encapsulation design, since it will release a similar proportion of iron and ascorbic acid, which will act as an antioxidant, maintaining the reduced state of iron and, therefore, facilitating its absorption.

5. Acknowledgments

The authors acknowledge the financial support from the Spanish Agencia Estatal de Investigación, Proyectos de I+D+I, Programas Estatales de Generación de Conocimiento y Fortalecimiento Científico y Tecnológico del Sistema de I+D+i y de I+D+i Orientada a los Retos de la Sociedad, del

Plan Estatal de Investigación Científica y Técnica y de Innovación 2017-2020, with the reference PID2020-116816RB-I00. Juan Ángel Tomás-Egea wants to thank the FPI Predoctoral Program of the Universitat Politècnica de València for its support.

6. References

Aguirre-Calvo, T.R. *et al.* (2020) 'Effect of in vitro digestion-fermentation of Ca(II)-alginate beads containing sugar and biopolymers over global antioxidant response and short chain fatty acids production', *Food Chemistry*, 333, p. 127483. doi:10.1016/j.foodchem.2020.127483.

Aguirre-Calvo, T.R., Busch, V.M. and Santagapita, P.R. (2017) 'Stability and release of an encapsulated solvent-free lycopene extract in alginate-based beads', *LWT*, 77, pp. 406–412. doi:10.1016/j.lwt.2016.11.074.

Anderson, G.J., Frazer, D.M. and McLaren, G.D. (2009) 'Iron absorption and metabolism', *Current Opinion in Gastroenterology*, 25(2), pp. 129–135. doi:10.1097/MOG.0b013e32831ef1f7.

Apoorva, A. *et al.* (2020) 'Novel pH-sensitive alginate hydrogel delivery system reinforced with gum tragacanth for intestinal targeting of nutraceuticals', *International Journal of Biological Macromolecules*, 147, pp. 675–687. doi:10.1016/j.ijbiomac.2020.01.027.

Berezovskiy, Y.M., Korolev, I. and Sarantsev, T.A. (2020) 'Calculation of heat capacity in meat during its freezing considering phase change', *Theory and practice of meat processing*, 5(1), pp. 22–26. doi:10.21323/2414-438X-2020-5-1-22-26.

Brunton, N.P. *et al.* (2006) 'The use of dielectric properties and other physical analyses for assessing protein denaturation in beef biceps femoris muscle during cooking from 5 to 85°C', *Meat Science*, 72(2), pp. 236–244. doi:10.1016/j.meatsci.2005.07.007.

Castro-Giraldez, M. *et al.* (2010) 'Low-frequency dielectric spectrum to determine pork meat quality', *Innovative Food Science & Emerging Technologies*, 11(2), pp. 376–386. doi:10.1016/j.ifset.2010.01.011.

Castro-Giraldez, M. *et al.* (2014) 'Thermodynamic approach of meat freezing process', *Innovative Food Science & Emerging Technologies*, 23, pp. 138–145. doi:10.1016/j.ifset.2014.03.007.

Castro-Giraldez, M., Fito, P.J. and Fito, P. (2010) 'Non-equilibrium thermodynamic approach to analyze the pork meat (Longissimus dorsi) salting process', *Journal of Food Engineering*, 99(1), pp. 24–30. doi:10.1016/j.jfoodeng.2010.01.023.

Charles, C.V. (2012) 'Iron deficiency anemia: a public health problem of global proportions', *Public health–methodology, environmental and systems*, (2012), p. 109.

Colinet, I. *et al.* (2009) 'New amphiphilic and pH-sensitive hydrogel for controlled release of a model poorly water-soluble drug', *European Journal of Pharmaceutics and Biopharmaceutics*, 73(3), pp. 345–350. doi:10.1016/j.ejpb.2009.07.008.

Criado, P. *et al.* (2019) 'Effect of cellulose nanocrystals on thyme essential oil release from alginate beads: study of antimicrobial activity against Listeria innocua and ground meat shelf life in combination with gamma irradiation', *Cellulose*, 26(9), pp. 5247–5265. doi:10.1007/s10570-019-02481-2.

Cuibus, L. *et al.* (2014) 'Application of infrared thermography and dielectric spectroscopy for controlling freezing process of raw potato', *Innovative Food Science & Emerging Technologies*, 24, pp. 80–87. doi:10.1016/j.ifset.2013.11.007.

De Benoist, B. *et al.* (2008) 'Worldwide prevalence of anaemia 1993-2005; WHO global database of anaemia'.

Deladino, L. *et al.* (2008) 'Encapsulation of natural antioxidants extracted from Ilex paraguariensis', *Carbohydrate Polymers*, 71(1), pp. 126–134. doi:10.1016/j.carbpol.2007.05.030.

Durán, E. *et al.* (2017) 'Encapsulación de hierro: Otra estrategia para la prevención o tratamiento de la anemia por deficiencia de hierro', *Revista chilena de nutrición*, 44(3), pp. 234–243.

Estevinho, B.N. *et al.* (2013) 'Microencapsulation with chitosan by spray drying for industry applications – A review', *Trends in Food Science & Technology*, 31(2), pp. 138–155. doi:10.1016/j.tifs.2013.04.001.

Gambár, K. and Márkus, F. (1993) 'On the global symmetry of Thermodynamics and Onsager's reciprocity relations', 18(1), pp. 51–58. doi:10.1515/jnet.1993.18.1.51.

Gholamian, S., Nourani, M. and Bakhshi, N. (2021) 'Formation and characterization of calcium alginate hydrogel beads filled with cumin seeds essential oil', *Food Chemistry*, 338, p. 128143. doi:10.1016/j.foodchem.2020.128143.

Hellmuth, O., Schmelzer, J.W.P. and Feistel, R. (2020) 'Ice-Crystal Nucleation in Water: Thermodynamic Driving Force and Surface Tension. Part I: Theoretical Foundation', *Entropy*, 22(1), p. 50. doi:10.3390/e22010050.

Hoseyni, S.Z. *et al.* (2021) 'Release of catechin from Azivash gum-polyvinyl alcohol electrospun nanofibers in simulated food and digestion media', *Food Hydrocolloids*, 112, p. 106366. doi:10.1016/j.foodhyd.2020.106366.

Liakos, I. *et al.* (2013) 'Controlled antiseptic release by alginate polymer films and beads', *Carbohydrate Polymers*, 92(1), pp. 176–183. doi:10.1016/j.carbpol.2012.09.034.

Miere, F. *et al.* (2019) 'Natural Polymeric Beads for Encapsulation of Stellaria media Extract with Antioxidant Properties', *Materiale plastice*, 56(4), pp. 671–679.

Moschona, A. and Liakopoulou-Kyriakides, M. (2018) 'Encapsulation of biological active phenolic compounds extracted from wine wastes in alginate-chitosan microbeads', *Journal of Microencapsulation*, 35(3), pp. 229–240. doi:10.1080/02652048.2018.1462415.

Najafi-Soulari, S., Shekarchizadeh, H. and Kadivar, M. (2016) 'Encapsulation optimization of lemon balm antioxidants in calcium alginate hydrogels', *Journal of Biomaterials Science, Polymer Edition*, 27(16), pp. 1631–1644. doi:10.1080/09205063.2016.1226042.

Orozco-Villafuerte, J. *et al.* (2019) 'Evaluation of the protection and release rate of bougainvillea (Bougainvillea spectabilis) extracts encapsulated in alginate beads', *Journal of Dispersion Science and Technology*, 40(7), pp. 1065–1074. doi:10.1080/01932691.2018.1496834.

Rahman, M.S. and Labuza, T.P. (2020) 'Water activity and food preservation', in *Handbook of food preservation*. Boca Raton, USA: CRC Press, pp. 487–506.

Roos, Y.H. (2021) 'Glass Transition and Re-Crystallization Phenomena of Frozen Materials and Their Effect on Frozen Food Quality', *Foods*, 10(2), p. 447. doi:10.3390/foods10020447.

Santagapita, P.R., Mazzobre, M.F. and Buera, M.P. (2011) 'Formulation and Drying of Alginate Beads for Controlled Release and Stabilization of Invertase', *Biomacromolecules*, 12(9), pp. 3147–3155. doi:10.1021/bm2009075.

Santagapita, P.R., Mazzobre, M.F. and Buera, M.P. (2012) 'Invertase stability in alginate beads: Effect of trehalose and chitosan inclusion and of drying methods', *Food Research International*, 47(2), pp. 321–330. doi:10.1016/j.foodres.2011.07.042.

Schmelzer, J.W.P. *et al.* (2018) 'Kauzmann paradox and the crystallization of glass-forming melts', *Journal of Non-Crystalline Solids*, 501, pp. 21–35. doi:10.1016/j.jnoncrysol.2017.11.045.

Sermini, C.G., Acevedo, M.J. and Arredondo, M. (2017) 'Biomarkers of Metabolism and Iron Nutrition', *Revista peruana de medicina experimental y salud publica*, 34(4), pp. 690–698. doi:10.17843/rpmesp.2017.344.3182.

Shang, L., Guo, W. and Nelson, S.O. (2015) 'Apple Variety Identification Based on Dielectric Spectra and Chemometric Methods', *Food Analytical Methods*, 8(4), pp. 1042–1052. doi:10.1007/s12161-014-9985-5.

Sharp, P. and Srai, S.K. (2007) 'Molecular mechanisms involved in intestinal iron absorption', *World journal of gastroenterology: WJG*, 13(35), p. 4716.

Talens, C., Castro-Giraldez, M. and Fito, P.J. (2016) 'A thermodynamic model for hot air microwave drying of orange peel', *Journal of Food Engineering*, 175, pp. 33–42. doi:10.1016/j.jfoodeng.2015.12.001.

Tomas-Egea, J.A. *et al.* (2021) 'Hot Air and Microwave Combined Drying of Potato Monitored by Infrared Thermography', *Applied Sciences*, 11(4), p. 1730. doi:10.3390/app11041730.

Tomas-Egea, J.A., Fito, P.J. and Castro-Giraldez, M. (2019) 'Analysis of Apple Candying by Microwave Spectroscopy', *Foods*, 8(8), p. 316. doi:10.3390/foods8080316.

Trabelsi, S., Roelvink, J. and Russell, R.B. (2014) 'Investigating the Influence of Aging on Radiofrequency Dielectric Properties of Chicken Meat', *Journal of Microwave Power and Electromagnetic Energy*, 48(4), pp. 215–220. doi:10.1080/08327823.2014.11689885.

Traffano-Schiffo, M.V., Aguirre Calvo, T.R., *et al.* (2017) 'Alginate Beads Containing Lactase: Stability and Microstructure', *Biomacromolecules*, 18(6), pp. 1785–1792. doi:10.1021/acs.biomac.7b00202.

Traffano-Schiffo, M.V., Castro-Giraldez, M., Colom, R.J., *et al.* (2017) 'Development of a Spectrophotometric System to Detect White Striping Physiopathy in Whole Chicken Carcasses', *Sensors*, 17(5), p. 1024. doi:10.3390/s17051024.

Traffano-Schiffo, M.V., Castro-Giraldez, M., Fito, P.J., *et al.* (2017) 'Encapsulation of lactase in Ca(II)-alginate beads: Effect of stabilizers and drying methods', *Food Research International*, 100, pp. 296–303. doi:10.1016/j.foodres.2017.07.020.

Traffano-Schiffo, M.V., Castro-Giraldez, M., Herrero, V., *et al.* (2018) 'Development of a non-destructive detection system of Deep Pectoral Myopathy in poultry by dielectric spectroscopy', *Journal of Food Engineering*, 237, pp. 137–145. doi:10.1016/j.jfoodeng.2018.05.023.

Traffano-Schiffo, M.V., Castro-Giraldez, M., Fito, P.J., *et al.* (2018) 'Gums induced microstructure stability in Ca(II)-alginate beads containing lactase analyzed by SAXS', *Carbohydrate Polymers*, 179, pp. 402–407. doi:10.1016/j.carbpol.2017.09.096.

Traffano-Schiffo, M.V., Castro-Giraldez, M., Colom, R.J., *et al.* (2018a) 'Innovative photonic system in radiofrequency and microwave range to determine chicken meat quality', *Journal of Food Engineering*, 239, pp. 1–7. doi:10.1016/j.jfoodeng.2018.06.029.

Traffano-Schiffo, M.V., Castro-Giraldez, M., Colom, R.J., *et al.* (2018b) 'New Spectrophotometric System to Segregate Tissues in Mandarin Fruit', *Food and Bioprocess Technology*, 11(2), pp. 399–406. doi:10.1007/s11947-017-2019-8.

Traffano-Schiffo, M.V. *et al.* (2021) 'New methodology to analyze the dielectric properties in radiofrequency and microwave ranges in chicken meat during postmortem time', *Journal of Food Engineering*, 292, p. 110350. doi:10.1016/j.jfoodeng.2020.110350.

Tu, J. *et al.* (2005) 'Alginate microparticles prepared by spray–coagulation method: Preparation, drug loading and release characterization', *International Journal of Pharmaceutics*, 303(1), pp. 171–181. doi:10.1016/j.ijpharm.2005.07.008.

Velázquez-Varela, J. *et al.* (2018) 'Study of the cheese salting process by dielectric properties at microwave frequencies', *Journal of Food Engineering*, 224, pp. 121–128. doi:10.1016/j.jfoodeng.2017.12.024.

Zhang, L., Lyng, J.G. and Brunton, N.P. (2007) 'The effect of fat, water and salt on the thermal and dielectric properties of meat batter and its temperature following microwave or radio frequency heating', *Journal of Food Engineering*, 80(1), pp. 142–151. doi:10.1016/j.jfoodeng.2006.05.016.

Conclusiones

Potato drying using HAD combined with microwaves

It is possible to apply FTIR to a HAD-MW combined drying process using an oven grill door with a mesh size that allows the hot air and photon radiation in the infrared spectrum to cross it, but not the photons in the microwave spectrum. As a result, the evolution of the drying process can be determined through the surface temperature of the sample.

It is shown that the higher effect of microwaves in the drying process occurs at moistures above the drying critical moisture, where the water molecules reduce their mobility and hinder the induction phenomena.

In a combined drying process of hot air and microwaves at temperatures lower than spontaneous evaporation and in samples with a characteristic dimension less than the microwave penetration depth, it is possible to conclude that the convection heating is mostly transformed into surface water evaporation, with negligible thermal conduction from the surface. Furthermore, microwave radiation is mostly transformed into an increase in the internal energy of the food, that is, an increase in the internal temperature, from the centre to the surface.

Chicken breast freezing

The critical temperatures of the food freezing process, initial freezing temperature, the freezing temperature of sample with the maximally freeze-concentrated solute matrix or the glass transition temperature of the maximally freeze-concentrated solute matrix of chicken breast have been determined by means of calorimetry techniques, being similar than those of other authors. Moreover, these temperatures were determined using

photospectrometry in radiofrequency range, showing that this technique is fast, reliable, and easy to implement in a dynamic freezing system.

Apple candying

The use of specific frequencies of the dielectric properties in γ-dispersion did not allow us to correctly analyse the mobility of water and it makes it necessary to determine the dielectric properties at the relaxation frequency. It was demonstrated that the dielectric constant (at relaxation frequency) was linearly related to the water activity and not to the moisture, it means that it was affected by water mobility and therefore by the structure. In addition, it was possible to determine sucrose supersaturation processes by analysing the relaxation frequency, which depends on the deformation of the water molecule. Therefore, it was demonstrated that the use of dielectric properties in γ-dispersion at relaxation frequency allowed us not only to monitor the OD and HAD processes of the apple candying, but also to predict the supersaturation state of the liquid phase until vitrification.

Release kinetics of microencapsulated compounds

A system for measuring the release of microencapsulated active compounds was developed from impedance measurements in the radio frequency range. This system was tested with calcium alginate beads encapsulating iron ions and ascorbic acid as active compounds.

The prediction and measurement potential of this sensor was improved by developing a thermodynamic model that allows quantifying kinetic design parameters such as the phenomenological coefficient.

The sensor was tested in an aqueous liquid medium in the pH range in which digestive media are found in the stomach phase, in order to determine interferences in impedance measurements in the radio frequency range, showing great precision in the measurements and no interference with the medium. However, an effect of pH was observed on the swelling processes of the beads, possibly induced by ion–ion relationships in the gel matrix of calcium alginate.

The phenomenological coefficients obtained are in the same range of values, for iron ($2–5.6 \cdot 10^{-10}$ $mol^2/J\ s\ m^2$) and ascorbic acid ($3.7–9.8 \cdot 10^{-10}$ $mol^2/J\ s\ m^2$), showing adequate encapsulation design, since it will release a similar proportion of iron and ascorbic acid, which will act as an antioxidant, maintaining the reduced state of iron and, therefore, facilitating its absorption.

Bibliografía

Agre, P., Bonhivers, M. and Borgnia, M.J. (1998) 'The Aquaporins, Blueprints for Cellular Plumbing Systems', *Journal of Biological Chemistry*, 273(24), pp. 14659–14662. doi:10.1074/jbc.273.24.14659.

Ahmad, R.S., Imran, A. and Hussain, M.B. (2018) *Nutritional Composition of Meat*, *Meat Science and Nutrition*. IntechOpen. doi:10.5772/intechopen.77045.

Ahmed, I., Qazi, I.M. and Jamal, S. (2016) 'Developments in osmotic dehydration technique for the preservation of fruits and vegetables', *Innovative Food Science & Emerging Technologies*, 34, pp. 29–43. doi:10.1016/j.ifset.2016.01.003.

Ahmed, J., Thomas, L. and Khashawi, R. (2020) 'Influence of hot-air drying and freeze-drying on functional, rheological, structural and dielectric properties of green banana flour and dispersions', *Food Hydrocolloids*, 99, p. 105331. doi:10.1016/j.foodhyd.2019.105331.

Al-Obaidi, M.A., Kara-Zaitri, C. and Mujtaba, I.M. (2017) 'Scope and limitations of the irreversible thermodynamics and the solution diffusion models for the separation of binary and multi-component systems in reverse osmosis process', *Computers & Chemical Engineering*, 100, pp. 48–79. doi:10.1016/j.compchemeng.2017.02.001.

Amin, B. *et al.* (2019) 'A review of the dielectric properties of the bone for low frequency medical technologies', *Biomedical Physics & Engineering Express*, 5(2), p. 022001. doi:10.1088/2057-1976/aaf210.

Anderson, G.J., Frazer, D.M. and McLaren, G.D. (2009) 'Iron absorption and metabolism', *Current Opinion in Gastroenterology*, 25(2), pp. 129–135. doi:10.1097/MOG.0b013e32831ef1f7.

Apoorva, A. *et al.* (2020) 'Novel pH-sensitive alginate hydrogel delivery system reinforced with gum tragacanth for intestinal targeting of nutraceuticals', *International Journal of Biological Macromolecules*, 147, pp. 675–687. doi:10.1016/j.ijbiomac.2020.01.027.

Ashtiani, S.-H.M., Sturm, B. and Nasirahmadi, A. (2018) 'Effects of hot-air and hybrid hot air-microwave drying on drying kinetics and textural quality of nectarine slices', *Heat and Mass Transfer*, 54(4), pp. 915–927. doi:https://doi.org/10.1007/s00231-017-2187-0.

Auksornsri, T. *et al.* (2018) 'Dielectric properties of rice model food systems relevant to microwave sterilization process', *Innovative Food Science & Emerging Technologies*, 45, pp. 98–105. doi:10.1016/j.ifset.2017.09.002.

Aviara, N.A. and Ajibola, O.O. (2002) 'Thermodynamics of moisture sorption in melon seed and cassava', *Journal of Food Engineering*, 55(2), pp. 107–113. doi:10.1016/S0260-8774(02)00023-7.

Baranowski, P. *et al.* (2012) 'Detection of early bruises in apples using hyperspectral data and thermal imaging', *Journal of Food Engineering*, 110(3), pp. 345–355. doi:10.1016/j.jfoodeng.2011.12.038.

Barrón-Hoyos, J.M. *et al.* (2013) 'Protein Quality Evaluation of Animal Food Proteins by In-Vitro Methodologies', 2013. doi:10.4236/fns.2013.44048.

Bertram, H.C., Purslow, P.P. and Andersen, H.J. (2002) 'Relationship between Meat Structure, Water Mobility, and Distribution: A Low-Field Nuclear Magnetic Resonance Study', *Journal of Agricultural and Food Chemistry*, 50(4), pp. 824–829. doi:10.1021/jf010738f.

Bhalekar, A.A. and Andresen, B. (2017) 'Thermodynamic stability of irreversible processes. A Gibbs-Duhem type theory and the fourth law of thermodynamics', *F. Kongoli, A. Buhl, T. Turna, M. Mauntz, W. Williams, J. Rubinstein, PL Fuhr, M. Morales-Rodriguez (eds.)*, pp. 109–122.

Bozkir, H. *et al.* (2019) 'Influence of ultrasound and osmotic dehydration pretreatments on drying and quality properties of persimmon fruit', *Ultrasonics Sonochemistry*, 54, pp. 135–141. doi:10.1016/j.ultsonch.2019.02.006.

Brunton, N.P. *et al.* (2006) 'The use of dielectric properties and other physical analyses for assessing protein denaturation in beef biceps femoris muscle during cooking from 5 to 85°C', *Meat Science*, 72(2), pp. 236–244. doi:10.1016/j.meatsci.2005.07.007.

Calvo-Schwarzwälder, M. (2019) 'A Non-local Formulation of the One-Phase Stefan Problem Based on Extended Irreversible Thermodynamics', in Korobeinikov, A. *et al.* (eds) *Extended Abstracts Spring 2018*. Cham: Springer International Publishing (Trends in Mathematics), pp. 225–229. doi:10.1007/978-3-030-25261-8_33.

Campbell, N.A. and Reece, J.B. (2008) *Transparency acetates for Biology*. San Francisco, EE. UU.: Benjamin Cummings, Pearson Education. Available at: https://www.pearson.com/uk/educators/higher-education-educators/product/Campbell-Transparency-Acetates-for-Biology-8th-Edition/9780321523280.html (Accessed: 12 August 2021).

Castro-Giraldez, M., Fito, P.J., Chenoll, C., *et al.* (2010) 'Development of a dielectric spectroscopy technique for the determination of apple (Granny Smith) maturity',

Innovative Food Science & Emerging Technologies, 11(4), pp. 749–754. doi:10.1016/j.ifset.2010.08.002.

Castro-Giraldez, M., Botella, P., *et al.* (2010) 'Low-frequency dielectric spectrum to determine pork meat quality', *Innovative Food Science & Emerging Technologies*, 11(2), pp. 376–386. doi:10.1016/j.ifset.2010.01.011.

Castro-Giraldez, M., Fito, P.J., Toldrá, F., *et al.* (2010) 'Physical sensors for quality control during processing', in *Handbook of Meat Processing*. Wiley-Blackwell Publishing USA, pp. 443–456.

Castro-Giraldez, M., Tylewicz, U., *et al.* (2011) 'Analysis of chemical and structural changes in kiwifruit (Actinidia deliciosa cv Hayward) through the osmotic dehydration', *Journal of Food Engineering*, 105(4), pp. 599–608. doi:10.1016/j.jfoodeng.2011.03.029.

Castro-Giraldez, M., Fito, P.J., *et al.* (2011) 'Application of microwaves dielectric spectroscopy for controlling osmotic dehydration of kiwifruit (Actinidia deliciosa cv Hayward)', *Innovative Food Science & Emerging Technologies*, 12(4), pp. 623–627. doi:10.1016/j.ifset.2011.06.013.

Castro-Giraldez, M., Dols, L., *et al.* (2011) 'Development of a dielectric spectroscopy technique for the determination of key biochemical markers of meat quality', *Food Chemistry*, 127(1), pp. 228–233. doi:10.1016/j.foodchem.2010.12.089.

Castro-Giraldez, M. *et al.* (2012) 'Study of the puffing process of amaranth seeds by dielectric spectroscopy', *Journal of Food Engineering*, 110(2), pp. 298–304. doi:10.1016/j.jfoodeng.2011.04.012.

Castro-Giraldez, M. *et al.* (2013) 'Study of pomegranate ripening by dielectric spectroscopy', *Postharvest Biology and Technology*, 86, pp. 346–353. doi:10.1016/j.postharvbio.2013.07.024.

Castro-Giraldez, M. *et al.* (2014) 'Thermodynamic approach of meat freezing process', *Innovative Food Science & Emerging Technologies*, 23, pp. 138–145. doi:10.1016/j.ifset.2014.03.007.

Castro-Giraldez, M., Fito, P.J. and Fito, P. (2010a) 'Application of microwaves dielectric spectroscopy for controlling pork meat (Longissimus dorsi) salting process', *Journal of Food Engineering*, 97(4), pp. 484–490. doi:10.1016/j.jfoodeng.2009.11.005.

Castro-Giraldez, M., Fito, P.J. and Fito, P. (2010b) 'Non-equilibrium thermodynamic approach to analyze the pork meat (Longissimus dorsi) salting process', *Journal of Food Engineering*, 99(1), pp. 24–30. doi:10.1016/j.jfoodeng.2010.01.023.

Charles, C.V. (2012) 'Iron deficiency anemia: a public health problem of global proportions', *Public health–methodology, environmental and systems*, (2012), p. 109.

Chen, C. and Qin, H. (2019) 'A Mathematical Modeling of the Reverse Osmosis Concentration Process of a Glucose Solution', *Processes*, 7(5), p. 271. doi:10.3390/pr7050271.

Churio, O., Pizarro, F. and Valenzuela, C. (2018) 'Preparation and characterization of iron-alginate beads with some types of iron used in supplementation and fortification strategies', *Food Hydrocolloids*, 74, pp. 1–10. doi:10.1016/j.foodhyd.2017.07.020.

Ciampa, F. *et al.* (2018) 'Recent Advances in Active Infrared Thermography for Non-Destructive Testing of Aerospace Components', *Sensors*, 18(2), p. 609. doi:10.3390/s18020609.

Colinet, I. *et al.* (2009) 'New amphiphilic and pH-sensitive hydrogel for controlled release of a model poorly water-soluble drug', *European Journal of Pharmaceutics and Biopharmaceutics*, 73(3), pp. 345–350. doi:10.1016/j.ejpb.2009.07.008.

Colucci, D., Maniaci, R. and Fissore, D. (2019) 'Monitoring of the freezing stage in a freeze-drying process using IR thermography', *International Journal of Pharmaceutics*, 566, pp. 488–499. doi:10.1016/j.ijpharm.2019.06.005.

Cook, M.T. *et al.* (2012) 'Microencapsulation of probiotics for gastrointestinal delivery', *Journal of Controlled Release*, 162(1), pp. 56–67. doi:10.1016/j.jconrel.2012.06.003.

Costa, N. *et al.* (2007) 'The use of thermography on the slaughter-line for the assessment of pork and raw ham quality', *Italian journal of animal science*, 6(sup1), pp. 704–706. doi:https://doi.org/10.4081/ijas.2007.1s.704.

Criado, P. *et al.* (2019) 'Effect of cellulose nanocrystals on thyme essential oil release from alginate beads: study of antimicrobial activity against Listeria innocua and ground meat shelf life in combination with gamma irradiation', *Cellulose*, 26(9), pp. 5247–5265. doi:10.1007/s10570-019-02481-2.

Cuibus, L. *et al.* (2014) 'Application of infrared thermography and dielectric spectroscopy for controlling freezing process of raw potato', *Innovative Food Science & Emerging Technologies*, 24, pp. 80–87. doi:10.1016/j.ifset.2013.11.007.

De Benoist, B. *et al.* (2008) 'Worldwide prevalence of anaemia 1993-2005; WHO global database of anaemia'.

Dean, D.A. *et al.* (2008) 'Electrical Impedance Spectroscopy Study of Biological Tissues', *Journal of electrostatics*, 66(3–4), pp. 165–177. doi:10.1016/j.elstat.2007.11.005.

Dehghannya, J. *et al.* (2019) 'Ultrasound-assisted intensification of a hybrid intermittent microwave - hot air drying process of potato: Quality aspects and energy consumption', *Ultrasonics*, 96, pp. 104–122. doi:10.1016/j.ultras.2019.02.005.

Dehghannya, J., Bozorghi, S. and Heshmati, M.K. (2018) 'Low temperature hot air drying of potato cubes subjected to osmotic dehydration and intermittent microwave: drying kinetics, energy consumption and product quality indexes', *Heat and Mass Transfer*, 54(4), pp. 929–954. doi:10.1007/s00231-017-2202-5.

Dehghannya, J., Hosseinlar, S.-H. and Heshmati, M.K. (2018) 'Multi-stage continuous and intermittent microwave drying of quince fruit coupled with osmotic dehydration and low temperature hot air drying', *Innovative Food Science & Emerging Technologies*, 45, pp. 132–151. doi:10.1016/j.ifset.2017.10.007.

Demirel, Y. and Gerbaud, V. (2019a) 'Fundamentals of Equilibrium Thermodynamics', in Demirel, Y. and Gerbaud, V. (eds) *Nonequilibrium Thermodynamics (Fourth Edition)*. Elsevier, pp. 1–85. doi:10.1016/B978-0-444-64112-0.00001-0.

Demirel, Y. and Gerbaud, V. (2019b) 'Fundamentals of Nonequilibrium Thermodynamics', in Demirel, Y. and Gerbaud, V. (eds) *Nonequilibrium Thermodynamics (Fourth Edition)*. Elsevier, pp. 135–186. doi:10.1016/B978-0-444-64112-0.00003-4.

Ertbjerg, P. and Puolanne, E. (2017) 'Muscle structure, sarcomere length and influences on meat quality: A review', *Meat Science*, 132, pp. 139–152. doi:10.1016/j.meatsci.2017.04.261.

Fang, Y. *et al.* (2007) 'Multiple Steps and Critical Behaviors of the Binding of Calcium to Alginate', *The Journal of Physical Chemistry B*, 111(10), pp. 2456–2462. doi:10.1021/jp0689870.

Ferreira, D.S. (2020) 'Thermal imaging as a tool in food analysis', *Journal of Spectral Imaging*, 9. doi:10.1255/jsi.2020.a7.

Fito, P. *et al.* (2007) 'Advanced food process engineering to model real foods and processes: The "SAFES" methodology', *Journal of Food Engineering*, 83(2), pp. 173–185. doi:10.1016/j.jfoodeng.2007.02.017.

Fito, P. *et al.* (2008) 'Advanced Food Products & Process Engineering (SAFES) I: Concepts & Methodology', in Gutiérrez-López, G. *et al.* (eds) *Food Engineering: Integrated Approaches*. New York, NY: Springer (Food Engineering series), pp. 117–137. doi:10.1007/978-0-387-75430-7_7.

Fito, P.J. *et al.* (2020) *Balances de materia y energía en ingenieria de bioprocesos*. Editorial Universitat Politècnica de València. Available at: http://hdl.handle.net/10251/151115.

Gabriel, C. and Peyman, A. (2018) 'Dielectric Properties of Biological Tissues; Variation With Age', in Ram, J.L. and Conn, P.M. (eds) *Conn's Handbook of Models for Human Aging (Second Edition)*. Academic Press, pp. 939–952. doi:10.1016/B978-0-12-811353-0.00069-5.

Gandomi, H. *et al.* (2016) 'Effect of chitosan-alginate encapsulation with inulin on survival of Lactobacillus rhamnosus GG during apple juice storage and under simulated gastrointestinal conditions', *LWT - Food Science and Technology*, 69, pp. 365–371. doi:10.1016/j.lwt.2016.01.064.

Gan-Mor, S. *et al.* (2011) 'Adapted thermal imaging for the development of postharvest precision steam-disinfection technology for carrots', *Postharvest Biology and Technology*, 59(3), pp. 265–271. doi:https://doi.org/10.1016/j.postharvbio.2010.10.003.

Gaussorgues, G. and Chomet, S. (1993) *Infrared thermography*. Springer Science & Business Media.

Gholamian, S., Nourani, M. and Bakhshi, N. (2021) 'Formation and characterization of calcium alginate hydrogel beads filled with cumin seeds essential oil', *Food Chemistry*, 338, p. 128143. doi:10.1016/j.foodchem.2020.128143.

Glowacz, A. (2021) 'Fault diagnosis of electric impact drills using thermal imaging', *Measurement*, 171, p. 108815. doi:10.1016/j.measurement.2020.108815.

Godfray, H.C.J. *et al.* (2018) 'Meat consumption, health, and the environment', *Science*, 361(6399). doi:10.1126/science.aam5324.

Gonçalves, B.J. *et al.* (2016) 'Using infrared thermography to evaluate the injuries of cold-stored guava', *Journal of Food Science and Technology*, 53(2), pp. 1063–1070. doi:10.1007/s13197-015-2141-4.

Gowen, A.A. *et al.* (2010) 'Applications of thermal imaging in food quality and safety assessment', *Trends in food science & technology*, 21(4), pp. 190–200. doi:https://doi.org/10.1016/j.tifs.2009.12.002.

Green, D.W. and Southard, M.Z. (2019) *Perry's chemical engineers' handbook*. McGraw-Hill Education.

Guil Guerrero, J.L. (2001) *Bioquímica y tecnología de la carne*. Almería, (Tc0534).

Gutiérrez, J.D. *et al.* (2017) 'Dynamic measurement of dielectric properties of food snack pellets during microwave expansion', *Journal of Food Engineering*, 202, pp. 1–8. doi:10.1016/j.jfoodeng.2017.01.021.

Hamm, R. (1972) 'Kolloidchemie des Fleisches'. Available at: https://agris.fao.org/agris-search/search.do?recordID=US201300476178 (Accessed: 10 July 2021).

Hawton, M. (2019) 'Maxwell quantum mechanics', *Physical Review A*, 100(1), p. 012122. doi:10.1103/PhysRevA.100.012122.

Hellmuth, O., Schmelzer, J.W.P. and Feistel, R. (2020) 'Ice-Crystal Nucleation in Water: Thermodynamic Driving Force and Surface Tension. Part I: Theoretical Foundation', *Entropy*, 22(1), p. 50. doi:10.3390/e22010050.

Hernandez-Gomez, E.-S. *et al.* (2021) 'Dielectric properties of Mexican sauces for microwave-assisted pasteurization process', *Journal of Food Science*, 86(1), pp. 112–119.

Herrera, L. (2017) 'The Gibbs paradox, the Landauer principle and the irreversibility associated with tilted observers', *Entropy*, 19(3), p. 110.

Horowitz, W. (2000) *Moisture in dried fruits. Method 934.06*, *Official Methods of Analysis of AOAC International,*. Association of Official Analytical Chemists International.

Hoseyni, S.Z. *et al.* (2021) 'Release of catechin from Azivash gum-polyvinyl alcohol electrospun nanofibers in simulated food and digestion media', *Food Hydrocolloids*, 112, p. 106366. doi:10.1016/j.foodhyd.2020.106366.

Howell, J.R. *et al.* (2020) *Thermal radiation heat transfer*. CRC press.

Hudait, A. and Molinero, V. (2014) 'Ice Crystallization in Ultrafine Water–Salt Aerosols: Nucleation, Ice-Solution Equilibrium, and Internal Structure', *Journal of the American Chemical Society*, 136(22), pp. 8081–8093. doi:10.1021/ja503311r.

Huff Lonergan, E., Zhang, W. and Lonergan, S.M. (2010) 'Biochemistry of postmortem muscle — Lessons on mechanisms of meat tenderization', *Meat Science*, 86(1), pp. 184–195. doi:10.1016/j.meatsci.2010.05.004.

Huff-Lonergan, E. (2010) 'Chemistry and Biochemistry of Meat', in *Handbook of Meat Processing*. John Wiley & Sons, Ltd, pp. 3–24. doi:10.1002/9780813820897.ch1.

Hughes, J.M. *et al.* (2014) 'A structural approach to understanding the interactions between colour, water-holding capacity and tenderness', *Meat Science*, 98(3), pp. 520–532. doi:10.1016/j.meatsci.2014.05.022.

Içier, F. and Baysal, T. (2004) 'Dielectrical Properties of Food Materials—1: Factors Affecting and Industrial Uses', *Critical Reviews in Food Science and Nutrition*, 44(6), pp. 465–471. doi:10.1080/10408690490886692.

Ihara, S. *et al.* (2019) 'Nondestructive Evaluation of Wet Aged Beef by Novel Electrical Indexes: A Preliminary Study', *Foods*, 8(8), p. 313. doi:10.3390/foods8080313.

İlter, I. *et al.* (2018) 'Microwave and hot air drying of garlic puree: drying kinetics and quality characteristics', *Heat and Mass Transfer*, 54(7), pp. 2101–2112. doi:10.1007/s00231-018-2294-6.

Jaitovich, A.A. and Bertorello, A.M. (2006) 'Na+, K+-ATPase: An Indispensable Ion Pumping-Signaling Mechanism Across Mammalian Cell Membranes', *Seminars in Nephrology*, 26(5), pp. 386–392. doi:10.1016/j.semnephrol.2006.07.002.

James, C., Purnell, G. and James, S.J. (2015) 'A Review of Novel and Innovative Food Freezing Technologies', *Food and Bioprocess Technology*, 8(8), pp. 1616–1634. doi:10.1007/s11947-015-1542-8.

Jensen, J. *et al.* (2011) 'The Role of Skeletal Muscle Glycogen Breakdown for Regulation of Insulin Sensitivity by Exercise', *Frontiers in Physiology*, 2. doi:10.3389/fphys.2011.00112.

Kent, M. (2001) 'Microwave measurements of product variables', in *Instrumentation and sensors for the food industry*. Elsevier, pp. 233–279.

Kim, Hee-Jin *et al.* (2020) 'Comparison of the quality characteristics of chicken breast meat from conventional and animal welfare farms under refrigerated storage', *Poultry Science*, 99(3), pp. 1788–1796. doi:10.1016/j.psj.2019.12.009.

Kim, H.-W. *et al.* (2017) 'Probiotic supplementation and fast freezing to improve quality attributes and oxidation stability of frozen chicken breast muscle', *LWT*, 75, pp. 34–41. doi:10.1016/j.lwt.2016.08.035.

Kim, H.-W. *et al.* (2018) 'Effects of aging/freezing sequence and freezing rate on meat quality and oxidative stability of pork loins', *Meat Science*, 139, pp. 162–170. doi:10.1016/j.meatsci.2018.01.024.

Kita, A. (2002) 'The influence of potato chemical composition on crisp texture', *Food Chemistry*, 76(2), pp. 173–179. doi:10.1016/S0308-8146(01)00260-6.

Knorr, D. and Watzke, H. (2019) 'Food Processing at a Crossroad', *Frontiers in Nutrition*, 0. doi:10.3389/fnut.2019.00085.

Lee, K.Y. and Mooney, D.J. (2012) 'Alginate: Properties and biomedical applications', *Progress in Polymer Science*, 37(1), pp. 106–126. doi:10.1016/j.progpolymsci.2011.06.003.

Lewicki, P.P. (2006) 'Design of hot air drying for better foods', *Trends in Food Science & Technology*, 17(4), pp. 153–163. doi:10.1016/j.tifs.2005.10.012.

Li, D., Zhu, Z. and Sun, D.-W. (2018) 'Effects of freezing on cell structure of fresh cellular food materials: A review', *Trends in Food Science & Technology*, 75, pp. 46–55. doi:10.1016/j.tifs.2018.02.019.

Li, Y. *et al.* (2020) 'Radio-frequency dielectric relaxation behavior of selected vegetable tissues: Spectra analysis with logarithmic derivative method and simulation with double-shell model', *Journal of Food Engineering*, 277, p. 109914. doi:10.1016/j.jfoodeng.2020.109914.

Liakos, I. *et al.* (2013) 'Controlled antiseptic release by alginate polymer films and beads', *Carbohydrate Polymers*, 92(1), pp. 176–183. doi:10.1016/j.carbpol.2012.09.034.

Ling, B., Lyng, J.G. and Wang, S. (2018) 'Radio-frequency treatment for stabilization of wheat germ: Dielectric properties and heating uniformity', *Innovative Food Science & Emerging Technologies*, 48, pp. 66–74. doi:10.1016/j.ifset.2018.05.012.

Liu, J. *et al.* (2016) 'On the water-holding of myofibrils: Effect of sarcoplasmic protein denaturation', *Meat Science*, 119, pp. 32–40. doi:10.1016/j.meatsci.2016.04.020.

Liu, Y. *et al.* (2019) 'Drying characteristics, microstructure, glass transition temperature, and quality of ultrasound-strengthened hot air drying on pear slices', *Journal of Food Processing and Preservation*, 43(3), p. e13899. doi:10.1111/jfpp.13899.

Lucchi, E. (2018) 'Applications of the infrared thermography in the energy audit of buildings: A review', *Renewable and Sustainable Energy Reviews*, 82, pp. 3077–3090. doi:10.1016/j.rser.2017.10.031.

Lyng, J.G., Zhang, L. and Brunton, N.P. (2005) 'A survey of the dielectric properties of meats and ingredients used in meat product manufacture', *Meat Science*, 69(4), pp. 589–602. doi:10.1016/j.meatsci.2004.09.011.

Maraj, M. *et al.* (2019) 'Dielectric and Energy Storage Properties of Ba(1−x)CaxZryTi(1−y)O3 (BCZT): A Review', *Materials*, 12(21), p. 3641. doi:10.3390/ma12213641.

Martinoia, E. *et al.* (2018) 'The multifaceted roles of plant vacuoles'. Oxford University Press.

Martinoia, E., Massonneau, A. and Frangne, N. (2000) 'Transport Processes of Solutes across the Vacuolar Membrane of Higher Plants', *Plant and Cell Physiology*, 41(11), pp. 1175–1186. doi:10.1093/pcp/pcd059.

Masanes, L. and Oppenheim, J. (2017) 'A general derivation and quantification of the third law of thermodynamics', *Nature Communications*, 8(1), p. 14538. doi:10.1038/ncomms14538.

Maurel, C. and Chrispeels, M.J. (2001) 'Aquaporins. A Molecular Entry into Plant Water Relations', *Plant Physiology*, 125(1), pp. 135–138. doi:10.1104/pp.125.1.135.

Mello, P.A., Barin, J.S. and Guarnieri, R.A. (2014) 'Microwave Heating', in Flores, É.M. de M. (ed.) *Microwave-Assisted Sample Preparation for Trace Element Analysis*. Amsterdam: Elsevier, pp. 59–75. doi:10.1016/B978-0-444-59420-4.00002-7.

Meola, C., Boccardi, S. and Carlomagno, G. maria (2017a) 'Infrared Thermography Basics', in Meola, C., Boccardi, S., and Carlomagno, G. maria (eds) *Infrared Thermography in the Evaluation of Aerospace Composite Materials*. Woodhead Publishing, pp. 57–83. doi:10.1016/B978-1-78242-171-9.00003-6.

Meola, C., Boccardi, S. and Carlomagno, G. maria (2017b) 'Nondestructive Testing With Infrared Thermography', in Meola, C., Boccardi, S., and Carlomagno, G. maria (eds) *Infrared Thermography in the Evaluation of Aerospace Composite Materials*. Woodhead Publishing, pp. 85–125. doi:10.1016/B978-1-78242-171-9.00004-8.

Miere, F. *et al.* (2019) 'Natural Polymeric Beads for Encapsulation of Stellaria media Extract with Antioxidant Properties', *Materiale plastice*, 56(4), pp. 671–679.

Milford, A.B. *et al.* (2019) 'Drivers of meat consumption', *Appetite*, 141, p. 104313. doi:10.1016/j.appet.2019.06.005.

Mohos, F.Á. (2018) 'A new model of thermodynamics. Extension of chemical thermodynamics to complex materials of cellular structure', *Acta Alimentaria*, 47(3), pp. 267–282. doi:10.1556/066.2018.47.3.2.

Molina-Terriza, G., Torres, J.P. and Torner, L. (2007) 'Twisted photons', *Nature Physics*, 3(5), pp. 305–310. doi:10.1038/nphys607.

Möllmann, K.-P. *et al.* (2005) 'Selected critical applications for thermography: Convections in fluids, selective emitters and highly reflecting materials', in *In: InfraMation 2005: proceedings/sponsored and published by the Inframation Training Center.... Vol. 6, 161-174*, pp. 161–174.

Moraga, M.J. *et al.* (2009) 'Effect of vacuum impregnation with calcium lactate on the osmotic dehydration kinetics and quality of osmodehydrated grapefruit', *Journal of Food Engineering*, 90(3), pp. 372–379. doi:10.1016/j.jfoodeng.2008.07.007.

Moschona, A. and Liakopoulou-Kyriakides, M. (2018) 'Encapsulation of biological active phenolic compounds extracted from wine wastes in alginate-chitosan microbeads', *Journal of Microencapsulation*, 35(3), pp. 229–240. doi:10.1080/02652048.2018.1462415.

Mujumdar, A.S. (ed.) (2014) *Handbook of Industrial Drying*. 4th edn. Boca Raton: CRC Press. doi:10.1201/b17208.

Muñiz-Becerá, S., Méndez-Lagunas, L.L. and Rodríguez-Ramírez, J. (2017) 'Solute Transfer in Osmotic Dehydration of Vegetable Foods: A Review', *Journal of Food Science*, 82(10), pp. 2251–2259. doi:10.1111/1750-3841.13857.

Muñoz, I. *et al.* (2018) 'Dielectric properties of milk during ultra-heat treatment', *Journal of Food Engineering*, 219, pp. 137–146. doi:10.1016/j.jfoodeng.2017.09.025.

Najafi-Soulari, S., Shekarchizadeh, H. and Kadivar, M. (2016) 'Encapsulation optimization of lemon balm antioxidants in calcium alginate hydrogels', *Journal of Biomaterials Science, Polymer Edition*, 27(16), pp. 1631–1644. doi:10.1080/09205063.2016.1226042.

Navarrete, N.M. *et al.* (2003) 'Diseño y construcción de una instalación experimental para el estudio de la cinética de secado combinado por aire caliente y microondas', *Alimentación, equipos y tecnología*, 22(181), pp. 101–106.

Nelson, S.O. and Datta, A.K. (2001) 'Dielectric properties of food materials and electric field interactions', in *Handbook of microwave technology for food application*. CRC Press, pp. 93–138.

Nida, S., Moses, J.A. and Anandharamakrishnan, C. (2021) 'Isochoric Freezing and Its Emerging Applications in Food Preservation', *Food Engineering Reviews* [Preprint]. doi:10.1007/s12393-021-09284-x.

Offer, G. *et al.* (1989) 'The structural basis of the water-holding, appearance and toughness of meat and meat products', *Food structure*, 8(1), p. 17.

Onsager, L. (1931a) 'Reciprocal Relations in Irreversible Processes. I.', *Physical Review*, 37(4), pp. 405–426. doi:10.1103/PhysRev.37.405.

Onsager, L. (1931b) 'Reciprocal Relations in Irreversible Processes. II.', *Physical Review*, 38(12), pp. 2265–2279. doi:10.1103/PhysRev.38.2265.

Onwude, D.I. *et al.* (2019) 'The effectiveness of combined infrared and hot-air drying strategies for sweet potato', *Journal of Food Engineering*, 241, pp. 75–87. doi:10.1016/j.jfoodeng.2018.08.008.

Orozco-Villafuerte, J. *et al.* (2019) 'Evaluation of the protection and release rate of bougainvillea (Bougainvillea spectabilis) extracts encapsulated in alginate beads', *Journal of Dispersion Science and Technology*, 40(7), pp. 1065–1074. doi:10.1080/01932691.2018.1496834.

Osornio-Rios, R.A., Antonino-Daviu, J.A. and Romero-Troncoso, R. de J. (2019) 'Recent Industrial Applications of Infrared Thermography: A Review', *IEEE Transactions on Industrial Informatics*, 15(2), pp. 615–625. doi:10.1109/TII.2018.2884738.

Palacz, M. *et al.* (2021) 'Experimental analysis of freezing process of stationary food samples inside a hydrofluidisation freezing chamber', *International Journal of Refrigeration* [Preprint]. doi:10.1016/j.ijrefrig.2021.06.034.

Pereira, P.M. de C.C. and Vicente, A.F. dos R.B. (2013) 'Meat nutritional composition and nutritive role in the human diet', *Meat Science*, 93(3), pp. 586–592. doi:10.1016/j.meatsci.2012.09.018.

Phisut, N. (2012) 'Factors affecting mass transfer during osmotic dehydration of fruits', *International Food Research Journal*, 19(1), p. 7.

Prithani, R. and Dash, K.K. (2020) 'Mass transfer modelling in ultrasound assisted osmotic dehydration of kiwi fruit', *Innovative Food Science & Emerging Technologies*, 64, p. 102407. doi:10.1016/j.ifset.2020.102407.

Puolanne, E. and Halonen, M. (2010) 'Theoretical aspects of water-holding in meat', *Meat Science*, 86(1), pp. 151–165. doi:10.1016/j.meatsci.2010.04.038.

Putić, L. *et al.* (2021) 'A universal transportation model for reverse osmosis systems', *Computers & Chemical Engineering*, 148, p. 107264. doi:10.1016/j.compchemeng.2021.107264.

Rahman, M.S. and Labuza, T.P. (2020) 'Water activity and food preservation', in *Handbook of food preservation*. Boca Raton, USA: CRC Press, pp. 487–506.

Ramya, V. and Jain, N.K. (2017) 'A Review on Osmotic Dehydration of Fruits and Vegetables: An Integrated Approach', *Journal of Food Process Engineering*, 40(3), p. e12440. doi:10.1111/jfpe.12440.

Ratti, C. (2001) 'Hot air and freeze-drying of high-value foods: a review', *Journal of Food Engineering*, 49(4), pp. 311–319. doi:10.1016/S0260-8774(00)00228-4.

Regier, M., Knoerzer, K. and Schubert, H. (2016) *The microwave processing of foods*. Woodhead publishing.

Rockland, L.B. and Beuchat, L.R. (eds) (2020) *Water Activity: Theory and Applications to Food: Theory and Applications to Food*. Boca Raton: Routledge. doi:10.1201/9780203734148.

Roos, Y.H. (2021) 'Glass Transition and Re-Crystallization Phenomena of Frozen Materials and Their Effect on Frozen Food Quality', *Foods*, 10(2), p. 447. doi:10.3390/foods10020447.

Roudaut, G. *et al.* (2004) 'Molecular mobility around the glass transition temperature: a mini review', *Innovative Food Science & Emerging Technologies*, 5(2), pp. 127–134. doi:10.1016/j.ifset.2003.12.003.

Sanchez-Sabate, R. and Sabaté, J. (2019) 'Consumer Attitudes Towards Environmental Concerns of Meat Consumption: A Systematic Review', *International Journal of Environmental Research and Public Health*, 16(7), p. 1220. doi:10.3390/ijerph16071220.

Santagapita, P.R., Mazzobre, M.F. and Buera, M.P. (2011) 'Formulation and Drying of Alginate Beads for Controlled Release and Stabilization of Invertase', *Biomacromolecules*, 12(9), pp. 3147–3155. doi:10.1021/bm2009075.

Santagapita, P.R., Mazzobre, M.F. and Buera, M.P. (2012) 'Invertase stability in alginate beads: Effect of trehalose and chitosan inclusion and of drying methods', *Food Research International*, 47(2), pp. 321–330. doi:10.1016/j.foodres.2011.07.042.

Santos, G.T. *et al.* (2018) 'Irreversible thermodynamics analysis of ellipsoidal wheat kernel drying, aiming at the evaluation of phenomenological properties', *Drying Technology*, 36(9), pp. 1117–1127. doi:10.1080/07373937.2017.1386667.

Schmelzer, J.W.P. *et al.* (2018) 'Kauzmann paradox and the crystallization of glass-forming melts', *Journal of Non-Crystalline Solids*, 501, pp. 21–35. doi:10.1016/j.jnoncrysol.2017.11.045.

Self, J. *et al.* (2018) 'The Interplay between Salt Association and the Dielectric Properties of Low Permittivity Electrolytes: The Case of LiPF6 and LiAsF6 in Dimethyl Carbonate', *The Journal of Physical Chemistry C*, 122(4), pp. 1990–1994. doi:10.1021/acs.jpcc.7b11060.

Sermini, C.G., Acevedo, M.J. and Arredondo, M. (2017) 'Biomarkers of Metabolism and Iron Nutrition', *Revista peruana de medicina experimental y salud publica*, 34(4), pp. 690–698. doi:10.17843/rpmesp.2017.344.3182.

Sfarra, S. *et al.* (2020) 'Evaluating the freeze–thaw phenomenon in sandwich-structured composites via numerical simulations and infrared thermography', *Journal of Thermal Analysis and Calorimetry* [Preprint]. doi:10.1007/s10973-020-09985-1.

Shang, L., Guo, W. and Nelson, S.O. (2015) 'Apple Variety Identification Based on Dielectric Spectra and Chemometric Methods', *Food Analytical Methods*, 8(4), pp. 1042–1052. doi:10.1007/s12161-014-9985-5.

Sharp, P. and Srai, S.K. (2007) 'Molecular mechanisms involved in intestinal iron absorption', *World journal of gastroenterology: WJG*, 13(35), p. 4716.

Shete, Y.V. *et al.* (2018) 'Reviews on osmotic dehydration of fruits and vegetables', *Journal of Pharmacognosy and Phytochemistry*, 7(2), pp. 1964–1969.

Shiratake, K. and Martinoia, E. (2007) 'Transporters in fruit vacuoles', *Plant Biotechnology*, 24(1), pp. 127–133.

Shukla, T.P. and Anantheswaran, R.C. (2001) 'Ingredient interactions and product development for microwave heating', in *Handbook of Microwave Technology for Food Application*. CRC Press, pp. 387–428.

Soares de Melo, J.C. *et al.* (2020) 'Drying of Oblate Spheroidal Solids via Model Based on the Non-Equilibrium Thermodynamics', *Diffusion Foundations*, 25, pp. 83–98. doi:10.4028/www.scientific.net/DF.25.83.

Sonego, J.M. *et al.* (2016) 'Ca(II) and Ce(III) homogeneous alginate hydrogels from the parent alginic acid precursor: a structural study', *Dalton Transactions*, 45(24), pp. 10050–10057. doi:10.1039/C6DT00321D.

Song, Q. *et al.* (2020) 'Design of Capacitive Paddy Moisture Sensor Based on Electrical Impedance Spectroscopy Analysis', *Applied Sciences*, 10(11), p. 3968. doi:10.3390/app10113968.

Stegner, M., Schäfernolte, T. and Neuner, G. (2019) 'New Insights in Potato Leaf Freezing by Infrared Thermography', *Applied Sciences*, 9(5), p. 819. doi:10.3390/app9050819.

Taiz, L. *et al.* (2015) 'Plant physiology and development', *Plant physiology and development*. [Preprint], (Ed. 6). Available at: https://www.cabdirect.org/cabdirect/abstract/20173165866 (Accessed: 11 July 2021).

Talens, C., Castro-Giraldez, M. and Fito, P.J. (2016a) 'A thermodynamic model for hot air microwave drying of orange peel', *Journal of Food Engineering*, 175, pp. 33–42. doi:10.1016/j.jfoodeng.2015.12.001.

Talens, C., Castro-Giraldez, M. and Fito, P.J. (2016) 'A thermodynamic model for hot air microwave drying of orange peel', *Journal of Food Engineering*, 175, pp. 33–42. doi:http://dx.doi.org/10.1016/j.jfoodeng.2015.12.001.

Talens, C., Castro-Giraldez, M. and Fito, P.J. (2016b) 'Study of the effect of microwave power coupled with hot air drying on orange peel by dielectric spectroscopy', *LWT - Food Science and Technology*, 66, pp. 622–628. doi:10.1016/j.lwt.2015.11.015.

Talens, C., Castro-Giraldez, M. and Fito, P.J. (2018) 'Effect of microwave power coupled with hot air drying on sorption isotherms and microstructure of orange

peel', *Food and bioprocess technology*, 11(4), pp. 723–734. doi:https://doi.org/10.1007/s11947-017-2041-x.

Tanaka, M. and Sato, M. (2007) 'Microwave heating of water, ice, and saline solution: Molecular dynamics study', *The Journal of Chemical Physics*, 126(3), p. 034509. doi:10.1063/1.2403870.

Tasoniero, G. *et al.* (2020) 'Effect of spaghetti meat abnormality on broiler chicken breast meat composition and technological quality1', *Poultry Science*, 99(3), pp. 1724–1733. doi:10.1016/j.psj.2019.10.069.

Teseme, W.B. and Weldeselassie, H.W. (2020) 'Review on the Study of Dielectric Properties of Food Materials', *American Journal of Engineering and Technology Management*, 5(5), pp. 76–83.

Tomas-Egea, J.A. *et al.* (2021) 'Hot Air and Microwave Combined Drying of Potato Monitored by Infrared Thermography', *Applied Sciences*, 11(4), p. 1730. doi:10.3390/app11041730.

Tomas-Egea, J.A., Fito, P.J. and Castro-Giraldez, M. (2019) 'Analysis of Apple Candying by Microwave Spectroscopy', *Foods*, 8(8), p. 316. doi:10.3390/foods8080316.

Trabelsi, S., Roelvink, J. and Russell, R.B. (2014) 'Investigating the Influence of Aging on Radiofrequency Dielectric Properties of Chicken Meat', *Journal of Microwave Power and Electromagnetic Energy*, 48(4), pp. 215–220. doi:10.1080/08327823.2014.11689885.

Traffano-Schiffo, M.V. *et al.* (2014) 'Thermodynamic model of meat drying by infrarred thermography', *Journal of Food Engineering*, 128, pp. 103–110. doi:10.1016/j.jfoodeng.2013.12.024.

Traffano-Schiffo, M.V. *et al.* (2015) 'Study of the application of dielectric spectroscopy to predict the water activity of meat during drying process', *Journal of Food Engineering*, 166, pp. 285–290. doi:10.1016/j.jfoodeng.2015.06.030.

Traffano-Schiffo, M.V. *et al.* (2016) 'Effect of pulsed electric fields pre-treatment on mass transport during the osmotic dehydration of organic kiwifruit', *Innovative Food Science & Emerging Technologies*, 38, pp. 243–251. doi:10.1016/j.ifset.2016.10.011.

Traffano-Schiffo, M.V., Aguirre Calvo, T.R., *et al.* (2017) 'Alginate Beads Containing Lactase: Stability and Microstructure', *Biomacromolecules*, 18(6), pp. 1785–1792. doi:10.1021/acs.biomac.7b00202.

Traffano-Schiffo, M.V., Castro-Giraldez, M., Colom, R.J., *et al.* (2017) 'Development of a Spectrophotometric System to Detect White Striping Physiopathy in Whole Chicken Carcasses', *Sensors*, 17(5), p. 1024. doi:10.3390/s17051024.

Traffano-Schiffo, M.V., Castro-Giraldez, M., Fito, P.J., *et al.* (2017) 'Encapsulation of lactase in Ca(II)-alginate beads: Effect of stabilizers and drying methods', *Food Research International*, 100, pp. 296–303. doi:10.1016/j.foodres.2017.07.020.

Traffano-Schiffo, M.V., Castro-Giraldez, M., Herrero, V., *et al.* (2018) 'Development of a non-destructive detection system of Deep Pectoral Myopathy in poultry by dielectric spectroscopy', *Journal of Food Engineering*, 237, pp. 137–145. doi:10.1016/j.jfoodeng.2018.05.023.

Traffano-Schiffo, M.V., Castro-Giraldez, M., Colom, R.J., *et al.* (2018a) 'Innovative photonic system in radiofrequency and microwave range to determine chicken meat quality', *Journal of Food Engineering*, 239, pp. 1–7. doi:10.1016/j.jfoodeng.2018.06.029.

Traffano-Schiffo, M.V., Castro-Giraldez, M., Colom, R.J., *et al.* (2018b) 'New Spectrophotometric System to Segregate Tissues in Mandarin Fruit', *Food and Bioprocess Technology*, 11(2), pp. 399–406. doi:10.1007/s11947-017-2019-8.

Traffano-Schiffo, M.V. *et al.* (2021) 'New methodology to analyze the dielectric properties in radiofrequency and microwave ranges in chicken meat during postmortem time', *Journal of Food Engineering*, 292, p. 110350. doi:10.1016/j.jfoodeng.2020.110350.

Tu, J. *et al.* (2005) 'Alginate microparticles prepared by spray–coagulation method: Preparation, drug loading and release characterization', *International Journal of Pharmaceutics*, 303(1), pp. 171–181. doi:10.1016/j.ijpharm.2005.07.008.

Usamentiaga, R. *et al.* (2014) 'Infrared Thermography for Temperature Measurement and Non-Destructive Testing', *Sensors*, 14(7), pp. 12305–12348. doi:10.3390/s140712305.

Velázquez-Varela, J., Fito, P.J. and Castro-Giraldez, M. (2014) 'Thermodynamic analysis of salting cheese process', *Journal of Food Engineering*, 130, pp. 36–44. doi:10.1016/j.jfoodeng.2014.01.017.

Wahid, T.Z.A. (2018) 'Irreversible Thermodynamic of a New Model of the Collision Term of the Boltzmann Kinetic Equation Dealing with Gas Mixture affected by a Centrifugal Field', *arXiv preprint arXiv:1811.10887* [Preprint].

Wang, G.-B. and Zhang, X.-R. (2021) 'Thermodynamic evaluation of heat transfer heterogeneity: Comparative case studies on air cooling methods for postharvest apples', *Case Studies in Thermal Engineering*, 24, p. 100832. doi:10.1016/j.csite.2020.100832.

Wang, H. *et al.* (2017) 'Controlling of growth performance, lipid deposits and fatty acid composition of chicken meat through a probiotic, Lactobacillus johnsonii during subclinical Clostridium perfringens infection', *Lipids in Health and Disease*, 16(1), p. 38. doi:10.1186/s12944-017-0408-7.

Wang, Q. *et al.* (2019) 'Quality evaluation and drying kinetics of shitake mushrooms dried by hot air, infrared and intermittent microwave–assisted drying methods', *LWT*, 107, pp. 236–242. doi:https://doi.org/10.1016/j.lwt.2019.03.020.

Wang, X. *et al.* (2019) 'Effect of vacuum and ethanol pretreatment on infrared-hot air drying of scallion (Allium fistulosum)', *Food Chemistry*, 295, pp. 432–440. doi:10.1016/j.foodchem.2019.05.145.

Watanabe, F. (2007) 'Vitamin B12 Sources and Bioavailability', *Experimental Biology and Medicine*, 232(10), pp. 1266–1274. doi:10.3181/0703-MR-67.

Wei, S. *et al.* (2019) 'Simulation and experimental studies of heat and mass transfer in corn kernel during hot air drying', *Food and Bioproducts Processing*, 117, pp. 360–372. doi:10.1016/j.fbp.2019.08.006.

Williams, P. (2007) 'Nutritional composition of red meat', *Nutrition & Dietetics*, 64(s4), pp. S113–S119. doi:10.1111/j.1747-0080.2007.00197.x.

Wood, J.D. *et al.* (2008) 'Fat deposition, fatty acid composition and meat quality: A review', *Meat Science*, 78(4), pp. 343–358. doi:10.1016/j.meatsci.2007.07.019.

Xiong, S. *et al.* (2020) 'Thermodynamic analysis of CaO enhanced steam gasification process of food waste with high moisture and low moisture', *Energy*, 194, p. 116831. doi:10.1016/j.energy.2019.116831.

Xu, W. *et al.* (2018) 'Temperature gradient control during microwave combined with hot air drying', *Biosystems Engineering*, 169, pp. 175–187. doi:10.1016/j.biosystemseng.2018.02.013.

Yang, C. *et al.* (2021) 'Experimental investigation on rock mechanical properties and infrared radiation characteristics with freeze-thaw cycle treatment', *Cold Regions Science and Technology*, 183, p. 103232. doi:10.1016/j.coldregions.2021.103232.

You, Y., Kang, T. and Jun, S. (2021) 'Control of Ice Nucleation for Subzero Food Preservation', *Food Engineering Reviews*, 13(1), pp. 15–35. doi:10.1007/s12393-020-09211-6.

Zeeb, B. *et al.* (2015) 'Formation and characterization of filled hydrogel beads based on calcium alginate: Factors influencing nanoemulsion retention and release', *Food Hydrocolloids*, 50, pp. 27–36. doi:10.1016/j.foodhyd.2015.02.041.

Zeuthen, T. (2010) 'Water-Transporting Proteins', *Journal of Membrane Biology*, 234(2), pp. 57–73. doi:10.1007/s00232-009-9216-y.

Zhang, L., Lyng, J.G. and Brunton, N.P. (2007) 'The effect of fat, water and salt on the thermal and dielectric properties of meat batter and its temperature following microwave or radio frequency heating', *Journal of Food Engineering*, 80(1), pp. 142–151. doi:10.1016/j.jfoodeng.2006.05.016.

Zhang, P., Zhu, Z. and Sun, D.-W. (2018) 'Using power ultrasound to accelerate food freezing processes: Effects on freezing efficiency and food microstructure', *Critical Reviews in Food Science and Nutrition*, 58(16), pp. 2842–2853. doi:10.1080/10408398.2018.1482528.

Zhang, Y. and Ertbjerg, P. (2019) 'On the origin of thaw loss: Relationship between freezing rate and protein denaturation', *Food Chemistry*, 299, p. 125104. doi:10.1016/j.foodchem.2019.125104.

Zhang, Z. *et al.* (2016) 'Protein encapsulation in alginate hydrogel beads: Effect of pH on microgel stability, protein retention and protein release', *Food Hydrocolloids*, 58, pp. 308–315. doi:10.1016/j.foodhyd.2016.03.015.

Zhao, S. *et al.* (2020) 'Direct preparation of dialysate from tap water via osmotic dilution', *Journal of Membrane Science*, 598, p. 117659. doi:10.1016/j.memsci.2019.117659.

Zhou, X. *et al.* (2019) 'Combined radio frequency-vacuum and hot air drying of kiwifruits: Effect on drying uniformity, energy efficiency and product quality', *Innovative Food Science & Emerging Technologies*, 56, p. 102182. doi:10.1016/j.ifset.2019.102182.

Anexos

Artículos publicados en congresos internacionales

21st International Drying Symposium
IDS'2018

UNIVERSITAT POLITÈCNICA DE VALÈNCIA

Thermodynamic model of freeze-drying of poultry breast using infrared thermography

J.A. Tomas-Egea [1], M. Castro-Giraldez [1] and P.J. Fito [1]

[1] Instituto Universitario de Ingeniería de Alimentos para el Desarrollo, Universitat Politècnica de València, Camino de Vera s/n, 46022 Valencia, Spain

21st International Drying Symposium

https://doi.org/10.4995/IDS2018.2018.7756

Published: September 2018

Food dehydration is one of a main process to preserve meal. In order to optimize a freeze-drying operation a physic model is needed to well describe the thermodynamic behaviours involved in this process. In this work, a thermographic camera and different physicochemical determinations are used to monitor many phenomena that occur during the lyophilisation of poultry breast. Finally, a non-continuous irreversible thermodynamic model, based on thermal infrared measures and in shrinkage/swelling mechanism, has been developed, which explains the behaviours produced throughout the meat freeze-drying process.

Keywords: freeze-drying; thermodynamic model; infrared thermography; poultry.

Thermodynamic model of freeze-drying of poultry breast using infrared thermography

J.A. Tomas-Egea [1], M. Castro-Giraldez [1] and P.J. Fito [1]

[1] Instituto Universitario de Ingeniería de Alimentos para el Desarrollo, Universitat Politècnica de València, Camino de Vera s/n, 46022 Valencia, Spain

Abstract: Food dehydration is one of a main process to preserve meal. In order to optimize a freeze-drying operation a physic model is needed to well describe the thermodynamic behaviours involved in this process. In this work, a thermographic camera and different physicochemical determinations are used to monitor many phenomena that occur during the lyophilisation of poultry breast. Finally, a non-continuous irreversible thermodynamic model, based on thermal infrared measures and in shrinkage/swelling mechanism, has been developed, which explains the behaviours produced throughout the meat freeze-drying process.

Keywords: freeze-drying; thermodynamic model; infrared thermography; poultry.

1. Introduction

Lyophilisation is a drying process that consists in sublimate ice into vapour, producing water desorption, and one possibility can be to bring the product below the triple point (273.16 K and 611.73 Pa) of the water state diagram. This process gets very low water activities and does not heat the product, which is an advantage when thermolabile compounds are present (Ratti, 2001; Freire et al., 2014; Moses et al., 2014). Once the product has frozen below its eutectic point and generated vacuum, the product begins the elimination of water in two consecutive phases: sublimation and evaporation. When the frozen product reaches the vapour pressure, the freezing water fraction of the product is sublimated starting from the surface, creating a sublimation front that advances towards the centre. With the advance of the front, there is a zone that has sublimated the freezing water, but still has water adsorbed as liquid phase (Duan et al., 2016; Ramšak et al., 2017). The steam, coming from the front, causes a mechanical drag of the adsorbed water, which removes it and causes its desorption by evaporation.

Considering the importance of dehydration processes to conserve food, it is necessary to study them closely. For this, the process can be modelled with equations such as the Gibbs free energy, which can describe the thermodynamic behaviour of the food throughout the process. These equations have been used previously in orange peel (Talens, Castro-Giraldez and Fito, 2016) and pork meat (Traffano-Schiffo et al., 2014). The water transport it's also modelled in pork meat (Clemente et al., 2011) and tomato (Akanbi, Adeyemi and Ojo, 2006). Also, another freeze-dried products has been modelled like Strawberries (Hammami and René, 1997) or black currant

juice (Irzyniec, Klimczak and Michalowski, 1995) as well as generic mathematical models (Nakagawa and Ochiai, 2015).

Infrared thermography is a technique that allows to predict the temperature along a surface by receiving the flow of photons emitted by a body. Therefore, the possibility of monitoring the process with this technology gives us the ability to develop kinetic models of drying, thanks to the possibility of follow the temperature distribution over a surface, over a period of time (Vadivambal and Jayas, 2011).

The aim of this research is the development of a thermodynamic model of freeze-drying process of poultry meat using infrared thermography.

2. Materials and Methods

2.1. Experimental procedure

For the experimental phase, poultry breast samples (Pectoralis major) were used. Cylinders of 2 cm in diameter and 2 cm in height were obtained by a punch. The cutting of the cylinders was perpendicular to the fibres. Two cylinders were used for each lyophilisation and this operation was carried out in triplicate. The samples were frozen at -40 °C and introduced into the dry chamber of the lyophilizer, at a distance of 1.5 cm between them. During the lyophilisation, the temperature of the surface in one of the two chicken cylinders, as well as the reference material and the environment was controlled by type K thermocouples. In addition, the thermographic camera was introduced inside the lyophilizer for a continuous recording of the process.

In order to characterize the samples, this determinations were made before and after the lyophilisation: mass, water activity, humidity and volume. In addition, the density of frozen and lyophilized product was determined.

2.2. Physicochemical measurements

The mass of the samples was determined with a Mettler Toledo AB304-S balance, with an accuracy of ± 0.001 g. The humidity of the sample was obtained following the ISO 1442 (1997) standard for meat products, drying the samples at 110 ºC and atmospheric pressure for 48 hours until reach a constant mass. The water activity was determined with a dew point hygrometer Aqualab®, series 3 TE, with an accuracy of ± 0.003. The volume was determined by image analysis, using Adobe© Photoshop CS6 software. The density of frozen and lyophilized sample was determined by the pyknometer method. All measurements were made in triplicate.

2.3. Freeze drying operation

The thermographic camera was placed at 15 cm from the samples, with an angle of 0° and focusing the flat surface of the cylindrical samples. A reference material of known emissivity (ε = 0.95) (Optris GmbH, Berlin, Germany) was placed between both samples.

The control of the temperature during the lyophilisation, the inside, the reference material and the sample, was carried out with three K-type thermocouples, all of them connected to an Agilent 34901A multiplexer (Agilent Technologies, Malaysia); for the automatic recording of the measurements, the Agilent data acquisition equipment 34972A (Agilent Technologies, Malaysia) was used. The internal pressure control was carried out with the lyophilizer's own pressure sensor.

The lyophilizer used for the experimental was the Lioalfa-6 from Telstar, Germany. With a working pressure of 35 to 50 Pa and a cooling circuit at -45 ºC. All the cables and sensors necessary for the data collection were introduced in the dry chamber replacing the original stopper of the lyophilizer with one of rubber, and filled in with silicone to achieve the necessary vacuum.

2.4. Infrared measurements

The thermal images were acquired using the Optris PI 160 thermographic camera (Optris GmbH, Berlin, Germany). It uses a two-dimensional focal plane array with 160x120 pixels, a spectral range of 7.5 to 13 μm, a resolution of 0.05 °C and an accuracy of ± 2 %. The camera covers a temperature range of -20 to 900 °C. It has a field of vision of 23° x 17° with a minimum distance of 2 cm. The camera uses Optris PI Connect software (Optris GmbH, Berlin, Germany).

3. Results

The temperature values obtained from the thermographic camera are not real, therefore, the correction developed by Traffano-Schiffo (Traffano-Schiffo et al., 2014) was applied.

When the sublimation front advances, it alters the composition of the sample. The areas that have already been sublimated reduce their heat transmission because a loss of water, which causes a change in trend in the evolution of temperature with respect to time. Figure 8.1.1 shows this change in trend. So, the sublimation temperature and the process time can be extracted for each point of the sample's profile.

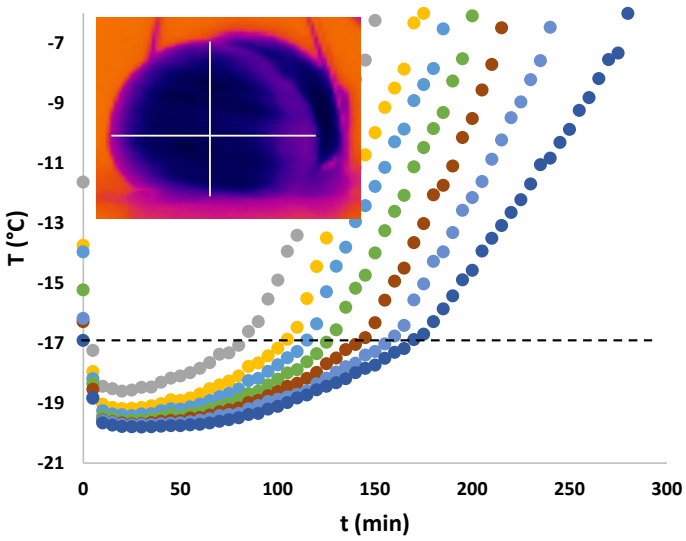

Figure 8.1.1. Evolution of the temperature for different points of the profile over time.

With the sublimation temperature it is possible to calculate the water activity (a_w) using the Fontan and Chirife equation (1981) (Equation 8.1.1).

$$-\ln(a_w) = 9.6934 \cdot 10^{-3} \cdot \Delta T_f + 4.761 \cdot 10^{-6} \cdot \Delta T_f^2 \qquad (8.1.1)$$

where: ΔT_f = difference between the initial freezing temperature and the sample (K).

From this a_w and the poultry sorption isotherm at low temperatures, it is possible to obtain the non-freezeable water fraction (x_w^{NF}) of the product at the sublimation time. The isotherm parameters modelled by Delgado and Sun (Delgado and Sun, 2002), by GAB are $x_{w0} = 11.009 - 0.4589T + 0.0116T^2$; $C = -3423.2 + 1144T - 77.248T^2 + 1.4357T^3$; $K = 0.9419 - 0.0034T + 0.0006T^2 - 0.00001T^3$. Subtracting to the overall water fraction, the non-freezeable water, it is possible to obtain the ice fraction.

Once the lyophilisation process has begun, sample can be divided in two volumetric areas: the sublimated zone (partially dehydrated) and frozen zone, separated by the sublimation front (Figure 8.1.2). When the frozen water sublimates, appears a vapour flux from the sublimation front to the surface, crossing the sublimated zone and evaporating a part of adsorbed water by mechanical dragging. Mass of each zone throughout the process has been estimated using the volume difference between cylinders and the density of freeze-dried and frozen product.

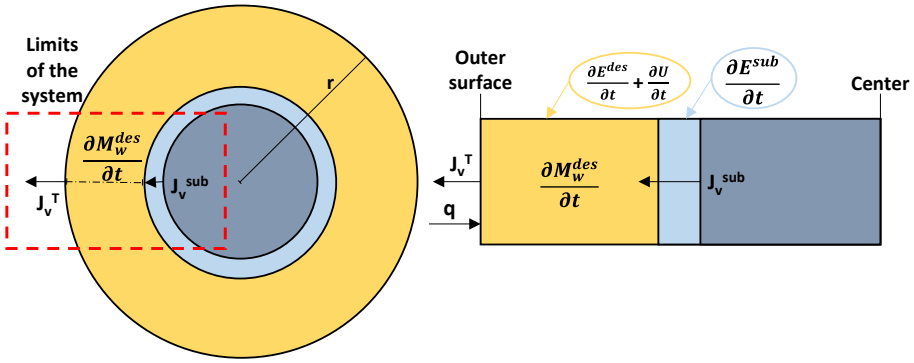

Figure 8.1.2. Diagram of the different zones and phenomena. Sublimated area; sublimation front; frozen zone. The limits of the system are highlighted in red, enlarged to the right with the molar and energy balances.

In order to obtain the different mechanism involved in the freeze-dry process, it is necessary to estimate the water flux, using a molar water balance in the sublimated zone (Equation 8.1.2).

$$J_v^T \cdot S_{ext} = J_v^{sub} \cdot S_{sub} + \frac{\partial M_w^{des}}{\partial t \cdot M_{rw}} \qquad (8.1.2)$$

When the vapour flux comes from the sublimation can be calculated as follows (Equation 8.1.3):

$$J_v^{sub} = \frac{x_w^f \cdot \rho_{wf} \cdot \Delta r}{\Delta t \cdot M_{rw}} \quad (8.1.3)$$

where: J_v^T = overall vapour flux leaving the system ($mol \cdot s^{-1} \cdot m^{-2}$); S_{ext} = external surface of the cylinder (m^2); J_v^{sub} = sublimated vapour flux ($mol \cdot s^{-1} \cdot m^{-2}$); S_{sub} = surface of the sublimation front (m^2); M_w^{des} = evaporated water mass (kg); t = process time (s); x_{wf} = freezed water mass fraction ($kg \cdot kg^{-1}$); ϱ_{wf} = density of frozen water ($kg \cdot m^{-3}$); M_{rw} = Molecular water mass (18 $g \cdot mol^{-1}$). The last term of mass balance represents the negative accumulation of adsorbed water molecules induced by mechanical drag of these molecules by the strong vapour streams produced in the sublimation front.

In order to continue determine the mechanism of water dehydration, the equation 8.1.4 that describes the free energy variation was applied (Castro-Giraldez, Fito and Fito, 2010).

$$dG = -SdT + VdP + Fdl + \psi de + \sum_i \mu_i \, dn_i \quad (8.1.4)$$

where: SdT = entropic term related to heat flux; VdP = mechanical energies related to the variation of pressure; Fdl = mechanical energies related to the elongation force (resistance of the tissue to expand); ψde = effect of the electric field induced by ions; $\sum_i \mu_i \, dn_i$ = summation of the chemical potentials of the species "i", with the rest of the variables state are constant.

When the variation of free energy is represented per mole of water, the extended water chemical potential is obtained (Equation 8.1.5).

$$\Delta \mu_w = \frac{\Delta G}{\Delta n_w} \quad (8.1.5)$$

where: $\Delta\mu_w$ = water chemical potential ($J \cdot mol^{-1}$); ΔG = Gibbs free energy variation (J); Δn_w = water moles (mol).

Combining the equations 8.1.4 and 8.1.5, the equation 8.1.6 is obtained, which describes the water chemical potential in the system described in Figure 8.1.2 (sublimated zone). In this equation, the last term is not included, because the desorption caused by the difference between water activities in the sample is negligible compared with the entropic term and those of mechanical energies. Moreover, ψde term also is negligible since the sample only presents native ions.

$$\Delta\mu_w^{des} = s_w \Delta T + v_w \Delta P + F_w dl \tag{8.1.6}$$

where: s_w = partial water molar entropy ($J \cdot K^{-1} \cdot mol^{-1}$); ΔT = gradient of temperature between surface and sublimation front (K); υ_w = partial water molar volume ($m^3 \cdot mol^{-1}$); ΔP = pressure variation (Pa); $F_w dl$ = elongation force (J). It is possible to estimate the entropic and the pressure term by using the sublimation temperature and its corresponded sublimation pressure obtained from Figure 8.1.2.

Applying the Onsager relations (Castro-Giraldez, Fito and Fito, 2010), the water molar flux is related to the water chemical potential, working as a driving force for water transport, through the phenomenological coefficient (Equation 8.1.7).

$$J_w^T = L_w \cdot \Delta\mu_w \tag{8.1.7}$$

where: J_w = water molar flux ($mol \cdot s^{-1} \cdot m^{-2}$); L_w = phenomenological coefficient ($mol^2 \cdot J^{-1} \cdot s^{-1} \cdot m^{-2}$); $\Delta\mu_w$ = water chemical potential ($J \cdot mol^{-1}$).

From the equation 8.1.7 it is possible to calculate the phenomenological coefficient after 200 min, where value remains constant because the sublimation front is reaching the centre and the swelling resistance of the tissue is negligible ($L_w = 1.14 \cdot 10^{-5}$ $mol^2J^{-1}s^{-1}m^{-2}$). Therefore, applying this value along the treatment it is possible to estimate the elongation term (Figure 8.1.3a). Using the expansion of the sublimated area, and estimating the ice space loosed in the sublimation it is possible to calculate the increment of the porosity ($\Delta\varepsilon$). Figure 8.1.3b shows the relation between the elongation term and the increment of the porosity, where it is possible to observe that the swelling process of tissue is proportional to the reduction of the elongation term, reducing the swelling resistance of the tissue reaching its maximum expansion in its minimum resistance.

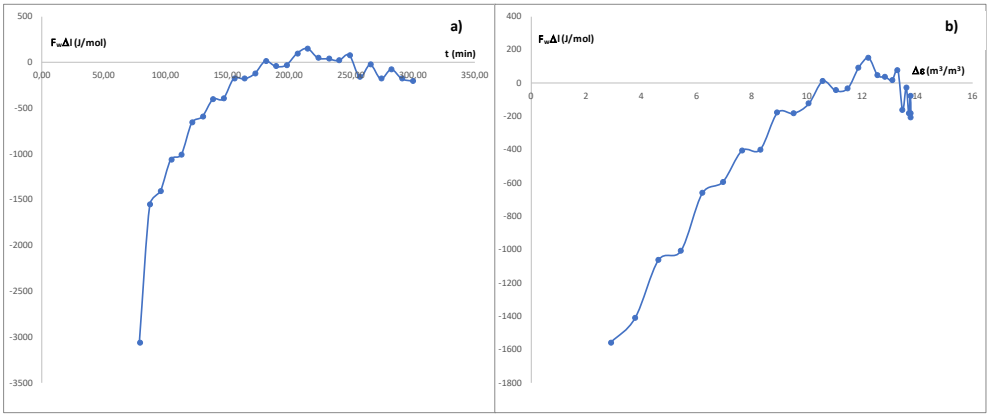

Figure 8.1.3. a) Elongation term vs process time; b) Elongation term vs increment of the porosity.

4. Conclusions

Has been developed a non-continuous irreversible thermodynamic model based in thermal infrared measures and in shrinkage/swelling mechanism that explains the behaviours produced throughout the meat freeze-drying process.

5. Acknowledgments

The authors acknowledge the financial support from: the Spanish Ministerio de Economía, Industria y Competitividad, Programa Estatal de I+D+i orientada a los Retos de la Sociedad AGL2016-80643-R, Agencia Estatal de Investigación (AEI) and Fondo Europeo de Desarrollo Regional (FEDER). Juan Ángel Tomás Egea wants to thank the FPI Predoctoral Program of the Universitat Politècnica de València for its support.

6. References

Akanbi, C.T., Adeyemi, R.S. and Ojo, A. (2006) 'Drying characteristics and sorption isotherm of tomato slices', *Journal of food engineering*, 73(2), pp. 157–163.

Castro-Giraldez, M., Fito, P.J. and Fito, P. (2010) 'Non-equilibrium thermodynamic approach to analyze the pork meat (Longissimus dorsi) salting process', *Journal of Food Engineering*, 99(1), pp. 24–30. doi:10.1016/j.jfoodeng.2010.01.023.

Clemente, G. *et al.* (2011) 'Drying modelling of defrosted pork meat under forced convection conditions', *Meat Science*, 88(3), pp. 374–378.

Delgado, A.E. and Sun, D.-W. (2002) 'Desorption isotherms and glass transition temperature for chicken meat', *Journal of food engineering*, 55(1), pp. 1–8.

Duan, X. *et al.* (2016) 'Technical aspects in freeze-drying of foods', *Drying Technology*, 34(11), pp. 1271–1285.

Freire, F.B. *et al.* (2014) 'Trends in modeling and sensing approaches for drying control', *Drying Technology*, 32(13), pp. 1524–1532.

Hammami, C. and René, F. (1997) 'Determination of freeze-drying process variables for strawberries', *Journal of food engineering*, 32(2), pp. 133–154.

Irzyniec, Z., Klimczak, J. and Michalowski, S. (1995) 'Freeze-drying of the black currant juice', *Drying technology*, 13(1–2), pp. 417–424.

Moses, J.A. *et al.* (2014) 'Novel drying techniques for the food industry', *Food Engineering Reviews*, 6(3), pp. 43–55.

Nakagawa, K. and Ochiai, T. (2015) 'A mathematical model of multi-dimensional freeze-drying for food products', *Journal of food engineering*, 161, pp. 55–67.

Ramšak, M. *et al.* (2017) 'Freeze-drying modeling of vial using BEM', *Engineering Analysis with Boundary Elements*, 77, pp. 145–156.

Ratti, C. (2001) 'Hot air and freeze-drying of high-value foods: a review', *Journal of Food Engineering*, 49(4), pp. 311–319. doi:10.1016/S0260-8774(00)00228-4.

Talens, C., Castro-Giraldez, M. and Fito, P.J. (2016) 'A thermodynamic model for hot air microwave drying of orange peel', *Journal of Food Engineering*, 175, pp. 33–42. doi:10.1016/j.jfoodeng.2015.12.001.

Traffano-Schiffo, M.V. *et al.* (2014) 'Thermodynamic model of meat drying by infrarred thermography', *Journal of Food Engineering*, 128, pp. 103–110. doi:10.1016/j.jfoodeng.2013.12.024.

Vadivambal, R. and Jayas, D.S. (2011) 'Applications of Thermal Imaging in Agriculture and Food Industry—A Review', *Food and Bioprocess Technology*, 4(2), pp. 186–199. doi:10.1007/s11947-010-0333-5.

21st International Drying Symposium
IDS'2018

UNIVERSITAT POLITÈCNICA DE VALÈNCIA

Study of the hot air drying process of chicken breast by non-invasive techniques

J.A. Tomas-Egea [1], M. Castro-Giraldez [1], R.J. Colom [2] and P.J. Fito [1]

[1] Instituto Universitario de Ingeniería de Alimentos para el Desarrollo, Universitat Politècnica de València, Camino de Vera s/n, 46022 Valencia, Spain
[2] Instituto de Instrumentación para Imagen Molecular, Universitat Politècnica de València, Camino de Vera s/n, 46022 Valencia, Spain

21st International Drying Symposium

https://doi.org/10.4995/IDS2018.2018.7733

Published: September 2018

Food drying is one of the main unit operations for food preservation and it is based on the difference of chemical potential between the product and a fluid with lower chemical potential. The objective of this work was the development of a thermodynamic model of chicken meat drying process using infrared thermography; also, the viability of using dielectric spectroscopy as a monitoring system was analysed. A thermodynamic model has been developed to predict the expansion/contraction phenomena of poultry meat throughout the drying process. Moreover, it was demonstrated that permittivity is a non-destructive method to monitor the evolution of drying process.

Keywords: poultry meat; hot air drying; permittivity; infrared; drying kinetics.

Study of the hot air drying process of chicken breast by non-invasive techniques

J.A. Tomas-Egea [1], M. Castro-Giraldez [1], R.J. Colom [2] and P.J. Fito [1]

[1] Instituto Universitario de Ingeniería de Alimentos para el Desarrollo, Universitat Politècnica de València, Camino de Vera s/n, 46022 Valencia, Spain

[2] Instituto de Instrumentación para Imagen Molecular, Universitat Politècnica de València, Camino de Vera s/n, 46022 Valencia, Spain

Abstract: Food drying is one of the main unit operations for food preservation and it is based on the difference of chemical potential between the product and a fluid with lower chemical potential. The objective of this work was the development of a thermodynamic model of chicken meat drying process using infrared thermography; also, the viability of using dielectric spectroscopy as a monitoring system was analysed. A thermodynamic model has been developed to predict the expansion/contraction phenomena of poultry meat throughout the drying process. Moreover, it was demonstrated that permittivity is a non-destructive method to monitor the evolution of drying process.

Keywords: poultry meat; hot air drying; permittivity; infrared; drying kinetics.

1. Introduction

Food drying is one of the main unit operations to preserve food (Ratti, 2001). The process is carried out by the difference of chemical potential between the product and a fluid (hot air) with lower chemical potential. Drying is based on three stages: induction period, period of constant drying speed and period of decreasing drying speed. During the first stage, the water transport occurs due to the difference of chemical potential between the food and the hot air, increasing the temperature of the surface. In the second stage, all the heat is used to evaporate the water, which comes from the inside faster than it evaporates from the surface, therefore, its temperature does not change. After this, the product is dried until the speed with which the water reaches the surface is less than the rate of evaporation and the heat received is used to evaporate the water as well as to heat the product.

Given the importance and extended use of hot air drying in the food industry, to model the behaviour of the sample that occurs during dehydration is very useful to optimize the industrial process. A similar thermodynamic model was already reported for hot air drying process of pork meat (Traffano-Schiffo et al., 2014). Several authors have modelled the water transport of other products like red pepper (Doymaz and Pala, 2002), salty pork meat (Gou, Comaposada and Arnau, 2002), apple (Wang et al., 2007) and sweet potato (Diamante and Munro, 1991).

The permittivity (ε) is the physical property that describes the interaction between a flux of photons and the medium through which photons circulate. Thus, the analysis of the electrical properties of a flux of

photons when it passes through a biological system allow determining the quantity and state of the chemical species of the system. Infrared thermography is a technique that provides information about the heat transfer in meat tissues (Workmaster, Palta and Wisniewski, 1999) and consists in the measurement of the infrared radiation emitted by a body surface getting an image of its thermal distribution. Thus, infrared thermography and the permittivity analysis, offer the possibility to analyse the process by a non-destructive way.

The objective of this work is the development of a thermodynamic model of the chicken meat drying process using infrared thermography; also the viability of using dielectric spectroscopy as a monitoring system is analysed.

2. Materials and Methods

2.1. Raw material

The experiments were carried out using boneless broiler breasts (Pectoralis major) obtained from a local supermarket. Cylinders of poultry breast were used for each analysis (2 cm of diameter and 1 cm of height); the cylinders were cut in perpendicular direction to the fibres.

2.2. Experimental procedure

Two samples were placed inside the hot air dryer. The drying operation was carried out, for a period of 67 hours, at a temperature of 40 °C and an air velocity of 1.5 $m \cdot s^{-1}$. One of the samples was hung from a Mettler Toledo PG503-S balance (precision of ± 0.01 g) in order to register the mass throughout the drying process. The other sample was placed on the right side

of the dryer on a grid. This sample allow controlling continuously the surface temperature. Moreover, two needle electrodes sensor was placed on this sample to measure the permittivity by continuous radiofrequency spectrophotometry. The flat face of both cylindrical samples was located in perpendicular to the drying air. A reference material of known emissivity (ε = 0.95 - Optris GmbH) was placed next to the samples. Also, the temperature of the drying air, sample, reference material and environment were measured with K-thermocouples connected to an Agilent multiplexer 34901A (Agilent Technologies, Malaysia) and registered by an Agilent Data Acquisition equipment 34972A (Agilent Technologies, Malaysia). After the drying treatment, the samples were kept in aqualab® disposable sample cups, sealed with parafilm® for further analysis.

Water activity, moisture and volume were measured in fresh samples and also in dried samples. Mass, permittivity and thermal images were registered continuously as was explained above.

2.3. Infrared measurements

The infrared analysis was carried out following the method described by Traffano-Schiffo (Traffano-Schiffo et al., 2014), using an infrared camera (Optris PI® 160 thermal imager, Optris GmbH, Berlin, Germany) installed in front of the sample, at an angle of 0º relative to the plane in which the samples were placed. The camera uses a two-dimensional Focal Plane array with 160x120 pixels, a spectral range of 7.5-13 μm, resolution of 0.05 °C and an accuracy of ± 2 %. The camera covers at a temperature range of -20 to 900 ° C. It has a field of vision of 23 ° x 17 ° with a minimum distance of 2 cm. The camera uses Optris PI Connect software (Optris GmbH, Berlin, Germany).

2.4. Radiofrequency measurements

The sensor used was developed by the Dielectric Properties Laboratory (Instituto Universitario de Ingeniería de Alimentos para el Desarrollo IIAD) and the Instituto de Instrumentación para Imagen Molecular (I3M) both belonging to the Universitat Politècnica de València (UPV), Valencia, Spain. It consists of two needle electrodes located on both sides of the cylindrical face of the sample. The sensor is connected to an Agilent 4294A impedance analyser. The measuring frequency range is from 40 Hz to 1 MHz and the calibration is performed in open and short-circuit.

2.5. Physicochemical measurements

Water activity was determined with a dew point hygrometer Aqualab®, series 3 TE, with an accuracy of ± 0.003. The mass of the samples was determined with a Mettler Toledo AB304-S balance, with an accuracy of ± 0.001 g. The volume was determined with Adobe© Photoshop CS6 software by image analysis. Moisture was obtained with the ISO 1442 (1997) standard for meat products, drying the samples at 110 ºC and atmospheric pressure until reaching a constant mass.

3. Results

The monitoring of the process with the thermographic camera need a correction in the temperature values, that was made by Traffano-Schiffo (Traffano-Schiffo et al., 2014).

With the evolution of the real temperature obtained by the camera and the physicochemical determinations, it is possible to apply irreversible thermodynamics to model the drying process, in order to analyse the

influence of the structure in the water transport during drying. For this purpose, the Gibbs free energy variation (Equation 8.1.1) (Castro-Giraldez, Fito and Fito, 2010) was applied in the system interface described in Figure 8.1.1.

$$dG = -SdT + VdP + Fdl + \psi de + \sum_i \mu_i \, dn_i \qquad (8.1.1)$$

where: SdT represents the entropic term related to heat fluxes; VdP represents the mechanical energies related to the variation of pressure; Fdl represents the mechanical energies related to the elongation force; and ψde represents the effect of the electric field induced by solved ions. The term $\sum_i \mu_i \, dn_i$ corresponds to the activity term and is the addition of the chemical potentials of the "i" component, being constant the rest of state variables.

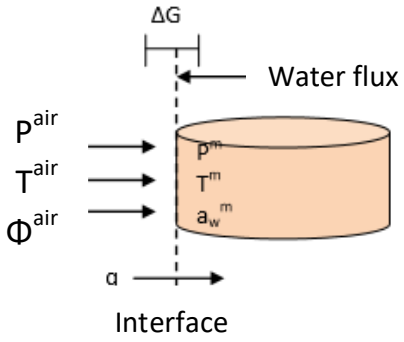

Figure 8.1.1. Diagram of the interface of the chicken sample during drying.

Considering the variation of free energy per mole of water, it is possible to define the extended chemical potential of water according to Equation 8.1.2.

$$\Delta\mu_w = \frac{\Delta G}{\Delta n_w} \quad (8.1.2)$$

where: $\Delta\mu_w$ = chemical potential of water ($J \cdot mol^{-1}$); ΔG = variation of Gibbs free energy (J); Δn_w = moles of water (mol).

Combining the last two equations, the equation 8.1.3 is obtained. The terms Fdl and ψde of Equation 8.1.1 could be neglected, since the muscle tissue is elastic and the meat only has native ions.

$$\Delta\mu_w = -s_w\,(T^{air} - T^m) + v_w\,(P^{air} - P^m) + RRT^m \ln\frac{a_w^m}{\varphi^{air}} \quad (8.1.3)$$

where: s_w = partial molar entropy of the water ($J \cdot K^{-1} \cdot mol^{-1}$); T = temperature (K); υ_w = partial molar volume of water ($m^3 \cdot mol^{-1}$); P = pressure (Pa); R = constant of ideal gases (8.314472 $J \cdot K^{-1} \cdot mol^{-1}$); a_w = water activity of sample; φ = relative ambient humidity. Being the superindexes: m = sample; air = air.

With the temperatures obtained by means of infrared thermography and the evolution of the moisture of the sample, estimated with the variation of mass during the process and the initial moisture, the entropic term can be calculated. For the activities term, a sorption isotherm of poultry was obtained and modelled by GAB (x^0_w = 0.077, C = 420, K = 0.98) (Figure 8.1.2). Finally, the term of mechanical energies of the equation 8.1.3 (second term) cannot be calculated, since the pressure variation of the sample cannot be measured.

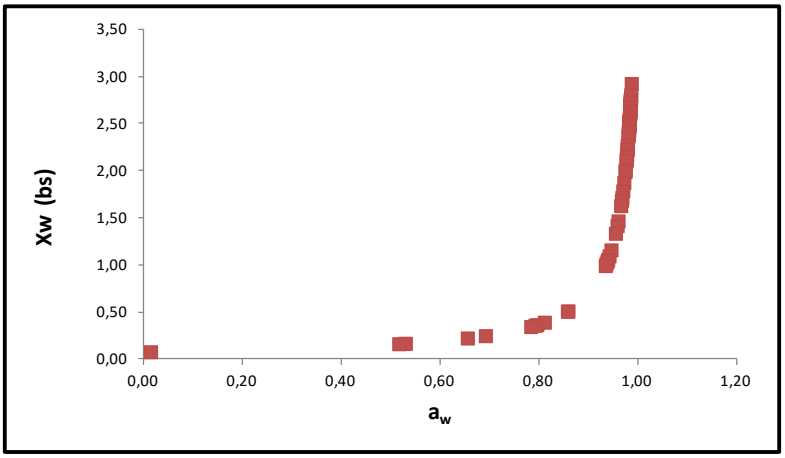

Figure 8.1.2. Poultry sorption isotherm.

According to Onsager's relations (Castro-Giraldez, Fito and Fito, 2010), the molar water flux is related to its chemical potential, which acts as a driving force for water transport, by means of the phenomenological coefficient (Equation 8.1.4). The phenomenological coefficient is constant in reversible processes, but if the storage of mechanical energy produces irreversible breaks in the medium, the phenomenological coefficient will evolve as a function of the transformation suffered by the tissue.

$$J_w = L_w \cdot \Delta\mu_w \tag{8.1.4}$$

where: J_w = molar flow of water ($mol \cdot s^{-1} \cdot m^{-2}$); L_w = phenomenological coefficient ($mol^2 \cdot J^{-1} \cdot s^{-1} \cdot m^{-2}$); $\Delta\mu_w$ = chemical potential of water ($J \cdot mol^{-1}$).

In order to obtain the phenomenological coefficient, water flux was estimated as follows (Equation 8.1.5):

$$J_w = \frac{\Delta M_w^m \cdot M_0^m}{\Delta t \cdot S^m \, Mr_w} \tag{8.1.5}$$

where: J_w = water flux (mol·s^{-1}·m^{-2}); ΔM^m_w = variation of water mass of the sample (kg); M^m_0= initial mass of the sample (kg); Δt = time of the process (s), S^m = surface of the sample (m^2); Mr_w = molecular mass of water (18 g·mol^{-1}).

As was explained above, it is not possible to calculate the mechanical term of the chemical potential, therefore the chemical potential of water was determined without considering the mechanical terms ($\Delta\mu^*_w$). With the water flux and the chemical potential of water was determined without considering the mechanical terms, the phenomenological coefficient was estimated (Equation 8.1.6).

$$L^*_w = \frac{J_w}{\Delta\mu^*_w} \tag{8.1.6}$$

In Figure 8.1.3 it can be appreciated that there is a linear relation between L^*_w and J_w after 15 minutes of drying. Therefore, following that linear prediction of the phenomenological coefficient it is possible to estimate the mechanical terms with Equation 8.1.7 (Figure 8.1.4).

$$v_w\,\Delta P = \Delta\mu_w - \Delta\mu^*_w \tag{8.1.7}$$

The evolution of the mechanical energy indicates that there is an expansion of the tissue during the first 400 minutes, followed by a contraction associated with the remaining functioning of the muscle from that time (Figure 8.1.4).

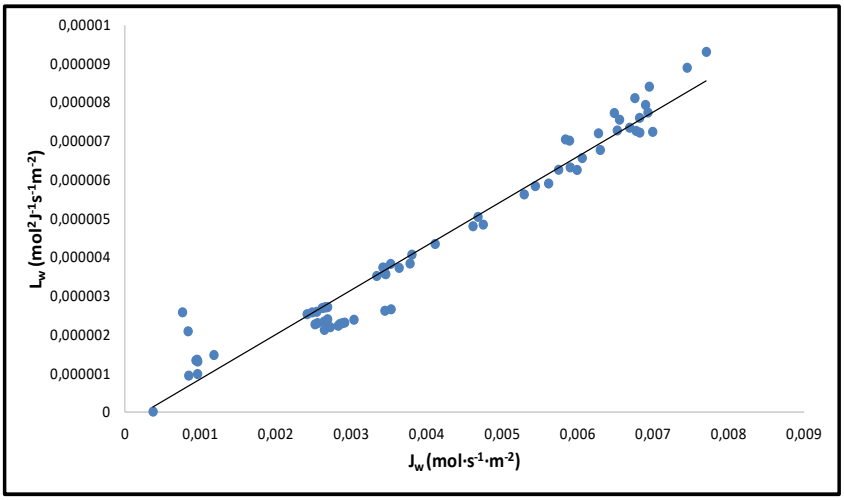

Figure 8.1.3. Relation between the phenomenological coefficient, without considering the mechanical terms, and the water flux from 15 minutes of drying until the end of the treatment.

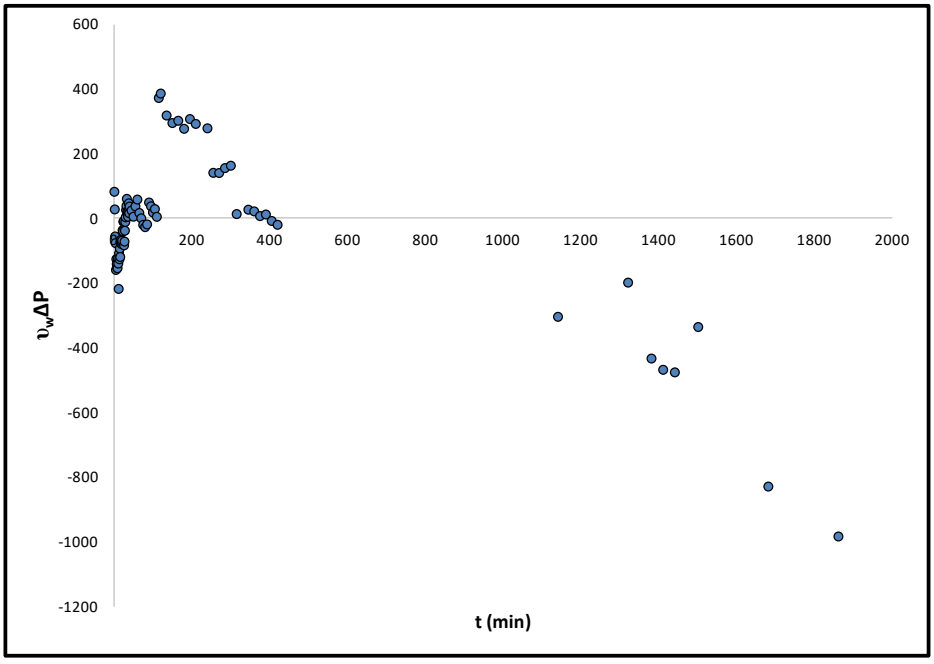

Figure 8.1.4. Evolution of mechanical energy, developed from the thermodynamic model, throughout the drying treatment.

The permittivity in radiofrequency was measured throughout the drying treatment. It was found a linear relation between the dielectric constant in α-dispersion (40 Hz) and the number of water molecules when the sample still presents liquid phase, since this dispersion is fundamentally related to the mobility of the ions dissolved in meat liquid phase. With the drying time, the content of the liquid phase begins to decrease (samples with adsorbed water only) and also the mobility of the ions. The value of the dielectric constant in this dispersion becomes practically null.

4. Conclusions

It has been demonstrated that infrared thermography is a good technique to monitor the process of drying in poultry meat, providing information of heat transfer in biological tissues, being possible to obtain the evolution of the emissivity of the meat. Thus, with this technique, it is possible to non-invasively obtain the surface temperature of the sample during the treatment.

A thermodynamic model has been developed to predict the expansion/contraction phenomena of poultry meat throughout the drying process, as well as to evaluate the driving forces of the drying process.

Finally, a direct relation between the permittivity in α-dispersion with regard to the number of water molecules has been demonstrated. It can be concluded that the permittivity is a non-destructive and rapid method to monitor the evolution of the drying process.

5. Acknowledgments

The authors acknowledge the financial support from: the Spanish Ministerio de Economía, Industria y Competitividad, Programa Estatal de I+D+i orientada a los Retos de la Sociedad AGL2016-80643-R, Agencia Estatal de Investigación (AEI) and Fondo Europeo de Desarrollo Regional (FEDER). Juan Ángel Tomás Egea wants to thank the FPI Predoctoral Program of the Universitat Politècnica de València for its support.

6. References

Castro-Giraldez, M., Fito, P.J. and Fito, P. (2010) 'Non-equilibrium thermodynamic approach to analyze the pork meat (Longissimus dorsi) salting process', *Journal of Food Engineering*, 99(1), pp. 24–30. doi:10.1016/j.jfoodeng.2010.01.023.

Diamante, L.M. and Munro, P.A. (1991) 'Mathematical modelling of hot air drying of sweet potato slices', *International journal of food science & technology*, 26(1), pp. 99–109.

Doymaz, I. and Pala, M. (2002) 'Hot-air drying characteristics of red pepper', *Journal of food engineering*, 55(4), pp. 331–335.

Gou, P., Comaposada, J. and Arnau, J. (2002) 'Meat pH and meat fibre direction effects on moisture diffusivity in salted ham muscles dried at 5° C', *Meat Science*, 61(1), pp. 25–31.

Ratti, C. (2001) 'Hot air and freeze-drying of high-value foods: a review', *Journal of Food Engineering*, 49(4), pp. 311–319. doi:10.1016/S0260-8774(00)00228-4.

Traffano-Schiffo, M.V. *et al.* (2014) 'Thermodynamic model of meat drying by infrarred thermography', *Journal of Food Engineering*, 128, pp. 103–110. doi:10.1016/j.jfoodeng.2013.12.024.

Wang, Z. *et al.* (2007) 'Mathematical modeling on hot air drying of thin layer apple pomace', *Food Research International*, 40(1), pp. 39–46.

Workmaster, B.A.A., Palta, J.P. and Wisniewski, M. (1999) 'Ice nucleation and propagation in cranberry uprights and fruit using infrared video thermography', *Journal of the American Society for Horticultural Science*, 124(6), pp. 619–625.

Otras participaciones en congresos internacionales

Study of water behaviour with dielectric spectroscopy of poultry meat during hot air drying

Congreso: XII International Workshop on Sensors and Molecular Recognition

Fecha: julio 2018

Participación: presentación oral

Organizadores:

- Instituto Interuniversitario de Investigación de Reconocimiento Molecular y Desarrollo Tecnológico (IDM)
- Universitat Politècnica de València
- Universitat de València

Study of water behaviour with dielectric spectroscopy of poultry meat during hot air drying

J.A. Tomas-Egea [1], M. Castro-Giraldez [1], R.J. Colom [2] and P.J. Fito [1]

[1] Instituto Universitario de Ingeniería de Alimentos para el Desarrollo, Universitat Politècnica de València, Camino de Vera s/n, 46022 Valencia, Spain

[2] Instituto de Instrumentación para Imagen Molecular, Universitat Politècnica de València, Camino de Vera s/n, 46022 Valencia, Spain

Abstract: Poultry meat has increased their sales in recent years due to a combination between low price and low-fat content compared to pork and beef, and it is expected to be the most produced type of meat in the World. In this context, it is necessary to improve the processes that are involved the poultry meat, more concretely drying. Spectrophotometry has been widely used for monitoring food processes based in permittivity. The interaction of the photon flux with a biological tissue allows to study and quantify the chemical species present. Taking this into account, the aim of this research is to develop a monitoring tool for poultry drying process using dielectric properties. The experiments were carried out drying cylinders of poultry breast in a hot air dryer. The dehydration was monitored in continuous with K type thermocouples and a thermographic camera for the temperature, a precision balance for the mass and a radiofrequency sensor connected to an Agilent 4294A impedance analyser for the permittivity. The sensor consists of two needles with bluntended. Also, the moisture, volume and water activity were determined before and after the drying operation. The results allowed

us to find a direct relation between the permittivity in the α-dispersion range and the number of water molecules in the surface, following the water flux and; therefore, it is possible to use the permittivity for monitoring the drying mechanisms.

Keywords: poultry meat; radiofrequency; drying.

1. Introduction

Currently, poultry meat, with pork and beef, is one of the most sold type of meat and that sales are rising (Best, 2011). This privileged position is mainly due to a low price and a higher nutritional value compared to its competitors. This type of meat has high amounts of water, so if it is not going to be consumed fresh it is essential to apply conservation operations. Given its widespread consumption, it can be very useful to improve its food safety and process monitor. To optimize the conservation processes, may be a good tool to use the spectrophotometry in the radiofrequency range (Joo et al., 2011).

This technique, capable of measuring the dielectric properties of tissues by measuring the permittivity, is being widely used in human medicine to determine evolutions of myopathies (Traffano-Schiffo et al., 2017) and differentiate varieties of apples in the food industry (Shang, Guo and Nelson, 2015). Also, this technology has been used to develop sensors capable of detecting the white strips of the breasts (Joo et al., 2011), which diminish their nutritional value, and the deep pectoral myopathy in whole chickens.

Permittivity is the physical property that describes the interaction between a photon flux and the medium through which said photons circulate. Low frequency photons, such as those found in radiofrequency and microwaves, generate low energy interactions, which causes their penetration to be very high, allowing the use of this physical property to analyse complex tissues. That is, by analysing the electrical properties of a photon flux when it passes through a biological system, it is possible to determine the quantity

and state of the chemical species present that interact with that flow. The permittivity (ε*) can be defined by Equation 8.2.1.

$$\varepsilon^* = \varepsilon' + \varepsilon'' \tag{8.2.1}$$

where: ε' corresponds to the dielectric constant and ε" to the loss factor.

The dielectric constant (ε') represents the proportion of electrical energy that is stored in the tissue, and the loss factor (ε'') represents the electrical energy transformations in other energies.

The permittivity of the biological tissue presents different dispersions or interactions depending on the frequency range of the photons that circulate. Within the range of radiofrequency, alpha and beta dispersions can be distinguished (Schwan, 1957). The α dispersion occurs in the range from Hz to kHz and represents the orientation of mobile charges within the biological system (Kuang and Nelson, 1998). The β dispersion occurs in the range from a few kHz to MHz and describes the interactions with fixed or low mobility charges (Wolf et al., 2012). β dispersion is divided into two parts: first, the interactions related with the kHz range, which includes the interactions with charges belonging to structural macromolecules that makes up the solid phase of the system; second, the interactions in the MHz range, where the charges associated with the surface tension or interfacial polarizations of the solid surfaces that are in contact with the fluid medium are found.

2. Materials and Methods

For this experiment, chicken cylindrical samples of 2 cm in diameter and 1 cm in height were used. These samples were extracted from boneless chicken breasts (*Pectoralis major*) with a punch. To these chicken cylinders, determinations of mass, water activity, moisture and volume were applied before and after drying with hot air. The water activity was measured with a Decagon dew point hygrometer of the Aqualab®, model series 3 TE and moisture following ISO 1442 of 1997.

The hot air-drying process of the samples was carried out at 40 °C and an air velocity of 1.5 m/s for 67 hours. In addition, the process was continuously monitored by a thermographic camera (Optris PI 160) and K-type thermocouples connected to a datalogger (Agilent 34972A) to measure the temperature, a balance (Mettler Toledo® AB304-S) to measure the mass and an impedance analyser to measure the permittivity in the radiofrequency range.

An Optris PI® 160 infrared camera (Optris GmbH, Berlin, Germany) was installed in front of the sample to monitor the entire drying process. This camera works at wavelengths between 780 μm and 14 μm and uses a two-dimensional focal plane with 160 x 120 pixels, in a spectral range of 7.5 to 13 μm, with a resolution of 0.05 °C and a precision of ± 2 %. It is accompanied by Optris PI Connect software (Optris GmbH, Berlin, Germany) for the analysis of the results. To correct the temperature measured with the thermographic camera, the method developed by Traffano-Schiffo (Traffano-Schiffo et al., 2014) was applied from the Stefan-Boltzman equation (Equation 8.2.2). A reference material with known emissivity (ε =

0.95 - Optris GmbH, Berlin, Germany) was placed next to the sample under study in order to correct the emissivity of the sample. The temperatures of the lateral sample, the reference material with known emissivity and the dryer environment were monitored with K-type thermocouples connected to an Agilent 34901A multiplexer (Agilent Technologies, Malaysia) and registered by Agilent 34972A data acquisition system (Agilent Technologies, Malaysia).

$$E_T = \varepsilon \sigma T^4 \tag{8.2.2}$$

where: E = energy flow received by the infrared camera ($W \cdot m^{-2}$); ε = emissivity of the body; σ = Stefan-Boltzman constant ($5.67 \cdot 10^{-8}$ $W \cdot m^2 \cdot K^{-4}$); T = temperature (K).

The sensor used for measuring the dielectric properties of the sample was developed by the Dielectric Properties Laboratory (Instituto Universitario de Ingeniería de Alimentos para el Desarrollo IIAD) and the Instituto de Instrumentación para Imagen Molecular (I3M) both belonging to the Universitat Politècnica de València (UPV), Valencia, Spain. It consists of two needle electrodes located on both sides of the sample on the cylindrical face. The sensor is connected to an Agilent 4294A impedance analyser. The measuring frequency range is from 40 Hz to 1 MHz and the calibration is performed in open and short.

3. Results

The Infrared thermography allows a non-invasive monitoring of the temperature of the sample throughout the process, but the temperature measured with the infrared camera is not the real temperature. The error

caused by the environment and the fluid that separates it from the sample must be corrected with Equation 8.2.3 (Traffano-Schiffo et al., 2014).

$$E_T = F\,\varepsilon_m \sigma T_m^4 + (1 - \varepsilon_e)\sigma T_e^4 - (1 - \tau_{air}) F\,\varepsilon_m \sigma T_m^4 \qquad (8.2.3)$$

where: E_T = energy measured by the pirosensor ($W \cdot m^{-2}$); F = geometric factor; ε = emissivity (-); σ = Stefan-Boltzman constant ($5.67 \cdot 10\text{-}8\ W \cdot m^{-2} \cdot K^{-4}$); T = temperature (K); τ = transmittance. The subscripts being: m = sample; e = environment; air = air. The first term represents the flow of energy emitted by the sample, the second is the flow of energy reflected by the environment and the third term indicates the flow of energy absorbed by the air. The geometric factor is 1, since the camera's disposition angle allows it (0º). The third term is considered negligible due to the short distance between the sample and the pirosensor.

Once that correction has been made, it is possible to develop a mapping of emissivity related to the energy received by the camera and, once this data is available, with a simple algorithm it is possible to follow the evolution of the temperature of any poultry sample dried with hot air in an industry, through a thermographic camera.

According to Onsager's relations, the water flux (J_w) is related to its chemical potential ($\Delta\mu_w$), by means of the phenomenological coefficient (L_w) (Equation 8.2.4).

$$J_w = L_w \cdot \Delta\mu_w \qquad (8.2.4)$$

Depending on how the coefficient evolves, different phenomena that occur in the sample can be observed.

The water flux that leaves the system (Equation 8.2.5), can be calculated using the data obtained from the balance and other determinations.

$$J_w = \frac{\Delta M_w^m \cdot M_0^m}{\Delta t \cdot S^m \, Mr_w} \tag{8.2.5}$$

where: ΔM^m_w = variation of water mass of the sample (kg); M^m_0 = initial mass of the sample (kg); Δt = time of the process (s), S^m = surface of the sample (m^2); Mr_w = molecular mass of water (18 $g \cdot mol^{-1}$).

The water chemical potential, which acts as its driving force (Equation 8.2.6), is calculated from the temperature data measured continuously and different determinations.

$$\Delta\mu_w = -s_w \, (T^{air} - T^s) + v_w \Delta P + RT^s \ln \frac{a_w^s}{\varphi^{air}} \tag{8.2.6}$$

where: s_w = partial molar entropy of the water ($J \cdot K^{-1} \cdot mol^{-1}$); T = temperature (K); υ_w = partial molar volume of water ($m^3 \cdot mol^{-1}$); P = pressure (Pa); R = constant of ideal gases (8.314472 $J \cdot K^{-1} \cdot mol^{-1}$); a_w = water activity; φ = relative ambient moisture. Being the superscript: s = sample; air = air.

The mechanical term cannot be measured, so the evolution of the phenomenological coefficient calculated without it (L^*_w) was studied in search of trends. After 15 min of drying, it is possible to appreciate a linear relation between L^*_w and J_w. Therefore, following that linear prediction of the phenomenological coefficient it is possible to estimate the mechanical terms with Equation 8.2.7 (Figure 8.2.1).

$$v_w \, \Delta P = \Delta\mu_w - \Delta\mu_w^* \tag{8.2.7}$$

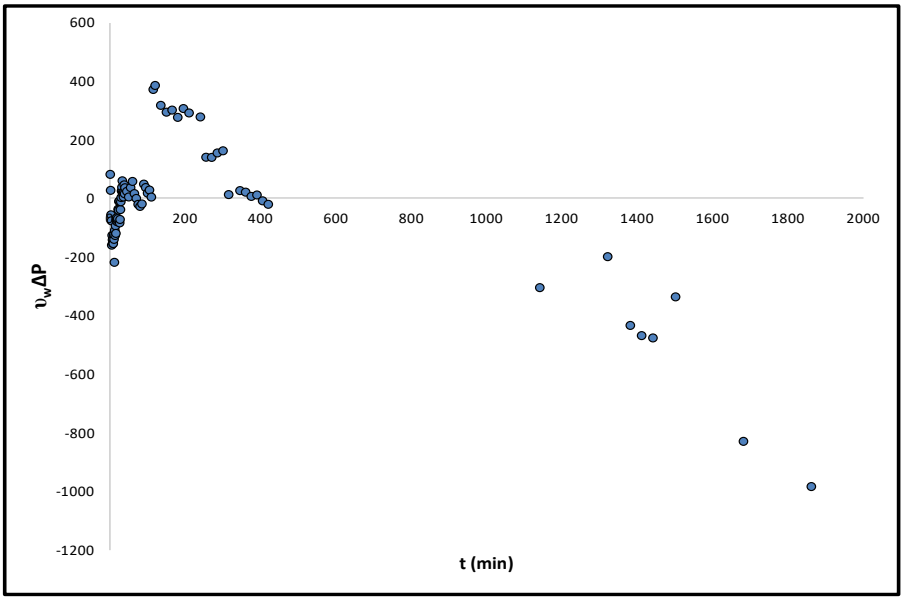

Figure 8.2.1. Evolution of the mechanical energy.

The evolution indicates that there is an expansion of the tissue during the first 400 minutes, followed by a contraction associated with the remaining functioning of the muscle from that time.

The permittivity in radiofrequency was measured throughout the drying treatment. With the obtained data, the evolution of the spectrum of the dielectric constant measured throughout the treatment can be seen in Figure 8.2.2. The value of the permittivity in the α and β dispersions is decreasing throughout the treatment due to the fact that the humidity of the sample during drying, and with this the mobility of the existing ions in the meat is reduced, as well as the mobility of the fixed charges respectively.

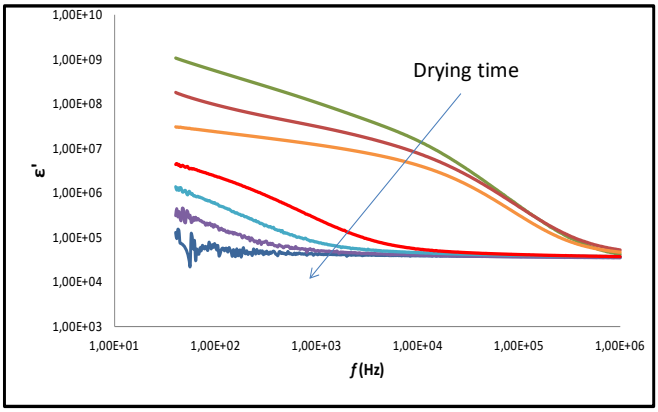

Figure 8.2.2. Spectrum of dielectric constant.

The value of the dielectric constant in dispersion α (40 Hz) and in dispersion β (10 kHz) and its relationship with the number of water molecules in the sample was studied (equation 8.2.8).

$$N_w = \frac{X_w^m \, N_A}{Mr_w} \tag{8.2.8}$$

where N_w represents the water molecules (water molecules / g dry matter), X^m_w the moisture of the sample (dm), N_A the number of Avogadro ($6.022 \cdot 10^{23}$ mol^{-1}) and Mr_w the molecular mass of the water (18 g mol^{-1}).

Figure 8.2.3 shows a linear relation ($R^2 = 0.926$) between the dielectric constant in the α dispersion (40 Hz) and its relation to the number of water molecules when the sample presents a liquid phase, and this dispersion is fundamentally related to mobility of the ions dissolved in the liquid phase of the meat. From an advanced drying time, the content of the liquid phase begins to decrease (samples with water adsorbed only) and with it, the mobility of the ions, the value of the dielectric constant in this dispersion becomes practically zero. Therefore, the amount of water molecules present

in the medium can be measured indirectly, analysing the mobility of mobile loads.

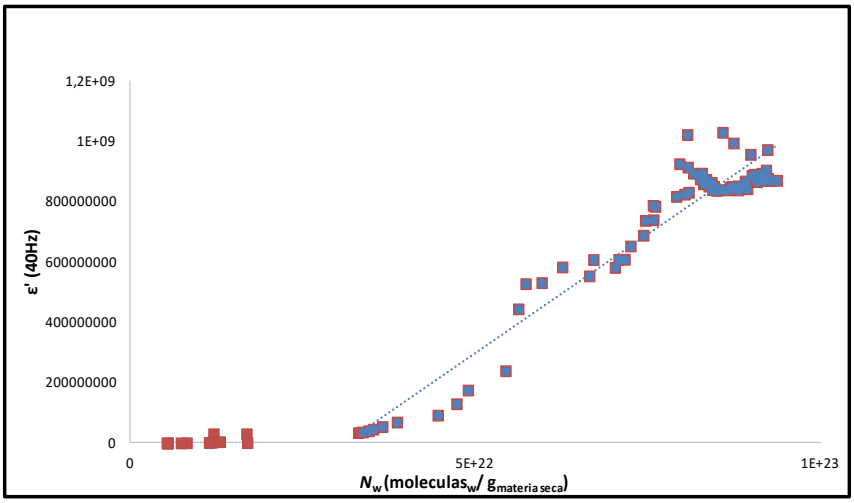

Figure 8.2.3. Relation between the dielectric constant in α-dispersion and the number of water molecules.

4. Conclusions

It has been demonstrated that infrared thermography is a good tool to control the drying process of chicken meat, being possible through emissivity, obtain the evolution of the surface temperature in a non-invasive way. In addition, thermodynamic models have been developed that predict water behaviour and expansion/shrinkage phenomena.

Also, a direct relationship between the permittivity in the α dispersion with respect to the number of water molecules has been demonstrated. Thus, we can conclude that the permittivity is a non-destructive and quick method to monitor the evolution of the drying process.

5. Acknowledgments

The authors acknowledge the financial support from: the Spanish Ministerio de Economía, Industria y Competitividad, Programa Estatal de I+D+i orientada a los Retos de la Sociedad AGL2016-80643-R, Agencia Estatal de Investigación (AEI) and Fondo Europeo de Desarrollo Regional (FEDER). Juan Ángel Tomás Egea wants to thank the FPI Predoctoral Program of the Universitat Politècnica de València for its support.

6. References

Best, P. (2011) 'Worldwide poultry meat production, consumption forecasts', *Rockford, IL, USA* [Preprint].

Joo, I. *et al.* (2011) 'Stress (tako-tsubo) cardiomyopathy following radiofrequency ablation of a liver tumor: a case report', *Cardiovascular and interventional radiology*, 34(2), pp. 86–89.

Kuang, W. and Nelson, S.O. (1998) 'Low-frequency dielectric properties of biological tissues: a review with some new insights'.

Schwan, H.P. (1957) 'Electrical properties of tissue and cell suspensions', in *Advances in biological and medical physics*. Elsevier, pp. 147–209.

Shang, L., Guo, W. and Nelson, S.O. (2015) 'Apple Variety Identification Based on Dielectric Spectra and Chemometric Methods', *Food Analytical Methods*, 8(4), pp. 1042–1052. doi:10.1007/s12161-014-9985-5.

Traffano-Schiffo, M.V. *et al.* (2014) 'Thermodynamic model of meat drying by infrarred thermography', *Journal of Food Engineering*, 128, pp. 103–110. doi:10.1016/j.jfoodeng.2013.12.024.

Traffano-Schiffo, M.V. *et al.* (2017) 'Development of a Spectrophotometric System to Detect White Striping Physiopathy in Whole Chicken Carcasses', *Sensors*, 17(5), p. 1024. doi:10.3390/s17051024.

Wolf, M. *et al.* (2012) 'Relaxation dynamics of a protein solution investigated by dielectric spectroscopy', *Biochimica et Biophysica Acta (BBA)-Proteins and Proteomics*, 1824(5), pp. 723–730.

Sizing burner in drying operations by using alternative energies with environmental sustainability

Congreso: IV International Congress of Food Science and Technology

Fecha: febrero 2017

Participación: presentación en póster

Organizadores:

- Asociación Valenciana de Estudiantes y Profesionales en Ciencia y Tecnología de los Alimentos (AVECTA)
- Universitat de València

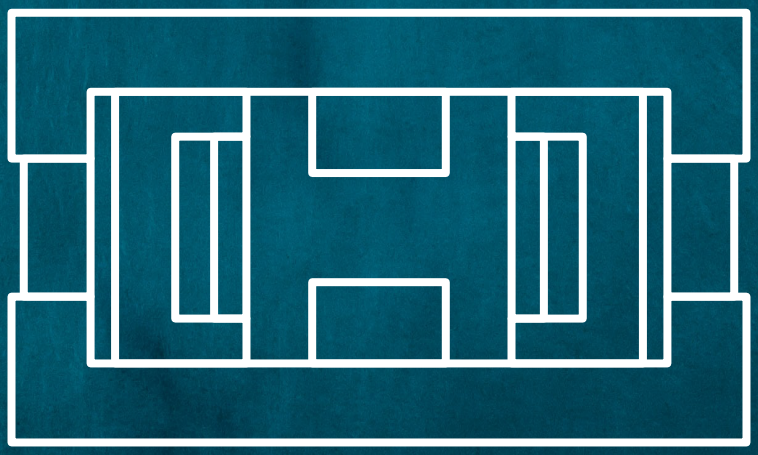

UNIVERSITAT
POLITÈCNICA
DE VALÈNCIA